Phase Transition and Magnetoelectric Properties of $BiFeO_3$-$RMnO_3$ (R: Y^{3+}, Gd^{3+}, Dy^{3+}) and $Bi_{1-x}Ba_xFe_{1-x}Zr_xO_3$ Multiferroic Nanoceramics

thesis submitted to the

National Institute of Technology, Rourkela

for award of the degree of

Doctor of Philosophy in Physics

By

Satya Narayan Tripathy

Under the Supervision of

Dr. Dillip K. Pradhan

Department of Physics and Astronomy
National Institute of Technology, Rourkela-769008.

DEDICATION

To My Parents, Sister

and

Sweet Memories…

DECLARATION

The present dissertation is based on the work carried out at the "Ferroics Laboratory" in the Department of Physics and Astronomy, National Institute of Technology, Rourkela under the supervision of **Dr. Dillip K. Pradhan.** The work was done during the period July 2009 to March 2014. All experiments have been conducted by the author, except the following characterization works. The transmission electron microscopies (TEM) of nanoparticles were carried out by Dr. Shrabanee Sen, Sensor and Actuator Division, Central Glass and Ceramics Research Institute, Kolkata. The Vibrating sample magnetometry (VSM) and magneto-dielectric measurements were measured at Department of Physics, University of Puerto Rico, USA by Dr. Ratnakar Palai. The field emission scanning electron microscopies of some samples were also carried out by Dr. S. R. Das at Birck Nanotechnology Center, Purdue University.

Whenever I have used any materials (*i.e.*, data, theoretical analysis, figures, and text) from other sources, I have given due credit to them by citing them in the text of the thesis and giving their details in the references. Further, I have taken permission from the copyright owners of the sources, whenever necessary.

Satya N. Tripathy
Department of Physics and Astronomy
National Institute of Technology, Rourkela-769008.
Odisha, INDIA.

Department of Physics and Astronomy
National Institute of Technology, Rourkela
Sundargarh-769008, Odisha, INDIA.

Dr. Dillip K. Pradhan
Assistant Professor

CERTIFICATE

This is to certify that the thesis entitled **"Phase Transition and Magnetoelectric Properties of $BiFeO_3$-$RMnO_3$ (R: Y^{3+}, Gd^{3+}, Dy^{3+}) and $Bi_{1-x}Ba_xFe_{1-x}Zr_xO_3$ Multiferroic Nanoceramics"** submitted by **Satya Narayan Tripathy** to the National Institute of Technology, Rourkela for the award of the degree of **Doctor of Philosophy in Physics** is a bonafide record of research work carried out by him under my supervision. In my opinion, the thesis has fulfilled the requirements for which it is being submitted. The contents of the thesis, in full or in parts, have not been submitted to any other Institute or University for the award of any degree or diploma.

Dillip K. Pradhan
(Thesis Supervisor)

ACKNOWLEDGEMENTS

First of all I would like to thank my thesis advisor **Dr. Dillip K. Pradhan** for giving me the opportunity and freedom to work with this project. I would also like to express my deep sense of gratitude and indebtness to my supervisor for his constant encouragement, constructive guidance and inspiration during my research work. I thank you Sir for your help, inspiration and blessings.

I also would like to express my gratitude to my doctoral scrutiny committee members (DSC): Prof. Dillip K. Bisoyi, Prof. Pawan Kumar, Prof. Prakash N. Vishwakarma and Prof. Swedesh Pratihar for their invaluable, insightful comments and suggestions that improved the quality of this work. I also must acknowledge Dr. Sunil K. Sarangi, Director, National institute of Technology, Rourkela for providing me a platform to carry out this research.

I express my heartfelt thanks to Prof. R. N. P. Choudhary (SOA, Bhubaneswar) for his fruitful suggestions and help to my research work.

My special note of appreciation is for Prof. Braja G. Mishra (Department of Chemistry, NIT Rourkela) for his immense support during the synthesis of my samples and Dr. Mandar M. Shirlokar (Hefei National Laboratory for Physical Sciences at the Microscale, China), Dr. Sverre Magnus Selbach (Norwegian University of Science and Technology, Norway) and Mr. Uday K. Sahu (Department of Metallurgical and Materials Engineering, NIT Rourkela) for helping me in X-ray diffraction analysis and valuable suggestions. I also extend my thank to Prof. S. K. Pratihar (Department of Ceramic Engineering, NIT Rourkela) and Dr. Kunal Pal (Department of Biotechnology and Medical Engineering, NIT Rourkela) for providing me the DSC characterization facilities. For FESEM measurements, I would also like to acknowledge Dr. Shrabanee Sen (CGCRI, Kolkata) and Dr. S. R. Das (Purdue University, USA). I also take pleasure in expressing my heart-felt thanks to Dr. Ratnakar Palei and Mr. Dhiren K. Pradhan (University of Puerto Rico, USA) for helping me in magneto-dielectric measurements. I am also thankful to Dr. Rainer Schmidt (Universidad Complutense de Madrid, GFMC, Dpto. Física

Aplicada III, Facultad de Ciencias Físicas, Madrid, Spain) for his fruitful suggestion on magneto-impedance spectroscopy.

I am very much grateful to Dr. Karuna K. Mishra (University of Tennessee, USA), Dr. Ashok Kumar (National Physical Laboratory, Delhi) and Dr. Sunanda Patri for their valuable suggestions and critical reading of the thesis.

I would like to thank everyone in the "Ferroics Laboratory" for making it such a wonderfully diverse, inspiring and fun environment to work in. I would also like to thank my research colleagues and friends Mr. Auroprashad Mohanty, Mr. Tapabrata Dam, Mr. Sanjay K. Swain, Mr. Satya B. Satpathy, Mr. Ganesh K. Sahoo, Mrs. Krishna Raut, Mr. Shuvendu Tripathy, Mr. Soumyaranjan Mohapatra, Mrs. Sunita Nanda, Miss. Rima Sahani, Mr. Karan K. Pradhan, Mr. Mukesh Kumar, Dr. Naresh Kumar, Dr. Paresh K. Majhi, Dr. Punyatoya Mishra, Dr. Alekha Mishra, Dr. Tanmaya Badapanda, Mr. Bijuni Sutar and Dr. Sanjit K. Roy (VIT, Vellore) for their friendly cooperation and help in various ways and making my stay at NIT, Rourkela filled with a lot of memorable moments.

I would also like to thank all the faculty members of Department of Physics and Astronomy for their fruitful suggestions for the thesis.

I express my deep gratitude to my grandmother (Late. Sachhi Tripathy) parents (Mr. Purna Chandra Tripathy, Mrs. Pramodini Tripathy), sister (Mrs. Vijaya Laxmi Tripathy), wife (Smrutimayee Sarangi), first cousin (Mr. Sashanka Sekhar Mahapatra) and brother in law (Mr. Biranchi Narayan Dash) whose support, guidance and love have been a major driving force in this entire period of research. I am very much thankful to sweet loving memories of some people during my stay at NIT.
I have spent seven wonderful years in Rourkela, and I owe that to all my friends here, thank you, all of you !!!

Satya N. Tripathy

ABSTRACT

Magnetoelectric multiferroics have triggered the attention of scientific community because of their intriguing fundamental physics and novel multifunctional device applications. $BiFeO_3$ has been established as a prototype multiferroic materials having perovskite structure. However, the potentials of this material are yet to be realized due to several difficulties in synthesis, characterization and attaining the desired value of magnetoelectric coupling. The physical properties and the phase transition of this material vary as a function of intensive parameters (*i.e.,* temperature, frequency, pressure, electric field and magnetic field). In the present dissertation, we have fabricated nanoceramic solid solution of $(1-x)BiFeO_3-xRMnO_3$ (R: Y^{3+}, Gd^{3+}, Dy^{3+}) and $Bi_{1-x}Ba_xFe_{1-x}Zr_xO_3$ with an aim to demonstrate enhanced magnetoelectric multiferroic properties. These modifications have induced a compositional driven structural phase transition and morphotropic phase boundary in the solid solution. The field emission scanning electron micrographs shows polycrystalline nature of microstructure. Temperature dependent dielectric study of $BiFeO_3$ shows anomaly near antiferromagnetic transition temperature, 364 °C suggesting the signature of mgnetoelectric coupling in the material. The antiferromagnetic ordering temperature decreases towards room temperature with increase in composition. Improved ferroelectric hysteresis loops at room temperature have been observed. The grain and grain boundary contributions from the overall electrical properties have been separated using complex impedance spectroscopic analysis. The temperature variation of the bulk and grain boundary electrical conductivity obeyed the Arrhenius behavior suggesting the thermally activated conduction mechanism. The magnetization versus magnetic field curve for $YMnO_3$ modified $BiFeO_3$ samples has exhibited a switching behavior at low fields. Enhanced magnetization properties have been observed in $GdMnO_3$ and $DyMnO_3$ modified $BiFeO_3$. A cross-over from antiferromagnetism to weak ferromagnetism is observed at $x = 0.1$ for Ba-Zr co-substituted $BiFeO_3$with enhanced magnetization. The behavior of the magnetic hysteresis loops observed at room temperature suggests the suppression of space modulated spin structure. At room temperature, the dielectric permittivity of all the samples decreases with increasing magnetic field. The enhanced magnetoelectric coupling coefficient $(\varepsilon(H)-\varepsilon(0))/\varepsilon(0)$ are found to be -5.5% ($x = 0.2$), -8% ($x = 0.15$) and -18% ($x = 0.2$) for $YMnO_3$, $GdMnO_3$ and $DyMnO_3$ modification respectively at 2 Tesla. The temperature dependent dielectric properties, frequency dependent magneto-capacitance and magneto-impedance measurements demonstrate the signature of magnetoelectric coupling in the materials.

Key Words: Multiferroics; Ceramics Oxide; Crystal structure; Perovskite; Dielectric Properties; Magnetoelectric Properties.

CONTENTS

Chapter-1

Introduction

1.1 Preamble

The interaction between charges and spins in solids is one of the most exciting and fundamental aspects of modern condensed matter physics. Magnetoelectric multiferroics represent a unique class of functional materials, where the primary ferroics (*i.e.,* ferroelectric, ferroelastic and ferromagnetic/antiferromagnetic) ordering coexist. The properties of multiferroic systems are often superior to those of conventional materials because they allow a mutual coupling between ferroic order parameters due to the interaction between spin and charge. This interesting phenomena is called as *magnetoelectric coupling*. Further, multiferroics provide a unique opportunity to exploit several functionalities in a single material which have potential applications in various multifunctional devices such as multiple state memory elements, spintronics and transducers. Therefore, these systems are recently drawing huge attention of scientific community. In fact multiferroics are rare in nature due to the chemical incompatibility and mutual exclusiveness of electric and magnetic ordering. So, combining the magnetic and electric ordering in the same phase becomes a big challenge since its discovery. Among the limited choices, Lead free bismuth ferrite ($BiFeO_3$) with perovskite structure has remained as the prototype multiferroic due to its unique high ferroelectric Curie and antiferromagnetic Neel temperatures. The origin of ferroelectricity in $BiFeO_3$ is due to stereochemistry of Bi 6s orbitals, while the spin of transition metal cation Fe^{3+} is responsible for G-type antiferromagnetic ordering with a long range spin cycloid modulation of period 620 Å. However for its technological applications, there are several major issues yet to be resolved and the origin of the problems warrants further investigation of its resolution. In the present thesis work, we explore the effects of fabrication of solid solution of $BiFeO_3$ with rare-earth manganites $RMnO_3$ (R: Y^{3+}, Gd^{3+}, Dy^{3+}) and $Bi_{1-x}Ba_xFe_{1-x}Zr_xO_3$ on structural, microstructural, dielectric and multiferroic properties at nano scale. Fabrications of solid solutions offer the possibility of driving the crystal symmetry of $BiFeO_3$ near to a morphotropic phase boundary and improving its multiferroic properties by bringing the ferroic transition temperature towards the room temperature. Emphasis will also be given to understand the mechanism behind the magnetoelectric coupling along with structure-property relationship.

1.2 Primary Ferroics

A primary ferroic material represents the existence of either a spontaneous magnetization, or a spontaneous polarization, or a spontaneous stain without the application of external switching force (*i.e.*, magnetic field (**H**), electric field (**E**), or mechanical stress (**σ**)) [1]. These spontaneous order parameters (*i.e.*, magnetization (**M**), polarization (**P**), stain (**ε**)) can be reoriented by an external switching force below a characteristic temperature called as Curie temperature [1]. A domain is a region of the crystal refers to the alignment of the order parameter in a single direction [2]. The domains are randomly oriented prior to the application of a switching force (**E**, **H**, **σ**) thus; no net order parameter persists in the sample. As field is applied and increased, the domains aligned with the fields leading to a net order parameter. At higher fields, the order parameter saturates ($\mathbf{H_s}$, $\boldsymbol{\varepsilon_s}$, $\mathbf{P_s}$) and even if the field is reduced to zero, still there exist a finite order parameter known as remanent order parameter (H_r, ε_r, P_r). So, the M-H/ ε-σ/ P-E response gives rise to hysteresis behavior [2]. The primary ferroic materials could be characterized by a hysteresis response in the external switching force as shown in Figure 1.1.

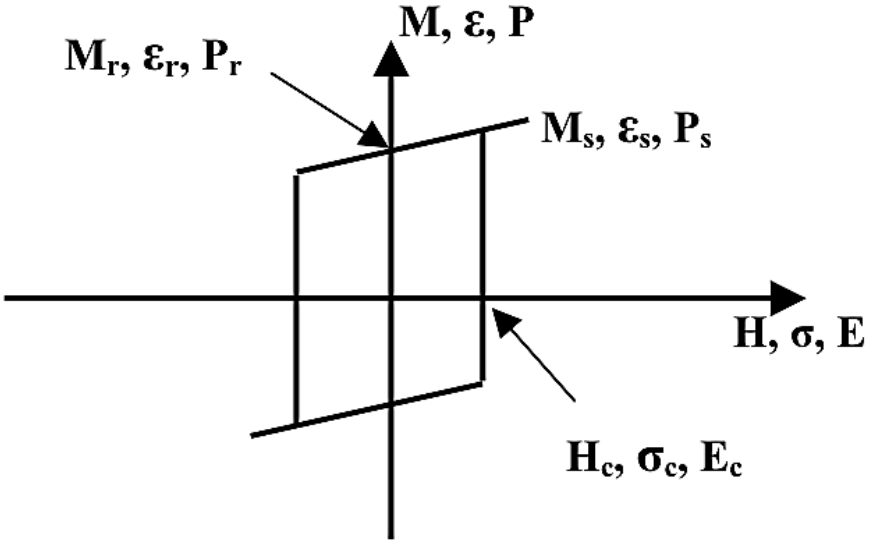

Figure 1.1 Schematic of a hysteresis loop showing the coercive field, remanent and saturation magnetization, strain and polarization for different order parameter [1].

1.3 Ferroelectricity and Related Materials

The phenomenon of ferroelectricity was first discovered in Rochelle salt (Sodium Potassium tartrate tetra hydrate: ($NaKC_4H_4O_4$. $4H_2O$)) in 1920s by J. Valasek [3]. Unfortunately, Rochelle salt showed ferroelectricity with a narrow range of temperature and loses its ferroelectric properties if the composition is slightly altered. These two reasons made it unattractive for practical device applications. During 1930s the phenomenon of ferroelectricity was also discovered in phosphates and arsenates, of which the principal example was Potassium di-hydrogen phosphate, KH_2PO_4 (commonly known as KDP) with a single transition temperature around 122 K [4]. After that, in 1945s ferroelectric behavior was observed in $BaTiO_3$ having perovskite structure [5-8]. This discovery triggered the attention during that time (2nd world war) because it bagged quite a number of "*firsts*"; first ferroelectric without hydrogen bonds, first ferroelectric with more than one ferroelectric phase, first ferroelectric with paraelectric phase. Since then ferroelectric properties have been identified in several structural families. Ferroelectric materials are classified as (i) corner sharing oxygen octahedral (*i.e.,* Perovskite, Tungsten bronze, Pyrochlore, Bismuth layer), (ii) hydrogen bonded radicals (*e.g.,* KDP), (iii) organic polymers (*e.g.,* PVDF, $(CH_2\text{-}CF_2)_n$) [9]. Although all the structural families mentioned above display ferroelectricity, but perovskite structural family shows a greater potential for its suitable properties for novel multifunctional device applications.

Dielectrics belong to a group of insulators, which can be polarized by the action of an applied electric field. These are broadly divided into two classes such as (i) polar dielectrics and (ii) non-polar dielectrics [10]. A dielectric having finite and permanent polarization even in the absence of electric field is known as polar dielectrics. Ferroelectrics are non-linear polar dielectrics. Some outstanding properties of the ferroelectric materials are [11]: (i) they have permanent dipole and so their molecular structures are lack of center of symmetry, (ii) all ferroelectric crystals must be piezoelectric though the converse is not true, (iii) all ferroelectric materials have one or more Curie temperature, (iv) structural change takes place at Curie temperature, (v) immediately above the Curie temperature, the dielectric permittivity of the ferroelectric material obeys Curie-Weiss law, and (vi) a ferroelectric is generally defined as one which exhibits hysteresis loop [11].

The structure and symmetry of a material plays an important role in the ferroelectric phase transition phenomena. In crystallography, there are 7 crystal systems which can be classified into 14 *Bravais lattices*. Further, these 7 crystal systems are classified into 32 point groups. Out of 32 point groups, 11 are centrosymmetric (non-polar). This leaves 21 non-centrosymmetric groups (except point group-432), 20 are piezoelectric [1-2, 11]. A piezoelectric material is one that undergoes a change in polarization when stress is applied. In converse effect, after applying an electric field, the crystal will be stretched or compressed (strain is developed) depending on the electric field's orientation to the polarization of the crystal. 10 out of the 20 point groups are called pyroelectric (*i.e.*, polarization changes with application of temperature). Those pyroelectric materials whose polarization cane be reversed by the application of electric field known as ferroelectric. Hysteresis loop is the signature of ferroelectric materials. Ferroelectric materials are used for a large number of applications including high-permittivity capacitors, memory devices and electric-optic devices. Symmetry hierarchies for ferroelectric materials is shown in Figure1.2

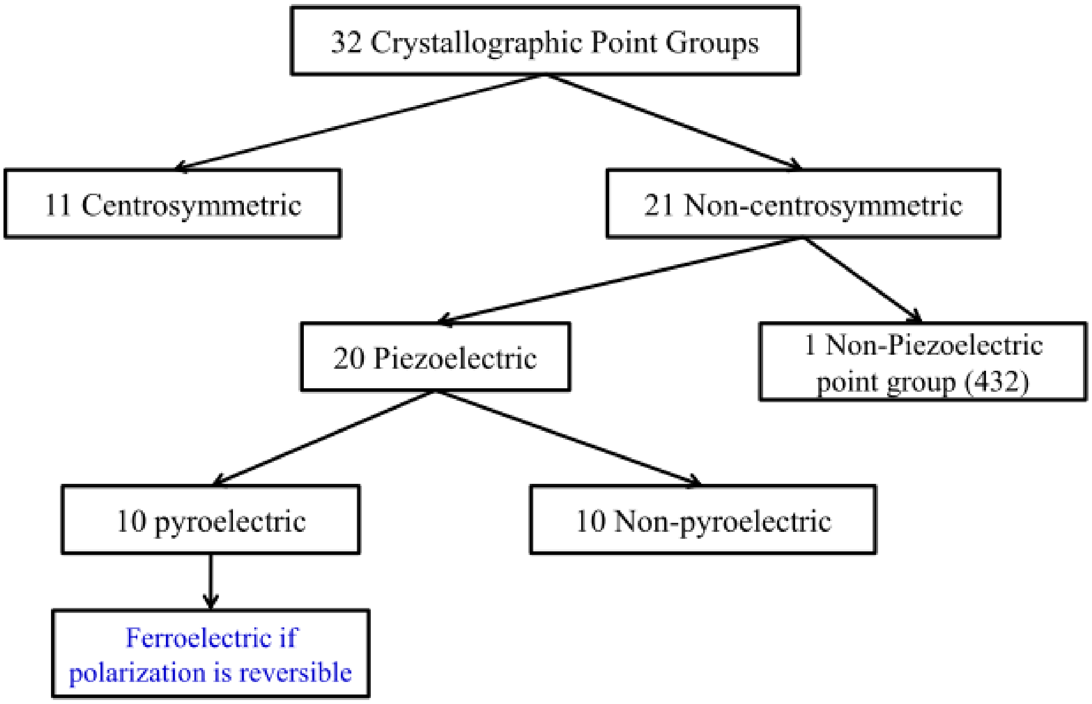

Figure 1.2 Symmetry hierarchies for ferroelectric materials [1].

Ferroelectric materials undergo a structural phase transition from a polar to a non-polar structure. All ferroelectric materials have a transition temperature called the Curie point (T_C) [12-13]. At temperature $T > T_C$, the crystal does not exhibit ferroelectricity *i.e.,* it is paraelectric, while for $T < T_C$ it is ferroelectric. On decreasing the temperature through the Curie point, a ferroelectric crystal undergoes a structural phase transition from a centrosymmetric non-polar, (*i.e.*, paraelectric) to a non-centrosymmetic polar structure (*i.e.*, ferroelectric state). If there is more than one ferroelectric phase, the temperature at which the crystal transforms from one ferroelectric phase to another is called the transition temperature. Near the Curie point or phase transition temperature, thermodynamic properties including dielectric, elastic, optical, and thermal constants show anomalous behavior. A maximum value of the relative permittivity is observed at the Curie temperature due to the phase change from a paraelectric phase to a ferroelectric phase. The temperature dependence of the dielectric permittivity above the Curie point ($T > T_C$) in ferroelectric crystals is governed by the Curie-Weiss law [12-13]:

$$\varepsilon = \varepsilon_0 + \frac{C}{T - T_C}$$

where ε is the permittivity of the material, ε_0 is the permittivity of vacuum, C is the Curie constant and T_C is the Curie temperature.

1.4 Ferromagnetism and Related Materials

The phenomenon of magnetism is familiar to mankind for thousands of years. Lodestone (Fe_3O_4) was the first permanent magnetic material to be identified and studied extensively [14]. Three principal sources of magnetic moment of an atom/ion are: (i) the spin of electrons (ii) electron orbital angular momentum about the nucleus and (iii) a change in the orbital moment by an applied magnetic field. The first two effects give paramagnetic contributions to the magnetization and the third one gives rise to diamagnetic contribution [14].

The magnetic properties in a crystal depend on the following factors: (i) the magnetic property associated with each atom/ion and (ii) the mutual interactions between these magnetic moments. When there are unpaired electrons, every atom/ion has a net magnetic moment. Depending on the interactions between the magnetic moments; the crystal may display (i) paramagnetism (PM)

(ii) ferromagnetism (FM) (iii) antiferromagnetism (AFM) and (iv) ferrimagnetism (FIM) (c.f. Figure 1.3). In a paramagnetic material, alignment of adjacent moments is not possible due to thermal instability. Ferromagnetism involves parallel aligned adjacent moments associated with domains. Antiferromagnetic order consists of antiparallel aligned equal moments. Ferrimagnetic order involves antiparallel unequal moments, resulting in a non-zero net magnetization [14].

Ferromagnetism is a very strong magnetic interaction as compared with paramagnetic and diamagnetic behaviors. It is characterized by a transition temperature *i.e.*, Curie temperature, T_C above which the crystal becomes paramagnetic. Below this temperature, it is ferromagnetic. Antiferromagnetic materials occur commonly among transition metal compounds, especially oxides. Generally, antiferromagnetic order may exist at sufficiently low temperatures, vanishing at and above a certain temperature, the Néel temperature (T_N). Above the Néel temperature, the material display paramagnetic behavior. The magnetic susceptibility, $\chi = M/H$, which defines the degree of magnetization of a material in response to a magnetic field, is an indication of their magnetic behavior. If χ is positive, the material is paramagnetic and the magnetic field is strengthened by the presence of the material. If χ is negative then the material is diamagnetic and the magnetic field is weaken in the presence of the material [14-15].

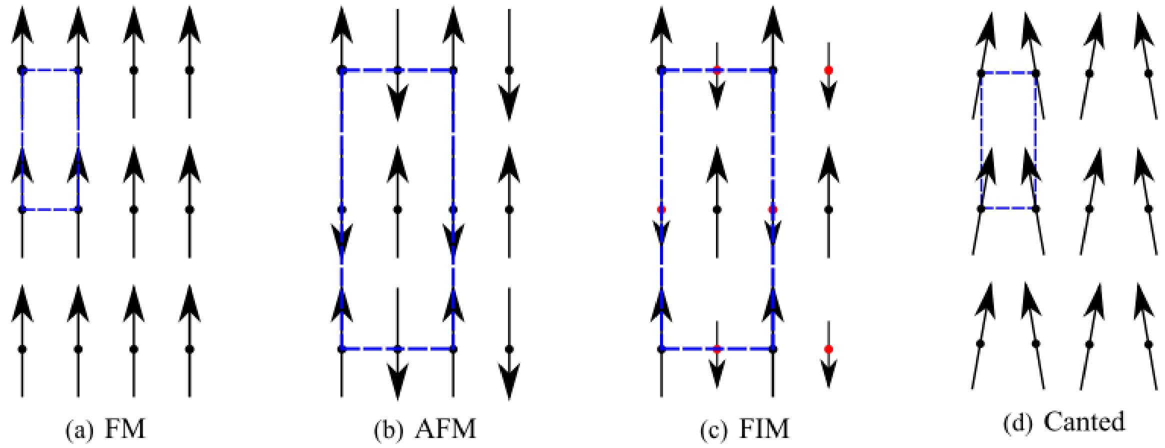

Figure 1.3 Schematic diagrams showing the spins of **(a)** ferromagnet, **(b)** antiferromagnet, **(c)** ferrimagnet and **(d)** canted antiferromagnetic [14].

1.5 Multiferroics and Related Materials

Multiferroic materials display simultaneously two or more primary ferroic order parameters (*i.e.*, ferroelectric, ferromagnetic and ferroelastic) in a single phase and enable a coupling interaction between them [16]. This coupling is called the magnetoelectric (ME) effect which allows a mutual control of magnetization and electric polarization in these materials [17-19]. Because of these unique properties, multiferroic materials can have many interesting potential device applications such as multiple state memory elements, electric field controlled ferromagnetic resonance devices, transducers, spintronics and terahertz radiation [16]. Figure 1.4 shows the coupling between ferroic order parameters in multiferroics.

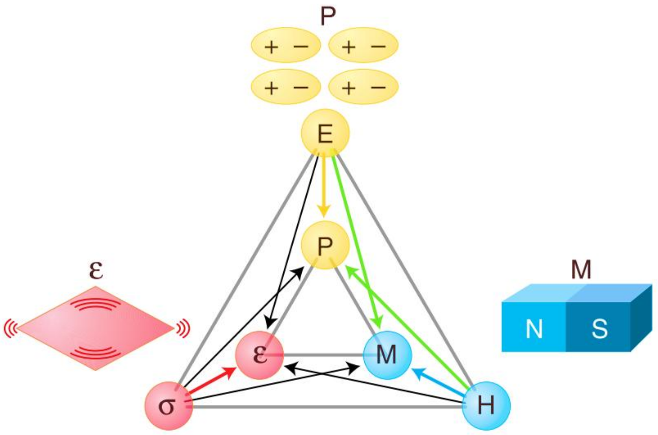

Figure 1.4 Phase control in ferroics and multiferroics: The electric field **E**, magnetic field **H**, and stress **σ** control the electric polarization **P**, magnetization **M** and strain **ε**, respectively [20].

Multiferroic materials are rare in nature due to the chemical incompatibility and mutual exclusiveness of ferroelectric and ferromagnetic ordering [21]. N. A. Hill suggested that *d*-orbital occupancy of the B-site cation in perovskite (ABO_3) materials plays a crucial role in reducing the tendency to show ferroelectricity [21]. Eventually this mechanism reduces the chance for the material to be a multiferroic, unless there are other possible mechanisms (such as ferroelectricity via lone pair mechanism) that allow for this phenomenon *e.g.*, $BiFeO_3$ [22].

In multiferroics, coupling between (anti-) ferroelectricity and (anti-) ferromagnetism will lead to the magnetoelectric effect which means magnetic polarization will be induced by applying an external electric field or vice versa [16-17]. The effects can be linear or/and non-linear with respect to the external fields, which can be obtained from the differentiation of the expansion of the free energy of a material. According to Landau-Devonshire theory, the polarization and magnetization for a multiferroic system are defined as differentiation of free energy (F);

$$M_i(\vec{E},\vec{H}) = \frac{-\partial F}{\partial H_i} = M_i^S + \mu_0\mu_{ij}H_j + \alpha_{ij}E_i + \beta_{ijk}E_iH_j + \frac{1}{2}\gamma_{ijk}E_jE_k - ...$$

$$P_i(\vec{E},\vec{H}) = \frac{-\partial F}{\partial E_i} = P_i^S + \varepsilon_0\varepsilon_{ij}E_j + \alpha_{ij}H_j + \frac{1}{2}\beta_{ijk}H_jH_k + \gamma_{ijk}H_iH_j - ...$$

Where *E*, *H*, P^s, M^s are electric field, magnetic field, polarization, and magnetization, respectively. Here α corresponds to linear magnetoelectric effect. The parameters β and γ refer to higher order magnetoelectric coefficients. The primary ferroic order parameters can be categorized by their behavior under space and time inversion [23] as shown in Figure 1.5. Ferroelasiticity and ferroelectricity involve spatial inversion whereas ferromagnetism displays time reversal. Magnetoelectric multiferroics correspond to simultaneous violation of space and time inversion symmetry. The phenomenon of ferrotroidicity, which is the order parameter of multiferroics is still under debate [24].

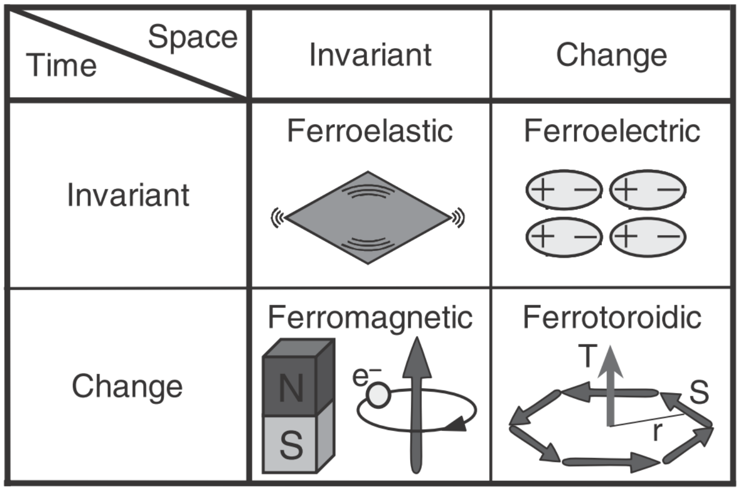

Figure 1.5 Forms of ferroic orders and their transformation properties under the parity operations of spatial inversion and time reversal symmetry [25].

Multiferroics have been classified in to two types according to their origin of microscopic mechanism *i.e.*, (a) Type-I multiferroics and (b) Type-II multiferroics. In Type-I multiferrroics ferroelectricty and magnetism appear from different independent sources leading to weak ME coupling [16-17, 22, 26]. In these materials (Examples: $BiFeO_3$, $YMnO_3$), ferroelectric transition temperature is higher than magnetic ordering transition temperature. On the contrary, in Type-II multiferroics (Examples: $TbMnO_3$ and $TbMn_2O_5$), ferroelectric ordering appears from magnetic ordering (origin from same source) suggesting a strong magnetoelectic coupling [26, 27]. The microscopic origin of multiferroism found in Type-I and Type-II multiferroics are shown in Figure 1.6 and Figure 1.7 respectively.

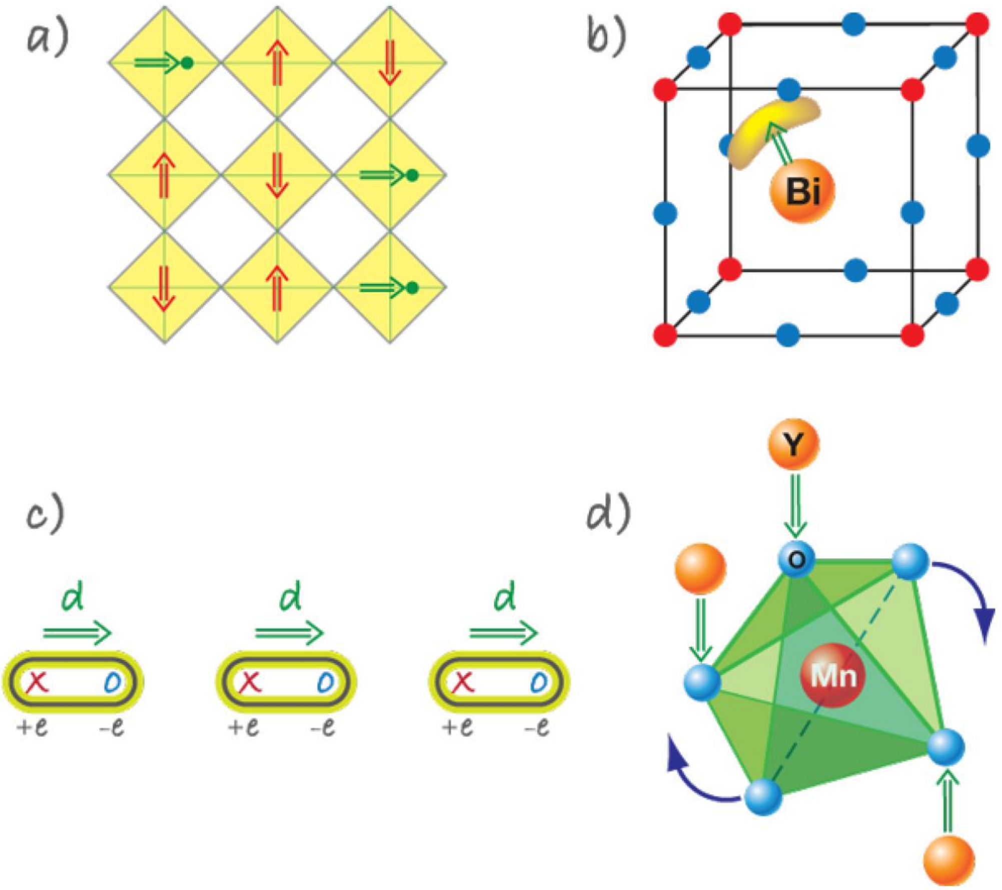

Figure 1.6 Microscopic mechanism found in multiferroics: **(a)** In mixed perovskites with ferroelectric active d^0 ions (green circles) and magnetic d^n ions (red) **(b)** lone-paired multiferroics **(c)** charge-ordered multiferroics **(d)** geometric multiferroics [22].

1.5.1 Type-I Multiferroics

A. *Mixed Pervoskites*: This is a straight forward approach to achieve both magnetism and ferroelectricity in a single phase perovskite compound. For example, in $PbFe_{1/2}Nb_{1/2}O_3$ the origin of ferroelectricity is attributed to off-centre shifts of Nb^{5+} whereas the magnetism is due to Fe^{3+} ion. These systems display low magnetoelectric coupling [28].

B. *Ferroelectricty due to Lone Pair*: In $BiFeO_3$, the outer $6s^2$ lone pair of electrons does not participate in chemical bond and hybridize with an empty p orbital which gives rise to a structural distortion and induces ferroelectricity. This is an example of the second-order *Jahn–Teller* effect. The origin of magnetism is due to the presence of Fe^{3+} transition metal ion. Hence multiferroicity is achieved [29].

C. *Ferroelecticty due to Charge Ordering*: This phenomenon of charge ordering appears in transition metal compounds with transition metal ion with different valancies. If after the charge ordering both site and bond turn out to be inequivalent, then this gives rise to ferroelectricty. The appearance of magnetism is attributed to transitional metal ion. Example: $Pr_{0.5}Ca_{0.5}MnO_3$ [30].

D. *Geometrically Driven Ferroelectricity*: Ferroelectricity in the hexagonal manganites is driven by geometric and electrostatic mechanisms. For example ferrolecticity in $YMnO_3$ is caused by the tilting of rigid block of MnO_5 while magnetism is due to Mn^{3+} ion [31].

1.5.2 Type-II Multiferroics

In type-II multiferroics (*i.e.,* magnetically driven multiferroics), FE is caused by magnetic ordering which leads to the strong coupling. The possible origins of this behavior are two. The first involves an inverse *Dzyaloshinskii-Moriya effect*, which functions in systems with non-collinear spin structures, usually spiral magnetic structures (*i.e.,* in which spins rotate around an axis perpendicular to the propagation vector of the spiral). Thus it requires the direct action of the spin-orbit interaction [16-17, 32-41]. The induced electric polarization is orthogonal to the propagation vector and lies in the spiral plane. This mechanism is responsible of ME effect in systems like $TbMnO_3$, $Ni_3V_2O_8$, $MnWO_4$ and $BaNiF_4$ [32-41]. The second mechanism is based on *magneto-striction* and can take place also in collinear magnetic structures, not requiring the presence of spin-orbit coupling. In $HoMnO_3$ *magneto-striction* gives rise to multiferroic behavior through the presence of a periodic collinear spin arrangement of the up-up-down-down type that can induce electric polarization via *exchange-striction* mechanism [16-17].

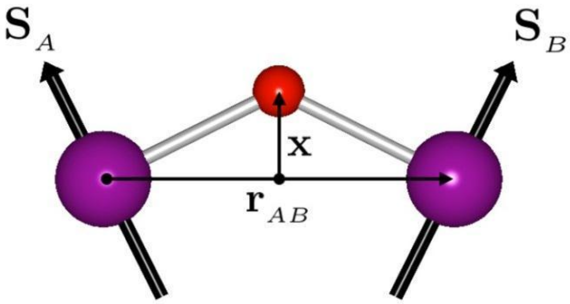

Figure 1.7 Dzyaloshinskii-Moriya effects: The coupling between spins S_A and S_B on sites A and B respectively takes the form $H_{DM} = (x \times r_{AB}).(S_A \times S_B)$ where the coupling constant depends on the vector r_{AB} connecting the site A to the site B, and on the displacement "x "of the ligand ion from the AB line. The anti-symmetric exchange mechanism giving rise to ferroelectricity [36].

1.6 Perovskite Structure

The term ‘perovskite’ relates to a large family of crystals with structures similar to that of the mineral $CaTiO_3$. This was named after the Russian mineralogist Count Lev Aleksevich von Perovski [42]. The perovskite structure is represented by ABX_3 which comprises of corner-linked octahedra of X anions with ‘B’ cations at their centers and ‘A’ cations in the interstices formed by the anion octahedral as shown in Figure 1.8. In general, ‘A’ ion has 12-fold cuboctahedral coordination whereas ‘B’ is octahedrally coordinated by the X cations. The valence of the A cation ranges from +1 to +3 and the B cation from +3 to +6. The ionic radii of ‘A’ atoms are larger than the 'B' atoms and X is typically either oxygen or a fluorine ion. The ideal perovskite structure is cubic symmetry (space group $Pm\bar{3}m$) with lattice constant around ~ 4 Å. The cations may occupy 1*a* or 1*b* positions and the oxygens occupy 3*c* or 3*d* Wyckoff positions. The two possibilities of occupation offer two different views of the unit cell by shifting the origin (0, 0, 0) to (½, ½, ½) as shown in Figure 1.8 [42]. The cubic prototype structure is always expected at high temperature and at high pressure for all perovskites. Perovskites have attracted much attention due to coupling of spin, charge and orbital ordering which offers wide range of electric, magnetic, transport and multiferroic properties [42].

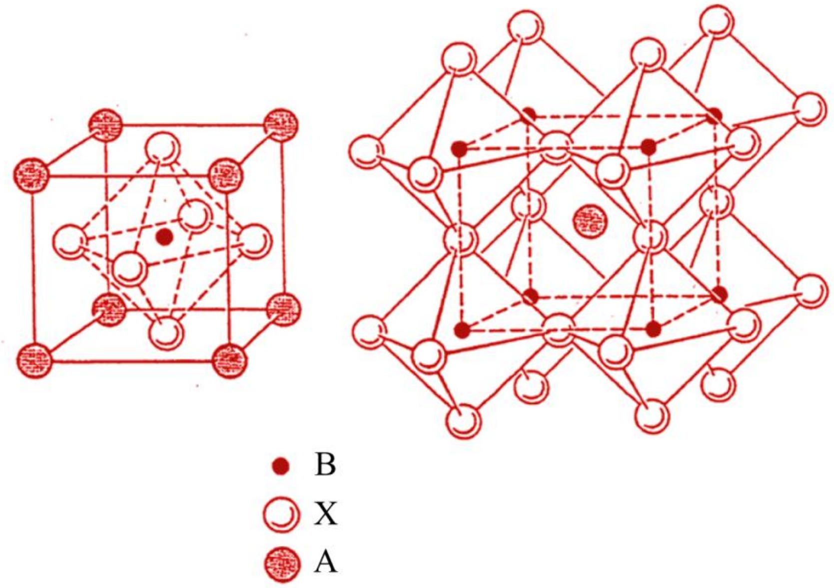

Figure 1.8 Schematic view of the cubic prototype perovskite-type structure with the formula ABX_3.

1.6.1 Perovskite Deformation

In perovskite structure, the structural phase transitions are attributed to doping or changes in the physical parameters (*i.e.*, temperature, pressure, electric field). The perovskite structure is very flexible because it can accommodate atoms of variable valence. The physical properties (*i.e.*, ferroelectricity, colossal magneto-resistance, superconductivity, charge ordering and spin-dependent transport) of the perovskites are influenced by structural changes which are significant from application point of view [42-46].

The modifications or deformations in the perovskite structure are mainly due to the following effects: (a) cation displacement, (b) octahedron distortion and (c) anion octahedron tilt. Cation displacement is found in ferroelectric materials whereas octahedron distortion occurs in magnetic perovskites. Tilt is a more complex deformation which corresponds to the rotation of neighboring octahedrons. The classic formula describing the deformation of perovskite was proposed by Goldschmidt [42-46].

$$\text{"Goldschmidt tolerance factor"} = t = \frac{r_A + r_X}{\sqrt{2}(r_B + r_X)}$$

Here, r_A, r_B and r_X are the radii of A, B and X ions. Considering the ionic radii change in different chemical environments, the revised formula is:

$$t = \frac{d_{A-X}}{\sqrt{2}d_{B-X}}$$

Here, $d_{A\text{-}O}$ and $d_{B\text{-}O}$ are the distances between cations (A or B) and anion (X).

A perovskite structure is said to be stable if "t" lies in the range $0.80 < t < 1.1$. It has been seen that $t > 1.0$ normally favors tetragonal distortions whereas $t < 1.0$ favors orthorhombic or monoclinic symmetries. The ideal perovskite structure ($t = 1.0$) is cubic symmetry. It is to be noted that many ferroelectric compounds crystallize in a rhombohedral structure (*R3c*) while magnetic perovskites crystallize in an orthorhombic structure (*Pbnm/ Pnma*) [42-46].

1.7 Prototype Multiferroic $BiFeO_3$: Phase Diagram and Physical Properties

Although, the idea of combining ferroic order parameters conceived in 1960s, the incompatibility and mutual exclusiveness stood as a big obstacle on its path. Again with the discovery of some promising perovskites, hexagonal manganites and composites, a breakthrough in the field of multiferroics has been achieved in recent years [16-17]. The limiting factors for simultaneous existence of electric and magnetic ordering are: (i) FE are insulators while FM are metals, (ii) the d^0 *vs.* d^n problem and (iii) there are thirteen point groups which allow both FE and FM [21]. Although the observation of multiferroic materials rare in nature, still there several multiferroics have been identified and studied since its discovery. Those widely studied materials are *Boracites* ($Ni_3B_7O_{13}I$, $Cr_3B_7O_{13}Cl$) [47], *Fluorides* $BaMF_4$ (M: Mn, Fe, Co, Ni) [48], *Magnetite* Fe_3O_4**,** (Y/Yb)MnO_3 [49], *Pyroxenes* $AMSi_2O_6$ (A: mono or divalent metal, M: di or trivalent metal) [50], $RMnO_3$ (R: Dy, Tb, Ho, Y, Lu) [51-52], RMn_2O_5 (R: Nd, Sm, Dy, Tb) [53] and $BiBO_3$ (B : Mn, Fe) [54, 55]. Among the limited choices, $BiFeO_3$ (BFO) with a distorted perovskite ABO_3 structure is a robust multiferroic material owing to its high ferroelectric transition temperature (T_C ~ 830 °C) and antiferromagnetic Néel temperature (T_N ~ 370 °C) [56]. BFO is probably the most well-studied Bi-based multiferroic perovskite due to its multiferroic properties as well as it is lead free, which makes it more suitable for possible novel multifunctional applications [16-17, 54].

The crystal structure of $BiFeO_3$ is rhombohedral with *R3c* space group and can be viewed as a 3D network of corner-sharing FeO_6 octahedra with 12-coordinated Bi cations having lattice parameter: $a_r = 5.63$ Å, rhombohedral angle $\alpha_r = 59.35°$, or alternatively as a hexagonal structure with parameters $a_{hex} = 5.58$ Å and $c_{hex} = 13.87$ Å [54, 57]. The atomic positions of Bi^{3+}, Fe^{3+} and O^{2-} in the hexagonal setting of *R3c* space group is shown in Table 1.1 as per *Megaw and Darlington* formalism [58, 59]. Coordinates of all the atoms in the asymmetric unit cell of *R3c* space group can also be written as a function of the displacement parameters; *s*, *t*, *d* and *e* as shown in Figure 1.9.

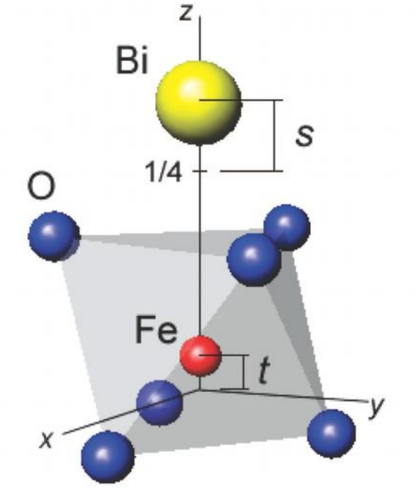

Figure 1.9 As per Megaw and Darlington formalism of $BiFeO_3$, displacement parameters *s* and *t* of Bi^{3+} and Fe^{3+}, along the hexagonal $[001]_{hex}$ axis. Spontaneous polarization P_s is parallel to the [001] axis and anti-ferrodistortive rotation of the oxygen octahedron is about the $[001]_{hex}$ axis [58].

Table 1.1 The atomic positions of Bi^{3+}, Fe^{3+} and O^{2-} in the hexagonal setting of *R3c* space group as per Megaw and Darlington formalism [58, 59].

Ions	x	y	z
Bi^{3+}	0.0	0.0	$\frac{1}{4} + s = 0.3$
Fe^{3+}	0.0	0.0	$t = 0.02$
O^{2-}	$\frac{1}{6} - 2e - 2d = 0.23$	$\frac{1}{3} - 4d = 0.34$	$\frac{1}{12}$ (Fixed)

The parameters s and t describe the polar displacement of cations Bi^{3+} and Fe^{3+} along polar axis; $[111]_{rh}$ of the rhombohedral axis or $[001]_h$ the hexagonal axis. The displacement parameter *e* of oxygen O^{2-} from its ideal position is related to the tilt angle (ω) of anti-phase rotation of the oxygen octahedra about the $[111]_{rh}$ rhombohedral direction and can be expressed as $\omega = \tan^{-1}(4e3^{1/2})$ [58, 59]. This rotation angle of the oxygen octahedral (ω) is an important structural parameter to describe the perovskites. The parameter d is related to the distortion of the FeO_6 octahedra. The z coordinate of the oxygen ion is fixed at $z = 1/12$. The displacement parameter of Bi^{3+} (s) is larger than the displacements parameter of Fe^{3+} (t). These displacements are cooperative and in the same direction, since the parallel displacements are energetically strongly favored compared to antiparallel due to electrostatic repulsion between the cations. The cooperative displacement (s-t) is shown to have a linear relation to the crystallographic spontaneous polarization of some perovskites. For $BiFeO_3$, ω is calculated to be around 11°–14° about the polar [111] axis, which is directly related to Fe–O–Fe angle, calculated to be around 154–156°[54]. The Fe–O–Fe angle is important because it controls both the magnetic exchange and orbital overlap between Fe and O ions and it determines the magnetic ordering temperature. Haumont *et al.* studied extensively the phase stability, the effect of temperature and high pressure on structural properties of multiferroic BFO [60-62].

The phase diagram of the system Bi_2O_3-Fe_2O_3 has been shown in Figure 1.10 and contain following phases at room temperature; *sillenite* (bismuth rich) with composition $Bi_{25}FeO_{39}$, the perovskite BFO and *mullite* having composition $Bi_2Fe_4O_9$ [54,63]. During the synthesis of $BiFeO_3$, the formation of the *sillenite* and *mullite* phases are quite natural. This becomes a challenge to get stoichiometric BFO and we have successfully synthesized the pure phase BFO which will be discussed in Chapter-3. According to the phase diagram, BFO is a stable compound up to the decomposition temperature (930-934 °C), where BFO melts incongruently. At approximately 825 °C there is a first-order transition to a high-temperature β phase that is accompanied by a sudden volume contraction [54, 63-64]. The transition is also accompanied by a peak in the dielectric constant vs. temperature plot; which has been taken as an indication of a ferroelectric–paraelectric transition. There are several controversies on the crystal structure of β phase of BFO and reported to be rhombohedral ($R\bar{3}c$) and monoclinic [54, 58, 60-64].

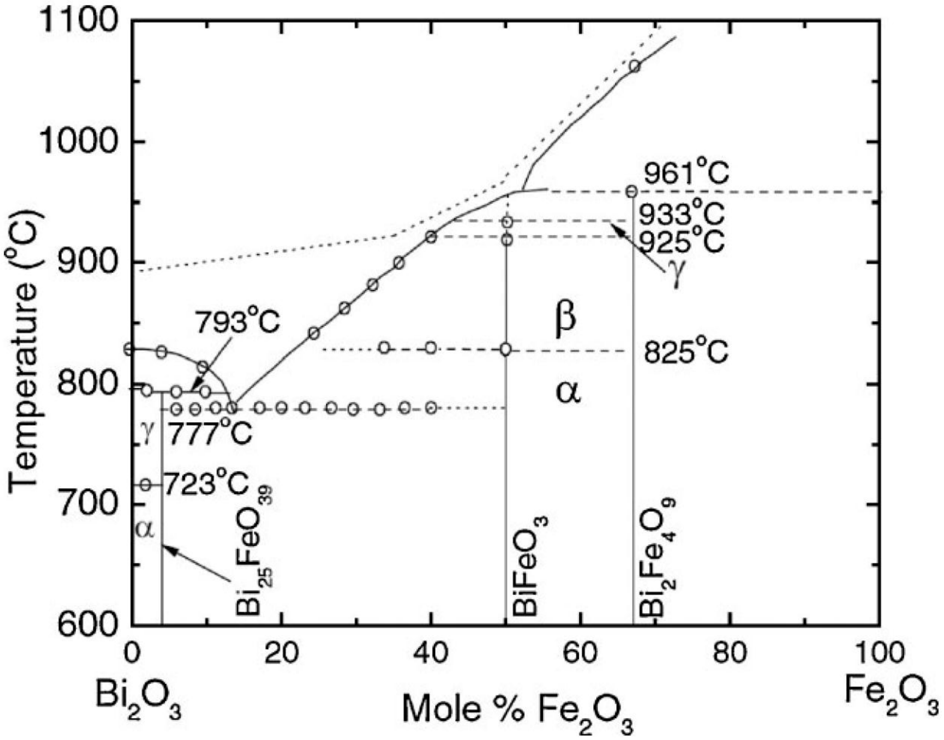

Figure 1.10 The phase diagram of the system Bi_2O_3 -Fe_2O_3 [63].

The origin of ferroelectricity in BFO is the due to stereochemistry of Bi $6s^2$ lone pair and the ferroelectric to paraelectric transition is around 825 °C [54, 56]. The ferroelectric polarization of bulk bismuth ferrite is along the diagonals of the perovskite unit cell (*i.e.*, $[111]_{\mathrm{rho}}$ / $[001]_{\mathrm{hex}}$). In early 70's the measurements of ferroelectric properties on bulk BFO yielded only small values of the polarization. Teague *et al.* observed a small value of remanent polarization (*i.e.*, $P_r = 3.5\mu C/cm^2$) even at higher field of 55 kV/cm at 80 K for single crystal of BFO [65]. They explained the small magnitude of saturation polarization (expected to be more by them) could be (i) due to high leakage current or (ii) only partial alignment of the domains. Later Lou *et al.* reported that magnetite phase formation takes place under voltage stressing which affect the multiferroic properties [66]. It took more than 30 years for accurate measurement of ferroelectric properties of BFO on high quality thin films and single crystals. Ramesh and his group first reported the significant remanent polarization in $BiFeO_3$ thin film, which is 15 times larger than bulk and this enormously inspired the research activity on this material [67]. The studies on thin film of BFO indicate that the defects cause the leakage current in the bulk samples. It was later verified that the formation of Fe^{2+} and oxygen deficiency gives rise to leakage current and its presence can be prevented by short sintering time with rapid heating rate. Different approaches have been attempted to reduce leakage current such as: synthesis using various soft chemical route, doping at A and B-site of BFO, growing high quality single crystal and thin films [16-17, 26-27, 54]. *Ab initio* calculations also agreed that the polarization of bulk $BiFeO_3$ is intrinsically high (ca. 90–100 $\mu C/cm^2$) and relatively insensitive to strain [54]. In contrast with the large polarization properties, the piezoelectric coefficient d_{33} is considerably smaller in $BiFeO_3$ (15-60 pm/V) than that of prototype ferroelectrics $BaTiO_3$, $PbTiO_3$ and $PbZr_{1-x}Ti_xO_3$ (100-200 pm/V) [54]. The room temperature dielectric permittivity ε_r ~ 30 is also small compared to the mentioned prototype ferroelectrics. A high ferroelectric transition temperature and remnant spontaneous polarization indicates that the ferroelectric polarization in $BiFeO_3$ is strong with respect to temperature and strain [16-17, 54].

The magnetic structure of $BiFeO_3$ is G-type anti-ferromagnetic with a modulated spiral spin structure having a long periodicity of 62 nm [16, 54]. The antiferromagnetic Neel temperature of BFO is reported to be 643 K [56]. The spin cycloid model of BFO was first reported by Sonowska in 1982 and verified using XRD, neutron and Mossabauer spectroscopy techniques 16, 54]. Spin glass behavior below 250 K and some anomalies at 150, 50, and 30K have also been reported from zero field cooled and field cooled magnetization investigations on single crystal of BFO [68-70]. Evidences for these magnetic phase transitions with magnetic origin are also observed at 90, 140, 200 and 250 K from Raman spectroscopic, dielectric and thermo mechanical studies [68-70]. Park *et al.* have reported the observation of strong size dependence magnetic properties in single crystalline bismuth ferrite nano particles and explained the enhanced magnetization properties in the frame work of uncompensated spin and strain anisotropies at the surface [71]. Recently it has been reported that room temperature ferromagnetism with high saturation magnetization of $0.4\mu_B$/Fe can be achieved for 4 nm BFO synthesized by combustion method [72-73]. The presences of long range spin cycloid collapse linear magnetoelectric effect and nullify remanent magnetization on macroscopic scale, which leads to a weaker quadratic magneto-electric behavior [16, 54]. At large magnetic fields (above 20 Tesla) the spin cycloid modulation can be destroyed and linear magnetoelectric coupling is possible [74]. The microscopic origin of magnetoelectric coupling is not fully understood, which attract the considerable attention of the scientific community [17]. Recent theoretical and experimental studies suggest that the appearance and improvement of magnetoelectric properties of BFO at room temperature can be achieved by destruction/ suppression of the spin cycloid [16, 17and 54].

Problems Addressed

Based on the above discussion, several major issues associated with $BiFeO_3$ are the following:

(1) Synthesis of stoichiometric/single phase $BiFeO_3$.
(2) High leakage current and dielectric loss.
(3) Weak magnetoelectric coupling at room temperature.
(4) Wide difference in ferroic phase transition temperatures (Curie temperature, T_C ~ 830 °C and Neel temperature T_N ~ 370 °C).

A lot of research works have been carried out around the globe to address the above mentioned problems. Various research groups are engaged to get rid of the problems, by adopting different strategies which are going to be discussed in the next section 1.7.1.

1.7.1 Chemical Modification in $BiFeO_3$

I. A-site Modification in $BiFeO_3$: Chemical substitution by rare-earth (RE) and diamagnetic cation at the Bi-site in BFO has been established to be an effective approach to stabilize the perovskite phase and reduce the leakage current with improved multiferroic properties. Several extensive studies have been attempted in A-site modified $BiFeO_3$ in search of novel multiferroic compound. Catalan *et al.* studied the effect of Ca^{2+} doping in $BiFeO_3$ and observed the increase in Neel temperature. They explained the effect of Ca^{2+} doping as chemical pressure and proposed that the magnetoelectric effect can be improved by decreasing the gap between magnetic and electric ordering temperatures [75]. The structural disorder in $Bi_xCa_{1-x}FeO_3$ perovskites and observation of enhanced magnetization properties are reported by Chen *et al.* [76]. Khomchenko *et al.* reported the effect of diamagnetic such as Ca^{2+}, Sr^{2+}, Pb^{2+}, and Ba^{2+} substitution on the crystal structure and multiferroic properties of the $BiFeO_3$ and observed improved multiferroic characteristics [77]. They also found improved multiferroic properties in Gd^{3+}, Dy^{3+}, Sm^{3+} and Nd^{3+} modified $BiFeO_3$ and reported a compositional driven structural phase transition from *R3c* to *Pnma*. Das *et al.* and Zhang *et al.* observed the improved ferroelectric and magnetic behavior in La^{3+} modified $BiFeO_3$ [78-79]. Using first principle calculations, Lee *et al*. reported the rhombhodral (*R3c*) and orthorhombic (*Pbnm*) morphotropic phase boundary in La^{3+} and Sm^{3+} modified $BiFeO_3$ at $x = 0.3$ and $x = 0.14$ respectively [80]. Jiang *et al*. studied the dielectric, ferroelectric and piezoelectric properties of La^{3+} and Tb^{3+} substituted $BiFeO_3$ prepared by spark plasma sintering procedure [81]. Yuan *et al.* observed improved piezoelectric, pyroelectric. ferroelectric behavior in Nd^{3+} modified $BiFeO_3$. They also reported the structural transition (*R3c* to *P1*) and ferroelectric to paraelectric transformation in Nd^{3+} and La^{3+}modified $BiFeO_3$ multiferroic ceramics. Further they observed the evidence of magnetoelectric coupling in $Bi_{0.875}Sm_{0.125}FeO_3$ ceramics [82-85]. The displacive phase transition and magnetic structure of Nd modified $BiFeO_3$ studied by Levin *et al.* [86]. Saxin *et al.* studied the effect of Sm^{3+} modification on crystal structure and found structural transition from *R3c* to orthorhombic *Imma* symmetry for $x = 0.30$ [87]. Balamurugan *et al.* observed improved multiferroic properties in $Bi_{1/2}Sr_{1/2}FeO_3$ system [88]. Mishra *et al.* reported the effect of Y^{3+} on improvement of dielectric properties and magnetic switching behavior in $BiFeO_3$ [89]. Zhang *et al.* studied the effect of diamagnetic doping Pb^{2+} on the crystal structure and magneto-dielectric properties of the $BiFeO_3$ [90]. Palker *et al.* observed the evidence of magnetoelectricity at room temperature in $Bi_{0.9-x}Tb_xLa_{0.1}FeO_3$ system [91]. Qian *et al.* studied the effect of improved multiferroic properties of $Bi_{1-x}Dy_xFeO_3$ nanoparticles [92]. The influence of the potassium (K^+) substitution on the structure of multiferroic $BiFeO_3$ and its relation with ferroelectric and magnetic properties was investigated for composition $Bi_{1-x}K_xFeO_3$ in the range 0.0 to 0.07 by Dhahri *et al* [93]. Troyanchuk *et al.* studied the structural transformation and magnetic properties of $Bi_{1-x}Ln_xFeO_3$: (Ln: La, Nd, Eu) multiferroics and observed enhanced magnetic properties [94]. Arya *et al.* reported the structural and improved multiferroic properties of $Bi_{1-x}In_xFeO_3$ ($0\leq x\leq 0.20$) nano particles [95]. Enhanced magnetic and dielectric properties of Eu modified BFO nano partices prepared by sol-gel method was reported by Chakrabarti *et al.* [96]. Unyal *et al.* reported the room temperature multiferroic properties of Eu modified BFO [97]. Suresh *et al.* studied the phase evolution and magnetic property Ho modified BFO [98].

II. B-site Modification in $BiFeO_3$: Numerous investigations have also been carried out using transition metal ion and non-magnetic dopants at B-site to improve the magnetic and magnetoelectric properties of $BiFeO_3$. Sosnowska *et al.* studied the crystal and magnetic structure of $BiMn_{0.2}Fe_{0.8}O_3$ system [99]. Kumar *et al.* reported the rapid liquid phase sintered

Mn^{3+} modified $BiFeO_3$ ceramics with enhanced polarization and weak magnetization properties. They also studied the effect of Ti substitution on magnetoelectic coupling of the system [100-101]. Yang *et al.* observed enhanced magneto-capacitance effect in Mn-modified BFO [102]. Hongri *et al.* reported the substantially enhanced ferroelectricity in Ti doped $BiFeO_3$ films [103]. Wei *et al.* observed the phenomenon of cross-over from antiferromagnetic to ferromagnetic in BFO due to non-magnetic Zr substitution [104]. Belik *et al.* reported the structure and magnetic properties of $BiFe_{0.75}Mn_{0.25}O_3$ perovskite prepared at ambient and high pressure [105]. Cheng *et al.* showed the improved magnetic properties in transition metals doped (*i.e.*, Co, Cr, Ni and Mn) $Bi_{0.8}La_{0.2}Nb_{0.01}Fe_{0.99}O_3$ ceramics [106]. Kawae *et al.* observed reduced leakage current behavior on Mn and Ti modified $BiFeO_3$ thin films prepared by pulsed laser deposition [107]. Palker *et al.* reported the effect of Mn^{3+} substitution on magnetoelectric properties of BFO. They showed that Mn enhances the magnetization properties and does not affect loss tangent of the BFO system [108]. Sahu *et al.* showed the enhanced magnetic properties by Mn modification of multiferroic $BiFeO_3$ system [109].

III. Co-substituted $BiFeO_3$: Although partial modification (either A or B-site) of the $BiFeO_3$ is effective to stabilize the perovskite structure, improve the multiferroic properties, and reducing the leakage current, to further enhance the ME coupling several researchers also implemented the idea of co-substitution. Yin *et al.* studied the effect of Ba-Mn co-substitution in $BiFeO_3$ prepared by solid-state reaction route [110]. They observed improved ferroelectric, magnetic and magneto-dielectric properties. Kumar *et al.* also reported the mechanical milling assisted synthesis of Ba–Mn co-substituted $BiFeO_3$ with improved ferroelectric and leakage behavior [111]. Pradhan *et al*. reported the improved magnetization properties of La-Mn substituted BFO [112]. Li *et al.* studied the structural transition and enhanced multiferroic behavior in $Bi_{(1-x)}Dy_xFe_{0.90}Mg_{0.05}Ti_{0.05}O_3$ system [113]. Yu *et al.* reported the enhanced electrical properties in La^{3+} and V^{5+} co-substituted $BiFeO_3$ ceramics prepared rapid liquid sintering technique [114]. Khomchenko *et al.* reported the structural transition and unusual magnetic behavior in Mn-modified $Bi_{1-x}Sm_xFeO_3$ perovskites. [115]. Reetu *et al.* observed improved dielectric and magnetic properties of Ca-Ti co-substituted $BiFeO_3$ ceramics [116]. Recently Xu *et al.* observed enhanced dielectric and multiferroic properties of single-phase Y and Zr co-substituted $BiFeO_3$ ceramics [117]. Jayakumar *et al.* prepared Ba and Mn substituted BFO through the pyrolysis of xerogel precursors and showed the theoretical and experimental evidence of enhanced magnetism in BFO [118]. Enhanced magnetic and dielectric properties of Eu^{3+} and Co^{3+} co-substituted BFO nanoparticles were reported by Chakarbarti *et al.* [119].

1.7.2 Solid Solutions of $BiFeO_3$ -ABO_3

Numerous studies have devoted to the solid solution of BFO with ABO_3 ferroelectric perovskite structures to improve the multiferroic characteristics for novel multifunctional device applications. Singh *et al.* observed the direct evidence of magnetoelectric coupling in $0.9BiFeO_3$–$0.1BaTiO_3$ using dielectric, magnetic, thermal and X-ray diffraction studies [120]. Wang *et al.* observed enhanced magnetoelectric coupling in $0.95BiFeO_3$-$0.05BaTiO_3$ ceramics using *in situ* high-resolution synchrotron X-ray diffraction and dielectric studies [121-122]. Yan *et al.* reported the effects of $Pb(Zr_{0.52}Ti_{0.48})O_3$ modification on the structural, electrical, ferroelectric and ferromagnetic properties of $BiFeO_3$ polycrystalline films [123]. They explained the improved multiferroic behavior due to suppression of spiral spin structure leading to enhancement of ferromagnetic properties due to Pb, Zr and Ti ions. Moreover strong magnetoelectric coupling in multiferroic $BiFeO_3$–$Pb(Zr_{0.52}Ti_{0.48})O_3$ composite films derived from electrophoretic deposition were also reported by them. Wu *et al.* reported a morphotropic phase boundary between rhombohedral (*R3c*) and tetragonal (*P4mm*) perovskite were found in the PZT modified BFO thin films [124]. Kothai *et al.* reported the giant tetragonality near the morphotropic phase boundary of $(1\text{-}x)BiFeO_3$-$xPbTiO_3$ the ferroelectric system [125]. Park *et al.* studied the compositional dependent magnetic properties of $BiFeO_3$-$BaTiO_3$ solid solution nanostructures and found improved multiferroic properties [126]. Choudhary *et al.* studied the structural and dielectric properties of mechano-chemically synthesized $BiFeO_3$–$Ba(Zr_{0.6}Ti_{0.4})O_3$ (BBFZT) solid solutions and observed that the values of loss tangent, leakage current and electrical conductivity of BFO were significantly improved on increasing $Ba(Zr_{0.6}Ti_{0.4})O_3$ concentration [127]. The multiferroism in mechanically processed $BiFeO_3$–$PbTiO_3$ ceramics with improved multiferroic behaviors have been investigated by Freitas *et al.* [128]. Ivanov *et al.* studied the influence of $PbZrO_3$ doping on the structural and magnetic properties of $BiFeO_3$ and found that $PbZrO_3$ doping is effective in improving the structural and magnetic properties of the solid solution [129]. Bhattacharjee *et al.* observed a morphotropic phase boundary (MPB) of width $\Delta x = 0.03$ for $(1\text{–}x)BiFeO_3$-$xPbTiO_3$ (BFO-PT) system which is associated with large tetragonality (*i.e.,* MPB correspond to $x = 0.31$ tetragonal phase *P4mm* and $x = 0.27$

rhombohedral phase *R3c*. They also reported an unambiguous evidence for magnetoelectric coupling in $0.73BiFeO_3$–$0.27PbTiO_3$ multiferroic system. Moreover an isostructural phase transition and associated giant negative thermal expansion for the tetragonal composition x = 0.31was also observed [130-133]. Patel *et al.* showed that $0.8BiFeO_3$–$0.2Pb(Fe_{0.5}Nb_{0.5})O_3$ is isostructural to $BiFeO_3$ and under goes a first-order phase transition from *R3c* to $Pm\bar{3}m$ directly without β phase. This isostructural phase of BFO does not suffer from any decomposition and melting problem like pure BFO [134]. Zhu *et al.* reported improved dielectric and ferroelectric properties of $(1-x)BiFeO_3$–$xPbTiO_3$ ceramics by aliovalent ionic substitution (Ti) which reduces the electrical conductivity [135]. Huo *et al.* synthesized solid solution of $(1-x)BiFeO_3$–$xNa_{0.5}K_{0.5}NbO_3$ ($0.06 \le x \le 0.30$) ceramics and observed enhanced ferroelectric and magneto-dielectric properties [136].

Recent experimental investigations suggest that the appearance and enhancement of ME coupling of BFO at RT can be realized by adopting the following strategies: (a) by destroying the long range spin cycloid, and/or (b) bringing the transition temperature T_C or T_N around room temperature. Kimura *et al.* and Palkar *et al.* independently concluded that the enhancement of magnetoelectric coupling takes places at ferroic transition temperatures T_C or T_N [55, 91]. Several approaches have been attempted by different research groups to enhance the ME coupling in BFO by adopting the above mentioned strategies [16-17, 54]. Those approaches are:

(1) Chemical substitution with diamagnetic, rare earths at the A-site and magnetic, non-magnetic dopant at B-site of ABO_3 perovskite [Ref: 75-119].
(2) Fabrication of solid solution of BFO with other ABO_3-type pervoskites [Ref: 120-136].
(3) Synthesizing BFO nanoparticles with crystallite size less than periodicity of helical order using various chemical routes [Ref: 56-58].
(4) Fabrication of epitaxial thin films [Ref: 16-17, 26-27, 54, 107].
(5) Application of high magnetic field around (> 20Tesla) [Ref: 74].

Based on the literature survey, the motivation of the thesis is to investigate the structural, microstructural, dielectric and multiferroic properties of solid solution BFO-$RMnO_3$ (R: Y^{3+}, $Gd^{3+,}$ Dy^{3+}) and $Bi_{1-x}Ba_xFe_{1-x}Zr_xO_3$ nanoceramics. The technical rational of the motivation is given below

(1) Solid solution of $BiFeO_3$ with $RMnO_3$ (R: Y^{3+}, $Gd^{3+,}$ Dy^{3+}) is expected to stabilize the perovskite structure and improve magnetoelectric properties. This may be due to the possibility of driving the crystal symmetry of BFO near to the morphotropic phase boundary (MPB) and improving its piezoelectric, magnetic and magnetoelectric properties. A further improvement in multiferroic properties can be achieved due to the size effect [Refs: 56, 58, 75-98, 120-136].

(2) As the transition temperature (T_N) of $RMnO_3$ is less than 100 K, synthesis of $BiFeO_3$–$RMnO_3$ (R: Y^{3+}, $Gd^{3+,}$ Dy^{3+}) nano solid solution could bring down the magnetic ordering temperature of parent BFO towards the room temperature. *Goodenough–Kanamori* rule suggests that a strong ferromagnetic interaction is expected between the empty Mn^{3+} orbital and filled Fe^{3+} orbital. Eventually, a decrease in T_N towards room temperature could be accomplished by substitution of Mn^{3+} ions at the Fe^{3+}-site of BFO [Refs: 99-102, 106, 108-106].

(3) Substitution with rare earths at Bi-site is expected to switching off the lone pair activity of Bi leading to the shift of FE transition towards room temperature [Refs: 75-98, 110-19, 120-136].

(4) Recently several studies have also been reported on the crystal structure stability and enhanced multiferroic properties of diamagnetic substituted BFO. The enhanced properties are due to suppression of long range spiral spin cycloid [Refs: 75, 76, 88, 116, 118].

(5) When Fe^{3+} ions is replaced by nonmagnetic ion (*e.g.*, Zr^{4+}) in the AFM ordering of Fe^{3+} sub-lattice, the balance between two adjacent anti parallel spin of Fe^{3+} gets perturbed. Eventually a ferromagnetic interaction via oxygen (instead of antiferromagnetic coupling) is preferred due to the straightening out of the Fe-O-Zr bond angle. Hence, Zr^{4+} substitution offers a unidirectional alignment of spins in the system leading to ferromagnetic behavior [104, 117].

(6) Improved ferroelectric and reduced leakage behavior in Mn and Ti modified $BiFeO_3$ thin films have also been reported [107].

1.8 Introduction to $RMnO_3$: Phase Diagram and Physical Properties

Rare-earth (RE) manganites ($RMnO_3$) have attracted the attention due to their strong magnetoelectric coupling, colossal magneto-resistance, charge ordering and recently discovered magnetic driven ferroelectricity. RE manganites form two distinct crystal structures depending on the ionic radii of the RE ions [16-17, 51-53, 26]. Compounds containing RE element with large ionic radii (R: La, Pr, Nd, Sm, Eu, Gd, Dy, Tb) are stabilized in an orthorhombic structure (*Pnma*/*Pbnm*) and compounds containing RE element with a smaller ionic radii (R: Ho, Er, Tm, Yb, Lu, Y, Sc, In) possess hexagonal crystal structure with the $P6_3cm$ space group. In the orthorhombic structure, the Mn and RE atoms form octahedrons with coordination numbers 6 and 12 respectively, whereas in hexagonal phase, the coordination numbers for Mn and RE are 5 and 7 respectively [16-17, 51-53, 26].

The transition in $RMnO_3$ from the orthorhombic perovskite phase to the hexagonal phase is promoted by inducing site disorder at the A-site. The phase separation exhibits very unusual thermodynamical behavior [16-17, 51-53, 26]. However, the orthorhombic perovskite structure can also be obtained from the corresponding hexagonal compounds under high pressure. For the RE manganites, the tolerance factor is conventionally regarded as the factor controlling the boundary between the hexagonal and orthorhombic structures as shown in Figure 1.11[137]. Closer to the phase boundary, the smaller the Goldschmidt factor and more is the distortion.

Neutron and magnetic experiments indicate that all orthorhombic $RMnO_3$ compounds are antiferromagnetic below a Néel temperature (T_N) ranging from 40 to 100 K depending on the ionic radius. The orthorhombic $RMnO_3$ compounds display super and double-exchange Mn-O-Mn interactions. In the recent years, the origins of ferroelectricity in orthorhombic RE manganites have been studied [16-17, 51-53, 26]. The explanations can be classified in two categories: first from the *non-collinear spiral ordering* and the second on the *non-symmetric interactions* in E-type antiferromagnets. Both type of ordering results atomic displacements and as a consequence electrical dipoles are created. Since these displacements arise from ordered magnetic state, therefore the induced electric dipoles are ordered as well. In conclusion, the origin of their ferroelectricity is due to lattice modulation accompanied by the antiferromagnetic order [16-17, 51-53, 26]. Hence they have a ferroelectric ordering temperature lower than magnetic ordering temperature with a small remnant polarization. Hexagonal rare earth manganites (R: Y to Lu) are antiferromagnetic and the T_N increases from 70 K to 90 K as the ionic radius decreases. They are proper ferroelectrics with T_C in the range of 600-1000 K, which are well above the room temperature. In conclusion, the origin of ferroelectricity in orthorhombic RMnO$_3$ emerged from the magnetic order, whereas in the hexagonal phase the sources for both ferroic orders are independent [16-17,51-53, 26].

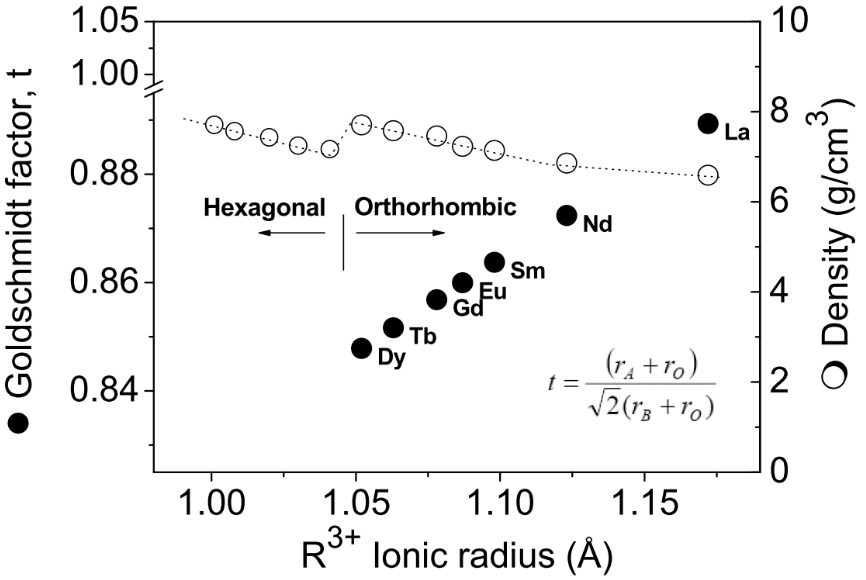

Figure 1.11 Variation of tolerance factor and density of RMnO$_3$ as function of ionic radius [137].

1.8.1 Solid Solutions of BiFeO$_3$ - RMnO$_3$

Recently, it has been found that fabrication of the solid solution of BiFeO$_3$ with different rare-earth manganites exhibit enhanced magnetoelectric properties. Lahmar *et al.* have observed the enhanced electrical and magnetic properties of BiFeO$_3$ –10% RMnO$_3$ (R: La, Eu, Gd, Tb, Dy) thin films. They observed reduced leakage current with improved polarization properties. Interestingly the addition of GdMnO$_3$ leads to a substantial increase in magnetization with moderate ferroelectric polarization [138]. Zhu *et al.* prepared the solid solution of (1-x) BiFeO$_3$-xDyFeO$_3$ and observed a structural phase transition from *R3c* to *Pbnm* at x = 0.1, with improved multiferroic behaviors [139]. The structural and dielectric properties of (1-x) BiFeO$_3$-xDyMnO$_3$ solid solution were reported by Ivanova *et al.* [140]. Nazarenko *et al.* observed structural transition from *R3c* to *Pbnm* at x = 0.1 in (1-x)BiFeO$_3$-xYMnO$_3$ solid solution [141]. To the best of our knowledge, the systematic study of solid solution of BFO-$RMnO_3$ (R: Y^{3+}, $Gd^{3+,}$ Dy^{3+}) using nanoceramics have not been carried out. This motivated us to study the phase transition and multiferroic behavior of the above mentioned compounds.

1.9 Materials Under Present Investigation

Although a great deal of work has been carried out in the search of new multiferroic materials based on perovskite structure, it is still important and challenging to design and synthesize multiferroic materials with improved magnetoelectric coupling to provide high performance multifunction device applications. In the present work, we study the systematic investigation on the structural, microstructural, dielectric, ferroelectric, magnetic and magneto-dielectric properties of solid solution of $BiFeO_3$ with rare-earth manganites $RMnO_3$ (R: Y^{3+}, Gd^{3+}, Dy^{3+}) and $Bi_{1-x}Ba_xFe_{1-x}Zr_xO_3$ nanoceramics. The materials under present investigation are:

(1) $(1-x)BiFeO_3$-$xYMnO_3$: $(0.0 \leq x \leq 0.2)$
(2) $(1-x)BiFeO_3$-$xGdMnO_3$: $(0.0 \leq x \leq 0.2)$
(3) $(1-x)BiFeO_3$-$xDyMnO_3$: $(0.0 \leq x \leq 0.2)$
(4) $Bi_{1-x}Ba_xFe_{1-x}Zr_xO_3$: $(0.0 \leq x \leq 0.1)$

The crystal structure transformation due to the change of composition in $BiFeO_3$ has been extensively studied in recent years because the phase instabilities at the phase boundary, which separates one polar phase from another polar phase or nonpolar phase, tends to induce significant dielectric and piezoelectric properties [80, 87, 94, 120, 124, 125, 130, 133, 134]. $BiFeO_3$ forms solid solution with ferroelectric perovskites and rare earth manganites ($RMnO_3$) over a wide compositional range and possesses different structural symmetry which displays intriguing multiferroic properties. Eventually a long range compositional sweep is essential to quantify the associated physical properties. Recent experimental investigation report that rare earth substituted $BiFeO_3$ displays a structural transition near composition $x \approx 0.1$ to 0.15 [54, 78-80, 94, 113, 115, 118]. Additionally, it is also important to study the multiferroic behavior in chemically substituted $BiFeO_3$ within parent rhombohedral crystal structure. Therefore we have selected gradual increase in composition from $x = 0.0$ to $x = 0.2$. As a result, it is anticipated that the selected composition range $(0.0 \leq x \leq 0.2)$ of examination may provide the experimental window to observe the phase boundary where maximum multiferroic properties can be achieved.

1.10 Objectives and Scope of the Present Work

The objectives of the present work have been defined on the basis of the existing problems, challenges and current status in the field of BFO based multiferroics. A brief outline is given as follows:

(1) To prepare pure phase nano-sized BFO, the solid solutions of $BiFeO_3$ with rare-earth manganites $RMnO_3$ (R: Y^{3+}, Gd^{3+}, Dy^{3+}) and $Bi_{1-x}Ba_xFe_{1-x}Zr_xO_3$ using auto-combustion technique.

(2) Studies of structural and microstructural properties of the BFO based solid solution by X-ray diffraction, transmission electron microscopy and scanning electron microscopy.

(3) Studies of dielectric properties in a wide range of temperature and frequency to find out the phase transitions in BFO based materials.

(4) Studies the electrical properties using complex impedance spectroscopic technique and explore the structure-property relationship.

(5) To study the electric polarization and magnetic hysteresis to provide the evidences of their ferroic properties and confirmation of multiferroism.

(6) To study the magnetoelectric coupling by magneto-dielectric measurement and magneto-impedance spectroscopic technique.

1.11 Outline of the Thesis

The thesis is divided into eight chapters, the contents of which are as follows:

(1) Chapter-1 gives a brief introduction to the broad area of ferroelectric and its related materials. A brief account on multiferroic phenomenon has been presented which covers an overview of the conceptual, theoretical and materials aspects. In addition to this, literature survey describing the chronological development and current status of the $BiFeO_3$ based compounds has been discussed. Based on the literature survey we have set our objective of the present study.

(2) In Chapter-2 the sample preparation technique is elucidated in detail. Some common analysis methods are surveyed and a brief description of the instruments/setups used in the present investigation is given.

(3) Chapter-3 describes the synthesis of pure phase nanoceramic BFO material using auto-combustion technique. The structural, microstructural, dielectric, and magnetoelectric properties have been studied in detail.

(4) Chapter-4 is devoted to the understanding of the compositional driven structural phase transition, microstructural, dielectric, ferroelectric, magnetic and magneto-dielectric properties of (1-x)$BiFeO_3$-$x$$YMnO_3$ for $0.0 \leq x \leq 0.2$ nano solid solution .

(5) Chapter-5 deals with a systematic study of composition driven structural transformation and evidence of intrinsic magneto-dielectric response of (1-x)$BiFeO_3$-$x$$GdMnO_3$ for $0.0 \leq x \leq 0.2$ solid solution using nanoceramics.

(6) In Chapter-6, we have systematically studied the structure and multiferroic properties of the solid solution of (1-x) $BiFeO_3$-$x$$DyMnO_3$ for $0.0 \leq x \leq 0.2$ nanoceramics.

(7) Chapter-7 deals with study of Ba-Zr co-substituted $BiFeO_3$ on crystal structure and its correlation with magnetoelectric response.

(8) A brief summary, conclusion and future scope of the work have been discussed in chapter-8.

1.12 References

[1] V. K. Wadhawan, smart Structures: Monographs on the Physics and Chemistry of Materials, Oxford University Press Inc., New York, 2007.

[2] M. E. Lines and A. M. Glass, Principles and Applications of Ferroelectrics and Related Materials, Oxford University Press Inc., New York, 2001.

[3] J. Valasek, American Physical Society Meeting, **17**, 475 (1920).

[4] J. J. Kim and J. Y. Huang, Phys. Rev. B., **38**, 11885 (1988).

[5] W. J. Merz, Phys. Rev., **76**, 1221(1949).

[6] W. J. Merz, Phys. Rev., **95**, 690 (1954).

[7] A. F. Devonshire, Philosophical Magazine Series: **7**, 40, 1040 (1949).

[8] A. F. Devonshire, Philosophical Magazine Series: **7**, 42, 333, 1065 (1951).

[9] G. H. Haertling, J. Am. Ceram. Soc., **82**, 797 (1999).

[10] P. S. Halasyamani and K. R. Poeppelmeier, Chem. Mater. **10**, 2753 (1998).

[11] F. Jona, G. Shirane, Ferroelectric Crystals, Dover Publications, Una Rep edition (1993).

[12] A. F. Devonshire Advances in Physics, **3**: 10, (1954).

[13] G. H. Kwei, A. C. Lawson, S. J. L. Billinge and S.W. Cbeong, J. Phys. Chem. **97**, 2368 (1993).

[14] B. D. Cullity and C. D. Graham, Introduction to Magnetic Materials, John Wiley & Sons and IEEE Press (2009).

[15] N. A. Spaldin, Magnetic Materials: Fundamentals and Applications, Cambridge University Press, The Edinburgh Building, Cambridge CB2 8RU, UK (2011).

[16] K.F. Wang, J.M. Liu, Z.F. Ren, Adv. Phys. **58**, 321 (2009).

[17] M. Fiebig, J. Phys. D: Appl. Phys. **38**, R123 (2005).

[18] H. Ohno, D. Chiba, F. Matsukura, T. Omiya, E. Abe, T. Dietl, Y. Ohno, K. Ohtani, Nature **408**, 944 (2000).

[19] T. Lottermoser, T. Lonkai, U. Amann, D. Hohlwein, J. Ihringer, M. Fiebig, Nature **430**, 541 (2004).

[20] N. A. Spaldin, M. Fiebig, Science **309**, 391(2005).

[21] N. A. Hill, J. Phys. Chem. B, **104**, 6694 (2000).

[22] D. Khomskii, Physics **2**, 20 (2009).

[23] H. Schmid, J. Phys.: Condens. Matter, **20**, 434201 (2008).

[24] B. B. Van Aken, J. P. Rivera, H. Schmid and M. Fiebig, Nature, **449**, 702 (2007).

[25] N. A. Spaldin, M. Fiebig and M. Mostovoy, J. Phys.: Condens. Matter, **20**, 434203 (2008).

[26] W. Prellier, M. P. Singh and P. Murugavel, J. Phys.: Condens. Matter, **17**, R803 (2005).

[27] S. Picozzi and C. Ederer, J. Phys.: Condens. Matter **21**, 303201 (2009).

[28] W. Kleemann, V.V. Shvartsman, and P. Borisov, Phys. Rev. Lett. **105**, 257202 (2010).

[29] R. V. Shpanchenko, V. V. Chernaya, A. A. Tsirlin, P. S. Chizhov, D. E. Sklovsky, and E. V. Antipov, Chem. Mater., **16**, 3267 (2004).

[30] J. Brink and D. I. Khomskii, J. Phys.: Condens. Matter, **20**, 434217 (2008).

[31] B. B. Aken, T. Palstra, A. Filippetti and N. A. Spaldin, Nature Materials, **3**, 164 (2004).

[32] M. Mostovoy, Phys. Rev. Lett. **96**, 067601 (2006).

[33] H. Katsura, N. Nagaosa, and A. V. Balatsky, Phys. Rev. Lett. **95**, 057205 (2005).

[34] A. I. Smirnov, L. E. Svistov, L. A. Prozorova, A. Zheludev, M. D. Lumsden, E. Ressouche, O. A. Petrenko, K. Nishikawa, S. Kimura,5 M. Hagiwara, K. Kindo, A.Ya. Shapiro and L. N. Demianets, Phys. Rev. Lett. **102**, 037202 (2009).

[35] P. Tolédano, Phys. Rev. B. **79**, 094416 (2009).

[36] I. A. Sergienko and E. Dagotto, Phys. Rev. B. **73**, 094434 (2006).

[37] C. D. Hu, Phys. Rev. B. **77**, 174418 (2008).

[38] H. Kimura, S. Kobayashi, S. Wakimoto, Y. Noda and K. Kohn, Ferroelectrics, **77**, 354 (2007).

[39] C. Wang, G. Guo, and L. He, Phys. Rev. Lett. **99**, 177202 (2007).

[40] A. B. Harris, T. Yildirim, A. Aharony, and O. Entin-Wohlman, Phys. Rev. B., **73,** 184433 (2006).

[41] J. J. Betouras, G. Giovannetti, and J. Brink, Phys. Rev. Lett. **98**, 257602 (2007).

[42] K. A. Muller and T. W. Kool, Properties of Perovskites and other Oxides, World Scientific Publishing Co. Pte. Ltd.

[43] D. M. Giaquinta and H. Loye, Chem. Mater., **6**, 365 (1994).

[44] M. A. Pena and J. L. G. Fierro, Chem. Rev., **101**, 1981(2001).

[45] A. M. Glazar, Acta Cryst. **A31**, 756 (1975).

[46] A. M. Glazar, Acta Cryst. **B28**, 3384(1972).

[47] M. N. Popova, Phys. Rev. B. **75**, 224435 (2007).

[48] C. Ederer and Nicola A. Spaldin, Phys. Rev. B. **74**, 024102 (2006).

[49] Il-Kyoung Jeong, N. Hurb and Th. Proffen, J. Appl. Cryst. **40**, 730 (2007).

[50] S Jodlauk, P Becker, J A Mydosh, D I Khomskii, T Lorenz, S V Streltsov, D C Hezel and L Bohatý, J. Phys.: Condens. Matter. **19**, 432201 (2007).

[51] T. Kimura and G. Lawes, T. Goto, Y. Tokura, A. P. Ramirez, Phys. Rev. B. 71, 224425 (2005).

[52] J. L. Ribeiro, Phys. Rev. B. **76**, 144417 (2007).

[53] C. R. dela Cruz, F. Yen, B. Lorenz, M. M. Gospodinov, C. W. Chu, W. Ratcliff, J. W. Lynn, S. Park, and S.-W. Cheong, Phys. Rev. B. **73**, 100406R (2006).

[54] G. Catalan and J. F. Scott, Adv. Mater. **21**, 2463 (2009).

[55] T. Kimura, S. Kawamoto, I. Yamed, M. Azuma, M. Tanky, and Y. Tokura, Phys. Rev. B **67**, 180401R (2003).

[56] S. M. Selbach, T. Tybell, M. Einarsrud, and T. Grande, Adv. Mater., **20**, 3692 (2008).

[57] J. D. Bucci, B.K. Robertson and W. J. James, Appl. Cryst. **5**, 187 (1972).

[58] S. M. Selbach, T. Tybell, M. Einarsrud, and T. Grande, Chem. Mater., **19**, 6478 (2007).

[59] H. D. Megaw and C. N. W. Darlington, Acta Cryst. **A31**, 161 (1975).

[60] R. Haumont, J. Kreisel, P. Bouvier, and F. Hippert, Phys. Rev. B, **73**, 132101 (2006).

[61] R. Haumont, Igor A. Kornev, S. Lisenkov, L. Bellaiche, J. Kreisel, and B. Dkhil, Phys. Rev. B **78**, 134108 (2008).

[62] R. Haumont, P. Bouvier, A. Pashkin, K. Rabia, S. Frank, B. Dkhil, W. A. Crichton, C. A. Kuntscher, and J. Kreisel., Phys. Rev. B **79**, 184110 (2009).

[63] R. Palai, R. S. Katiyar, H. Schmid, P. Tissot, S. J. Clark, J. Robertson, S. A. T. Redfern, G. Catalan, and J. F. Scott, Phys. Rev. B **77**, 014110 (2008).

[64] D. C. Arnold, K. S. Knight, F. D. Morrison, and P. Lightfoot, Phys. Rev. Lett. **102**, 027602 (2009).

[65] J. R. Teague, R. Gerson and W.J. James, Solid State Communications, **8**, 1073 (1970).

[66] X. J. Lou, C. X. Yang, T. A. Tang, Y. Y. Lin, M. Zhang and J. F. Scott, Appl. Phys. Lett. **90**, 262908 (2007).

[67] J. Wang, J. B. Neaton, H. Zheng, V. Nagarajan, S. B. Ogale, B. Liu, D. Viehland, V. Vaithyanathan, D. G. Schlom, U. V. Waghmare, N. A. Spaldin, K. M. Rabe, M. Wuttig, R. Ramesh, Science **299**, 1719 (2003).

[68] S. Vijayanand, M. B. Mahajan, H. S. Potdar, and P. A. Joy Phys. Rev. B **80**, 064423 (2009)

[69] J. F. Scott, M. K. Singh and R. S. Katiyar, J. Phys.: Condens. Matter **20**, 322203(2008).

[70] M. K Singh, R.S. Katiyar and J. F. Scott, J. Phys.: Condens. Matter **20**, 252203 (2008).

[71] T. Park, G. C. Papaefthymiou, A. J. Viescas, A. R. Moodenbaugh, and S. S. Wong, Nano Lett., **7**, 766 (2007).

[72] R. Mazumder, S. Ghosh, P. Mondal, Dipten Bhattacharya, S. Dasgupta, N. Das, and A. Sen, A. K. Tyagi, M. Sivakumar, T. Takami and H. Ikuta. J. Appl. Phys. **100**, 033908 (2006).

[73] R. Mazumder, P. Sujatha Devi, Dipten Bhattacharya,a P. Choudhury, A. Sen and M. Raja, Appl. Phys. Lett., **91**, 062510 (2007).

[74] B. Ruette, S. Zvyagin, A. P. Pyatakov, A. Bush, J. F. Li, V. I. Belotelov, A. K. Zvezdin, and D. Viehland, Phys. Rev. B. **69**, 064114 (2004).

[75] G. Catalan, K. Sardar, N.S. Church, J. F. Scott, R. J. Harrison, and S. A. T. Redfern, Phys. Rev. B. **79**, 212415 (2009).

[76] W. Chen, A. J. Williams, L. Martin, M. Li, D. C. Sinclair, W. Zhou, and J. P. Attfield, Chem. Mater., **21**, 2085 (2009).

[77] V. A. Khomchenko, M. Kopcewicz, A. M. L. Lopes, Y. G. Pogorelov, J. P. Araujo, J. M. Vieira and A. L. Kholkin, J. Phys. D: Appl. Phys. **41**,102003 (2008).

[78] S. Zhang, L. Pang, Y. Zhang, M. Lu, and Y. Chen, J. Appl. Phys. **100**, 114108 (2006).

[79] S. R. Das, R. N. P. Choudhary, P. Bhattacharya, R. S. Katiyarar P. Dutta, A. Manivannan, and M. S. Seehra, J. Appl. Phys. **101**, 034104 (2007).

[80] J. Lee, M. Oak, H. Choi, J. Sonc and H. M. Jang, J. Mater. Chem., **22**, 1667 (2012).

[81] Q. H. Jiang, F. T. Liu1, Ce-Wen Nan, Yuan-Hua Lin, M. J. Reece, H. X. Yan, H. P. Ning and Z. J. Shen, Appl. Phys. Lett. **95**, 012909 (2009).

[82] G. L. Yuan and Siu Wing Or, Appl. Phys. Lett. **88**, 062905 (2006).

[83] G. L. Yuan and Siu Wing Or, Appl. Phys. Lett. **89**, 052905 (2006).

[84] G. L. Yuan and Siu Wing Or, J. Appl. Phys., **100**, 024109 (2006).

[85] G. L. Yuan, S. W. Or and H. W. Chan, J. Phys. D: Appl. Phys. **40**, 1196 (2007).

[86] I. Levin, M. G. Tucker, H. Wu, V. Provenzano, C. L. Dennis, S. Karimi, T. Comyn, T. Stevenson, R. I. Smith, and I. M. Reaney, Chem. Mater., **23**, 2166 (2011).

[87] S. Saxin and C. S. Knee, Dalton Trans., **40**, 3462 (2011).

[88] K. Balamurugan, N. Harish Kumar, and P. N. Santhosha, J. Appl. Phys., **105**, 07D909 (2009).

[89] R. K. Mishra, Dillip K Pradhan, R N P Choudhary and A Banerjee, J. Phys.: Condens. Matter **20**, 045218 (2008).

[90] X. Zhang, Y. Sui, X. Wang, J. Tang, and W. Su, J. Appl. Phys., **105**, 07D918 (2009).

[91] V. R. Palkar, Darshan C. Kundaliya, S. K. Malik, and S. Bhattacharya Phys. Rev. B. **69**, 212102 (2004).

[92] F. Z. Qian, J. S. Jiang, S. Z. Guo, D. M. Jiang, and W. G. Zhang, J. Appl. Phys., **106**, 084312 (2009).

[93] J. Dhahri, M. Boudard, S. Zemni, H. Roussel and M. Oumezzine, Journal of Solid State Chemistry, **181**, 802 (2008).

[94] I. O. Troyanchuk, , M. V. Bushinsky, D. V. Karpinsky, O. S. Mantytskaya, V. V. Fedotova, and O. I. Prochnenko, Phys. Status Solidi **B 246**, 1901 (2009).

[95] G. S. Arya, R. K. Kotnala, and N. S. Negi, J. Appl. Phys., **113**, 044107 (2013).

[96] K. Chakrabarti, K. Das, B. Sarkar, and S. K. De J. Appl. Phys., **110**, 103905 (2011)

[97] P. Uniyal and K. L. Yadav, J. Appl. Phys., **105**, 07D914 (2009).

[98] P. Suresh, P. D. Babu, and S. Srinath, J. Appl. Phys., **115**, 17D905 (2014).

[99] I. Sosnowska, W. Schäfer, W. Kockelmann, K.H. Andersen, I.O. Troyanchuk, Appl. Phys. A. **74,** S1040 (2002).

[100] M. Kumar and K.L Yadav, J. Appl. Phys., **100**, 074111 (2006).

[101] M. Kumar and K.L Yadav, J. Appl. Phys., **91**, 242901 (2007).

[102] C.-H. Yang, T.Y. Koo, Y.H. Jeong, Solid State Communications **134**, 299 (2005).

[103] L. Hongri and S. Yuxia, J. Phys. D: Appl. Phys. **40**, 7530 (2007).

[104] J. Wei, R. Haumont, R. Jarrier, P. Berhtet, and B. Dkhil, Appl. Phys. Lett. **96**, 102509 (2010).

[105] A. A. Belik, A. M. Abakumov, A. A. Tsirlin, J. Hadermann, J. Kim, G. F. Tendeloo, and E. T Muromachi, Chem. Mater., **23**, 4505 (2011).

[106] Z. X. Cheng, X. L. Wang, Y. Du and S. X. Dou, J. Phys. D: Appl. Phys. **43**, 242001(2010).

[107] T. Kawae, Y. Terauchi, H. Tsuda, M. Kumeda, and A. Morimoto, Appl. Phys. Lett. **94**, 112904 (2009).

[108] V. R. Palkar, Darshan C. Kundaliya and S. K. Malik, J. Appl. Phys., **93**, 4337, (2003).

[109] J. Sahu and C.N. R. Rao., Solid State Sciences, **9**, 950(2007).

[110] L. H. Yin, W. H. Song, X. L. Jiao, W. B. Wu, X. B. Zhu, Z. R. Yang, J. M. Dai, R. L. Zhang and Y. P. Sun, J. Phys. D: Appl. Phys. **42**, 205402 (2009).

[111] K. S. Kumar, C. Venkateswaran, D. Kannan, B. Tiwari, M. S. Ramachandra Rao, J. Phys. D: Appl. Phys. **45**, 415302 (2012).

[112] Dillip K. Pradhan, R. N. P. Choudhary, C. Rinaldi, and R. S. Katiyar, J. Appl. Phys., **106**, 024102 (2009).

[113] N. Li, J. Wu, Y. Jiang, Z. Xie, L. Zheng and Z. Ye, J. Appl. Phys., **113**, 054102 (2013).

[114] B. Yu, M. Li, J. Wang, L. Pei, D. Guo and X. Zhao, J. Phys. D: Appl. Phys. **41**, 185401(2008).

[115] V. A. Khomchenko,I. O. Troyanchuk, M. I. Kovetskaya, and J. A. Paixao, J. Appl. Phys., **111**, 014110 (2012).

[116] Reetu, A. Agarwal, S. Sanghi, Ashima, and N. Ahlawat, J. Appl. Phys**.,** **113**, 023908 (2013)

[117] J. Xu, D. Xie, C. Yin, T. Feng, X. Zhang, G. Li, H. Zhao, Y. Zhao, S. Ma, T. Ren, Y. Guan, X. Gao, and Y. Zhao, J. Appl. Phys., **114**, 154103 (2013).

[118] O. D. Jayakumar, S. N. Achary, K. G. Girija, A. K. Tyagi, C. Sudakar, G. Lawes, R. Naik, J. Nisar, X. Peng, and R. Ahuja, Appl. Phys. Lett., **96**, 032903 (2010).

[119] K. Chakrabarti, K. Das, B. Sarkar, S. Ghosh, S. K. De, G. Sinha, and J. Lahtinen, Appl. Phys. Lett., **101**, 042401 (2012).

[120] A. Singh, V. Pandey, R. K. Kotnala, and D. Pandey, Phys. Rev. Lett., **101**, 247602 (2008).

[121] T.-H. Wang, Y. Ding, C.-S. Tu, Y.-D. Yao, K.-T. Wu, T.-C. Lin, H.-H. Yu, C.-S. Ku, and H.-Y. Lee, J. Appl. Phys., **109**, 07D907 (2011).

[122] T.-H. Wang, C.-S. Tu, H.-Y. Chen, Y. Ding, T. C. Lin, Y.-D. Yao, V. H. Schmidt, and K.-T. Wu, J. Appl. Phys., **109**, 044101 (2011).

[123] F. Yan, T. J. Zhu, M. O. Lai, and L. Lu, J. Appl. Phys., **110**, 114116 (2011).

[124] Y. Wu, J. Wan, C. Huang, Y. Weng, S. Zhao, J. Liu, and G. Wang, Appl. Phys. Lett., **93**, 192915 (2008).

[125] V. Kothai, A. Senyshyn, and R. Ranjan, J. Appl. Phys., **113**, 084102 (2013).

[126] T. Park, G. C. Papaefthymiou, A. J. Viescas, Y. Lee, H. Zhou, and S. S. Wong, Phys. Rev. B., **82**, 024431 (2010).

[127] R.N.P. Choudhary, K. Perez, P. Bhattacharya, R.S. Katiyar, Materials Chemistry and Physics **105**, 286 (2007).

[128] V. F. Freitas, L. F. Cótica, I.A. Santos, D. Garcia, J.A. Eiras , Journal of the European Ceramic Society, **31**, 2965 (2011).

[129] S.A. Ivanov, P. Nordblad, R. Tellgren, T. Ericsson,S.K. Korchagina, L.F. Rybakova , A. Hewat , Solid State Sciences **10**, 1875 (2008).

[130] S. Bhattacharjee, S. Tripathi, and D. Pandey, Appl. Phys. Lett., **91**, 042903 (2007).

[131] S. Bhattacharjee,. V. Pandey, R. K. Kotnala, and D. Pandey, Appl. Phys. Lett., **94**, 012906 (2009).

[132] S. Bhattacharjee and D. Pandey, J. Appl. Phys., **110**, 084105 (2011).

[133] S. Bhattacharjee, K. Taji, C. Moriyoshi, Y. Kuroiwa, and D. Pandey , Phys. Rev. B. **84**, 104116 (2011).

[134] J. Patel, A. Singh and D. Pandey, J. Appl. Phys., **107**, 104115 (2010).

[135] W.-M. Zhu and Z.-G. Yea, Appl. Phys. Lett., **89**, 232904 (2006).

[136] S.X. Huo, S.L. Yuan, Y. Qiu, Z.Z. Ma, C.H. Wang. Materials Letters **68**, 8 (2012).

[137] R.D. Shannon and C.T. Prewitt, Acta Cryst. **B25**, 925(1969).

[138] A. Lahmar, S. Habouti, M. Dietze, C. H. Solterbeck, and M. Es-Souni, Appl. Phys. Lett. **94**, 012903 (2009).

[139] W.H, Zhu, L.W. Su, Z.G. Ye and W Ren, Appl. Phys. Lett. **94**, 142908 (2009).

[140] V. V. Ivanova, V. V. Gagulin, S. K. Korchagina, Yu. A. Shevchuk, and V. V. Bogatko, Inorg. Mater. **39**, 745 (2003)

[141] A.V. Nazarenko, A. G. Razumnaya, M. F. Kupriyanov, Yu. V. Kabirov, A. G. Rudskaya, P. Yu. Teslenko, and N. B. Kofanova, Physics of the Solid State **53**, 1599 (2011).

Chapter-2

Experimental Procedure

In this Chapter, we describe briefly the general synthesis procedure for the preparation of the ceramic oxides and different experimental techniques employed for characterization of the materials.

2.1 Introduction

Sample synthesis and optimization of the physical properties for specific multifunctional device applications are the essential part in the field of material science [1]. Nowadays, many improved techniques are available in the literature for the synthesis of ultra-fine high purity and homogeneous ceramic powders. The ferroelectric/multiferroic materials can be synthesized in the form of single crystals or thin films or polycrystalline ceramics [2]. Polycrystalline ceramics (*i.e.,* assembly of small single crystals oriented with respect to each other in a more or less completely random way) have its own advantages over single crystals or thin films. Single crystals and thin films require highly sophisticated synthesis procedure, while the ceramics can be fabricated more easily and in a cost effective way in the form of polycrystalline materials [3]. The advantages of polycrystalline ceramic processing over single crystals are: (a) easier to fabricate into different shapes and sizes, (b) improved structural and microstructural (*i.e.,* grain shape, size and porosity, *etc*.) features [1-3]. These microstructural features (*e.g.,* presence of grain boundaries) gives rise to additional effect, which is not present in single crystals, but actually plays an important role in practice (c) thermal, chemical and mechanical stability features. In spite of brittle and non-ductile characteristics, the above mentioned outstanding features of ceramics justify their use in million dollar electronic, opto-electric and spintronics industries [4].

2.2 Methods for Ceramic Preparation

Ceramic processing involves a number of synthesis parameters and steps like mixing, calcination, sintering *etc.* which influence the chemical and physical properties of the materials [5]. The growing applications of ceramics have received increasing interest in the multidisciplinary field for their synthesis procedure. There are many synthesis techniques available for fabrication of nano materials using top-down and bottom-up approach. Nano materials have superior properties than bulk substances with wide range of applications. Important features of nano materials are (a) mechanical strength, (b) thermal stability (c) catalytic activity (d) electrical conductivity (e) magnetic properties and (f) optical properties [5]. It provides application in various fields such as quantum electronics, nonlinear optics, photonics, sensing, information storage and processing, adsorbents, catalysis, solar cells, superplastic ceramics [5-6].

There are mainly two approaches used for synthesis of ceramics oxides. One is chemical method (bottom-up) and the other is the mechanical method (top-bottom) [6]. (i) *Mechanical Methods*: synthesis of ceramics oxides using different mechanical methods include the mixed oxide process (MOP) or solid-state reaction process, high energy ball milling, attrition milling, vibratory milling, turbo milling, fluid energy milling, hammer milling, roll crushing *etc.* (ii) *Chemical Methods*: for the preparation of ceramics at nano scale in a controlled way, usually chemical methods are used. The chemical methods normally used for synthesis of ceramics are co-precipitation, sol-gel, decomposition of molecular precursors, hydrothermal, cryo-chemical, polymer pyrolysis, Pechini, citrate gel methods, aerosols and emulsions [6].

Mechanical method such as the conventional solid-state reaction method although successful for a large-scale production of bulk ceramic powders at its low cost, easy adaptability and has several limitations in the production of fine ceramics. In conventional solid-state method, high temperature and heating for prolonged time makes the particles coarse. The completeness of the reaction and uniformity of the product depend on particle size, homogeneity of the mixture, thermal schedule, and even on the atmosphere during calcination [5-6].

On the other hand, ceramic powders prepared in recent years by soft chemical methods have shown improvement in powder characteristics with respect to purity, homogeneity, stoichiometry, reactivity as well as particle size, shape, surface, and agglomeration behavior [7]. In chemical methods the starting materials are usually solutions that are mutually soluble in each other, thus producing a homogeneous precursor solution. The particle size of the powders obtained in this method is usually much finer than that of MOP powder. So, these powders are more reactive and need lower calcination temperature. Again the careful control of the removal of solvent leads to the production of crushable agglomerates. However, in many cases the chemical routes generally involve complex techniques as compared to the conventional methods. Thus an improved level of skill is required if the benefits are to be realized. Both methods have their own inherent advantages and disadvantages. Now we are going to discuss few synthesis routes for the preparation of ceramic oxides in the following section.

2.2.1 Solid-State Reaction Technique

The solid state reaction route is the most suitable and extensively used technique for the preparation of polycrystalline solids from a mixture of oxide and carbonates as reagents [3]. As generally solids do not participate in reaction at room temperature, so heat is required for solid precursors to carry out the reaction. The likelihood of the reaction of precursors is determined by thermodynamic free energy. The rate of reaction depends upon reaction conditions, structural properties of the reactants, surface area of the solids and their reactivity. Various steps in solid-state reaction process are represented in terms of a flow chart as shown in Figure 2.1.

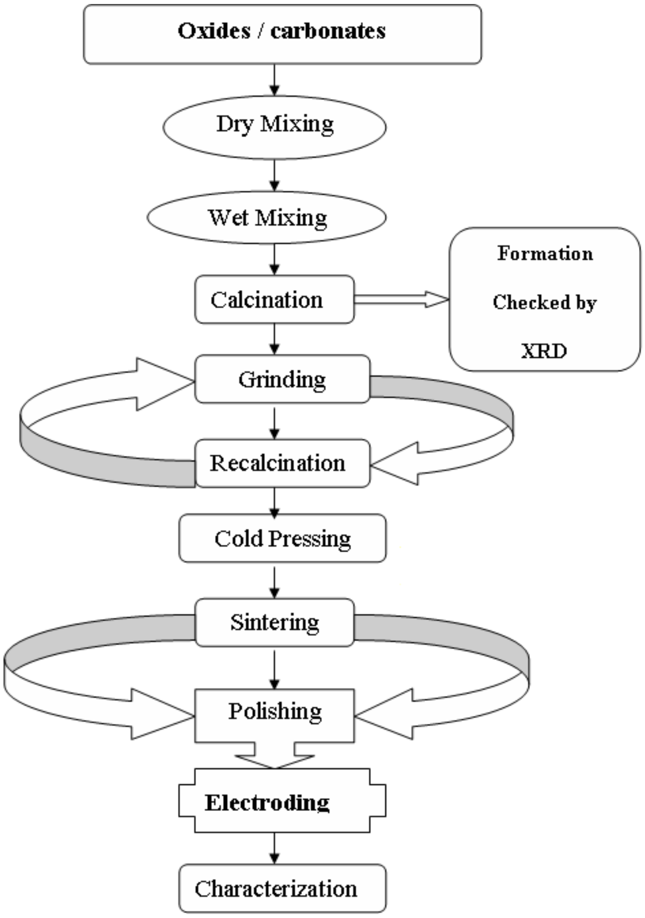

Figure 2.1 Flow chart for the preparation of ceramic samples by solid-state reaction technique.

The raw chemicals with high purity were used for the material synthesis. The required stoichiometric ratio amounts of reagents were dry mixed in an agate motar followed by wet mixing with acetone as medium. After proper mixing, mixed powders were calcined at different temperatures using a programmable furnace with intermediate grinding to avoid agglomeration of the particles. The calcined powder was subsequently grinded into fine powder and the phase formation is checked by X-ray diffraction technique at room temperature. The above calcined powders were mixed with PVA (polyvinyl alcohol which acts as a binder) in mortar and pestle. To get uniform and fine grain, the granules were passed through sieve. The binder mixed powder was compacted to form pellet by a hydraulic press at a suitable pressure using die set. The sintering of the pellet sample was carried out at an optimized temperature for densification. The sintered pellets were polished by emery paper and painted with silver paste as an electrode for electrical measurement. The painted samples were kept in the oven for 3 hrs. to evaporate the moisture in the sample, if any.

2.2.2 Synthesis of Nano Materials Using Chemical Methods

A. Coprecipitation Method

Coprecipitation reactions involve the simultaneous occurrence of nucleation, growth, coarsening, and/or agglomeration processes [8]. These reactions exhibit the following characteristics: (1) the products are generally insoluble species formed under the conditions of high super saturation. (2) Nucleation is a key step, and a large number of small particles will be formed. (3) Secondary processes, such as Ostwald ripening and aggregation dramatically affects the size, morphology, and properties of the products. Different types of co-precipitation synthesis methods are: (i) metals formed from aqueous solutions, (ii) reduction from non-aqueous solutions, (iii) electrochemical reduction, (iv) decomposition of organometallic precursors (v) oxides formed from aqueous and nonaqueous solutions, (vi) metal chalconides formed by reactions of molecular precursors, (vii) Microwave/sonication-assisted coprecipitation.

B. Sol-gel Processing

The sol-gel process is a versatile solution process for making ceramic and glass materials. In general, the sol-gel process involves the transition of a system from a liquid "sol" (mostly colloidal) into a solid "gel" phase [9]. A sol is a dispersion of the solid particles (~ 0.1-1 mm) in a liquid where only the Brownian motions suspend the particles. A gel is a state where both liquid and solid are dispersed in each other, which presents a solid network containing liquid components. In a typical sol-gel process, the precursor is subjected to a series of hydrolysis and polymerization reactions to form a colloidal suspension, or a "sol". Further processing of the "sol" enables one to make ceramic materials in different forms. Thin films can be produced on a piece of substrate by spin-coating. Applying the sol-gel process, it is possible to fabricate ceramic or glass materials in a wide variety of forms: ultra-fine or spherical shaped powders, thin film coatings, ceramic fibers, micro porous inorganic membranes, monolithic ceramics and glasses, or extremely porous aerogel materials [9-10]. The sol-gel coating process usually consists of 4 steps: (i) the desired colloidal particles dispersed in a liquid to form a sol. (ii) the deposition of sol solution produces the coatings on the substrates by spraying, dipping or spinning, (iii) the particles in sol are polymerized through the removal of the stabilizing components and produce a gel in a state of a continuous network, (iv) the final heat treatments pyrolyze the remaining organic or inorganic components and form an amorphous or crystalline coating, (v) the materials used in the preparation of the sol are usually inorganic metal salts or organometallic compounds such as metal alkoxides [9-10].

C. Hydrothermal Synthesis

In a sealed vessel (bomb, autoclave, etc.), solvents can be brought to temperatures well above their boiling points by increase in auto-genous pressures resulting from heating [11]. Performing a chemical reaction under such conditions is referred to as solvothermal processing or, in the case of water as solvent, hydrothermal processing. The advantages of the techniques are: (i) increased solubility, (ii) high temperature is replaced by high pressures. The disadvantages are: (ii) specialized equipment needed such as sealed vessel (bomb, autoclave).

D. Combustion Synthesis

Combustion synthesis (CS) or fire synthesis is also known as self-propagating high temperature synthesis [12]. To generate fire, an oxidizer, a fuel, and the right temperature are needed. All these three elements make up a fire triangle. Fire can be described as an uncontrolled combustion, which produces heat, light, and ash. The process makes use of highly exothermic redox chemical reactions between an oxidizer and a fuel. It is a versatile, simple and rapid process, which allows effective synthesis of a variety of nanosized materials. This process involves a self-sustained reaction in homogeneous solution of different oxidizers (*e.g.*, metal nitrates) and fuels (*e.g.*, urea, glycine, hydrazides). Depending on the type of the precursors, as well as on conditions used, the CS may occur as either volume or layer-by-layer propagating combustion modes. This process not only yields nanosized oxide materials but also allows uniform (homogeneous) doping of trace amounts of rare-earth impurity ions in a single step as shown in Figure 2.2 [13].

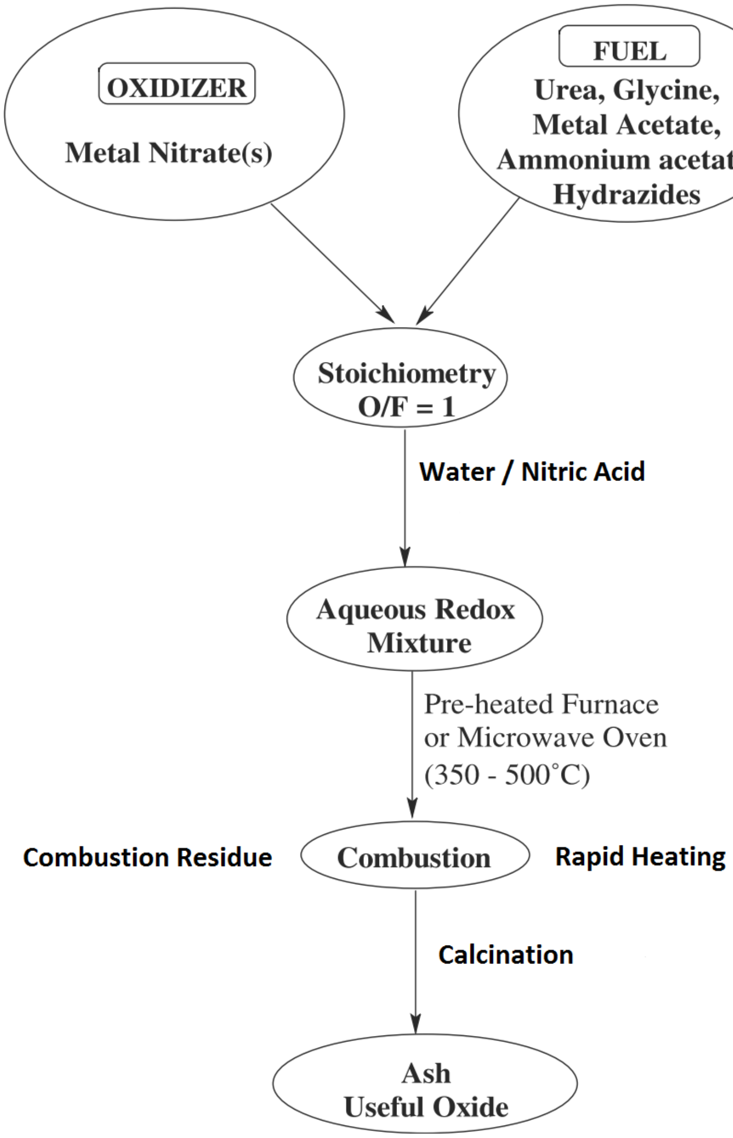

Figure 2.2 Flow chat for preparation of nanoceramics using auto-combustion method [13].

Simple methods for calculating thermo chemical parameters of fuel-oxidizer mixtures are desirable for various purposes in the field of propellants and explosives. The constitution of a fuel-oxidizer mixture is usually expressed in terms of parameters such as mixture ratio, equivalence ratio, elemental stoichiometric coefficient (φ) [14]. The highest heat (chamber temperature in the rocket motor) is produced when the equivalence ratio (φ = oxidizer/fuel ratio) is unity. The equivalence ratio of an oxidizer and fuel mixture is expressed in terms of the elemental stoichiometric coefficient. In this type of calculation, oxygen is the only oxidizing element; carbon, hydrogen, and metal cations are reducing elements and nitrogen is neutral. Oxidizing elements have positive valencies and reducing elements have negative valencies. The fuel to oxidizer ratio is calculated by summing of the total oxidizing and reducing valencies in the fuel and dividing its sum of total oxidizing and reducing valencies in the salt. The valencies of the elements have been assigned by assuming the oxidation state of the elements C, H, O, N, to be 4+, 1+, 2- and 0, respectively.

$$\sum \emptyset_e = \frac{\sum(Coefficient\ \ of\ elements\ in\ the\ molecular\ formula\ of\ Fuel) \times (Valency)}{\sum(Coefficient\ \ of\ elements\ in\ the\ molecular\ formula\ of\ Oxidizer\ Salt) \times (Valency)}$$

The auto-combustion technique offer advantages such as short preparation time, single step process, easy complex formation, low temperature requirement and nanoparticle synthesis capability. This type of stoichiometric balance of a redox mixture for a combustion reaction is fundamental to the synthesis of an oxide material by the solution combustion method [13]. Some important criteria that qualify an ideal fuel are: (1) be water soluble, (2) have low ignition temperature (<500 °C), (3) be compatible with metal nitrates, *i.e.*, the combustion reaction should be controlled smoothly and not lead to explosion, (4) evolve large amounts of gases that are of low molecular weight and harmless during combustion, (5) yield no other residual mass except the oxide in question, (6) be readily available or easy to prepare.

The advantages of CS process are: (a) it is an easy and fast process that uses relatively simple equipment, (b) composition, structure, homogeneity and stoichiometry of the products can be controlled, (c) formation of high-purity products is ensured by this method, (d) high exothermicity of the metal nitrate–fuel reaction permits incorporation of desired quantity of impurity ions or dopants in the oxide hosts to prepare solution combustion synthesis of oxide and stabilization of metastable phases is possible by this method, (e) formation of products of virtually any size (micron to nano) and shape (spherical to hexagonal) can be achieved by this process, (f) this method involves lower costs of preparation compared to conventional ceramic methods, (g) it is economically attractive and easy to scale up, (h) uniform distribution of the dopants takes place throughout the host material due to the atomic mixing of the reactants in the initial solution [15].

For auto combustion synthesis of samples, appropriate stoichiometric ratios of the high purity precursor materials such as metal nitrates (as oxidizers) are mixed with urea (fuel) with optimized fuel to oxidizer ratio. Then drop by drop water and/or Nitric acid are added to that mixture till the formation of gel. After that, the gel will be rapidly heated *(combustion)* in 400^0C (depending on melting temperature of fuel) in furnace for 30 minutes [15-16]. The gel instantaneously gets ignited generating a voluminous and spongy ceramic oxide called as *combustion residue*. The combustion residues are ground in the agate-motar followed by calcination. The formation of the single phase compounds are checked using X-ray diffraction technique. In the present study, polycrystalline nano $BiFeO_3$ powders were synthesized by auto-combustion method using urea as fuel and metal nitrates ($Fe(NO_3)_3.9H_2O$, $Bi(NO_3)_3.5H_2O$) as oxidizers. In order to optimize the single phase synthesis condition of $BiFeO_3$, different fuel to oxidizer ratios have been investigated.

The calcined powder are subsequently grinded into fine powder and the phase formation is checked by X-ray diffraction technique at room temperature. The above calcined powder was mixed with PVA (polyvinyl alcohol which acts as a binder) in mortar and pestle. To get uniform and fine grain, the granules were passed through sieve. The binder mixed powder was compacted to form pellet by a hydraulic press at suitable pressure using die set. The sintering of the pellet sample was carried out at an optimized temperature for densification. The sintered pellets were polished by emery paper and painted with silver paste as an electrode for electrical measurement. The painted samples were kept in the oven for 3 hrs. to evaporate the moisture in the sample, if any.

2.3 Experimental Techniques

In order to understand the chemistry and physics of materials, different aspects of the materials like structure, surface morphology, thermal, electrical, mechanical, optical *etc.* should be studied in details. In view of this, various experimental techniques are used to get a better understanding of structure-property relationship of solids. The basic working principle and importance of various experimental methods (used here) for characterization of materials are given below.

2.3.1 X-ray Diffraction Technique

X-ray diffraction (XRD) is a non-destructive technique to determine and study the crystal structure of crystalline materials. Physical properties of solids (*i.e.*, electrical, optical, magnetic, ferroelectric, *etc.*) are governed by the atomic arrangements of chemical species of the materials [17]. Therefore, crystal structure determination is an essential part of characterization of materials for device application. In polycrystalline materials, the randomness of crystallite orientation always allows a fraction of the sample to be suitably oriented with respect to the incident beam, which, in turn, enables for the appearance of diffraction peaks.

X-ray Diffraction technique is used to find out the crystal structure (*i.e.*, atomic arrangement of the materials) because 'd' the interplaner spacing of diffraction planes is of the order of X-ray wavelength λ. For a given d-spacing and wavelength λ, the various orders n of reflection occurs only at the precise values of angle θ, which satisfies the Bragg condition: $2d\sin\theta = n\lambda$ [18]. Some important characteristic features of the x-ray diffraction patterns are: (i) the Bragg angle θ depends on the interplaner spacing (d) of the set of planes and the wavelength λ of the X-ray, whereas the spacing d_{hkl} depends on the unit cell dimension of the sample, (ii) the relative intensity of the reflection lines depends on kind and number of atoms and their arrangements on the lattice planes reflecting the primary x-ray beam.

The accurate determination of lattice parameters provides an important basis in understanding the various properties of the materials. The calculation of lattice constants from the line positions (2θ) or d spacing can be estimated from a general formula [19]:

$$\frac{1}{d_{hkl}^2} = V^2(h^2b^2c^2sin^2\alpha + k^2c^2a^2sin^2\beta + l^2a^2b^2sin^2\gamma)$$

$$\mathrm{V} = \text{ unit cell volume} = abc(1 - cos^2\alpha - cos^2\beta - cos^2\gamma + 2cos\alpha\ cos\beta\ cos\gamma)^{1/2}$$

Where a, b, c, α, β and γ are lattice parameters and h, k, l are the Miller indices. Using the above formula, lattice parameters for all the compositions were found out.

For powder method, the intensity is given by:

$$\mathrm{I} = |\mathrm{F}|^2 \mathrm{J} \frac{(1+\cos^2 2\theta)}{\sin^2\theta\cos\theta} e^{-2\mathrm{M}}$$

Where, $\frac{(1+\cos^2 2\theta)}{\sin^2\theta\cos\theta}$ = Lorentz- polarization factor, $e^{-2\mathrm{M}}$ = temperature factor, F = structure factor and J = scale factor.

The modulus of structure factor |F| and the intensity are related by $|\mathrm{F}| \propto \mathrm{I}^2$ [19]. |F| can be calculated theoretically if the positions of the atoms (*i.e.*, x, y, z) in the unit cell are known using the following equation,

$$\mathrm{F}\ (hkl) = \sum_{j=1}^{N} f_j \exp 2\pi i\ (hx_j + ky_j + lz_j),$$

Where x_j, y_j and z_j are the fractional co-ordinates and f_j is the atomic scattering factor for the j^{th} atom in the unit cell, N being the total number of atoms in the cell. F is, in general, a complex number whose absolute value is defined as the ratio of the amplitudes.

$$|\mathrm{F}| = \frac{\text{amplitude of the wave scattered by all atoms of a unit cell}}{\text{amplitude of the wave scattered by an electron at origin}}$$

Structure factor thus is the manifestation of the nature of the constituent atoms and their arrangements in the unit cell. Determining the structure and refinement process of a phase from diffraction measurements on a polycrystalline sample can be divided into five steps: (i) measuring the positions of the peaks, (ii) determining the crystal system and the cell parameters, searching for systematic extinctions and determining the possible space groups, (iii) measuring the integrated intensities, (iv) suggesting a possible structure: creating a structural model with approximate values for the positions of the atoms, (v) refining the structure. This refinement is usually achieved using the Rietveld method [20].

In the present study, the phase formations and crystal structure determination of the compounds were carried out using X-ray powder diffractometer (PANalytical, PW3040, Netherlands) at room temperature. The X-ray diffraction (XRD) data were collected at very slow scan of 2° /min with a step size of 0.02° in a wide range of Bragg's angle 2θ ($20° \leq 2\theta \leq 80°$) using Cu-$K_{\alpha 1}$ radiation ($\lambda = 1.5405$ Å) with Nickel filter.

A. Rietveld Method

Hugo M. Rietveld, a Dutch physicist, demonstrated that accurate determination of crystal and magnetic structures is possible using neutron diffraction data from powders. His approach was later extended to X-rays and named as the "Rietveld Method". The technique allows a large amount of structural information to be extracted from the intensities of overlapping reflections, (*i.e.,* whether they are partially or completely overlapped) by treating each point in the pattern as an individually observed intensity and then comparing a simulated pattern with the experimentally obtained pattern. It is important to note that the Rietveld method is a 'structure refinement method' not a 'structure solution method' where a prior knowledge of the crystal structure is essential to begin the refinement [20].

The Rietveld refinement is a method where intensities obtained from XRD measurements of the crystalline samples allow to propose an approximate structural model. The process of successive profile refinements modulates different structural and microstructural parameters of the simulated pattern to fit the experimental diffraction pattern. Rietveld method perform a curve fitting by considering the observed intensity $y_{i(obs)}$ of each equally spaced steps i over the entire pattern including the background intensity and the sum of the contribution of reflections close to the i powder pattern step:

$$y_{i(obsserved)} = y_{i(background)} + \sum_{i} y_{i(Bragg)}$$

The Rietveld method is a refinement technique to minimize the residual S_y between the observed intensity $y_{i(obs)}$ and the calculated intensity $y_{i(calc)}$ by the best least-square fits to all the steps:

$$Sy = \sum_{i} \frac{(y_{i(obs)} - y_{i(calc)})^2}{y_{i(obs)}} = \sum_{i} w_i(y_{i(obs)} - y_{i(calc)})^2$$

Where w_i is statistical weight that equals $1/y_{i(obs)}$ and $y_{i(calc)}$ is the intensity of each step which can be calculated by a mathematical expression that includes the factors related to both the structure and the non-diffraction terms. Therefore a good initial structure model is required including information about space group, unit cell lattice parameters, atomic positions and instrumental details, where $y_{i(calc)}$ is expressed:

$$y_{i(calc)} = s \sum_{hkl} L_{hkl}\ |F_{hkl}|^2\ \emptyset(2\theta_i - 2\theta_{hkl}) P_{hkl} A + y_{i(background)}$$

where s is the scale factor, L_{hkl} contains the Lorentz polarization and multiplicity factors, F_{hkl} is the structure factor, $\emptyset(2\theta_i - 2\theta_{hkl})$ is the peak shape function which describes the effects of the instrument and the sample on the reflection profile, P_{hkl} is the preferred orientation function, A is the absorption factor and $y_{i(background)}$ is the background intensity at the step i of the diffraction pattern. During the refinement cycles, each of these terms and its parameters may be varied to improve the match between observed and calculated diffraction patterns. The fitting results can be estimated by examining a plot of the difference between observed and calculated patterns and several numerical terms can be used to estimate the goodness of the least-square refinements. These residual values are defined as [20]:

$$R_p = \frac{\sum \left| (y_{i(obs)} - y_{i(calc)}) \right|}{\sum (y_{i(obs)}}$$

$$R_{wp} = \left| \frac{\sum w_i(y_{i(obs)} - y_{i(calc)})^2}{\sum w_i\ (y_{i(obs)})^2} \right|^{1/2}$$

$$\boldsymbol{Goodness\ of\ Fit} \sim \chi^2 = \sum \frac{w_i(y_{i(obs)} - y_{i(calc)})^2}{n - p + c}$$

where *n* is the number of observations, *p* is the number of parameters and *c* is the number of constrains in the definition of goodness of fit. A good fit with the refined structure model will accompany with a low residual value. The R_{wp} is commonly considered since it contains S_y whose value to be minimized by the least-square refinements. The goodness of fit, which is directly proportional to S_y is ideally to be unity [20-21]. R factors are useful to evaluate the quality of the refinement. Out of the several R-factors, R_{wp} is statistically the most meaningful quantity since the numerator in the equation is minimized during the refinement. Ideally the final R_{wp} should approach the statistically R_{exp} value and therefore, χ^2 should approach 1.0. The so-called Bragg R factor provides a comparison between the observed intensity and the calculated intensity. However the final quality of a Rietveld refinement should be judged by the fit of the calculated pattern to the observed data [20-21].

In the present study, the Rietveld refinement was performed using the FULLPROF package [20-21]. The peak shapes were refined using pseudo-Voigt function/Thompson-Cox-Hastings modified pseudo-Voigt and background was modeled using six coefficients polynomial function/ liner interpolation. During the refinement process zero correction, scale factor, background, unit cell parameters, atomic positions, thermal parameters, half width parameters (U, V and W) and background were varied. The occupancy of all the atoms was kept fixed during refinement process. The peak profile function giving the best fit to the experimentally observed data was chosen and kept same for all within a series of patterns with varying composition.

B. X-ray Line Profile Analysis (XLPA)

X-ray diffraction peaks broaden when the crystal lattice become imperfect. In particular, the broadening in the XRD peaks occurs due to several causes such as (i) finite coherent length (small crystallite size), (ii) micro strains in the crystallite and (iii) staking disorder [22]. The diffraction profile from polycrystalline aggregate consisting of crystallites of all shapes and sizes in all orientations is represented by the Fourier series coefficients. According to convolution theorem, the Fourier transform of the nth order pure diffraction profile will be the product of nth order Fourier transforms of particle size ${A_L}^P$(n), strain ${A_L}^S$(n) and faulting ${A_L}^D$ (n) respectively [23] *.i.e.,*

$$A_L(n) = A_L^P(n)A_L^S(n)A_L^D(n)$$

Consequently,

$$\left[\frac{dA_L}{dL}\right]_{L=0} = \left[\frac{A_L^P}{dL}\right]_{L=0} = -\frac{1}{p}$$

Where, L = n*a*, '*a*' represents real distance in the crystallite and given by

$$\frac{2a(sin\theta_1 - sin\theta)}{\lambda} = \frac{2a(sin\theta - sin\theta_2)}{\lambda} = \frac{1}{2}$$

Here, θ refers to Braggs angle corresponding to peak position of intensity distribution for wavelength λ. θ_1, θ_2 are Bragg angles corresponding to peak position in the intensity distribution where tail merges in to the background. *p* is the crystallite size in the direction considered.

Mathematically, the most natural measure of broadening of the diffraction profile is the second moment or the variance which is the mean square deviation from its mean. The variance (W) of the x-ray line profile is given by $W = W_P + W_S + W_D$ [24].

Where W_P, W_S, W_D is the factor corresponding to crystallite size, lattice strain, layer disorder respectively. The variance of the X-ray line profile is represented by

$$Variance = W = \frac{\alpha(2\theta)\lambda}{2\pi^2 p' cos\theta} + \frac{S\lambda^2}{cos^2\theta}$$

$$S = \frac{< e^2 > - \frac{\beta_D^2}{\pi^2}}{d^2} \; and \; \frac{1}{p'} = \frac{1}{p} + \frac{\beta_D}{d}$$

β_D is the integral width of the defect profile, $<e^2>$ is the mean square strain, d is the inter planer spacing, $\alpha(2\theta)$ = total angular range in 2θ scale over which the measurements are being made. p' is the apparent particle size observed from variance method; *p* is true particle size calculated using Fourier line shape analysis. By knowing the value of p and p' we can calculated the value of β_D. Here 'g' is the mean fractional change in the interlayer distance in any given direction and γ be the transition probability *i.e.,* the proportion of the planes affected by disorder. For all the sample, we have calculated g and γ value from (0 0 l) reflection and the extracted values are

$$g = \frac{1}{\pi l} cot^{-1} \left(\frac{\pi \Delta}{\beta_D}\right) \; and \; \gamma = \frac{\beta_D}{\sin^2(\pi l g)}$$

Here Δ is the distance of the peak from the centroid of the diffraction profile. The dislocation density ρ, according to Williamson and Smallman [25] can be expressed as

$$\rho = \frac{2(3 < e^2 >)^{1/2}}{bp}$$

It is assumed that a = b, the lattice parameter of the sample.

In the present study, we have used BREADTH, freely available software [26] package for Fourier X-ray line profile analysis while for Variance-range analysis, program code has been written in *Fortran*-77 to analyze the broadened diffraction profile.

2.3.2 Field Emission Scanning Electron Microscopy (FESEM)

The Field emission scanning electron microscopy (SEM) is a useful technique to study the topography, morphology and composition of the materials with higher resolution. Electrons are liberated from a field emission source and accelerated in a high electrical field gradient [27]. Within the high vacuum column, these so-called primary electrons are focused and deflected by electronic lenses to produce a narrow scan beam that bombards the object. The interaction between electron and object/sample is shown in Figure 2.3.

The interaction of high-energy electrons with specimen leads to the excitation of a variety of signals, which can be used for characterization of microstructure and other related properties. This experiment is based on the principle of inelastic scattering of secondary electrons and subsequent imaging. The scattered secondary electrons are emitted from the sample surface are collected by the detector and subsequently produces an electronic signal. This signal is amplified and transformed to a video scan-image that can be seen on a monitor or to a digital image which can be saved and processed further. In order observe micrographs using a SEM, the objects are first made conductive for current. This is done by coating them with an extremely thin layer (1.5 - 3.0 nm) of gold/platinum. The objects must be able to sustain the high vacuum and the properties should not alter due to vacuum, for example by losing water molecules or gasses during SEM characterization. In a field emission (FE) scanning electron microscope, no heating is produced but a so-called "cold" source is employed. An extremely thin and sharp tungsten needle (tip diameter 10^{-7}–10^{-8} m) functions as a cathode in front of a primary and secondary anode. The voltage between cathode and anode is in the order of magnitude of 0.5 to 30 KV. The technique provides useful information regarding surface properties of a sample such as microstructure, grain dimension, grain orientation, phase identification and voids**.**

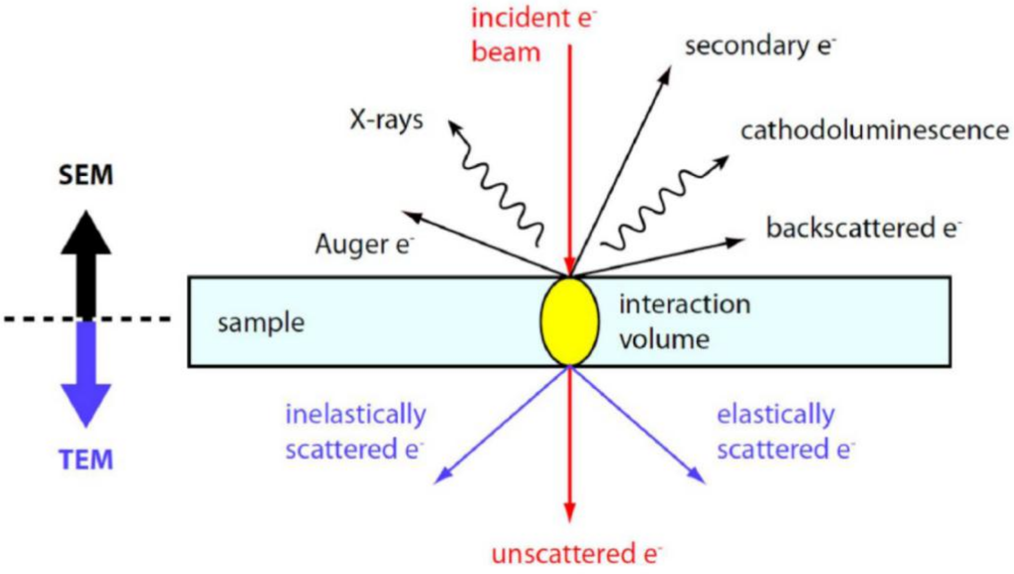

Figure 2.3 Electron and sample interaction in scanning electron microscopy (SEM) setup.

In the present study, Field emission scanning electron microscope (FESEM) (Model: SUPRA 35VP) and (Nova Nano SEM 450) were used to determine grain size, void and uniformity of sample matrix. The chemical compositions of the samples have been determined by Energy Dispersive X-Ray Spectrometry (EDX). The sample pellet was platinum coated for 15 minutes before being scanned under high resolution field emission gun.

2.2.3 Transmission Electron Microscopy (TEM)

TEM is considered to be an effective method, which provides a reliable estimation of crystallite size of nano particles. The TEM micrographs yield the following information: (1) Morphology: the size, shapes and arrangement of particles of the specimen (ii) Crystallographic information: the arrangement of atoms in the specimen, detection of atomic scale defects in areas of a few nanometers in diameter. (iii) Compositional information of the elements of the sample and their relative ratios in areas of nanometers [27].

The electron beam incident on the sample splits into three: transmitted electrons, back-scattered electrons and absorbed electrons. The transmitted electrons can be classified into three groups (a) direct transmitted electrons, which pass through the specimen with little change of direction or wavelength, (b) elastic scattered electrons, which undergo directional change due to atomic collision but retain their energy and (c) inelastic scattered electrons which undergo both directional change as well as partial energy loss. The ratio of directly transmitted electrons to that of elastically scattered electrons is related to contrast of image in TEM. The contrast in amorphous samples is primarily determined by mass thickness while in crystalline samples the images are influenced by Bragg's reflection.

In the present study, the structure and morphology of powders were studied with Techno $G^2$30STwin respectively. The powders were dispersed in ethanol/acetone with the help of an ultrasonic bath and then collected onto a carbon film mounted on electron microscope grids. Investigation was carried out at an accelerating voltage of 200 kV. Diffraction and scattering absorption contrasts, structure imaging and the selective area electron diffraction patterns were recorded.

2.3.4 Thermal Analysis

Thermal analysis is a study of experimental condensed matter physics where the properties of the materials are investigated as a function of temperature [28]. There are a large number of thermal analysis methods providing information regarding various aspects of the materials such as: phase transitions, transition temperature, heat of reaction, oxidative stability, purity, thermal stability, creep/stress relaxation, flexural modulus, energy dissipation, permittivity and loss factor etc. In practice thermal analysis gives properties like; enthalpy, thermal capacity, mass changes and the coefficient of heat expansion. Solid state chemistry uses thermal analysis for studying the reactions in the solid state, thermal degradation reactions, phase transitions and phase diagrams. Among various thermal analysis techniques, thermogravimetry analysis (TGA) and differential scanning calorimetric (DSC) are included in our study for analysis purpose.

TGA is basically used to determine the amount and the rate of weight change in the material as a function of temperature in a controlled atmosphere. The measured weight loss curve gives information on: (a) changes in sample composition (b) thermal stability (c) kinetic parameters for chemical reactions in the sample. Thermal events do not bring about a change in the mass of the sample, such as melting crystallization and glass transition cannot be detected by TGA, but those accompanying mass change, such as decomposition, sublimation, reduction, desorption, absorption and vaporization can be determined by this technique.

DSC as the name implies, is a technique involving the measurement of heat effect in a specimen while subjecting to a temperature scan. The heat effects are detected by measuring the differences in heat flow into or from the sample and a reference material as a function of temperature. Since the reference is thermally inert in the temperature range of interest, such measurement facilitates isolation of heat effect in the samples from the heat taken up for rising temperature of the specimen and its surroundings. The rate of heat exchange between the sample and its surroundings (while it undergoes a transition) can, therefore, be suitably amplified and recorded. DSC is employed to determine the quantity of heat that is either absorbed (endothermic) or released (exothermic) by a substance undergoing a physical or chemical change.

The simultaneous application of TG and DSC to the same sample in a single instrument provides more information due to the perfectly identical test conditions. In the present study, we have used NETZSCH analyzer for thermal analysis. Samples were heated in a platinum pan from room temperature to 900 °C at a heating rate of 10 °C/min under air atmosphere.

2.3.5 Dielectric Property Measurement

When electric field is applied to a dielectric material it becomes polarized due to induced dipole moment or reorientation of permanent dipole moments (local re-arrangement of charge) present in the sample. Under an external electric field (**E**), the electric displacement vector (**D**)

$$\mathbf{D} = \varepsilon\mathbf{E} = \varepsilon_0\,\mathbf{E} + \mathbf{P}$$

Where ε is the dielectric permittivity and P is called the polarization (dipole moment per unit volume) and can be expressed as.

$$\mathbf{P} = \chi_e\,\varepsilon_0\,\mathbf{E}$$

Where χ_e is the electric susceptibility and ε_0 is the free space permittivity ($8.85\text{x}10^{-12}$ F/m) [29].The induced dipole moment (**P**) is directly proportional to applied field (**E**) (low field magnitude) and by combining the above two equations, we can write

$$\frac{\boldsymbol{\varepsilon}}{\boldsymbol{\varepsilon_0}} = \boldsymbol{\varepsilon_r}$$

where ε_r is called the relative permittivity.

In an alternating electric field the dielectric permittivity or relative permittivity is a complex quantity and it is written as:

$$\boldsymbol{\varepsilon_r^*} = \boldsymbol{\epsilon^{/}} + \boldsymbol{\epsilon^{//}}$$

where the real part $\epsilon^{/}$ is known as dielectric permittivity or dielectric constant and the imaginary part $\epsilon^{//}$ is related to the energy loss in the system.

When a dielectric is subjected to the ac voltage, the electrical energy is absorbed by the material and is dissipated in the form of heat. The dissipation is called dielectric loss. In this case, the current lead the voltage by (90-δ), where δ is called the loss angle and tanδ is the electrical loss better known as tangent loss (See Figure 2.4).

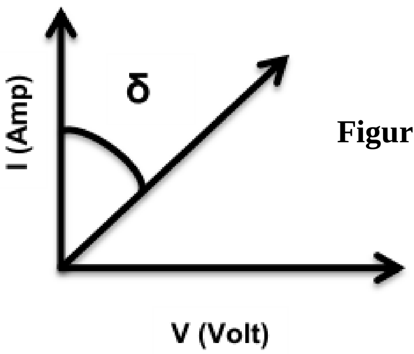

Figure 2.4 Phase diagram between current and voltage.

Loss tangent can be expressed as:

$$tan\delta = \frac{\boldsymbol{\epsilon}^{//}}{\boldsymbol{\epsilon}^{/}}$$

The dielectric property of a system highly depends on the frequency and temperature because of the various polarization mechanisms and as a consequence, resonance and relaxation effects occur as a function of frequency. When the applied frequency is in the same range as the relaxation time, resonance occurs.

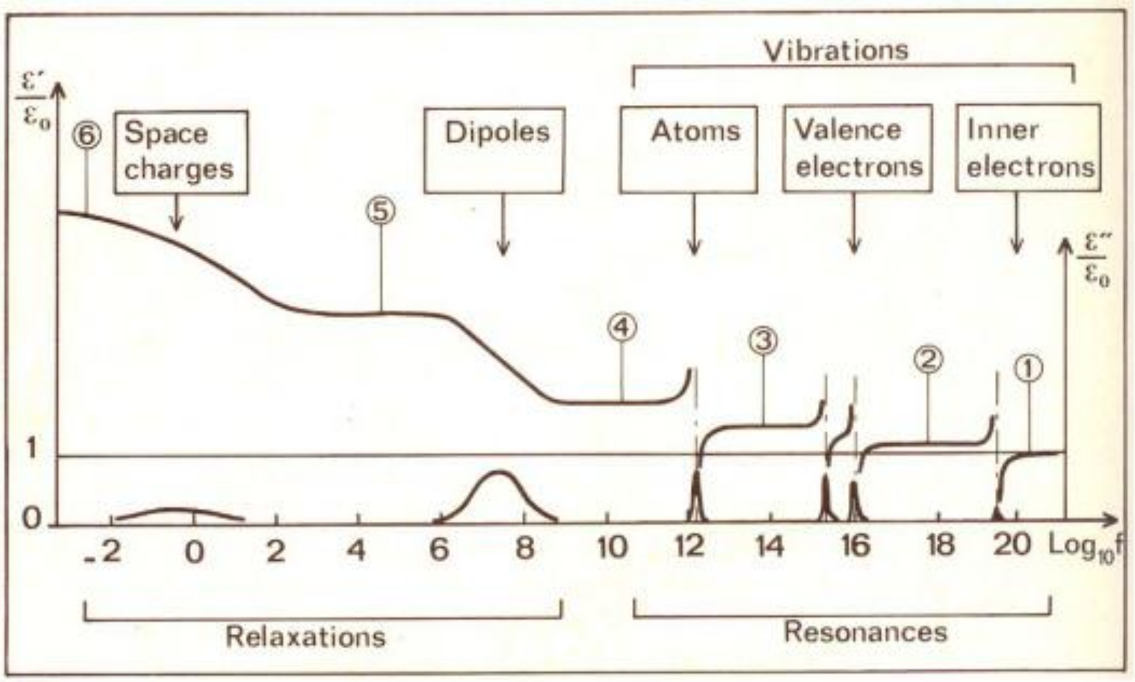

Figure 2.5 Variations of $\boldsymbol{\epsilon}^{/}$ and $\boldsymbol{\epsilon}^{//}$ with frequency [29].

Classification of Polarization

The frequency dependent dielectric properties can be explained by different types of polarization mechanisms as shown in Figure 2.5.

1. *Electronic polarization*: This effect occurs as a result of oscillation of the electronic charge relative to the nucleus under the influence of the electric field. Because of the low mass of electrons, these oscillations occur at very high frequencies, above 10^{14}-10^{16} Hz.

2. *Ionic polarization*: The displacement of cations and anions in an ionically-bonded crystal are physically displaced by the external electric field. The corresponding frequencies occur below the optical frequencies and in the infrared range (< 10^{13} Hz).
3. *Dipolar/orientational polarization*: Only substances with permanent dipole moments may possess an orientational polarization, which is described as the rotation of the permanent dipole moments into an applied electric field direction. This process contributes only at lower frequencies (< 10^{8} Hz).
4. *Space charge polarization*: This polarization is due to accumulation of free charges at interfaces between different environments. This contributes at lower frequencies (< 10^{4} Hz) [29].

In the present work, a computer controlled impedance analyzer (PSM-1735N4L NumetriQ: UK) was used to measure the dielectric and electric properties of the proposed materials. The silver electroded samples were used to perform the measurements. All the samples after electroding kept at 150 °C for few hours before taking any electrical measurements to remove moisture from the sample, if any. During the experiment, silica gel was also used inside the sample holder to get rid of the moisture. The electrical properties were measured as a function of temperature (25°C to 400°C) at different frequencies (100Hz-1MHz) at perturbation voltage 1V using laboratory designed sample holder and heating setup.

2.3.6 Complex Impedance Spectroscopy

Complex impedance spectroscopy (CIS) is an experimental technique used to examine, analyze and interpret electrical response of a polycrystalline sample in a wide range of frequencies [30]. The technique analyzes the ac response of a system to a small sinusoidal perturbation, and following estimation of the impedance as a function of the frequency. This technique also enables us to evaluate and separate the contribution to the overall electrical properties in frequency domain due to electrode reactions at the electrode/material interface, the migration of charge carriers (ions) through the grains and across the grain boundaries within the sample. The display of impedance data in the complex plane plot appears in the form of a succession of semicircles attributed to relaxation phenomena with different time constants due to the contribution of grain (bulk), grain boundary and interfacial polarization in a polycrystalline material. Hence, the contributions to the overall electrical property by various electrical phenomena in the material are separated out easily.

AC electrical data may be represented in any of the four basic formalisms which are interconnected to each other

$$\text{Complex impedance: } Z^{*}=Z'-j\,Z''$$
$$\text{Complex admittance: } Y^{*}=(Z^{*})^{-1}$$
$$\text{Complex permittivity: } \varepsilon^{*}=(j\omega C_{o}Z^{*})^{-1}=\varepsilon'-j\varepsilon''$$
$$\text{Complex modulus: } M^{*}=j\omega C_{o}Z^{*}=M'+jM''$$

Where $j=\sqrt{-1}$, $\omega=2\pi f$ is the angular frequency and $C_0=\varepsilon_0\,Ad^{-1}$ in which C_0 is the vacuum capacitance of the cell without the sample. *A* and *d* are the sample effective area and thickness respectively.

Sometimes it is difficult to interpret the data whether the response is due to long-range conductivity (delocalized) or dipole relaxation (localized) of materials. Both localized and delocalized conduction are bulk processes, and therefore this gives rise to the same geometrical capacitance. The use of the imaginary part of the impedance (Z'') and conductance (Y'') is particularly appropriate for resistive and/or conductive analysis (when the long range conductivity is dominant) whereas the imaginary part of the permittivity (ε''*)* and electrical modulus (M'') are suitable when localized relaxation dominates. In the case of multiferroic materials, a combination of all the impedance formalisms is the best strategy to distinguish between the ferroelectric and nonferroelectric properties of the materials [31-32].

There are several ways of presenting the data and the most common are as follows. (a) plots of the real and imaginary components either in logarithmic or in linear coordinates against frequency, (b) polar plots of the imaginary component against the real component on a linear presentation. The type of relaxation can be understood by shape of the plot as Debye, Cole–Cole, Cole–Davidson *etc.*, and also as a means of finding the equivalent circuit for the material [30]. The relationship between microstructure and electrical properties can be obtained from complex impedance plot. The impedance spectrum is characterized by the appearance of semicircular arcs due to different electrical microstructural contribution. The semicircle at lower frequency is due to the contribution of electrode-material interface, another semicircular arc at intermediate frequency is due to the contribution of grain boundary, and at high frequency the semicircular arc is due to the bulk response of the material as shown in Figure 2.6. The impedance data were measures at same conditions as dielectric characterization.

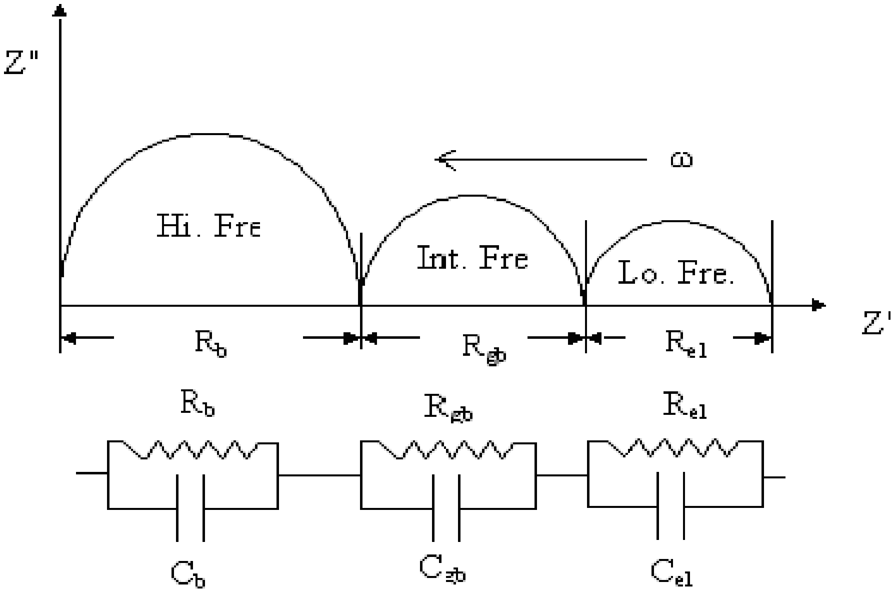

Figure 2.6 Relationship between microstructure-electrical properties in complex impedance plane and an electrical equivalent circuit in complex impedance plane. The intercept of the semicircular arcs on the real axis gives rise to the corresponding resistances such as Bulk, GB and interfacial.

2.3.7 Ferroelectric Hysteresis Measurement

The ferroelectric hysteresis loops of the materials studied in this work were characterized by Marine India PE loop tracer in silicon oil bath. The simplest method for measuring spontaneous polarization is the Sawyer and Tower method, as shown in Figure 2.7, in which C is the capacitance of the ferroelectric specimen and C_o is the standard capacitor [29]. The voltage across C should be sufficiently large to render a saturation in polarization, so V_o should be proportional to the polarization charge, $V_o = AP/C_o$, where A is the area of the specimen and P is the polarization. V is the applied voltage, which is usually an AC signal voltage of low frequencies. Thus, the applied field across the specimen is $F = V_c/d = (V - V_o)/d$. It is important to note that ferroelectric hysteresis at high frequency represent true polarization.

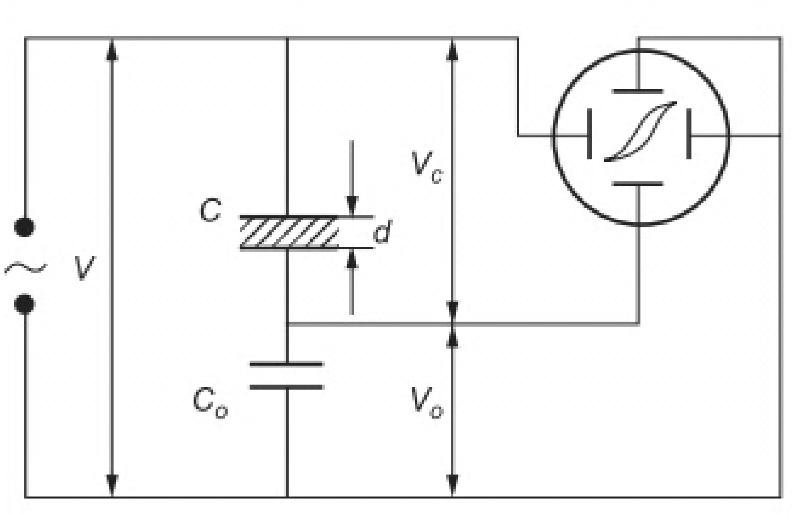

Figure 2.7 A Sawyer-Tower circuit for the measurement of ferroelectric hysteresis loop [29].

2.3.8 Vibrating Sample Magnetometer

A vibrating sample magnetometer (VSM) operates on Faraday's Law of Induction, which tells us that a changing magnetic field will produce an electric field [33]. This electric field can be measured and can tell us information about the changing magnetic field. A VSM is used to measure the magnetic behavior of magnetic materials.

In this experiment, the sample is vibrated by a known applied magnetic field (H) of frequency (ω) and change in magnetic flux (φ) in the sample induces an emf (V) across the coil according to Faraday's Law

$$V = -N\frac{d\varphi}{dt} = -NA\frac{dB}{dt} = -NA\mu_o\frac{d(H+M)}{dt}$$

Where A and N are the area and the number of turns in the coil respectively. μ_o is the vacuum permeability and M is the magnetization in the sample. The output voltage can be converted to magnetization on the basis of calibration in the system.

In the present study, the magnetic hysteresis (M-H hysteresis loop) behaviors of the samples were characterized by VSM Lakeshore up to a maximum field of ±2 Tesla at ambient.

2.3.9 Magneto-Dielectric Measurement

In the present study, the magneto-dielectric measurements were carried out in order to understand the magnetoelectric coupling in the material. The magneto-dielectric measurements were performed using a vibrating sample magnetometer (VSM Lakeshore model 142A) and a HIOKI 3532-50 LCR Hister at room temperature. The dielectric parameters (*i.e.*, capacitance, loss tangent, impedance, phase angle) at several magnetic field ($0 \leq H \leq 2$ Tesla: $\Delta H = 0.5$ Tesla) for all samples within the frequency range 100 Hz to 1 MHz at RT. The method of magneto-impedance spectroscopy was also employed to study the control of magnetic field on intrinsic bulk capacitance.

In the present work, all the proposed materials in Chapter-1 have been synthesized by auto-combustion technique. The sample synthesis conditions and geometrical parameters are listed in Table 2.1.

Table 2.1 Sample optimization conditions (calcination and sintering temperatures) and pellet specification of the combustion synthesized nano materials.

Sample Synthesis Conditions

Sample Name	Calcination Temperature	Sintering Temperature	Pellet Specification	
			Diameter (in cm)	Thickness (in cm)
$(1\text{-}x)BiFeO_3\text{-}xYMnO_3$				
x = 0.00	550^{o}C/ 3hrs.	700^{o}C/6hrs.	0.977	0.121
x = 0.025	600^{o}C/ 3hrs.	700^{o}C/6hrs.	1.006	0.111
x = 0.05	600^{o}C/ 3hrs.	700^{o}C/6hrs.	1.003	0.111
x = 0.075	600^{o}C/ 3hrs.	700^{o}C/6hrs.	1.005	0.110
x = 0.1	600^{o}C/ 3hrs.	700^{o}C/6hrs.	1.008	0.110
x = 0.15	650^{o}C/ 3hrs.	750^{o}C/6hrs.	1.004	0.113
x = 0.2	650^{o}C/ 3hrs.	750^{o}C/6hrs.	0.994	0.112
$(1\text{-}x)BiFeO_3\text{-}xGdMnO_3$				
x = 0.00	550^{o}C/ 3hrs.	700^{o}C/6hrs.	0.977	0.121
x = 0.025	700^{o}C/ 3hrs.	750^{o}C/ 6hrs.	0.994	0.105
x = 0.05	700^{o}C/ 3hrs.	750^{o}C/ 6hrs.	0.984	0.109
x = 0.075	700^{o}C/ 3hrs.	750^{o}C/ 6hrs.	0.994	0.104
x = 0.1	750^{o}C/ 3hrs.	780^{o}C/ 6hrs.	0.984	0.108
x = 0.15	750^{o}C/ 3hrs.	780^{o}C/ 6hrs.	0.994	0.108
x = 0.2	750^{o}C/ 3hrs.	780^{o}C/ 6hrs.	0.991	0.107
$(1\text{-}x)BiFeO_3\text{-}xDyMnO_3$				
x = 0.00	550^{o}C/ 3hrs.	700^{o}C/6hrs.	0.977	0.121
x = 0.025	700^{o}C/ 3hrs	750^{o}C/ 6hrs.	0.992	0.112
x = 0.05	700^{o}C/ 3hrs	750^{o}C/ 6hrs.	0.991	0.110
x = 0.075	700^{o}C/ 3hrs	750^{o}C/ 6hrs.	0.994	0.107
x = 0.1	700^{o}C/ 3hrs	750^{o}C/ 6hrs.	0.952	0.114
x = 0.15	750^{o}C/ 3hrs.	780^{o}C/ 6hrs.	0.985	0.105
x = 0.2	750^{o}C/ 3hrs.	780^{o}C/ 6hrs.	0.983	0.112
$Bi_{1-x}Ba_xFe_{1-x}Zr_xO_3$				
x = 0.00	550^{o}C/ 3hrs.	700^{o}C/6hrs.	0.977	0.121
x = 0.025	750^{o}C/ 3hrs.	780^{o}C/ 12hrs.	0.961	0.131
x = 0.05	750^{o}C/ 3hrs.	780^{o}C/ 12hrs.	0.954	0.132
x = 0.075	750^{o}C/ 3hrs.	780^{o}C/ 12hrs.	0.977	0.136
x = 0.1	750^{o}C/ 3hrs.	780^{o}C/ 12hrs.	0.983	0.166

2.4 References

[1] A. J. Moulson and J. M. Herbert, Electro ceramics: Materials, Properties and Application, John Wiley and Sons Inc., (2003).

[2] K. Uchino, Ferroelectric Devices, Marcel Dekker Inc., New York, (2000).

[3] R.N.P. Choudhary and S. K. Patri, Dielectric Materials: Introduction, Research and Applications, Nova Publishers, (2009).

[4] M. W. Barsoum, Fundamental of Ceramics, Institute of Physics Publishing Bristol and Philadelphia, (2003).

[5] M.N. Rahaman, Ceramic Processing and Sintering, Second Edition, Marcel Dekker Inc. New York.

[6] J.A. Rodríguez and M. F. García, Synthesis, Properties and Application of Oxide Nano materials, Wiley Interscience, John Wiley and Sons Inc., (2007).

[7] H. S. Nawla, Hand book of Nanostructured materials and Nano Technology, Academic Press, London, UK (2000).

[8] T. Ahn , J. Kim , H. Yang , J. Lee , and J. Kim, J. Phys. Chem. C, **116**, 6069 (2012).

[9] L. Hench and J. K. West, Chem. Rev., **90**, 33 (1990).

[10] C. J. Brinker and G. W. Scherer, Sol-Gel Science: The Physics and Chemistry of Sol-Gel Processing, Academic Press, UK (1990).

[11] S. Somiya and R. Roy, Bull. Mater. Sci., **23**, 453 (2000).

[12] S. T. Aruna and A. S. Mukasyan, Current Opinion in Solid State and Materials Science **12** 44 (2008).

[13] K.C. Patil, M.S. Hegde, T. Rattan, S. Aruna, Chemistry of Nanocrystalline Oxide Materials, World Scientific Publishing Co. Pte. Ltd., (2008).

[14] S.R. Jain, K.C. Adiga and V.R. P. Verneker, Combust. Flame, **40**, 71 (1981).

[15] S. N. Tripathy, B. G. Mishra, M. M. Shirolkar, S. Sen, S. R. Das, D. B. Janes, and D. K. Pradhan, Mater. Chem. Phys. **141**, 423 (2013).

[16] S. N. Tripathy, K. K. Mishra, S. Sen, B. G. Mishra, D. K. Pradhan, R.Palai, and D. K. Pradhan, J. Appl. Phys. **114**, 144104 (2013).

[17] Robert E. Dinnebier and Simon J. L. Billinge, Powder Diffraction: Theory and Practice, The Royal Society of Chemistry, Cambridge CB4 0WF, UK (2008).

[18] Vitalij K. Pecharsky and Peter Y. Zavalij, Fundamentals of Powder Diffraction and Structural Characterization of Materials, Springer (2009).

[19] B. D. Cullity, X-ray Diffraction, Addison-Wesley Publishing Company, Inc. (1956).

[20] R. A. Young, The Rietveld Method, Oxford University Press (1991).

[21] J. Rodriguez-Carvajal, Physica B **192**, 55 (1993).

[22] G.B. Mitra, S. Bhattacherjee, Acta Crystallogr. Sect. B: Struct. Sci. **26**, 2124 (1970).

[23] B.E. Warren, B.L. Averbach, J. Appl. Phys. **21**, 595 (1950).

[24] J.I. Langford, Nature **207**, 966 (1965).

[25] G.K. Williamson, R.E. Smallman, Philosophical Magazine **1,** 34 (1956).

[26] D. Balzar, J. Appl. Crystallogr. **28**, 244(1995).

[27] P. J. Goodhew, J. Humpphreys and R. Beanland, Electron Microscopy and Analysis, Taylor and Francis (2001).

[28] R. F. Speyer, Thermal Analysis of Materials, Marcel Dekker, Inc. New York (1994).

[29] K. C. Kao, Dielectric Phenomena of Solids, Elsevier Academic Press (2004).

[30] E. Barsoukov and J. R. Macdonald, Impedance Spectroscopy Theory, Experiment, and Applications, John Wiley & Sons, Inc., Hoboken, New Jersey (2005).

[31] R. Gerhardt, J. Phys. Chem. Solids **55**, 1491(1994).

[32] D. C. Sinclair and A. R. West, J. Appl. Phys. **66**, 3850 (1989).

[33] B. D. Cullity, C. D. Graham , Introduction to Magnetic Materials, John Wiley and sons. Inc., New Jersey (2009).

Chapter-3

Structural and Magnetoelectric Properties of Single Phase $BiFeO_3$ Nanoceramics

Part of the content of this chapter has been published in the journal "**Materials Chemistry and Physics**". Satya N. Tripathy**,** B. G. Mishra, M. M. Shirolkar, S. Sen, S. R. Das, D. B. Janes and Dillip K. Pradhan, **Mater. Chem. Phys. 141, 423 (2013).**

In this Chapter, we describe the optimization condition for synthesis of single phase $BiFeO_3$ (BFO) by auto-combustion technique. The prepared materials have been characterized by X-ray diffraction, transmission electron microscopy, field emission scanning electron microscopy, dielectric and magneto-dielectric measurements.

3.1 Introductory Remarks

It has already been discussed in the Chapter-1 that, one of the major issue associated with BFO is difficulty in fabricating/growing a single phase material. During synthesis, BFO phase is formed along with various impurity phases (*i.e.,* $Bi_2Fe_4O_9$, $Bi_{36}Fe_{24}O_{57}$ and $Bi_{25}FeO_{40}$) due to the kinetics of phase formation [1-2]. These secondary phases result high leakage current, poor ferroelectric properties, change in the stoichiometry of the desired sample and enhancement of magnetic properties which is not the intrinsic property of the material [1-2]. Cheng *et al.* reported that, $Bi_2Fe_4O_9$ is ferromagnetic at room temperature (RT) and undergoes a transition to antiferromagnetic state near 264 K [3]. The secondary phases Bi_2O_3, $Bi_2Fe_4O_9$ can also be removed by washing/leaching in HNO_3, but leaching leads to coarser powder and poor reproducibility [4]. It has also been reported that, a small amount of either divalent (Ca^{2+}, Sr^{2+}, Pb^{2+}, Ba^{2+}) or trivalent (La^{3+}, Nd^{3+}, Tb^{3+}, Sm^{3+}, Gd^{3+}) substitutions at Bi-site helps in stabilizing the single phase of BFO [5-7].

BFO shows G-type antiferromagnetic ordering at RT [6]. It has a helical magnetic spin cycloid with a wavelength of 620-640 Å resulting a weak local net magnetization, which averages to zero over a period of the incommensurate modulated spin structure [8]. This inhibits observation of the linear Magnetoelectric (ME) effect. Tae-Jin Park *et al.* observed that magnetization can be enhanced by suppression of spin cycloid by synthesizing nanoparticles less than 620 Å [9]. Selbach *et al.* prepared BFO nanoparticles by a modified Pechini method which show strong size dependence magnetic properties. They also explained size-dependent polar displacement of cations that reflects in increasing ferroelectric depolarization field with decrease in particle size [10]. Palker *et al.* studied the decrease in Neel temperature of BFO with decreasing particle size [11]. In other words, controlling particle size is one of the key factors to enhance the multiferroic properties of BFO.

Hence in order to overcome the above problems in terms of realistic applications of the material, synthesis of single phase bismuth ferrite nanoparticle with crystallite size less than 620 Å is essential. There are several methods available in the literature for synthesis of BFO, such as solid-state method, sol-gel method, precipitation/coprecipiation, hydrothermal synthesis, high energy ball milling, microwave and Pechini method [12-17]. These synthesis techniques potentially often produce secondary impurity phases due to longer duration of heat treatment, various steps and lots of parameter involved. Therefore, the synthesis of nano-sized BFO at low temperature and to avoid formation of unwanted phases is essential and promising. Alternatively, auto-combustion technique is offering advantages such as short preparation time, single step process, easy complex formation, low temperature requirement and nanoparticle synthesis capability [18].

In this chapter, we study the optimization condition for the synthesis of single phase BFO nano ceramics using auto-combustion method for different fuel to oxidizer ratio. A special attention is focused to calculate structural and microstructural parameters using Rietveld refinement and X-ray line profile analysis respectively. The dielectric and magnetoelectric properties of the nanosized BFO have also been investigated with wide range of experimental conditions.

3.2 Experimental Procedure

Polycrystalline BFO nano particles were prepared by auto-combustion method using urea as fuel and metal nitrates as oxidizers. Stoichiometric amount of $Bi(NO_3)_3.5H_2O$, $Fe(NO_3)_3.9H_2O$ and urea were dissolved in minimum amount of distilled water to prepare a homogenous gel. The gel was then transferred to a furnace preheated at 400 ^oC. The gel instantaneously gets ignited to generate a voluminous and spongy *combustion residue*. Using this procedure, materials with fuel to oxidizer ratio (F/O) ranging from 0.5 to 1.5 were prepared at a step of 0.25. The combustion residue was calcined at an optimized temperature 550 °C for 3 h in air atmosphere. The fuel to oxidizer ratio was calculated using the method described by Jain *et al.* [19]. Thermogravimetric analysis (TGA) and Differential scanning calorimetry (DSC) measurement were performed using a NETZSCH analyzer. Samples were heated in an alumina pan from room temperature to 900 °C at a heating rate of 10 °C/min in air. The formation of the single phase desired compounds was verified by X-ray diffraction technique. XRD data were collected at slow scan of 2° /min with a step size of 0.02° and in a wide range of Bragg's angle 2θ ($20° \leq 2\theta \leq 80°$) with Cu-$K_{\alpha 1}$ radiation (λ = 1.5405 Å). The measurements were carried out at room temperature using an X-ray powder diffractometer [Philips Analytical (PW 3040)]. The calcined powders were compacted into cylindrical pellets by hydraulic press with 6×10^7 kg.m^{-2} using polyvinyl alcohol (PVA) as binder. The pellets were sintered at 700 °C for 6 hrs. The surface morphology (grain size, distributions, and voids) of the pellets was recorded using Hitachi Field Emission Scanning Electron Microscope (FESEM) in secondary electron imaging mode at room temperature with various magnifications. TEM micrographs and selected area diffraction pattern (SAED) were obtained using a transmission electron microscope (TEM) Techno G^{2}30 STwin. For electrical characterization, both of the parallel surfaces of the pellets were coated with silver electrode. The silver electrode samples were dried at 150 ^{o}C for 2 h to remove moisture, if any. The dielectric parameters were measured in a wide frequency range (*i.e.*, 100 Hz to 1 MHz) using a computer-controlled impedance analyzer (PSM-1735: NumetriQ, N4L, UK) in the temperature range 25-400 ^{o}C. The magneto-dielectric measurement was performed using a vibrating sample magnetometer (VSM Lakeshore model 142A) and HIOKI 3532-50 LCR Hister at RT.

3.3 Results and Discussion

3.3.1 Thermal Analysis

Figure 3.1 shows the X-ray diffraction pattern of the combustion residue at RT for fuel to oxidizer ratio, F/O = 0.75. The pattern confirms the formation of almost amorphous phase as it is seen by the presence of several broad diffraction peaks.

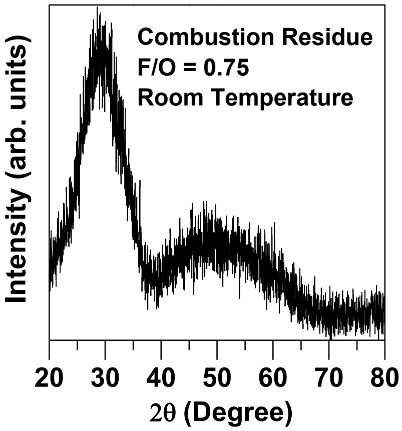

Figure 3.1 XRD pattern of combustion residue for F/O = 0.75 at RT.

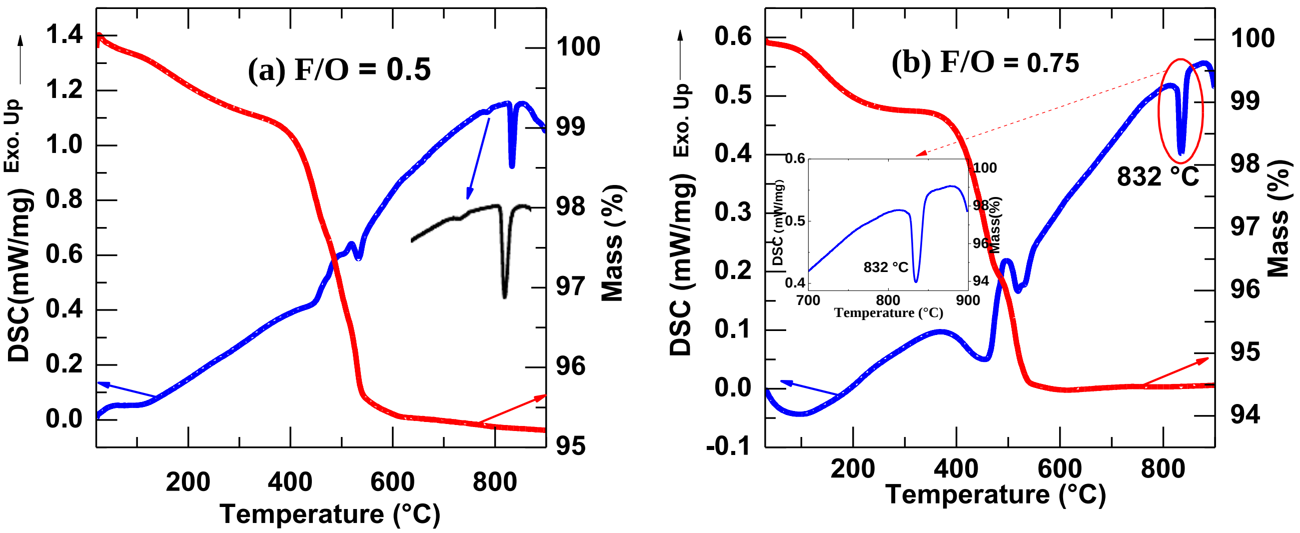

Figure 3.2(a) DSC-TGA thermo-gram of combustion residue for fuel to oxidizer ratio F/O = 0.5 (Inset-Magnified view of anomaly around 793 and 832 °C), **(b)** F/O = 0.75. (Inset- Magnified view of anomaly around 832 °C).

Figs 3.2 (a) and (b) show the DSC and TGA thermal analysis pattern of the combustion residue of $Fe(NO_3)_3.9H_2O$- $Bi(NO_3)_3.5H_2O$-Urea system from room temperature to 900 ^oC for F/O = 0.5 and F/O = 0.75 respectively. It has been observed that four progressive mass losses are found for the combustion residue on heating up to 550 ^oC and above this temperature it attain saturation (*i.e.*, temperature independent TGA thermo-gram). The observed mass losses in TGA pattern with increasing temperature corresponds to four decomposition stages. The first stage of mass loss occurs in the temperature range (50-150 ^oC) due to evaporation of water. This mass loss in the pattern is accompanied by a broad endothermic peak in DSC pattern. The second stage occurs (150-400 ^oC) is attributed to melting of urea. The third stage of mass loss in the temperature range 400-450 ^oC is because of complete decomposition of urea corresponding to an endothermic peak in DSC pattern. The final stage of mass loss (450-550 ^oC) due to nitrate and carbonaceous decomposition is also associated by an endothermic peak in DSC pattern. After 550 ^oC no mass loss is observed indicating the completion of reaction for formation of BFO oxide. From these studies, it can be inferred that a heat treatment of 550 ^oC to the minimum, requires transforming the combustion residue into final oxide of BFO. The endothermic peak around 832 ^oC shows the first order ferroelectric to paraelectric phase transformation in BFO [1, 6, 18]. For fuel to oxidizer ratio F/O = 0.5, we also observed a broad dip around 790 ^oC (along with 832 °C peak) which can be identified due to presence of secondary phases ($Bi_2O_3,$ $Bi_2Fe_4O_9$)

in the sample [1, 19]. But for fuel to oxidizer ratio F/O = 0.75 no evidence of the presence of secondary phase in the DSC pattern is observed. This novel method of growing BFO as consequence produces a pure phase material compared to other reported methods [12-17].

3.3.2 Structural and Microstructural Properties

Fig 3.3 (a) shows the Rietveld refinement result of room temperature X-ray diffraction pattern of BFO for $0.5 \leq F/O \leq 1.5$. It is observed that the crystalline phase is obtained when the samples

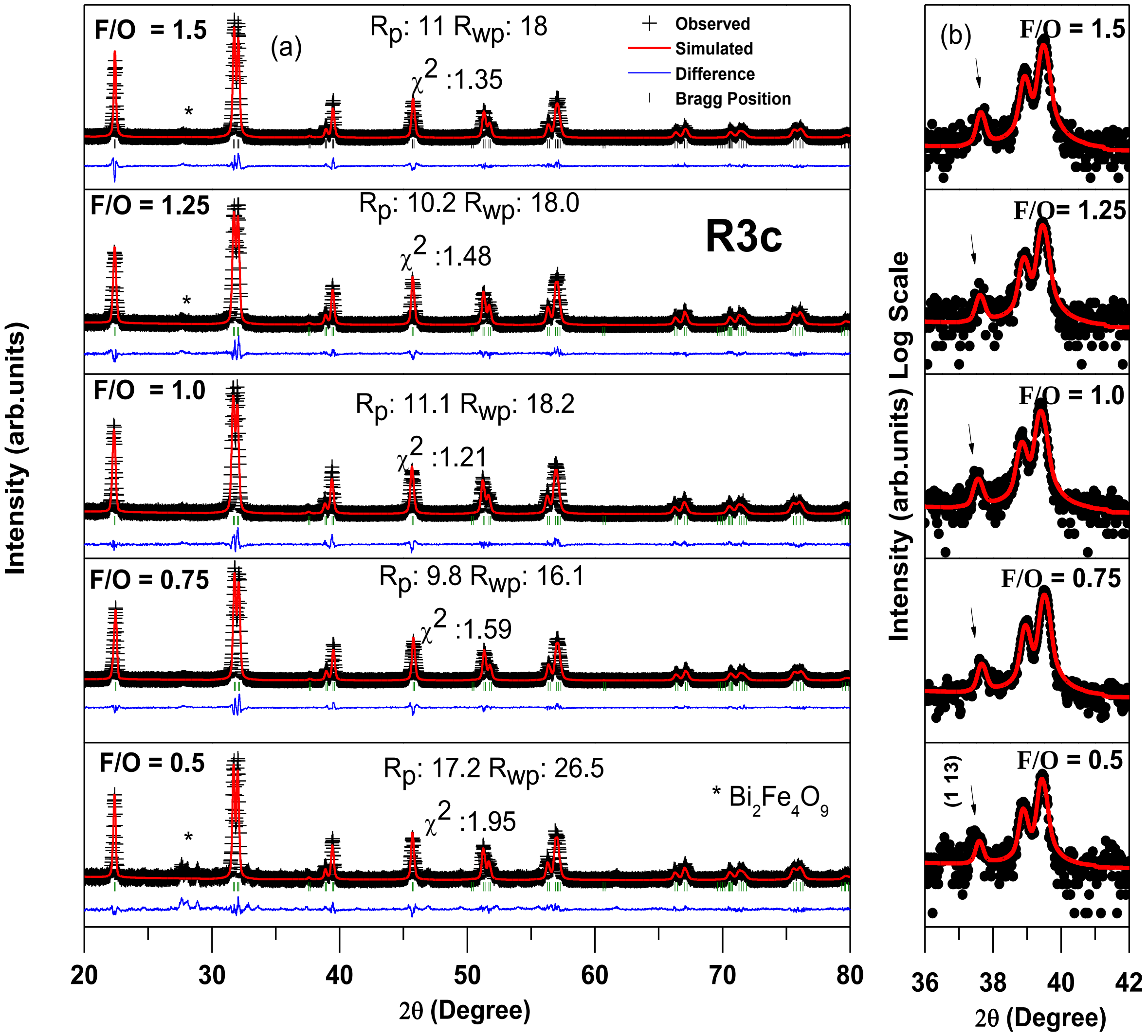

Figure 3.3(a) Rietveld refinement result of XRD pattern of BFO for $0.5 \leq F/O \leq 1.5$ at RT in linear scale. **(b)** Signature of super lattice (113) reflection around 38 degree indicating rhombohedral (*R3c*) structure for all F/O ratio (log scale).

are calcined at minimum temperature ~ 550 °C for 3 h. The X-ray diffraction pattern indicates the formation of perovskite structure. The effect of fuel to oxidizer ratio plays an important role for the formation of single phase, low temperature synthesized characteristic features with $BiFeO_3$ nano particles. As fuel to oxidizer ratio decreases from F/O = 1.5 to 0.75, the secondary phase content decreases and then suddenly increases for F/O = 0.5. From X-ray diffraction pattern, well within the experimental error it can be inferred that for fuel to oxidizer ratio F/O = 0.75 with minimum calcination temperature ~ 550 °C for 3 h is the most appropriate condition for synthesis of single phase BFO. The XRD patterns were refined by Rietveld analysis using FULLPROF package (Version-October 2011) [20]. The refinement was carried out using *R3c* space group. The existence of characteristic superlattice reflection (113) around ≈ 38 degree confirms rhombohedral (*R3c*) structure [10] as shown in Fig 3.3(b). In the refinement process, the background was modeled using Fourier filtering and peak shapes were described by Thompson-Cox-Hastings pseudo-Voigt function. The refinement process were carried out by allowing the variation of different parameters such as, cell parameters, zero correction, scale factors, background, half width parameters (U, V, W), atomic position parameters, isotropic thermal parameters and global parameters. The bond lengths and bond angles were calculated from the refined data with the help of FullProf Suite: G Fourier Package [20]. The refined parameters and goodness of the fitting parameters are listed in Table 3.1 and are comparable to those of literature values [6].

In order to investigate the microstructural parameters of the samples, X-ray line profile analysis (XLPA) was employed. The (102) and (204) reflections were analyzed by variance–range and Fourier method (c.f. Chapter-2) [21-22]. Emphasis was given here to those points corresponding to the tail region because of their greater sensitivity toward the variance. The variance – range ($W(2\theta)$ vs. $\alpha(2\theta)$) plot of F/O = 0.75 for peak around 45^o is shown in the Figure 3.4(a). The linearity of the variance-range plot confirmed that the background has been adjusted properly and it also established the correctness of data. From the slope of the plot, the apparent crystallite sizes (p') have been calculated. The intercept is along the negative side of the ordinate indicating that the faulting disorder is playing a more predominant role than the strain. True crystallite sizes were estimated from Fourier line shape analysis according to double-Voigt method. The line broadening parameters *i.e.,* peak shape parameter of (102) and (204) diffraction lines were obtained by fitting with pseudo-Voigt function. The parameters of pseudo-Voigt function were

Table 3.1 Rietveld refined structural parameters of BFO for $0.5 \leq F/O \leq 1.5$. The standard deviations are in parenthesis.

Parameters		F/O = 0.5	F/O = 0.75	F/O = 1.0	F/O = 1.25	F/O = 1.5
Lattice constants (Å)	*a*	5.5746 (13)	5.5775 (09)	5.5734 (09)	5.5765 (12)	5.5763 (08)
	c	13.8616 (32)	13.8695 (23)	13.8588 (24)	13.8659 (23)	13.8672 (22)
Volume (Å)^3		373.056 (15)	373.656 (11)	372.822 (14)	373.431 (11)	373.440 (10)
Atomic positions	Bi/**6a**	0; 0; 0	0; 0; 0	0; 0; 0	0; 0; 0	0; 0; 0
	Fe/**6a**	0; 0; 0.2215	0; 0; 0.2272	0; 0; 0.2209	0; 0; 0.2208	0; 0; 0.2512
	O/**18b**	0.4410; 0.0131; 0.9538	0.4441; 0.0106; 0.9569	0.4469; 0.0152; 0.9513	0.4462; 0.0120; 0.9521	0.4405; 0.0161; 0.9825
Fe-O-Fe (degree)		155.188	155.554	155.472	156.839	155.926
R_p		17.2	9.80	11.1	10.2	11
R_{wp}		26.5	16.1	18.2	18.0	18
χ^2		1.95	1.59	1.21	1.48	1.35

Table 3.2 Microstructural parameters estimated from X-ray line profile analysis.

F/O	Variance-Range Method		Fourier Method		g	γ	Dislocation Density ($\times 10^{15}$) lines/cm^2
	Size (Å)	Strain	Size (Å)	Strain ($\times 10^{-3}$)			
0.5	109	0.01163	193	2.98	0.96102	0.07742	11.4255
0.75	130	0.00221	242	2.6	0.88554	0.01147	1.81651
1.0	123	0.00335	294	2.31	0.82032	0.02594	2.91098
1.25	114	0.00337	266	2.48	0.96535	0.08463	3.17304
1.5	135	0.00145	246	2.9	0.98293	0.14858	1.14714

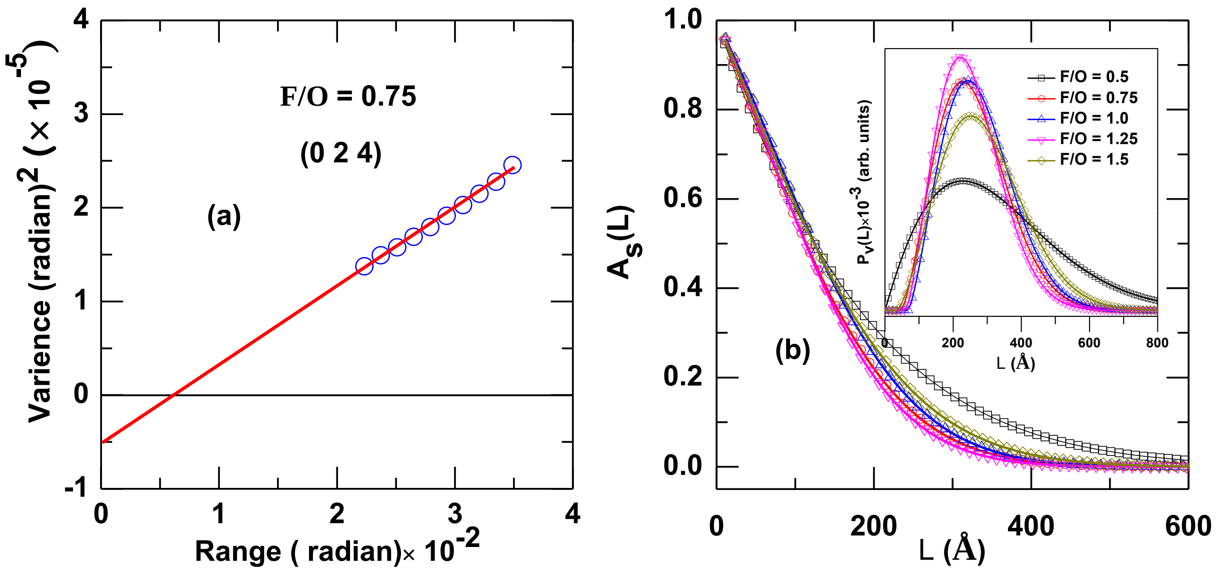

Figure 3.4 (a) Variance range plot of (2 0 4) plane of F/O = 0.75. **(b)** Cosine Fourier size coefficients A_s(L), of the X-ray line profile vs. coherent lengths L for (1 0 2)/ (2 0 4) reflection of BFO for 0.5 ≤ F/O ≤ 1.5. (Inset-Volume-weighted domain-size-distribution functions P_V(L) as a function of coherent lengths L.)

then converted into Voigt function parameters by BREADTH Programme, which calculates size and strain Fourier coefficients [23-24]. Coherently diffracting domain size was determined from the initial slope of Fourier size coefficients A_s(L) (*i.e.*, Cosine part of the calculated Fourier transform of the intrinsic peak profile under investigation) as represented in Fig 3.4(b). The calculated volume–weighted distribution P_V(L) (*i.e.*, the X-ray diffraction line profile of fine powder sample consisting of many crystallites with different sizes and shapes which can be represented mathematically by a size distribution function), as a function of Fourier length are shown Fig 3.4(b) (inset). For fuel to oxidizer ratio F/O = 0.5, it showed a wide range of crystallite size distribution varying about 50-900 Å. As the fuel to oxidizer ratio increases, size distribution function becomes narrower indicating a uniform crystallite size distribution. From the P_V(L) distribution average volume weighted crystallite sizes $<D>_v$ were calculated. The crystallite sizes estimated from variance range method gives a lower value than Fourier method. The reason may be due to (i) the differences in determination of the definitions and physical meaning of the different parameters involved in the measurements (ii) the various assumptions involved in separating the contributions due to crystallite size and distortions and (iii) variance method is highly range sensitive [21-24]. It is also to be recalled that the size obtained by the Fourier coefficients represents the volume average of the crystallite's dimension. The different microstructural parameters calculated from the variance and Fourier method are listed in the Table 3.2. The variation of g and γ shows a nearly similar trend having a higher order of magnitude than that of strain estimated from both of the XLPA methods. This confirms the negative intercept of Variance~ range plot. The dislocation density decreases with increase in fuel to oxidizer ratio.

Figure 3.5 represents transmission electron micrograph (TEM) for F/O = 0.75 powder sample along with the SAED pattern. For F/O = 0.75, the crystallite size was estimated to be ≈ 300 Å which suggest that the crystallite sizes of the system are less than that of spin cycloid. The crystallite sizes observed from TEM are in good agreement with X-ray line profile analysis well within the calculation error. The observed reflections from SAED pattern for F/O = 0.75 is in complete agreement with Rietveld refinement for *R3c* space group in the present study.

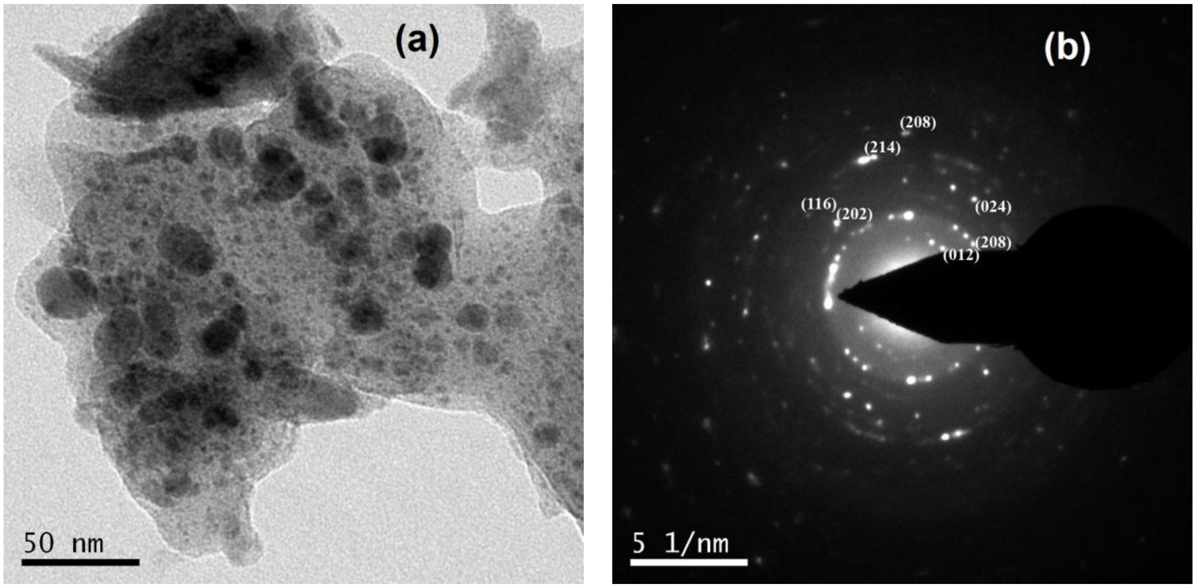

Figure 3.5 (a) Transmission electron micrograph (TEM) and **(b)** SAED pattern for F/O = 0.75.

The coalescing of crystallites to form grains, effect of grain size and grain growth on fuel to oxidizer ratio was studied using FESEM. With increase in fuel to oxidizer ratio grain size increased significantly to several microns and the porosity decreases systematically. Figure 3.6 compares the FESEM micrographs for F/O = 0.75 representing pure phase with optimum crystallite size at different magnifications. The polycrystalline grains are distributed inhomogenously throughout the sample matrix with certain degree of porosity. However, some grains (as seen in Fig 3.6(a)) still have ~ 100-200 nm size that is most probably in the growing stage. To further study the growth mechanism of these grains, we have zoomed the image in few locations and Figure 3.7(a) represents the magnified view of the grains for the sample with F/O = 0.75. The small grains retain their spherical shape; however, as it grows by coalescing different crystallites, it releases free energy in such a way that it forms polygons eventually. Another interesting fact to observe is that while the larger grains are almost formed, still few of their facets initiate fresh grain growth in the direction shown by the arrows. We were further able to image the grain-boundary region more clearly between various grains and Figure 3.7(b) represents a high resolution image of grain boundaries separating three different grains for F/O = 1.25. From this image, the grain boundary width was estimated to be ~ 20-25 nm.

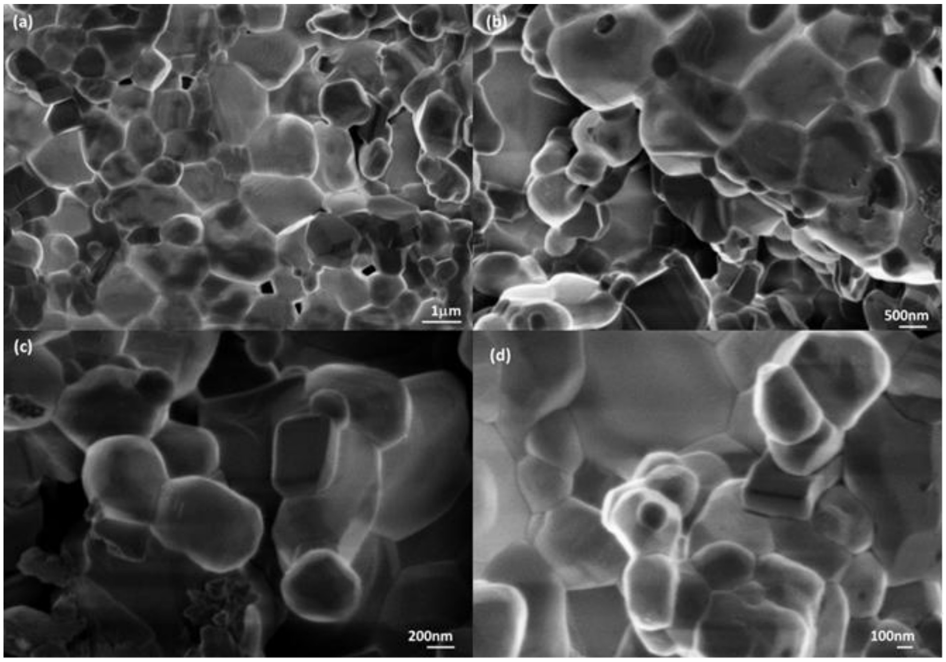

Figure 3.6 FESEM micrographs of F/O = 0.75 at various magnifications.

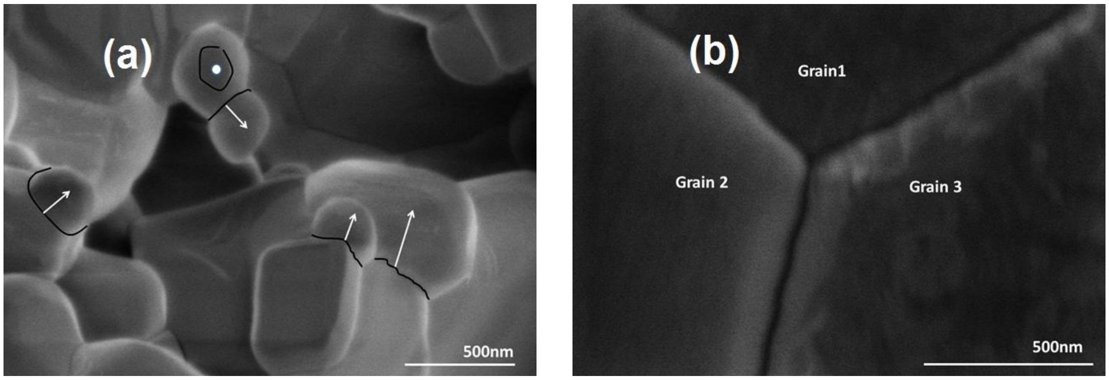

Figure 3.7 FESEM micrograph of **(a)** F/O = 0.75 signifying grain growth and **(b)** F/O = 1.25 at magnified view.

3.3.3 Dielectric Properties

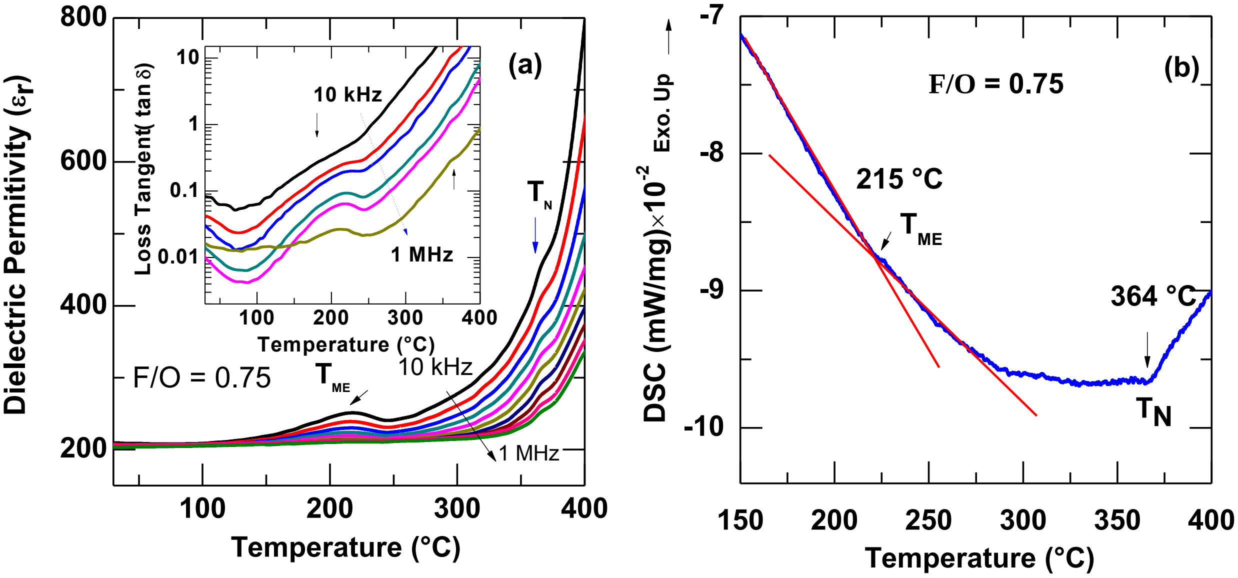

Figure 3.8 (a) Temperature dependent dielectric permittivity (ε_r) of F/O = 0.75 at different frequencies between 10 kHz-1MHz (Inset- tanδ *vs.* T) **(b)** DSC thermogram of calcined powder for F/O = 0.75.

Figure 3.8 (a) shows the temperature dependent dielectric permittivity (ε_r) for F/O = 0.75 in the frequency range 10 kHz-1MHz. On heating, two distinct dielectric anomalies are noticed and both the anomalies are also detected in the temperature dependent loss tangent (tan δ) (Inset-Fig.

3.8(a)). The first anomaly (*i.e.,* denoted as T_{ME}) around 215°C corresponds to the magnetoelectric coupling in the material [25]. The appearance of this anomaly can be explained by the Landau-Devonshire theory of phase transition and could be due to the destruction of space modulated spin structure below the magnetic ordering temperature of BFO [26]. Similar types of observations have also been reported in A-site modified BFO. The second dielectric anomaly (small kink) is observed around 364 °C corresponding to magnetic phase transition (T_{N}) of BFO. To obtain an insight into the anomaly, heat flow *v*s. temperature (DSC thermogram) has been plotted for calcined powder of pure phase BFO (*i.e.,* F/O = 0.75), as shown in Fig 3.8(b). It is found that, two endothermic peaks are observed around ~ 215 °C and ~ 364 °C in DSC thermogram (shown by changes in slope) and further supporting the dielectric studies. Schmidt *et al.* reported that, it is safe to conclude the intrinsic magnetoelectric effect in multiferroic systems based on following criterions: (a) an anomaly in temperature dependent dielectric permittivity at magnetic transition temperature, (b) change in dielectric permittivity with application of magnetic field [27]. Here the first criterion is satisfied. The proof of second criterion is discussed in the next section.

3.3.4 Magnetoelectric Coupling

Figure 3.9 (a) represents the frequency (100 Hz- 1MHz) dependence of dielectric permittivity for fuel to oxidizer ratio, F/O = 0.75 at RT for several static bias magnetic field ($0 \leq H \leq 2$ Tesla). It is observed that, (εr) decreases with increasing frequency which is a signature of polar dielectric materials. Here the dielectric permittivity is found to decrease with increasing static magnetic field representing negative coupling coefficient. Similar types of observations have been reported elsewhere [28]. In order to demonstrate the magneto electric coupling quantatively, the variation of dielectric permittivity (εr) and tangent loss (tanδ) (at constant frequencies 1 kHz and 200 kHz) as a function of magnetic field (-2 Tesla $\leq H \leq +2$ Tesla) was measured at room temperature and represented in Figure 3.9(b). The magneto-capacitance (MC %) and the magneto-loss (ML %) are calculated from the following formula given below [29] :

$$MC(\%) = \frac{\varepsilon\,(H) - \varepsilon(0)}{\varepsilon(0)} \times 100\,;\; ML(\%) = \frac{tan\delta\,(H) - tan\delta\,(0)}{tan\delta\,(0)} \times 100$$

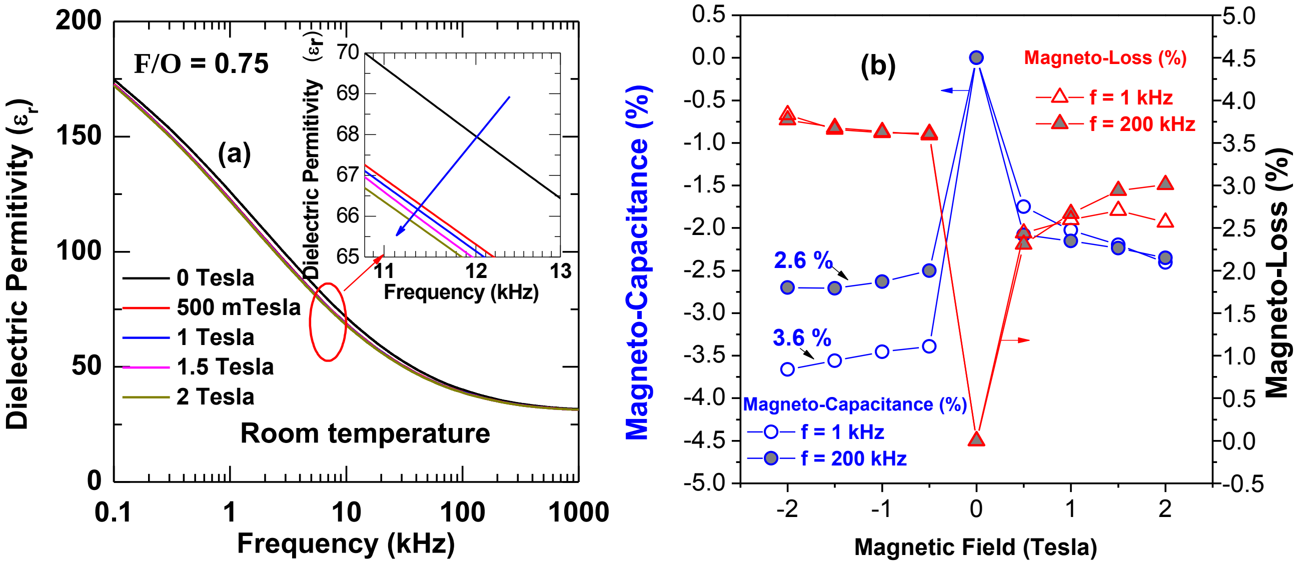

Figure 3.9 (a) Dielectric permittivity of F/O = 0.75 as a function of frequency at RT for several static bias magnetic field ($0 \leq H \leq 2$ Tesla) (Inset- Magnified view of frequency dependent ε_r and arrow indicates increasing magnetic field), **(b)** The magneto-capacitance ($\Delta\varepsilon$ %) and magneto-losses ($\Delta\tan\delta$ %) as a function of magnetic field at RT of F/O = 0.75 at 1 kHz and 200 kHz.

The result indicate, there is a significant increase in magneto-capacitance up to 3.6% and 2.6% at highest applied field H = 2 Tesla for 1 kHz and 200 kHz frequency respectively. In addition to the intrinsic magneto-electricity, contributions from extrinsic effects such as Maxwell-Wagner polarization and magneto resistance effects cannot be ruled out. That's why the magneto dielectric response is extracted for two (low and high) frequencies i.e., 1 kHz and 200 kHz (showing arrow mark in Figure 3.9 (a)). At 1 kHz, sizable difference is seen in the dielectric data of with and without field (Figure 3.9 (a)). However, as 1 kHz is in the dispersion region, another frequency i.e., 200 kHz is chosen. From the graph it is clear that at 200 kHz, the dispersion region is over. In general, the interfacial space charge polarizations are active up to ~200-300 Hz frequency range [29]. Since, the changes in magneto-capacitance is around 2.6 % even if 200 kHz, we believe that the observed ME effects are intrinsic in nature. Palker *et al.* reported that, when magnetic field is applied on a magneto-electric system, strain is induced. This strain develops stress in the material (for piezoelectric and ferroelectrics materials) leading to change in dielectric permittivity/ polarization [30]. Similar types of magneto-capacitance observations have also been reported by Yang *et al.* in the case of Mn-modified $BiFeO_3$ and Uniyal *et al.* in Ba doped $BiFeO_3$ thin films [31-32]. This satisfies the 2nd criterion for the observation of intrinsic magneto-electric effect in multiferroic systems.

3.4 Conclusions

High purity polycrystalline nano $BiFeO_3$ powders were synthesized by auto-combustion method using urea as fuel and metal nitrates ($Fe\ (NO_3)_3.9H_2O$, $Bi\ (NO_3)_3.5H_2O$) as oxidizers at minimum temperature ~ 550 °C. Single phase formation of the compound was confirmed by XRD analysis and DSC-TGA thermo-gram. DSC analysis revealed that the ferroelectric and antiferromagnetic ordering temperatures of $BiFeO_3$ are around 832 °C and 364 °C respectively. Rietveld analysis was carried out in order to calculate different structural parameters in the samples. Variance-range and Fourier analysis of broadened X-ray line profiles have provided quantitative and qualitative information on the evolution of microstructural parameters. FESEM micrographs showed the effect of fuel to oxidizer ratio on grain size evolution by systematic agglomeration of fewer numbers of crystallites to hundreds of crystallites. The temperature dependent dielectric studied show anomalies around 215 °C and 364 °C corresponding to magnetoelectric coupling and antiferromagnetic transition temperature of the material respectively. Magneto-dielectric measurement shows a significant increase in magneto-capacitance up to 3.6% at highest applied field H = 2 Tesla at RT. These findings provide the direct evidence of magnetoelectric coupling of low temperature synthesized nanoceramics prepared by auto-combustion technique.

3.5 References

[1] R. Palai, R.S. Katiyar, H. Schmid, P. Tissot, S.J. Clark, J. Robertson, S.A.T. Redfern, G. Catalan, J.F. Scott, Phys. Rev. B **77**, 014110 (2008).

[2] T.T. Carvalho, P.B. Tavares, Mater. Lett., **62**, 3984(2008).

[3] Z.X. Cheng, A.H. Li, X.L. Wang, S.X. Dou, K. Ozawa, H. Kimura, S.J. Zhang, T.R. Shrout, J. Appl. Phys. **103**, 07E507(2008).

[4] Q. Jiang, C. Nan, Y. Wang, Y. Liu, Z. Shen, J. Electroceram., **21**, 690(2008).

[5] M.B. Bellakki, V. Manivannan, C. Madhu, A. Sundaresan, Mater. Chem. Phys., **116**, 599 (2009).

[6] G. Catalan and J. F. Scott, Adv. Mater., **21**, 2463 (2009).

[7] C. Yang, D. Kan, I. Takeuchi, V. Nagarajan and J. Seidel, Phys. Chem. Chem. Phys., **14**, 15953 (2012).

[8] I. Sosnovska, T. P. Neumaier, E. Steichele, J. Phys. C: Solid State Physics **15**, 4835(1982).

[9] T. J. Park, G.C. Papaefthymiou, A.J. Viescas, A.R. Moodenbaugh, S.S. Wong, Nano Lett. **7**, 766(2007).

[10] S.M. Selbach, T. Tybell, M.-A. Einarsrud, T. Grande, Chem. Mater. **19**, 6478(2007).

[11] S. Shetty, V.R. Palkar, R. Pinto, Pramana **58**, 1027(2002).

[12] M. Valant, A.-K. Axelsson, N. Alford, Chem. Mater. **19**, 5431(2007).

[13] J.K. Kim, S.S. Kim, W.-J. Kim, Mater. Lett. **59**, 4006(2005).

[14] M.Y. Shami, M.S. Awan, M. Anis-ur-Rehman, J. Alloys Compd. **509**, 10144(2011).

[15] I. Szafraniak, M. Polomska, B. Hilczer, A. Pietraszko, L. Kepinski, J. Eur. Ceram. Soc. **27**, 4399(2007).

[16] E.d.A.V. Ferri, I.A. Santos, E. Radovanovic, R. Bonzanini, E.M. Girotto, J. Alloys Compd. **19**, 1153(2008).

[17] W. Luo, D. Wang, X. Peng, F. Wang, J. Sol-Gel Sci. Technol. **51**, 53(2009).

[18] R.N.P. Choudhary and S. K. Patri, Dielectric Materials: Introduction, Research and Applications, Nova Publishers, (2009).

[19] S. Das, S. Basu, J. Nanosci. Nanotechnol. **9**, 5622(2009).

[20] R. A. Young, The Rietveld Method, Oxford University Press (1991).

[21] B.E. Warren, B.L. Averbach, J. Appl. Phys. **21**, 595(1950).

[22] J.I. Langford, Nature **207**, 966(1965).

[23] D. Balzar *et al.* J. Appl. Crystallogr. **37**, 911(2004).

[24] D. Balzar, J. Appl. Crystallogr. **28**, 244(1995).

[25] G. L. Yuan and S. Or, J. Appl. Phys. **100,** 024109 (2006).

[26] L. Benguigui, Solid State Commun. **11**, 825 (1972).

[27] R. Schmidt *et al.*, Phys. Rev. B **86**, 035113 (2012).

[28] M. Li, M. Ning, Y. Ma, Q. Wu, C. K. Ong, J. Phys. D: Appl. Phys. **40**, 1603(2007).

[29] G. Catlan, Appl. Phys. Lett. **88**, 102902(2006).

[30] V. R. Palkar, D. C. Kundaliya, S. K. Malik, S. Bhattacharya, Phys. Rev. B **69**, 212102(2004).

[31] C. Yang, T. Y. Koo and Y. H. Jeong, Solid State Commun. **134**, 299(2005).

[32] P. Uniyal and K. L. Yadav, J. Phys.: Condens. Matter**. 21**, 405901(2009).

Chapter-4

Phase Transition and Magnetoelectric Coupling of $BiFeO_3$–$YMnO_3$ Multiferroic Nanoceramics

Part of the content of this chapter has been published in the journal "**Journal of Applied Physics".** Satya N. Tripathy, K. K. Mishra, S. Sen, B. G. Mishra, Dhiren K. Pradhan, R. Palai, and Dillip K. Pradhan, **J. Appl. Phys. 114, 144104 (2013).**

In this Chapter, we describe the synthesis of solid solution (1-x)$BiFeO_3$-$x$$YMnO_3$ (BFO-YM) for $0.0 \leq x \leq 0.2$ by auto-combustion technique and examination of the materials using X-ray diffraction, field emission scanning electron microscopy, transmission electron microscopy , dielectric, ferroelectric polarization (P-E loop), magnetic hysteresis (M-H loop), magneto-dielectric and magneto-impedance spectroscopic techniques.

4.1 Introductory Remarks

$BiFeO_3$ (BFO) is considered as a prototype multiferroic material due to its high ferroelectric (FE) Curie temperature (T_C ~ 832 °C) and antiferromagnetic (AFM) Néel temperature (T_N ~ 364 °C) [1-2]. The origin of FE in BFO is due to stereochemistry of Bi 6s orbitals while spin of transition metal ion Fe^{3+} is responsible for G-type AFM ordering with a long range spin cycloid modulation with periodicity 620-640 Å [1-2]. Therefore, both the linear magnetoelectric (ME) effect and remanent magnetization collapse on macroscopic scale and result to a weaker quadratic ME behavior.

Recent experimental and theoretical investigations suggest that the appearance and enhancement of ME coupling of BFO at room temperature (RT) can be realized by adopting the following approaches [3-4]: (a) destruction/suppression of the long range spin cycloid, and/or (b) bringing the ferroic transition temperature T_C or T_N around RT. Kimura *et al.* and Palkar *et al.* have independently concluded that the appearance and enhancement of ME coupling takes places at ferroic transition temperatures T_C or T_N [3-4]. Several approaches have been attempted by different research groups around the globe to enhance the ME coupling of BFO by adopting the above mentioned strategies. Those approaches are: (a) suitable chemical substitution (*i.e.,* diamagnetic and rare earth at Bi-site, magnetic and nonmagnetic at Fe-Site), (b) fabrication of solid solution of BFO with other ABO_3-type pervoskites (c) synthesizing BFO nanoparticles with crystallite size less than periodicity of helical order (d) fabrication of epitaxial thin films and (e) application of high magnetic field (c.f. Chapter-1) [5-13]. In the present work, we have explored the synthesis and ME properties of solid solution of BFO with rare earth (RE) manganite ($RMnO_3$) using nanoceramics.

Recently, RE manganites ($RMnO_3$) have attracted the attention due to their strong ME coupling. It has been found that the solid solution of BFO with different RE manganites exhibit enhanced ME properties [14-18]. Enhanced electrical and magnetic properties of $BiFeO_3$–10%$RMnO_3$ (R: La^{3+}, Eu^{3+}, Gd^{3+}, Tb^{3+}, and Dy^{3+}) thin films have been reported by

Lahmer *et al.* [15]. Zhu *et al.* observed a structural phase transition from *R3c* to *Pbnm* in (1-x)BiFeO$_3$-xDyFeO$_3$ solid solution at x = 0.1, with improved multiferroic properties [16]. Ivanova *et al.* studied the structural and dielectric properties of (1-x) BiFeO$_3$-xDyMnO$_3$ solid solution [17]. Nazarenko *et al.* reported the structural transition from *R3c* to *Pbnm* at x = 0.1 in (1-x)BiFeO$_3$-xYMnO$_3$ solid solution [18]. To the best of our knowledge, the solid solution of BiFeO$_3$–YMnO$_3$ systems has not been investigated systematically in detail. Hexagonal Yttrium manganite *h*-YMnO$_3$ (YM) is one of the geometrical multiferroic materials with high FE ordering (T_C ~ 930 K) and low antiferromagnetic ordering (T_N ~ 70 K) temperature [19]. The origin of FE in YMnO$_3$ is due to tilting of rigid MnO$_5$ block. YMnO$_3$ belongs to non-centosymmetic space group $P6_3cm$ at RT. As the T_N of YM is around 70 K, synthesis of (1-x)BiFeO$_3$–xYMnO$_3$ solid solution is expected to down the transition temperature (T_N) towards RT. It can be mentioned that Y^{3+} (~0.90 Å) is a non-rare earth cation with ionic radius comparable to RE dopant cations (La^{3+} ~ 1.03 Å, Gd^{3+} ~ 0.94 Å, Sm^{3+} ~ 0.96 Å) [20]. Substitution of Y^{3+} at Bi-site is expected to switching off the lone pair activity of Bi leading to shift the FE transition towards RT. Recently, Mishra *et al.* studied Y^{3+} modified BFO and observed improved dielectric properties and switching magnetic behavior [21]. Furthermore, Pradhan *et al.* found an enhanced magnetic properties of Mn modified Bi$_{0.9}$La$_{0.1}$FeO$_3$ system [22].

In the present chapter, we provide the systematic investigation on the structural, temperature dependent dielectric, ferroelectric, magnetic and magneto-dielectric properties of (1-x) BiFeO$_3$-xYMnO$_3$ for $0.0 \leq x \leq 0.2$ multiferroic nanoceramics. Emphasis has been given to understand the ME coupling with structure-property relationship and the effect of fabrication of solid solutions on the possibility of the compositional driven structural phase transition.

4.2 Experimental Procedure

Solid solutions of (1-x)BiFeO$_3$-xYMnO$_3$ (BFO-YM) for $0.00 \leq x \leq 0.2$ were synthesized using auto-combustion method. High purity (99.9%) grade chemicals of $Fe(NO_3)_3.9H_2O$, $Bi(NO_3)_3.5H_2O$, Y_2O_3, $(CH_3COO)_2Mn\cdot 4H_2O$ were used as oxidizers, while urea was taken as fuel. Stoichiometric amount of the above mentioned reagents with optimized fuel to oxidizer ratio, F/O = 0.75 were dissolved in minimum amount of distilled water/nitric acid to prepare a homogenous gel. The details of the synthesis procedure have been discussed in Chapter-3 (See Refs: 23-24). For x = 0.0, the combustion residue was calcined at an optimized temperature of 550 °C for 3 h in air atmosphere. The compounds with compositional range,

$0.025 \leq x \leq 0.1$ were calcined at 600 °C while those for $x = 0.15$ and $x = 0.2$ were calcined at 650 °C. The calcined powders were compacted into cylindrical pellets by hydraulic press with pressure 8×10^{7} $kg.m^{-2}$ using polyvinyl alcohol (PVA) as binder. For composition $0.0 \leq x \leq 0.1$ and $0.15 \leq x \leq 0.2$, the pellets were sintered at 700 °C and 750 °C respectively. All the experimental conditions for characterization of the proposed materials are same (explained in Chapter-3) except ferroelectric, magnetic hysteresis and FESEM measurements. The surface morphology (grain size, distributions, and voids) of the pellets were recorded using a scanning electron microscope SUPRA 35VP FESEM. The RT ferroelectric loops were measured using ferroelectric loop tracer (Model: Marine India) at 100 Hz. All the samples were polled with optimize voltage in a silicon bath before taking the measurement. Magnetization measurements (M-H hysteresis loop) were obtained using a VSM up to a maximum field of ±2 Tesla at ambient.

4.3 Results and Discussion

4.3.1 Structural and Microstructural Properties

Fig 4.1(a) displays the Rietveld refinement of X-ray diffraction pattern of the solid solution of $(1\text{-}x)BiFeO_3\text{-}xYMnO_3$ for $0.0 \leq x \leq 0.2$ at room temperature. In order to have a better understanding of the compositional driven structural phase transitions of the solid solution, we have carried out Rietveld refinement analysis using FULLPROF package [25]. The peak shapes were refined by pseudo-Voigt function, while background was modeled using liner interpolation method. In addition, zero correction, scale factor, background, unit cell parameters, atomic positions, thermal parameters, half width parameters (U, V and W) were varied during the refinement process. The occupancy of all the atoms was kept fixed during refinement. In Fig 4.1(a) the experimental data points are labeled as symbol (+) and simulated data are shown as solid line. Difference between theoretical and experimental data is shown as bottom-line. For pure $BiFeO_3$ ($x = 0.0$) a good match is obtained between observed and calculated pattern described by rhombohedral *R3c* space group with χ^2 value (goodness of fit) ~1.59. The unit cell parameters are found to be: a = 5.5779 (09) Å and c = 13.8710 (23) Å (hexagonal setting) which is in good agreement with crystal structure of BFO reported in the literature [1]. One can notice from the Fig 4.1(a) that with increasing YM composition up to $x = 0.1$, the X-ray diffraction patterns are similar to that of $BiFeO_3$. Therefore we have selected the *R3c* space group to refine the crystal structure. The crystal structure of the solid solution

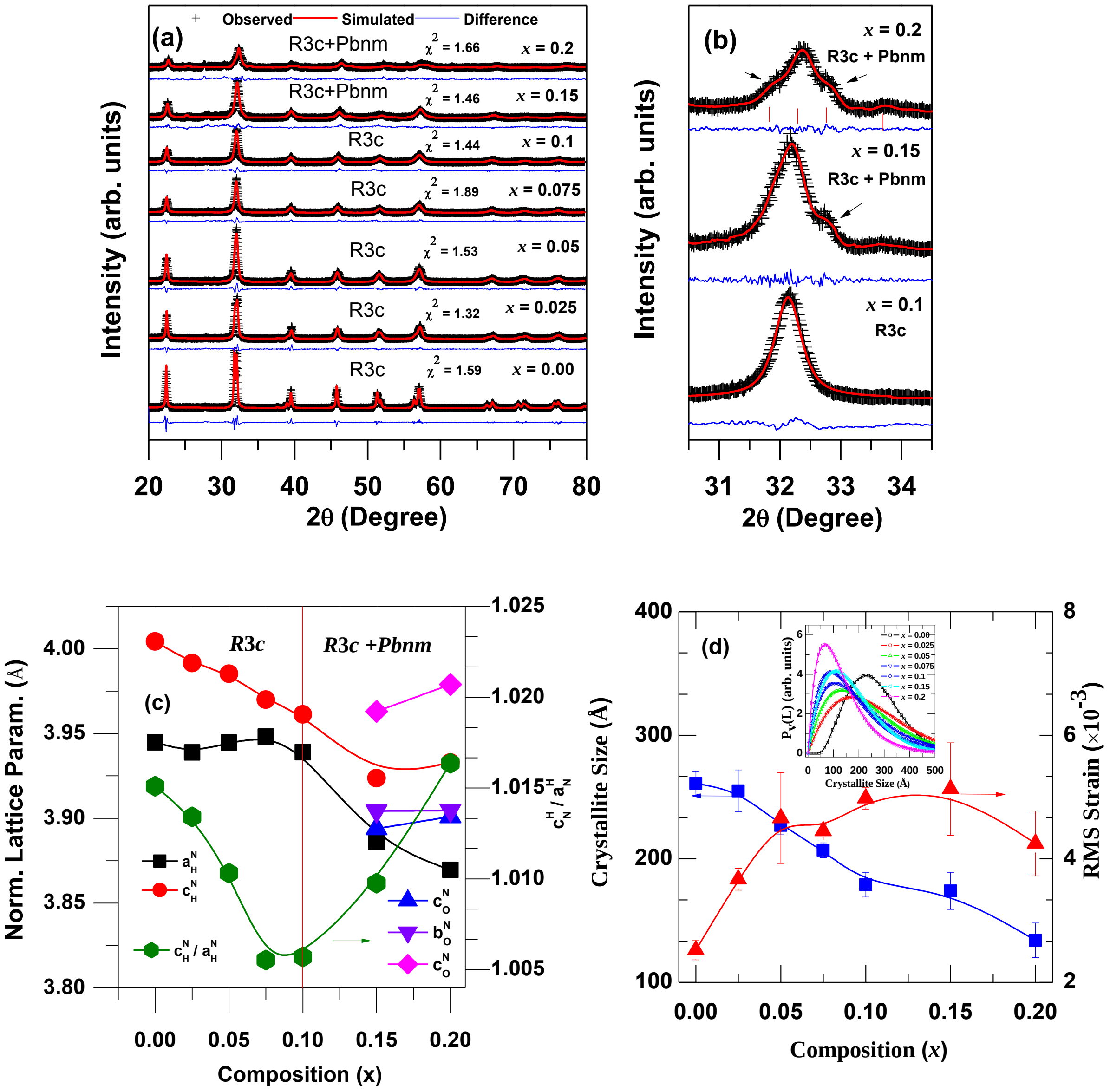

Figure 4.1 Rietveld refinement of X-ray diffraction patterns of the solid solution of (1-*x*) $BiFeO_3$ - $xYMnO_3$ for **(a)** $0.0 \leq x \leq 0.2$ at RT, **(b)** $x = 0.10$, $x = 0.15$ and $x = 0.20$ for the peak expanded in the 2θ regions around ~32° signifying the crossover from *R3c* to *R3c+Pbnm*. **(c)** Normalized lattice parameters (*i.e.*, $a_H^N = a_{Hex}/\sqrt{2}$, $c_H^N = c_{Hex}/\sqrt{12}$) and ($c_H^N / a_H^N$) of *R3c* phase as a function of composition (*x*) along with normalized lattice parameter of *Pbnm* phase (*i.e.*, $a_O^N \approx b_O^N \approx (2)^{-1/2} a_{orth}$, $c_O^N = c_{orth}/2$) and **(d)** Crystallite size and r. m. s strain estimated from Double-Voigt method as a function of *x* (Inset-$P_v(L)$ as a function of *x*).

remained in the rhombohedral structure with space group *R3c* up to $x = 0.1$ and a new phase is found above $x = 0.1$ along with the parent *R3c* phase, which is evident from the appearance and splitting of reflections in the diffraction pattern as shown in Fig. 4.1(b). Rietveld refinement result indicates a compositional driven structural phase transition after $x = 0.1$ *i.e.*, the crystal structure of the solid solution changed to a dual phase consisting of rhombohedral (*R3c*) and orthorhombic (*Pbnm*) symmetry. Note that *Pbnm* structure is commonly observed in perovskites, RE ortho-ferrites, manganites and also as the high temperature phase of $BiFeO_3$ [26-27]. With increasing in the concentrations of YM in solid solution, the transition from *R3c* to *R3c+Pbnm* is expected since Mn^{3+} cation weakly destabilizes *R3c* as compared to that of Fe^{3+}, whereas Y^{3+} strongly destabilizes *R3c* phase. The reasons for structural destabilization are as follows: (a) the lack of $6s^2$ lone pair in Y^{3+} and (b) chemical pressure of Y^{3+} is much smaller than Bi^{3+} [26-27]. Using Rietveld refinement for composition $x = 0.15$ and $x = 0.2$, we have estimated the percentage of each phases present in solid solution. It was found that $x = 0.15$, contains 61.77% of *R3c* and 38.23 % of *Pbnm* phase and $x = 0.2$, contains 52.42% of *R3c* and 47.58 % of *Pbnm* phase. The lattice parameters, Wyckoff notations and atomic positions for the coexisting *R3c* and *Pbnm* space groups are listed in Table 4.1 and Table 4.2 respectively.

Table 4.1 Lattice parameters of (1-*x*)BFO-*x*YM for $0.0 \leq x \leq 0.2$ estimated from Rietveld refinement with good-ness of fitting parameters. The standard deviations are in parenthesis.

Composition (*x*)	Space group	Lattice Parameters (Å)			R_p%	R_{wp}%
		a	*b*	*c*		
0.0	*R3c*	5.5779 (09)	5.5779 (09)	13.871 (23)	12.8	18.3
0.025	*R3c*	5.5694 (13)	5.5694(13)	13.8268 (32)	13.3	18.8
0.05	*R3c*	5.5776 (16)	5.5776(16)	13.8049 (41)	13.6	18.2
0.075	*R3c*	5.5827 (22)	5.5827(22)	13.7521 (59)	14.3	19.1
0.1	*R3c*	5.5696 (26)	5.5696(26)	13.722 (64)	13.9	19.0
0.15	*R3c* + *Pbnm*	5.4945 (33) 5.5059 (09)	5.4945(33) 5.5205 (15)	13.5918 (84) 7.9262 (10)	16.5	22.4
0.2	*R3c* + *Pbnm*	5.4716 (51) 5.5160 (58)	5.4716(51) 5.5212 (62)	13.6236 (84) 7.9579 (89)	18.2	25.0

Table 4.2 Wyckoff notation and atomic positions of (1-*x*)BFO-*x*YM for $0.0 \leq x \leq 0.2$ used in Rietveld refinement.

Composition (*x*)	Space group	Atom	Site	*x*	*y*	*z*
$0.00 \leq x \leq 0.1$	*R3c*	Bi/ Y	6*a*	0.0	0.0	0.0
		Fe/Mn	6*a*	0.0	0.0	0.2212
		O	18*b*	0.443	0.012	0.9543
0.15 and 0.2	*R3c* +*Pbnm*	Bi/Y	6*a*	0.0	0.0	0.0
		Fe/Mn	6*a*	0.0	0.0	0.2212
		O	18*b*	0.443	0.012	0.9543
		Bi/Y	4*c*	0.995	0.03	0.25
		Fe/Mn	4*a*	0.5	0.0	0.0
		O1	4*c*	0.05	0.49	0.25
		O2	8*d*	0.73	0.28	0.05

It has been observed that with the increase in *x*, there is a change in peak position, peak intensity and peak broadening in the diffraction patterns and reflects in terms of change in unit cell parameters. This may be due to the lattice strain or chemical pressure introduced by substitution of Y^{3+} and Mn^{3+} cation at A and B-site of $BiFeO_3$ respectively. In order to support the compositional driven structural phase transition as a function of composition, the normalized lattice parameters (*i.e.*, $a_H^N = a_{Hex}/\sqrt{2}$, $c_H^N = c_{Hex}/\sqrt{12}$), pseudo-tetragonality (c_H^N/a_H^N) of *R3c* phase are shown as a function of *x*, along with normalized lattice parameter of *Pbnm* phase ($a_O^N \approx b_O^N \approx (2)^{-1/2}a_{orth}$, $c_O^N = c_{orth}/2$) in Fig. 4.1(c). With increasing composition *x*, the normalized lattice parameter c_H^N decreases, whereas a_H^N is nearly constant up to $x = 0.1$ and then decreases with further increase in *x*. At $x = 0.1$ in *R3c* phase, a_H^N and c_H^N approaches to equal magnitude which is reflected in terms of decrease in pseudo-tetragonality. This may be due to the decrease in crystallite size and destabilization of *R3c* phase by Y^{3+} substitutions at A-site of $BiFeO_3$. After $x = 0.1$, pseudo-tetragonality increases with increase in composition (*x*) in *R3c*+*Pbnm* phase. For the ferroelectric phase transition, deviation of tetragonal distortion from unity ($c_H^N/a_H^N - 1$) represents crystallographic order parameter [28]. The anomaly in pseudo-tetragonality could be due to rhombohedral to rhombohedral plus orthorhombic phase transition. It is also evident from the Fig. 4.1 (c) that normalized lattice parameter of *Pbnm* phase increases with increase in x.

The variation of true crystallite sizes and lattice strain of (1-x) $BiFeO_3$-$x$$YMnO_3$ system as a function of composition are shown in Fig.4.1 (d). In this context, we have adopted Fourier X-ray line profile analysis based on Double-Voigt method using program BREADTH [29]. The same procedure has been adopted here to calculate the microstructural parameters as discussed in Chapter-3. It is clear from the Fig. 4.1 (d) that crystallite size decreases from 260 Å for x = 0.00 to 130 Å for x = 0.2. But the r.m.s. strain increases with increase in composition up to x = 0.10 and after that it gets saturated. Furthermore, this method also allows for determining accurately volume-weighted domain size distribution function, $P_v(L)$ as a function of crystallite size (L). Fig.4. 1(d)-inset shows that for x = 0.0 volume-weighted domain size $<D_V>$ ranges from 100 Å to 500 Å with maxima around 260 Å. It can be noted here that with increase in composition, distribution function, $P_v(L)$ become narrower. This signifies the uniform distribution of crystallite sizes.

Figure 4.2 represents transmission electron micrographs (TEM) for x = 0.0 and x = 0.1 powder samples along with the SAED patterns. For x = 0.00, the crystallite size was estimated to be ≈ 300 Å and decrease with increase in composition with partial agglomeration of particles. The observed crystallite sizes from TEM are in good agreement with X-ray line profile analysis well within the calculation error. The observed reflections from SAED pattern for x = 0.0 and x = 0.1 are in agreement with Rietveld refinement results for *R3c* space group.

The surface morphologies of (1-x) $BiFeO_3$-$x$$YMnO_3$ system, for x = 0.00, 0.5, 0.1, 0.2 observed by FESEM are displayed in Fig 4.3. The SEM micrographs of BFO-YM solid solution samples show uniform distribution of grains throughout the surface of the samples, whereas pure BFO sample shows some non-uniform distribution of the grains. The grains and grain boundaries are well defined in all the samples. A decrease in grain size was observed with increase in $YMnO_3$ content.

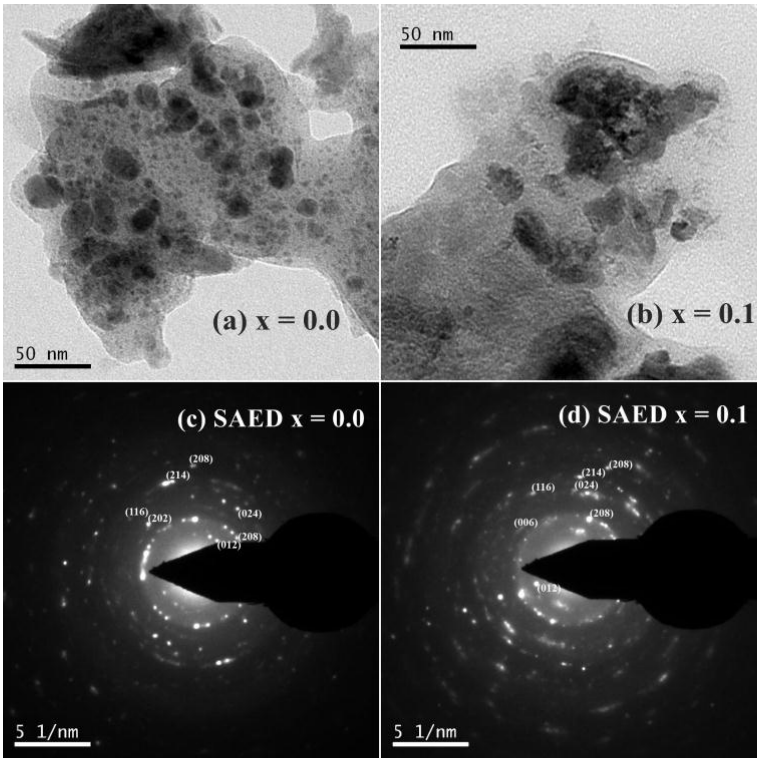

Figure 4.2 Transmission electron micrographs for **(a)** *x* = 0.00 and **(b)** *x* = 0.1. SAED patterns for **(c)** *x* = 0.00 and **(d)** *x* = 0.1.

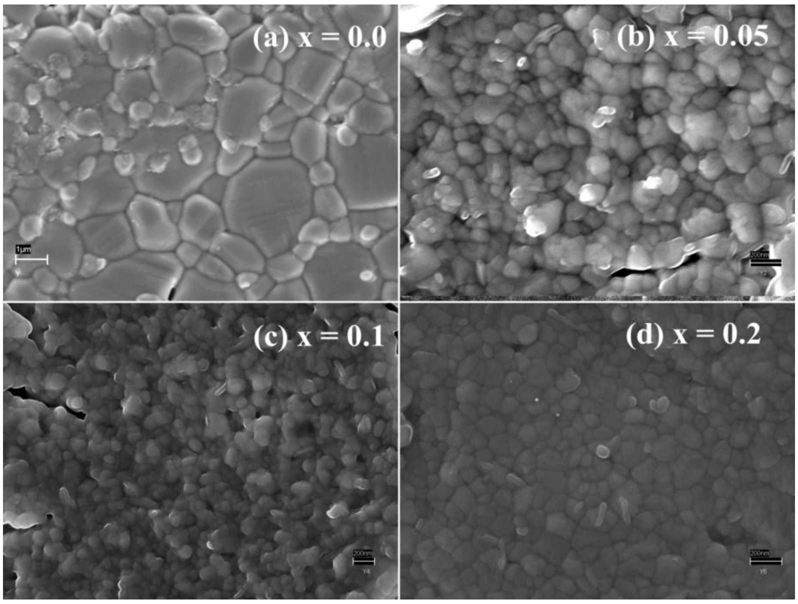

Figure 4.3 Field emission scanning electron micrographs of **(a)** *x* = 0.00 **(b)** *x* = 0.05 **(c)** *x* = 0.1 and (**d)** *x* = 0.2.

4.3.2 Dielectric Properties

Figs 4.4(a) and 4.4(b) illustrate the temperature dependence of the dielectric permittivity (ε_r) and the loss tangent (tan δ) of the solid solution (1-x) $BiFeO_3$-$x$$YMnO_3$ for $0.0 \leq x \leq 0.2$. It clearly demonstrates that for $x = 0.00$ [Inset-Fig. 4.4(a)] dielectric permittivity increases slowly with increase in temperature, and an anomaly is observed around ≈ 215 °C. Hereafter dielectric permittivity increases monotonically along with the appearance of a small kink around 364 °C corresponding to AFM ordering temperature of BFO. The anomaly around ≈ 215 °C could be due to ME coupling and can be explained on the frame work of Landau-Devonshire theory of phase transition in magneto-electrically ordered systems [30-31]. Interestingly, it is observed that with increase in composition, the dielectric transition peak around 215 °C gradually broadens and amplification of the 2nd anomaly (due to T_N) take place on and above $x = 0.075$. The anomaly observed at 310 °C for $x = 0.075$ corresponds to AFM ordering temperature of the system. This anomaly has also been found from the temperature dependence of loss tangent (tan δ), further supporting the AFM transition. Similar type of behavior of temperature dependent relative permittivity has also been reported by Yuan and Palkar *et al*. for A-site modified $BiFeO_3$ system [4, 30-31]. It is also evident from the Fig 4.4(a) that, for $x > 0.1$, both the dielectric anomalies amplified substantially with increase in composition (x) and shifts towards lower temperature side. The decrease in T_N with increase in composition could be due to reduction in unit cell volume. In order to understand this anomalies more precisely, the dielectric permittivity *vs.* temperature for several frequencies (1 kHz to 1MHz) for $x = 0.1$ and 0.2 have been analyzed and are shown as a representative plots in Figs 4.4(c) and 4.4(d) respectively. It can be noticed that the dielectric permittivity decreases with increase in frequency as expected for polar dielectric materials. It is also well established that systems having intrinsic bulk capacitance would only contribute to the dielectric constant at high frequencies. Catlan has reported that strong magneto-dielectric effects could appear through a combination of magneto resistance and the Maxwell-Wagner effect and is not related to true ME coupling [32]. In the present case, since the dielectric anomalies are well defined even after 100 kHz, the origin of the dielectric anomaly is only due to intrinsic bulk capacitance and hence the observed dielectric transitions are safely attributed to the effect of ME coupling. Temperature dependence of loss-tangent at (higher frequency) 100 kHz is shown in inset of Figs 4.4(c) and 4.4(d). For all compositions, loss tangent (at frequency 100 kHz) increases monotonically with increase in temperature except appearance of anomalies around ≈ 350 °C. This anomaly corresponds to the antiferromagnetic transition which has also been observed in ε_r vs. T plot. The increase in loss tangent value with *x* could be due to enhancement of d. c. conductivity with composition.

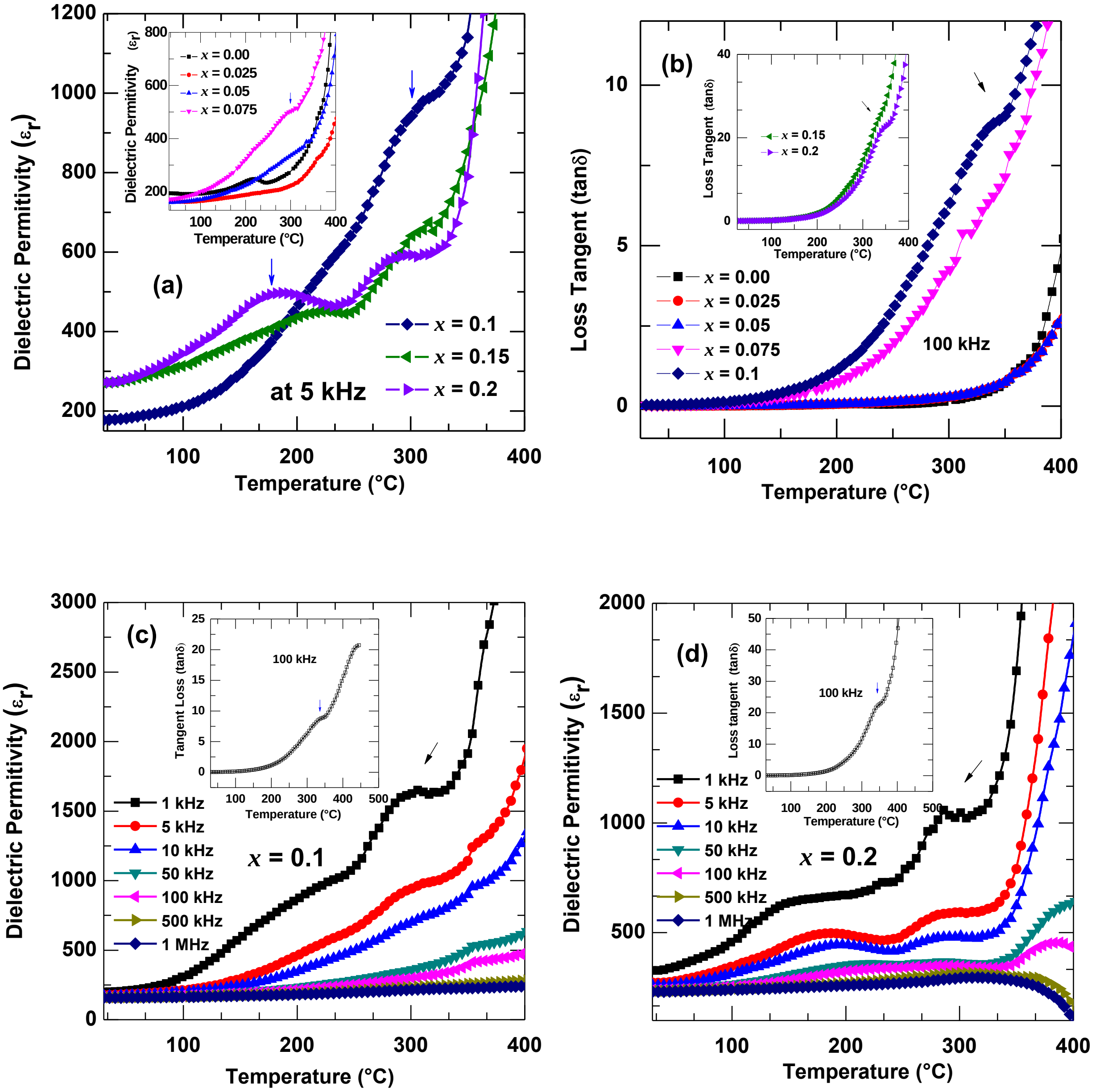

Figure 4.4 Temperature dependent dielectric parameters of (1-*x*) $BiFeO_3$ - *x*$YMnO_3$ system for $0.0 \leq x \leq 0.2$: **(a)** ε_r *vs.* T at 5 kHz, **(b)** tan δ *vs.* T at 100 kHz, temperature dependent ε_r at different frequencies between 1 kHz -1 MHz for **(c)** *x* = 0.1 and **(d)** *x* = 0.2 . (Inset-temperature dependence of tan δ at 100 kHz for **(c)** *x* = 0.1, and **(d)** *x* = 0.2.)

4.3.3 Ferroelectric Properties

Fig 4.5(a) and (b) shows the RT ferroelectric hysteresis loops of the solid solution of (1-*x*)BFO-*x*YM for $0.0 \leq x \leq 0.2$. It was found that for $x = 0.0$, the remnant polarization, coercive field and maximum polarization are 0.4μC/cm^2, 11.5 kV/cm and 1.3 μC/cm^2, respectively. The variable oxidation states of Fe (Fe^{+2} to Fe^{3+}) in the material is still unavoidable. As a result, the oxygen vacancies are required for charge compensation, which also leads to the high leakage current. Hence, the saturation in loop could not be observed even if maximum applied electric field due to the high conductivity [1-2]. It is to be noted that magnitude of remnant polarization decreases on increasing composition. This is due to the switching off the sterochemically active 6s^2 lone pair of Bismuth.

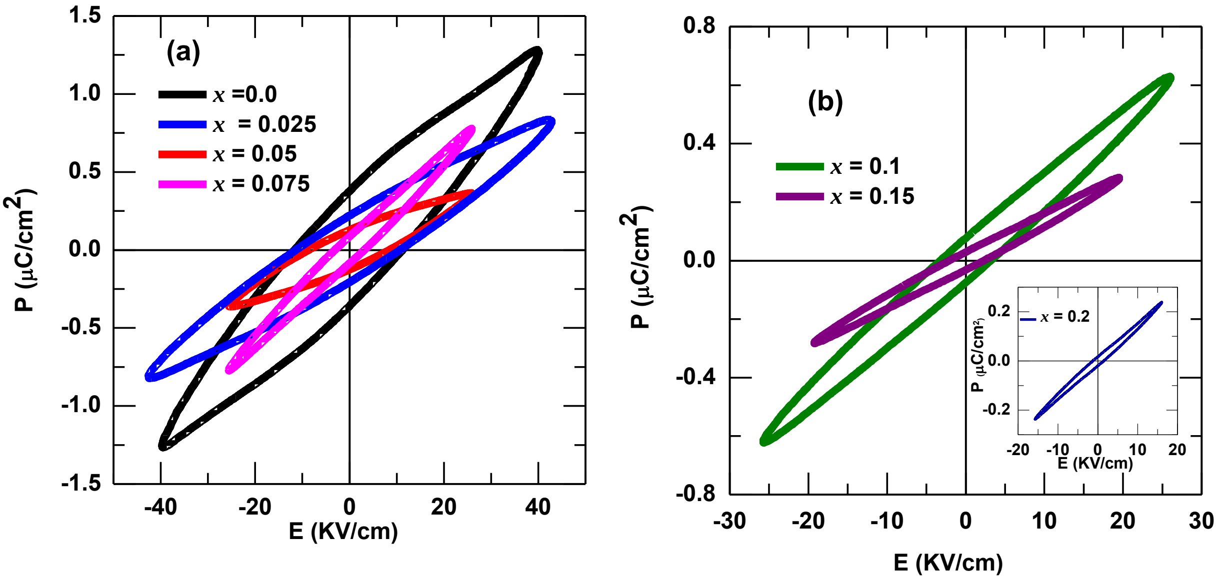

Figure 4.5 (a) Ferroelectric hysteresis loops (P-E) for (1-*x*) BiFeO$_3$-*x*YMnO$_3$ system for ($0.00 \leq x \leq 0.075$) **(b)** $0.1 \leq x \leq 0.2$ at RT.

4.3.4 Complex Impedance Studies

Complex impedance analysis is a powerful technique to study the electrical properties of materials over a wide range of frequency and temperature. Figure 4.6 represents the complex impedance spectra (*i.e.*, Nyquist plot: Imaginary Z vs. Real Z) of (1-*x*) BiFeO$_3$-*x*YMnO$_3$ for $0.0 \leq x \leq 0.2$ at different temperatures. For $x = 0.0$, at low temperatures (below 200 °C), a straight line is observed in impedance plot signifying the insulating property of the material.

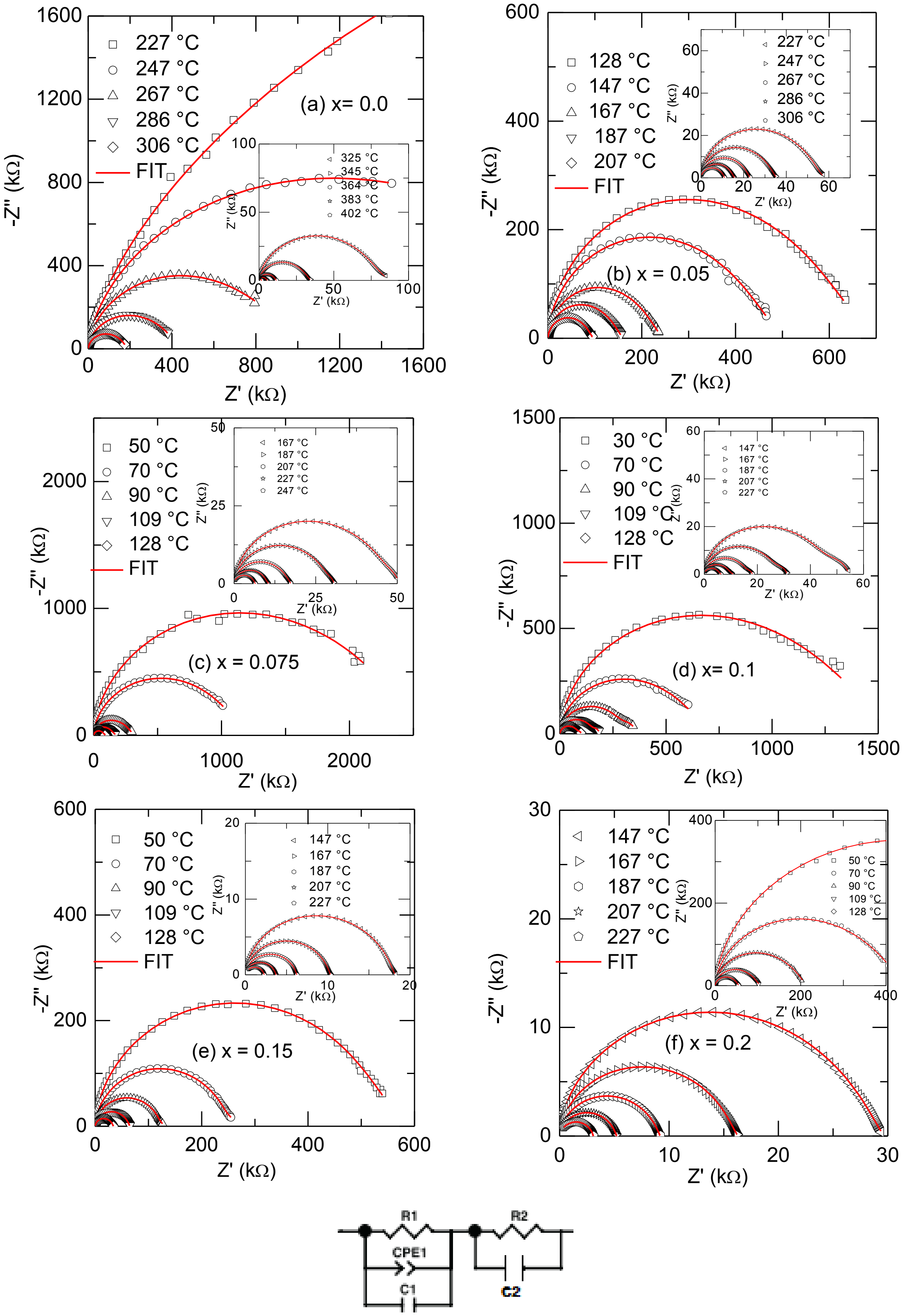

Figure 4.6 (a)-(f) Temperature dependent Nyquist Plot (-Z" vs. Z′) of (1-x) $BiFeO_3$-$x$$YMnO_3$ system for $0.0 \leq x \leq 0.2$ with equivalent circuit shown below.

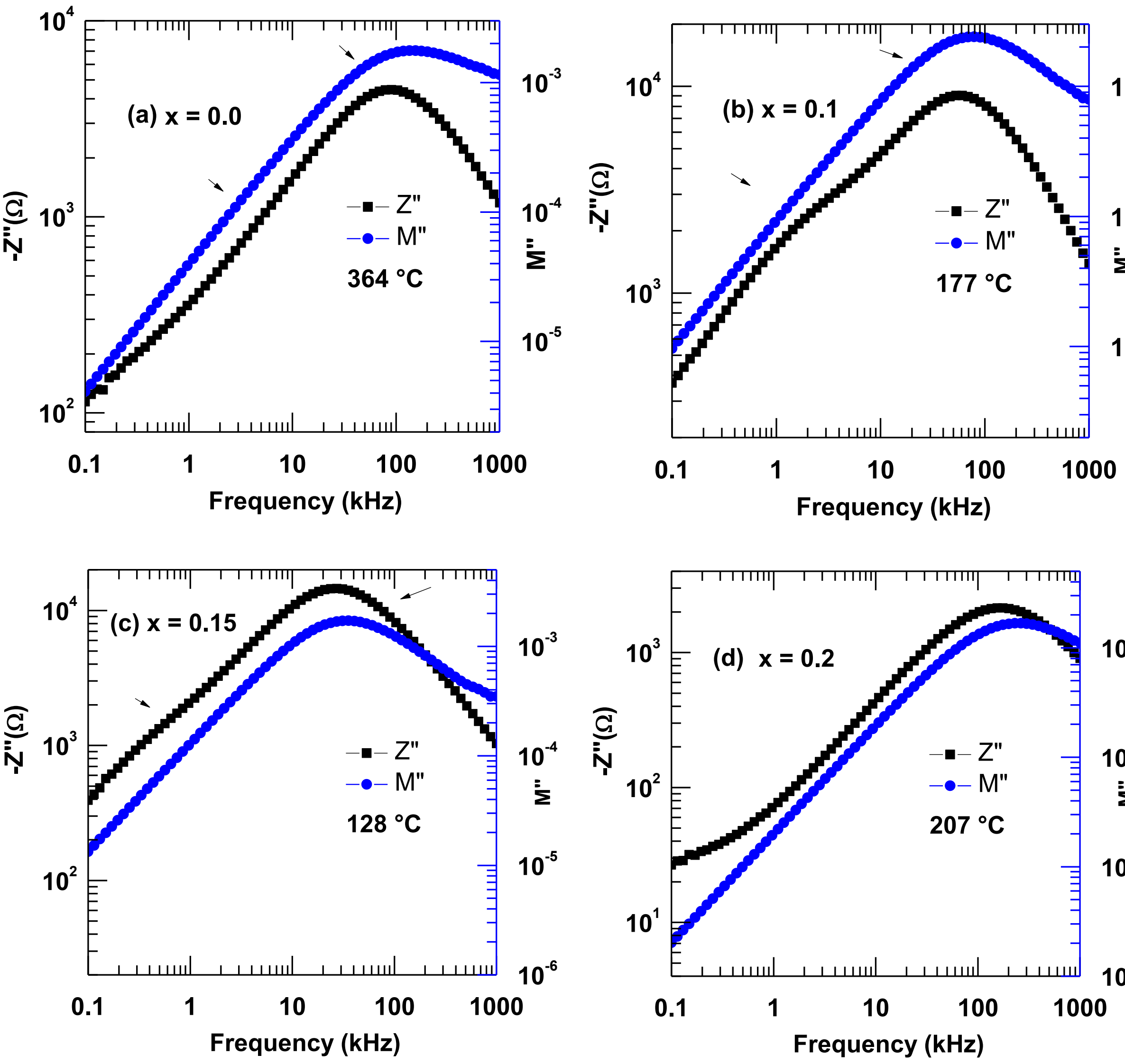

Figure 4.7 Combined impedance (-Z") and modulus spectroscopic (M") plot are plotted in log-log scale for **(a)** $x = 0.05$, **(b)** $x = 0.1$, **(c)** $x = 0.15$ and **(d)** $x = 0.2$.

Above 300 °C, a semicircular arc starts forming and finally semicircular arcs become prominent on increasing temperature. The presence of a single semicircular arc is due to the bulk property of the material. At higher temperature (>360 °C) the plot can be characterized by the presence of two overlapping semicircular arcs with their centers below the real axis. The high frequency semicircle is attributed to the bulk (grain) property of the material, whereas the low frequency arcs (at high temperature) are credited to the presence of grain boundary effect [33]. The intercept of the semicircular arcs on the real axis gives rise to bulk and grain boundary resistance of the materials. The bulk and grain boundary resistance (d. c.

resistance) of the samples decreases with rise in temperature as indicated by the corresponding reduction in the diameter of the semicircles on increasing temperature [33].

The assignment of the two semicircular arcs to the electrical response due to grain interior and grain boundary is consistent with the brick-layer model for a polycrystalline material [33-22]. For ideal Debye like ideal response, the equivalent circuit comprises of a parallel combination of a resistor and capacitor. The combined impedance and modulus spectroscopic plot (-Z'' and M'' vs. frequency) are plotted in log-log scale in order to highlight the departure from the ideality (See Figure 4.7). It has been found from the combined impedance and modulus spectroscopic that, the two peak maxima are not frequency-coincident, suggesting the departure from ideal Debye behavior and justify the presence of constant phase element [33-22]. The presence of constant phase element (CPE) representing the departure from Debye-like ideality. The CPE admittance is $Y(CPE) = A_0(j\omega)^n = A\omega^n + jB\omega^n$ with $A = A_0Cos(n\pi/2)$ and $B= A_0Sin(n\pi/2)$ where A_0 and n are frequency independent parameters usually depend on temperature, A_0 determines the magnitude of the dispersion and $0 \leq n \leq 1$. The CPE describes an ideal capacitor for n=1 and an ideal resistor for n=0. Similar types of reports are available in the literature [33-22]. So the high frequency semicircular arc can be modeled to an equivalent circuit of parallel combination of a resistance (bulk resistance), capacitance (bulk capacitance) along with a constant phase element, whereas the low frequency semicircular arc can be molded for parallel combination of a resistance (grain boundary resistance) and a capacitance (grain boundary capacitance). Both the equivalent circuit corresponding to grain and grain boundary contribution are connected in series for fitting the impedance data. The impedance data (symbols) have been fitted (solid line) with the above proposed model by the commercially available software ZSIMP-WIN Version 3 as shown in Fig. 4.6. For all YM modified BFO compounds we have adopted same equivalent circuit to fit the temperature dependent Nyquist Plot as shown in Fig 4.6.

The d. c. conductivity due to the bulk and grain boundary contributions have calculated from the resistances obtained after the fitting the impedance data using the formula, $\sigma_{dc} = \frac{1}{R} \times \frac{l}{A}$, where l = thickness, A = area and R = resistance. Fig. 4.8 shows the variation of dc conductivity (due to bulk and grain boundary) with inverse of absolute temperature (*i.e.*, σ_{dc} vs. $10^3/T$). It has been observed that the d. c. conductivity decreases with rise in temperature (*i.e.*, a decrease in the resistivity on rising temperature) suggesting the negative-temperature coefficient of resistance (NTCR) behavior, typically observed in semiconductors [33-22]. The temperature dependence of conductivity can be explained by the Arrhenius relation $\sigma = \sigma_P \exp(-E_a/kT)$, where k is the Boltzman constant, E_a is the activation energy and σ_P is the pre-exponential factor [22]. The value of E_a has been calculated from the slope of σ_{dc} versus $10^3/T$ (K^{-1}) plot. We observed two different slopes in Arrhenius plot suggesting two different conduction mechanisms (*i.e.*, activation energy values). The calculated activation energies for both grain and grain boundary are tabulated in Table 4.3.

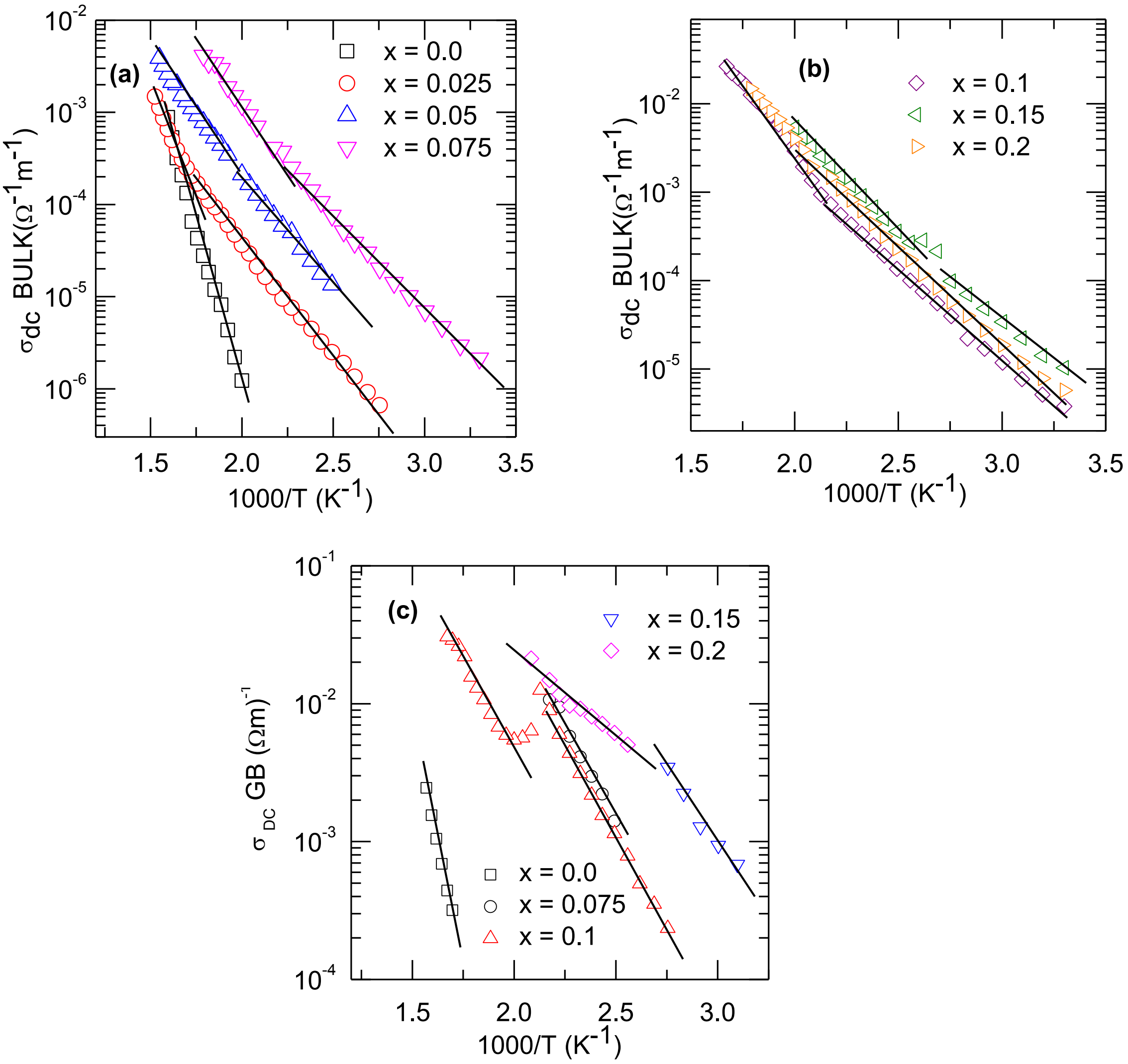

Figure 4.8 Variation in bulk and grain boundary conductivity with inverse of absolute temperature (*i.e.*, σ_{dc} vs. $10^3/T$) of (1-*x*)BFO-*x*YM for different *x*.

Table 4.3 Activation energy E_a (in eV) obtained from temperature dependent bulk resistance (R_B), grain boundary resistance (R_{GB}) for different compositions.

Composition (*x*)	Bulk (σ_{dc})		Grain Boundary (σ_{dc})
	Zone-I	Zone-II	
0.0	--	1.402	1.478
0.025	0.857	0.485	--
0.05	0.554	0.488	--
0.075	0.513	0.428	0.599
0.1	0.504	0.412	0.562
0.15	0.482	0.35	0.402
0.2	--	0.467	0.243

4.3.5 Magnetic Properties

Figs 4.9 (a) and (b) represent the magnetic hysteresis loops (M~H) of the solid solution of (1-*x*)$BiFeO_3$-*x*$YMnO_3$ for $0.00 \leq x \leq 0.2$ at room temperature. Interesting observations can be noticed from the compositional dependence of corercivity and remanent magnetization.

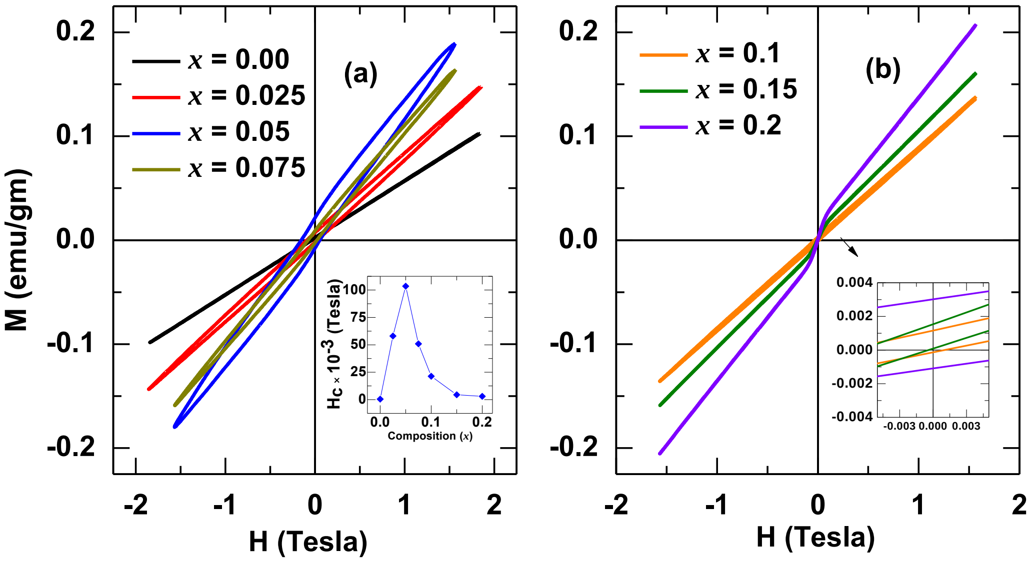

Figure 4.9 M-H hysteresis curves of (1-*x*) $BiFeO_3$-*x*$YMnO_3$ system **(a)** for $0.0 \leq x \leq 0.075$ at RT (Inset- Compositional dependence (*x*) of coercive field (H_c)), **(b)** for $0.1 \leq x \leq 0.2$ at RT (Inset-magnification at lower fields).

The M-H dependence for the parent $BiFeO_3$ is all most linear with no hysteresis and zero coercivity. This is understood on the line of cancelation effect of space modulated spin structure [1]. With increase in composition *x*, there is an increase in the magnetization value noticed. Furthermore, the magnitude of M for $x = 0.05$ is found to be one order of magnitude more than that of pure BFO system. This is associated with substantial hysteresis and finite coercivity, which represents a presence of long range canted antiferromagnetic order. The coercivity and remnant magnetization for $x = 0.05$ are found to be $H_c = 103$ mT and $M_r = 0.025$ emu/gm, respectively. Such enhanced corecivity could be attributed to induced lattice strain. Further increase in concentration leads to a small decrease in magnetization. For $x = 0.1$ *i.e.*, at the structural phase boundary (Sec. 4.3.1), the coercivity decreases to 21 mT. Fig. 4.9(a)-inset shows the variation of coercive field with composition *x*. A typical signature of sudden increases in magnetization value at lower field and then increases linearly with field (magnetic switching behavior) were observed for samples, $x = 0.15$ and $x = 0.2$. Similar switching behavior in Y^{3+} modified $BiFeO_3$ has been reported by Mishra *et al* [21]. It is to be noted that, switching behavior appears at room temperature and even at lower applied field. Moreover, it is of further interesting to demonstrate whether the origin of observed corecivity and remnant magnetization actually appear from the suppression of space modulated spin structure or caused by presence of impurity phase ($Bi_2Fe_4O_9$) and mixed valance state [2]. Hence essential resolutions are needed. These explanations are as follows (a) the magnetic ordering temperature of impurity phase $Bi_2Fe_4O_9$ is very much below room temperature. Hence its effect is null on remanent magnetization at room temperature. In addition to that, Fig 4.1(a) and (b) clearly demonstrates the absence of impurity phase, (b) synthesis of nanoceramics and (c) substitution of Y at A-site could also lead to collapse of space modulated spin structure and improve the magnetization [1, 30]. Hence we conclude that the improvement in observed magnetization is due to suppression of spin cycloid or structural instability due to the solid solution BFO with YM.

4.3.6 Magnetoelectric Coupling

The magnetoelectric (ME) coupling can be studied by switching electrical polarization (**P**) by the application of magnetic field or magnetization (**M**) by the application of electric field. However, a strong ME coupling between **M** and **P** has not been achieved in multiferroics because of the problem to sustain the high electric field necessary to switch the magnetization. The ME coupling can also be studied through the magneto-dielectric effect; study of dielectric and electrical properties under the application of magnetic field and vice versa. The dielectric constant relates to the index of the refraction (n) of the material $n = (\mu\varepsilon)^{1/2}$, where μ and ε are the permeability and permittivity of the material respectively. The tuning of refractive index by the application of a magnetic field would give rise a novel functionality to magnetoelectric and magneto-optic devices. In order to understand the ME coupling, we studied magneto-capacitance, magneto-impedance and dielectric properties under different magnetic fields at room temperature. It has been well established that the direct evidence of intrinsic/true magneto-electric coupling in multiferroic systems is based on following criterions: (a) an anomaly in temperature dependent dielectric permittivity around magnetic transition temperature and (b) the changes in the dielectric permittivity with application of magnetic field [34-35]. Figure 4.4 clearly shows unambiguous demonstration of first criterion. Figure 4.10 shows the frequency dependence of dielectric permittivity (ε_r), for $x = 0.05$, 0.1, 0.15 and 0.2 at room temperature for different static magnetic field ($0.0 \leq H \leq 2.0$ Tesla). It is also found that the dielectric permittivity decreases with an increase in the applied magnetic field throughout the investigated frequency range. This is in fact the indication of coupling between electric and magnetic ordering at room temperature. Hence the above mentioned second criterion is also satisfied. A possible mechanism for the coupling between the electric and magnetic ordering is in order. When magnetic field is applied to a multiferroic system, the material becomes strained. This strain in turn induces a stress on the piezoelectric (for all ferroelectrics are piezoelectric), which generates the electric field [35]. This field could orient the ferroelectric domains which lead to an enhancement of the polarization value. Eventually, change in dielectric permittivity occurs with application of magnetic field.

The quantitative measure of magnetoelectric coupling is represented in terms of magneto-capacitance (MC %) and the magneto-loss (ML %), magneto-impedance (MI %) and magneto-phase angle (MP %) defined as the following formula respectively [36].

$$MC\% = \frac{\varepsilon\,(H,T) - \varepsilon(0,T)}{\varepsilon(0,T)} \times 100;\; ML\% = \frac{tan\delta\,(H,T) - tan\delta(0,T)}{tan\delta(0,T)} \times 100$$

$$MI\% = \frac{Z\,(H,T) - Z(0,T)}{Z(0,T)} \times 100;\; MP\% = \frac{\theta\,(H,T) - \theta(0,T)}{\theta(0,T)} \times 100$$

Figure 4.11 illustrate (MC %), (ML %), (MI %) and (MP %) as a function of magnetic field, ($0 \leq H \leq 2$ Tesla) for composition range, $0.00 \leq x \leq 0.2$ at room temperature. It was observed

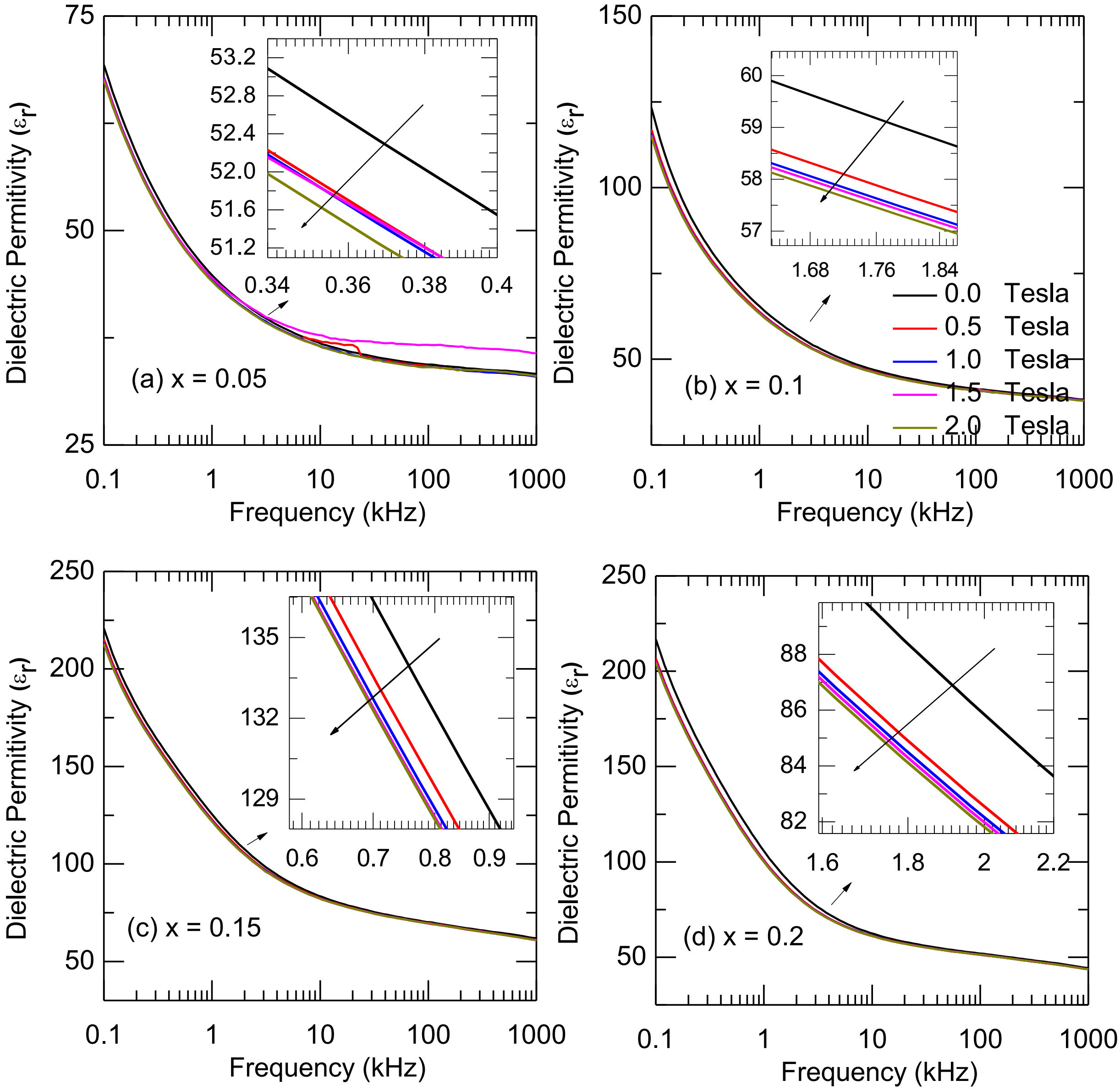

Figure 4.10 Frequency dependent behavior of dielectric permittivity (ε_r) for **(a)** $x = 0.05$, **(b)** $x = 0.1$, **(c)** $x = 0.5$ and **(d)** $x = 0.2$ under different magnetic fields, $0 \leq H \leq 2$ Tesla at RT. The arrow indicates increasing magnetic field strength.

that the magnitude of all the coupling coefficients increases with increasing composition. It is to be noted that enhanced magneto-capacitance value around -5.5% was observed for $x = 0.2$ at room temperature. The observed trend in magneto-dielectric response can be interpreted as follows: (a) synthesis of nano ceramic leads to introduction of strain (due to nano size effect) for all $YMnO_3$ modified $BiFeO_3$ samples leading to enhanced magneto-dielectric response, (b) structural investigation demonstrates a decrease in unit cell volume with increase in $YMnO_3$ content (increase in lattice strain) which improves ME coupling.

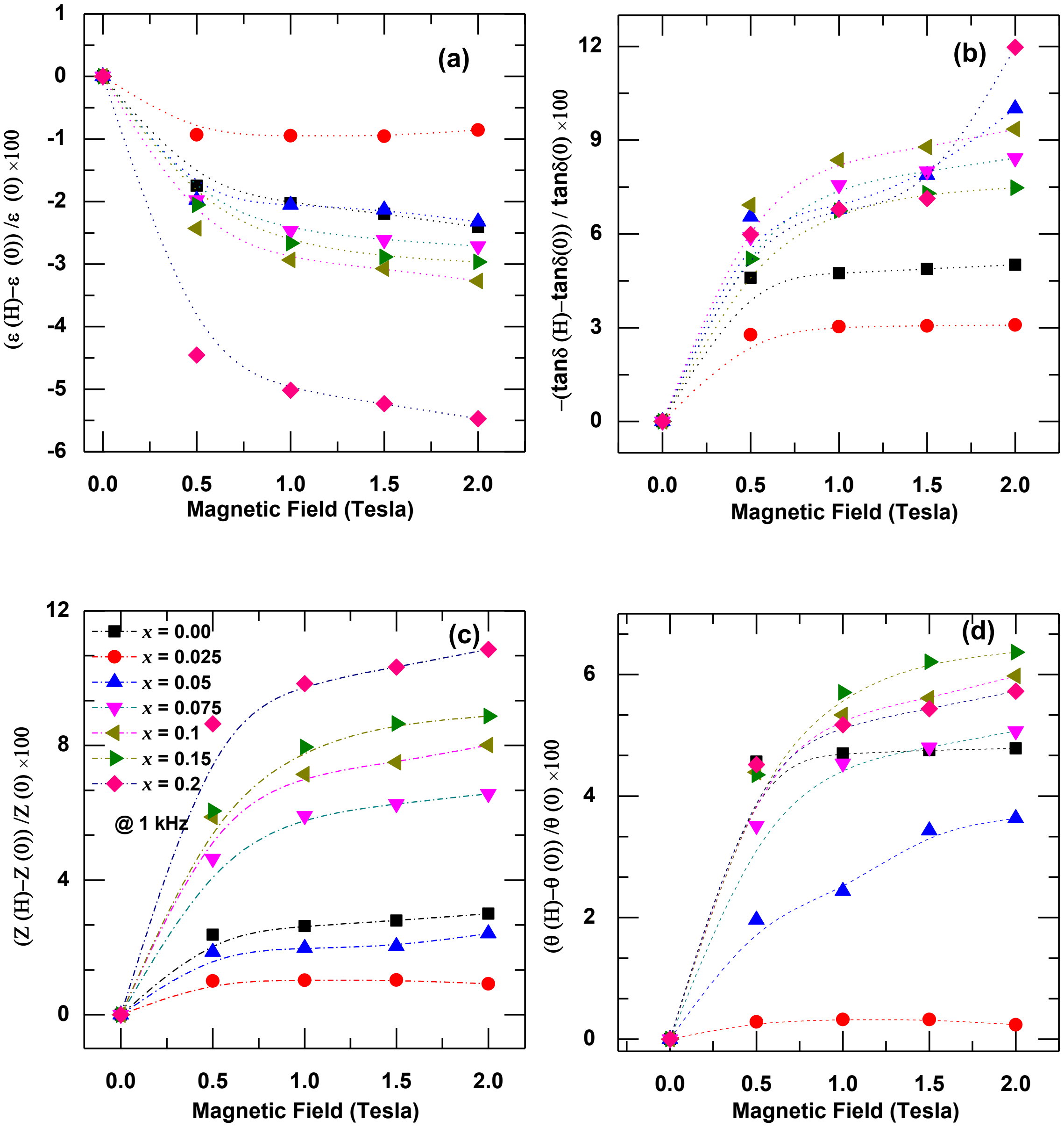

Figure 4.11 Magnetic field dependent behaviors of **(a)** dielectric permittivity (ε_r), **(b)** loss tangent (tan δ), **(c)** impedance (Z), **(d)** phase angle (θ) of (1-x)$BiFeO_3$ - $x$$YMnO_3$ system for $0.00 \leq x \leq 0.2$ at 1 kHz.

4.3.7 Magneto-Impedance Studies

Figure 4.12 shows the magnetic field dependent Niquist Plot of (1-x)BFO-xYM for $x = 0.05$, 0.1, 0.15 and 0.2 respectively at RT. For $0.025 \leq x \leq 0.1$, we observed appearance of single semi-circular arcs with non-Debye type behavior [33]. But $x = 0.15$ and $x = 0.2$, the impedance spectra displayed two overlapping semicircular arcs.

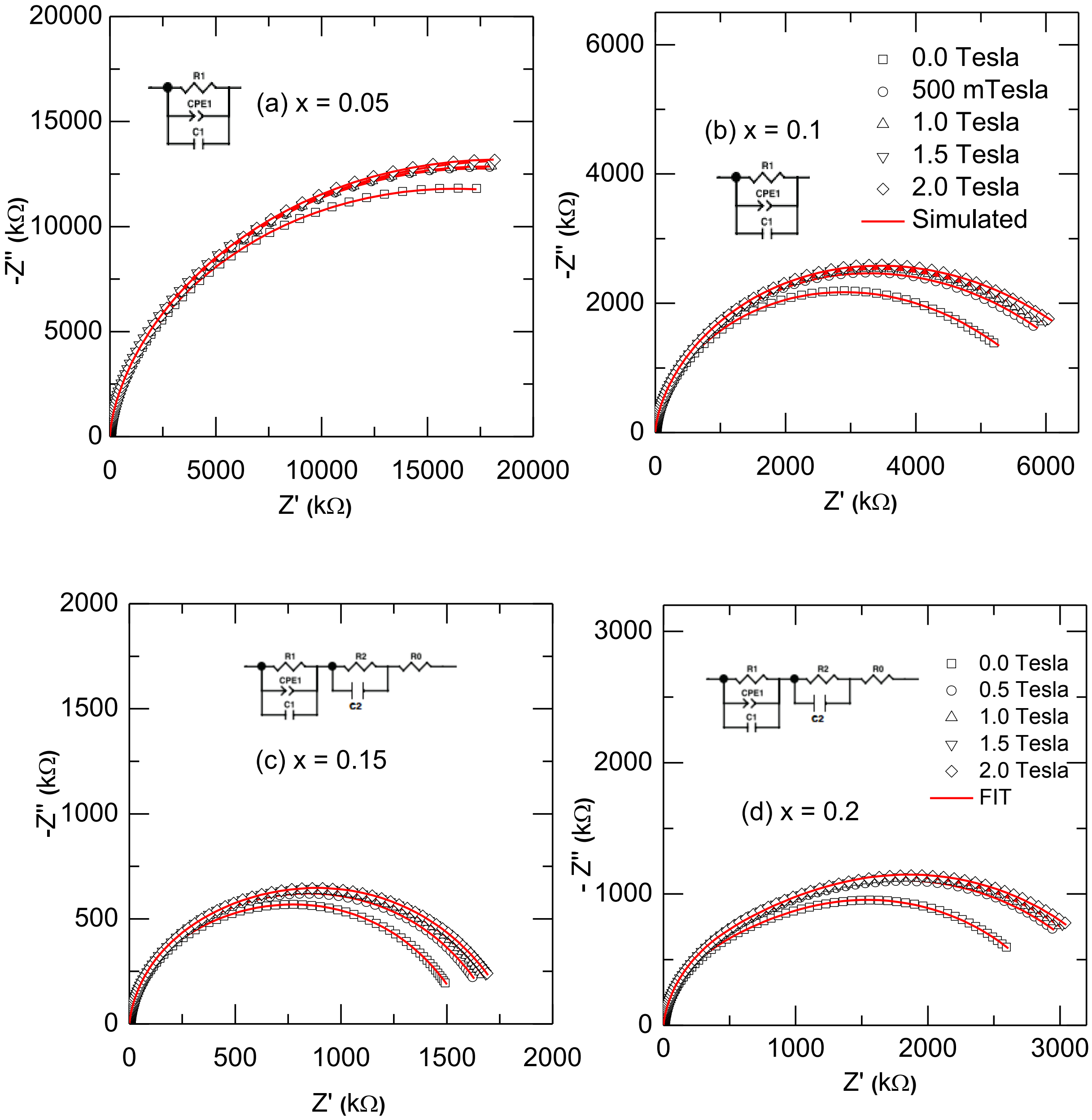

Figure 4.12 Magnetic Field dependent Nyquist Plot (-Z'' vs. Z′) of (1-x) $BiFeO_3$-$x$$YMnO_3$ system for **(a)** $x = 0.05$, **(b)** $x = 0.1$, **(c)** $x = 0.15$ and **(d)** $x = 0.2$ at RT (Inset-equivalent circuit).

Table 4.4 Bulk capacitance obtained from fitting of magnetic field dependent complex impedance plot at RT for different value of *x*.

Bulk Capacitance (10^{-11}) in F							
Field (T)	$x = 0.0$	$x = 0.025$	$x = 0.05$	$x = 0.075$	$x = 0.1$	$x = 0.15$	$x = 0.2$
0.0	4.174	1.548	2.039	2.174	2.363	4.225	3.293
0.5	4.145	1.529	2.024	2.159	2.342	4.176	3.254
1	4.152	1.529	2.021	2.158	2.342	4.172	3.239
1.5	4.152	1.53	2.22	2.155	2.345	4.173	3.241
2.0	4.152	1.529	2.031	2.157	2.341	4.17	3.243

Table 4.5 Bulk resistance obtained from fitting of magnetic field dependent complex impedance plot at RT for different value of *x*.

Bulk Resistance in Ohm							
Field (T)	$x = 0.0$ 10^6	$x = 0.025$	$x = 0.05$ 10^7	$x = 0.075$ 10^6	$x = 0.1$ 10^6	$x = 0.15$ 10^6	$x = 0.2$ 10^6
0	8.6176	--	3.837	8.178	6.635	1.43	2.782
0.5	9.3114	--	4.064	9.106	7.529	1.546	3.215
1	13.469	--	4.153	9.388	7.741	1.594	3.267
1.5	14.609	--	5.431	9.473	7.814	1.61	3.292
2	15.589	--	4.366	9.543	7.885	1.618	3.32

The high frequency semicircle corresponds to bulk contribution whereas low frequency is attributed to grain boundary property. We have fitted the magnetic field dependent Niquist plot using the equivalent circuit (discussed above) as shown in Fig 4.12 and a close agreement between the experimental value and the fitted lines have been observed. The bulk capacitance and resistance obtained from the fitting process are listed in Table 4.4 and 4.5. It is observed that bulk capacitance decrease on increasing magnetic field where as bulk resistance increases. This indicates the intrinsic evidence of magnetoelectric behavior in the YM modified samples. Similar types of reports are also available in the literature [34].

3.4 Conclusions

Solid solutions of (1-*x*)BFO-*x*YM for $0.0 \leq x \leq 0.2$ nanoceramics were synthesized by auto-combustion technique. Rietveld refinement result of X-ray diffraction pattern show a compositional driven structural phase transition from *R3c* to *R3c*+*Pbnm* after $x = 0.1$. TEM characterization showed that average crystallite size is around 30 nm. The grain size of the samples decreased with $YMnO_3$ incorporation. Temperature dependent dielectric study and room temperature magneto-dielectric measurements provide the direct evidence of magnetoelectric coupling in the material. Temperature dependent bulk and grain boundary conductivity obeys Arrhenius equation. Enhanced magneto-capacitance value around -5.5% was observed for $x = 0.2$ at RT. Magnetic transition temperature decreases with increase in *x* content. The remanent polarization decreases on increasing composition. The enhancement of remnant magnetization with $YMnO_3$ incorporation was found at room temperature and explained on the basis of collapse of space modulated spin cycloid. Magneto-impedance spectroscopy provided the signature of intrinsic magnetoelectric coupling in the material.

3.5 References

[1] G. Catalan, J.F. Scott, Adv. Mater. **21**, 2463 (2009).

[2] R. Palai, R.S. Katiyar, H. Schmid, P. Tissot, S.J. Clark, J. Robertson, S.A.T. Redfern, G. Catalan, J.F. Scott, Phys. Rev. B **77,** 014110 (2008).

[3] T. Kimura, S. Kawamoto, I. Yamed, M. Azuma, M. Tanky, and Y. Tokura, Phys. Rev. B **67**, 180401R (2003).

[4] V. R. Palkar, J. John, and R. Pinto, Appl. Phys. Lett. **80**, 1628 (2002).

[5] S. R. Das, R. N. P. Choudhary, P. Bhattacharya, R. S. Katiyar, P. Dutta, A. Manivannan, and M. S. Seehra, J. Appl. Phys. **101**, 034104 (2007).

[6] T.J. Park, G.C. Papaefthymiou, A.J. Viescas, A.R. Moodenbaugh, S.S. Wong, Nano Lett. **7**, 766 (2007).

[7] A. Singh, V. Pandey, R. K. Kotnala, and D. Pandey, Phys. Rev. Lett. **101**, 247602 (2008).

[8] T.H. Wang, Y. Ding, C.-S. Tu, Y.D. Yao, K.T. Wu, T.C. Lin, H.H. Yu, C.S. Ku, and H.-Y. Lee J. Appl. Phys. **109**, 07D907 (2011).

[9] V. A. Khomchenko, D. A. Kiselev, J. M. Vieira, Li Jian, A. L. Kholkin, A. M. L. Lopes, Y. G. Pogorelov, J. P. Araujo, and M. Maglione, J. Appl. Phys. **103**, 024105 (2008).

[10] P. Pandit, S. Satapathy, P. K. Gupta, and V. G. Sathe, J. Appl. Phys. **106**, 114105 (2009).

[11] V R Palkar, D C Kundaliya and S.C Malik J. Appl. Phys. **93**, 4337 (2003).

[12] J Wei, R Haumont, R Jarrier, P Berhtet, B. Dkhil, Appl. Phys. Lett. **96**, 102509 (2010).

[13] F. Bai, J. Wang, M. Wuttig, J. F. Li, and N. Wang, Appl. Phys. Lett. **86**, 032511 (2005).

[14] K.F. Wang, J.M. Liu, Z.F. Ren, Adv. Phys. **58**, 321 (2009).

[15] A. Lahmar, S. Habouti, M. Dietze, C. H. Solterbeck, and M. Es-Souni, Appl. Phys. Lett. **94**, 012903 (2009).

[16] W.H, Zhu, L.W. Su, Z.G. Ye and W Ren, Appl. Phys. Lett. **94**, 142908 (2009).

[17] V. V. Ivanova, V. V. Gagulin, S. K. Korchagina, Yu. A. Shevchuk, and V. V. Bogatko, Inorg. Mater. **39**, 745 (2003)

[18] A.V. Nazarenko, A. G. Razumnaya, M. F. Kupriyanov, Yu. V. Kabirov, A. G. Rudskaya, P. Yu. Teslenko, and N. B. Kofanova, Physics of the Solid State **53**, 1599 (2011).

[19] B Vanaken, T. Palstra, A. Filippetti, N. Spladin, Nat. Mater. **3**, 164 (2004).

[20] R. D. Shannon, and C. T. Prewitt, Acta Crystallogr. Sect. B: Struct. Crystallogr. Cryst. Chem. **25**, 925 (1969).

[21] R. K. Mishra , D. K. Pradhan , R. N. P. Choudhary and A. Banerjee, J. Phys.: Condens. Matter. **20,** 045218 (2008).

[22] D. K. Pradhan, R. N. P. Choudhary, C. Rinaldi and R. S. Katiyar J. Appl. Phys. **106,** 024102 (2009).

[23] S. N. Tripathy, B.G. Mishra, M. M. Shirolkar, S. Sen, S. R. Das, D. B. Janes, D. K. Pradhan, Mater. Chem. Phys. **141**, 423 (2013).

[24] S.R. Jain, K.C. Adiga, V.R. Pai Verneker, Combust. Flame **40**, 71 (1981).

[25] J. Rodriguez-Carvajal, Physica B **192**, 55 (1993).

[26] R. Haumount et al. Phys. Rev. B **79**, 184110 (2009).

[27] J. G. Bos, B. Aken, and T. M. Palstra, Chem. Mater. **13**, 4804 (2001).

[28] S.M. Selbach, T. Tybell, M.A. Einarsrud, T. Grande, Chem. Mater. **19**, 6478 (2007).

[29] D. Balzar, J. Appl. Crystallogr. **28**, 244(1995).

[30] G. L. Yuan and S. Or, J. Appl. Phys. **100,** 024109 (2006).

[31] L. Benguigui, Solid State Commun. **11**, 825 (1972).

[32] G. Catalan, Appl. Phys. Lett. **88**, 102902 (2006).

[33] D. C. Sinclair and A. R. West, J. Appl. Phys. **66**, 3850 (1989).

[34] R. Schmidt, J. Ventura, E. Langenberg, N. M. Nemes, C. Munuera, M. Varela, M. Hernandez, C. Leon, and J. Santamaria , Phys. Rev. B **86**, 035113 (2012).

[35] V.R. Palkar, D. C. Kundaliya, S. C. Malik and S. Bhattacharya, Phys. Rev. B **69**, 212102 (2004).

[36] P. Uniyal, K. L. Yadav, J. Phys.: Condens. Matter. **21,** 405901 (2009).

Chapter-5

Evidence of Intrinsic Magnetoelectric Coupling in $BiFeO_3$-$GdMnO_3$ Multiferroic Nanoceramics

Chapter-5 deals with the synthesis of (1-x)BiFeO$_3$-xGdMnO$_3$ (BFO-GM) solid solution for $0.0 \leq x \leq 0.2$ by auto-combustion method. The materials have been characterized and investigated using X-ray diffraction, field emission scanning electron microscopy, transmission electron microscopy, differential scanning calorimetry, dielectric, ferroelectric polarization (P-E loop), Impedance spectroscopic, magnetic hysteresis measurement (M-H loop), magneto-dielectric and magneto-impedance measurements with wide range of experimental conditions.

5.1 Introductory Remarks

In Chpater-1, we have extensively discussed the inherent problems associated with BFO and obstacles on its way for novel multifunctional device applications. In the present chapter, we have presented a suitable approach to improve the magnetoelectric coupling of parent BFO by fabrication of solid solutions with GdMnO$_3$ (GM).

The rare-earth (RE) manganite GM is an improper (*i.e.*, Type-II) multiferroic compound and crystallizes in orthorhombic crystal structure with *Pnma* space group [1-2]. The antiferromagnetic ordering temperature is well below RT (*i.e.,* T_N ~ 40 K). Due to spin-lattice coupling in GdMnO$_3$, ferroelectricity originates from antiferromagnetic ordering [1-2]. Consequently they exhibit ferroelectric ordering temperature (T_C ~ 12 K) lower than magnetic ordering temperature leading to strong magnetolectric coupling [1-3].

The motivation behind this chapter is as follows: (a) It has been reported that substitution with RE at Bi-site stabilize the perovskite structure, reduce the leakage current and suppress the spiral spin structure which in turn leads to release of latent magnetization [4], (b) As the T_N of GM is very low, so it is also probable that the solid solution of BFO with GM could bring down the magnetic ordering temperature of BFO towards the room temperature [1-2], (c) *Goodenough–Kanamori* rule suggests that a strong ferromagnetic interaction is expected between the empty Mn^{3+} orbital and filled Fe^{3+} orbital. Eventually, a decrease in T_N toward RT could be achieved by substitution of Mn^{3+} ions at the Fe^{3+} site of BFO [5], (d) several reports also have demonstrated the enhancement in multiferroic properties of BFO by synthesizing nanoparticles smaller than spin cycloid due to the size effect [6] and (e) the substitution of Gd^{3+} at Bi-site is expected to switching off the lone pair activity of Bi leading to shifting the FE transition towards RT [7]. Therefore, we expect that the synthesis of solid solution of BFO with GM could lower the ferroic ordering temperature (*i.e.,* T_N and T_C) towards RT and resulting a stronger magnetoelectric coupling.

In this present work, we have synthesized nanoceramic solid solution of (1-x)$BiFeO_3$–$x$$GdMnO_3$ for $0.0 \leq x \leq 0.2$ and systematically investigated in detail the structural, microstructural, thermal, dielectric, ferroelectric, magnetic, magnetoelectric and magneto-impedance properties. Emphasis has been given to synthesize phase pure solid solution of BFO with GM and investigate the possibility of the compositional driven structural phase transition and its correlation with the ME coupling.

5.2 Experimental Procedure

Nanoceramic solid solutions of (1-x)$BiFeO_3$-$x$$GdMnO_3$ (BFO-GM) for $0.0 \leq x \leq 0.2$ were synthesized using auto-combustion technique. During synthesis, high purity (99.9%) grade chemicals of $Fe(NO_3)_3.9H_2O$, $Bi(NO_3)_3.5H_2O$, Gd_2O_3, $(CH_3COO)_2Mn\cdot4H_2O$ were used as oxidizers, while urea was taken as fuel. The details of the synthesis procedure have been discussed earlier in Chapter-3 [See Ref: 8, 9-10]. For $x = 0.0$, the combustion residue was calcined at an optimized temperature of 550 °C for 3 h in air atmosphere. The compounds with compositional range, $0.025 \leq x \leq 0.1$ were calcined at 700 °C while those for $x = 0.15$ and $x = 0.2$ were calcined at 750 °C. The calcined powders were compacted into cylindrical pellets by hydraulic press with pressure 8×10^7 $kg.m^{-2}$ using polyvinyl alcohol (PVA) as binder. For composition $0.025 \leq x \leq 0.1$ and $0.15 \leq x \leq 0.2$, the pellets were sintered at 750 °C and 780 °C respectively. All the experimental conditions for characterization of the synthesized materials are same except DSC measurements discussed (c.f. Chapter-2). In the present investigation, we have used NETZSCH analyzer for DSC analysis. Samples were heated in a platinum pan from room temperature to 900 °C at a heating rate of 10 °C/min under air atmosphere to find out the phase transition in the materials.

5.3 Results and Discussion

5.3.1 Structural and Microstructural Properties

Figs 5.1(a) and (b) show the XRD pattern of the solid solution of (1-x)BFO-xGM for $0.0 \leq x \leq 0.2$ at RT. Structural analyses of the XRD pattern were carried out by Rietveld technique using FULLPROF package [11]. Details of the refinement procedure and conditions have been discussed in Chapter-4. The experimental data points are represented as symbol (+) and theoretical data points are shown in solid line as shown in Fig. 5.1(a).

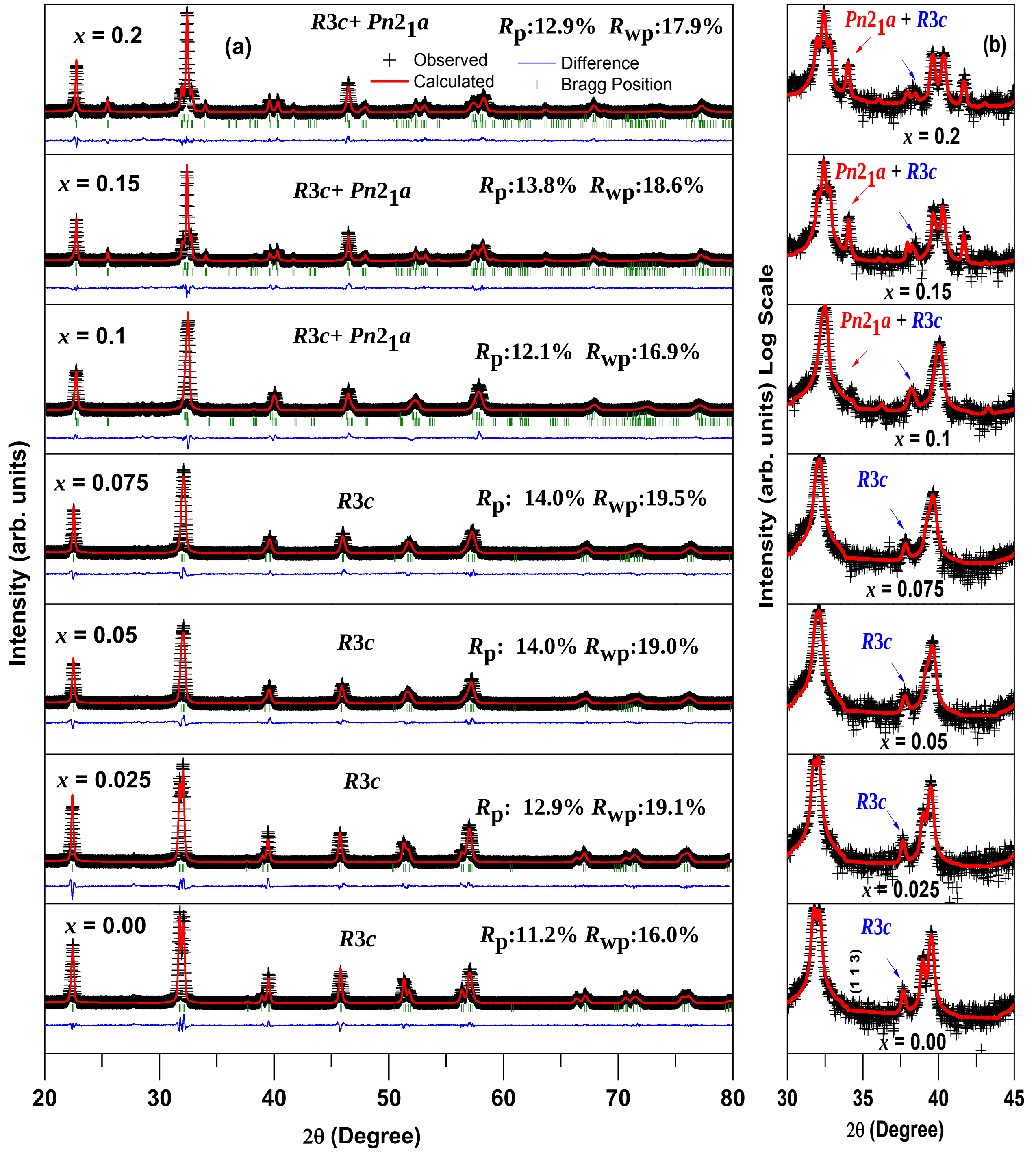

Figure 5.1(a) Rietveld refinement of X-ray diffraction patterns of solid-solution (1-*x*)BFO-*x*GM for $0.0 \leq x \leq 0.2$ at RT (linear scale), **(b)** the peak expanded in the 2θ regions 30 ° ≤ 2θ ≤ 40° signifying cross over from *R3c* to *R3c*+*Pn2₁a* (log scale).

The difference between observed and theoretical pattern and Bragg positions are shown at the bottom of the plot. There are three ions (Bi^{3+}/Gd^{3+}, $Fe^{3+}/Mn^{3+}$and O^{2-}) in the asymmetric unit cell of the rhombohedral perovskite *R3c* crystal structure. We have adopted the representations of atomic positions for hexagonal unit cell of *R3c* space group as per Megaw and Darlington formalism [12]. The coordinates of all the atoms in the asymmetric unit cell of the *R3c* space group can also be written as a function of the atomic displacement parameters *s, t, d,* and e : Bi^{3+}/Gd^{3+} (0, 0, $\frac{1}{4}+s$), Fe^{3+}/Mn^{3+} (0, 0, t), O^{2-} ($\frac{1}{6}-2e-2d$, $\frac{1}{3}-4d$, $\frac{1}{12}$). The parameters "s" and "t" describe the polar displacement of cations Bi^{3+}/ Gd^{3+} and Fe^{3+}/Mn^{3+} along the polar axis of the rhombohedral $[111]_{rh}$ or the hexagonal axis $[001]_{h}$. The displacement parameter "e" of oxygen O^{2-} from its ideal position is related to the tilt angle (ω) of antiphase rotation of the oxygen octahedra about the rhombohedral $[111]_{rh}$ direction through the expression $\omega = \tan^{-1}(4e3^{1/2})$. The parameter "*d*" is related to the distortion of the BO_6 (B: Fe^{3+}/Mn^{3+}) octahedral. The *z* coordinate of the oxygen ion is anchored at $z = 1/12$ [12]. Here it is worth noting that "s-t" is a cooperative displacement along $[111]_{rh}$. This represents the quantitative measure of crystallographic polarization and directly proportional to magnetic ordering temperature [13]. For pure BFO (*i.e., x* = 0.0) we obtain a best match between calculated and observed X-ray diffraction pattern for *R3c* space group (*i.e.,* goodness of fit: R_p= 9.8%, R_{wp}= 15.9%). The refined lattice parameters and volume of primitive unit cell of BFO are: *a* = 5.5779 (09) Å, *c* = 13.8710 (23) Å and 62.293 $Å^3$ respectively which are similar to the reported values [14]. It is observed that on increasing GM content up to *x* = 0.075, XRD patterns are analogues to the parent $BiFeO_3$. This is supported by existence of characteristic super lattice reflection (113) around ≈ 38 degree of rhombohedral *R3c* phase as shown in Fig 5.1(b) [13]. Therefore we have selected the *R3c* space group to refine the crystal structure up to *x* = 0.075. On and above *x* = 0.1, there is the splitting in the reflections, change in peak position, peak intensity and peak broadening in the diffraction pattern. Beyond *x* = 0.075 composition, the appearance of two crystallographic phases *i.e.,* rhombhodral and orthorhombic phases is evidenced by (i) appearance of (111) reflection around ≈ 25 degree, (ii) splitting of reflection around ≈ 32 degree and (iii) presence of super reflection (113) as shown in Figure 5.1(b). The existence of both rhomboheral and orthorhombic structure becomes more intensified and noticeable on increasing composition. For *x* = 0.2, the XRD pattern contains the reflections, which are the characteristics of *Pnma*/*Pbnm* space group similar to RE manganites [15]. The polar $Pn2_1a$ is sub-space group of nonpolar *Pnma* space group [15]. Therefore, we have carried out the Rietveld fittings using

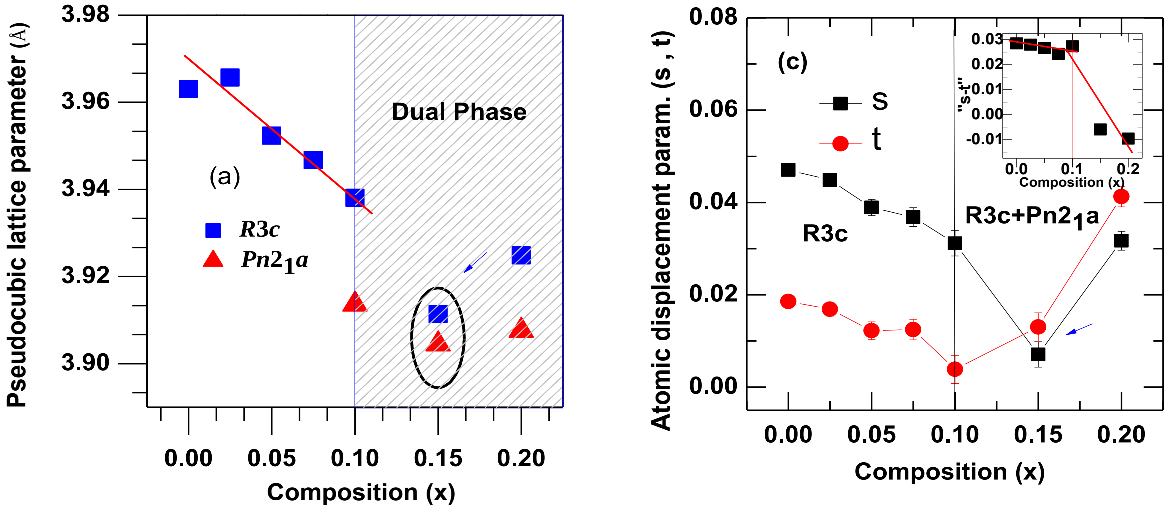

Figure 5.2 (a) Pseudo-cubic lattice parameter as a function of composition of (1-*x*)BFO-*x*GM for 0.0 ≤ *x* ≤ 0.2 and **(b)** Atomic displacement parameters (*i.e.*, s, t) as function of composition (Inset- Compositional dependence of "s-t").

dual phase model (*i.e.*, *R3c*+*Pn2₁a*) for composition range 0.1 ≤ *x* ≤ 0.2 and observed excellent fit. Similar type of dual phase model is reported on A-site modified BFO [16]. The appearance of orthorhombic symmetry or change of crystal structure starts at *x* = 0.1 (*i.e.*, structural phase boundary signifying threshold composition). For *x* = 0.1 composition, it is found that 86% of rhombohedral *R3c* phase and remaining 14% that of orthorhombic *Pn2₁a* phase, for *x* = 0.15, contains 42 % of *R3c* and 58 % of *Pn*2₁*a* phase and *x* = 0.2, contains 24 % of *R3c* and 76 % of *Pn*2₁*a* phase. The transition from rhombohedral to a mix phase consists of rhombohedral *plus* orthorhombic phase is expected and can be explained by strong destabilization of *R3c* structure by Gd^{3+} due to chemical pressure [15-16]. The lattice parameters of (1-*x*)BFO-*x*GM for 0.0 ≤ *x* ≤ 0.2 are listed in Table 5.1. It can be pointed out here that no traces of impurity phases (*i.e.*, $Bi_2Fe_4O_9$, $Bi_{25}FeO_{39}$, *etc.*) were noticed in the samples.

In order to establish the signature of compositional driven structural phase transition from *R3c* to *R3c*+*Pn2₁a*, we have plotted the pseudo-cubic lattice parameter as a function of composition and shown in Fig. 5.2 (a) Pseudo-cubic lattice parameter is defined as the cube root of the perovskite unit cell volume. It offers a convenient approach, because it brings down lattice parameter to the same scale of magnitude for better understanding and is a suitable probe to analyze structural phase transition [17]. Gavriliuk *et al.* reported that the pseudocubic lattice parameter decreases at a rate of approximately −0.01 Å/GPa [17].

Table 5.1 Lattice parameters of (1-x)BFO-xGM for $0.0 \le x \le 0.2$ estimated from Rietveld refinement with good-ness of fitting. The standard deviations are in parenthesis.

Composition	Space group	Lattice Parameters (Å)			χ^2
(x)		a	b	c	
0.0	*R3c*	5.5761 (09)	5.5761 (09)	13.8685 (23)	1.22
0.025	*R3c*	5.5832 (08)	5.5832 (08)	13.8615 (21)	1.21
0.05	*R3c*	5.5706 (11)	5.5706 (11)	13.7837 (28)	1.19
0.075	*R3c*	5.5642 (11)	5.5642 (11)	13.7568 (29)	1.30
0.1	*R3c* +	5.5551 (13)	5.55511 (13)	13.7113 (37)	1.20
	$Pn2_1a$	5.5476 (13)	7.78937 (19)	5.54864 (15)	
0.15	*R3c* +	5.5571 (12)	5.5571 (12)	13.4245 (33)	1.17
	$Pn2_1a$	5.5866 (11)	7.8098 (15)	5.45706 (11)	
0.2	*R3c* +	5.5805 (17)	5.5805 (17)	13.4504 (56)	1.15
	$Pn2_1a$	5.6010 (02)	7.8093 (04)	5.45655 (02)	

Table 5.2 Wyckoff notation and atomic positions of (1-x)BFO-xGM for $0.0 \le x \le 0.2$ used in Rietveld refinement technique.

Composition (x)	Space group	Atom	Site	x	y	z
$0 \le x \le 0.075$	*R3c*	Bi/ Gd	6*a*	0.0	0.0	0.03
		Fe/ Mn	6*a*	0.0	0.0	0.02
		O	18*b*	0.23	0.34	0.0833
$0.1 \le x \le 0.2$	*R3c* +$Pn2_1a$	Bi/ Gd	6*a*	0.0000	0.0000	0.03
		Fe/ Mn	6*a*	0.0000	0.0000	0.02
		O	18*b*	0.23	0.34	0.0833
		Bi/ Gd	4*a*	0.4513	0.2693	0.9994
		Fe/ Mn	4*a*	0.4671	0.0132	0.0021
		O	4*a*	0.4944	0.3063	0.1161
		O	4*a*	0.2134	-0.0214	0.7771
		O	4*a*	0.6730	0.9090	0.7993

Upon increasing composition up to $x = 0.1$, pseudo-cubic lattice parameter decreases and indicates an increase in lattice strain in *R3c* phase. It can be mentioned here that our central aim is to induce the strain in *R3c* phase for improvement of multiferroic properties. At $x = 0.15$, lattice parameter approaches equal magnitude signifying the equal fraction of *R3c* and $Pn2_1a$ phase. It is observed that crystallographic parameter "s-t" decreases with composition up to $x = 0.15$ suggesting decrease in magnetic ordering temperature (c.f. Fig 5.2 (b)) [7-13].We also observe sharp change in unit cell parameters (*i.e.,* volume contraction: abruptly from one constant value to another) at $x = 0.1$. The Wyckoff notation and atomic positions of coexistence of *R3c* and $Pn2_1a$ phases are tabulated in Table 5.2.

Figure 5.3(a) shows the compositional variation of the average crystallite sizes of (1-x)BFO-xGM for $0.0 \leq x \leq 0.2$. In this context, we have employed Fourier X-ray line profile analysis (XLPA) based on Double-Voigt method using program BREADTH as discussed in Chapter-2 [19]. The average crystallite size of the solid solution BFO-GM system varies in the range 200 Å to 300 Å. Further to support the XLPA analysis we have carried out TEM measurements for $x = 0.2$ as shown in Fig 5.3 (b). The average crystallite size was found to be ~ 300 Å with some agglomeration. Both the values of crystallite size obtained from XLPA and TEM characterization are nearly same. The observed reflections from SAED pattern for $x = 0.2$ are in agreement with Rietveld refinement results for $R3c+Pn2_1a$ space group as shown in inset of Fig 5.3(b).

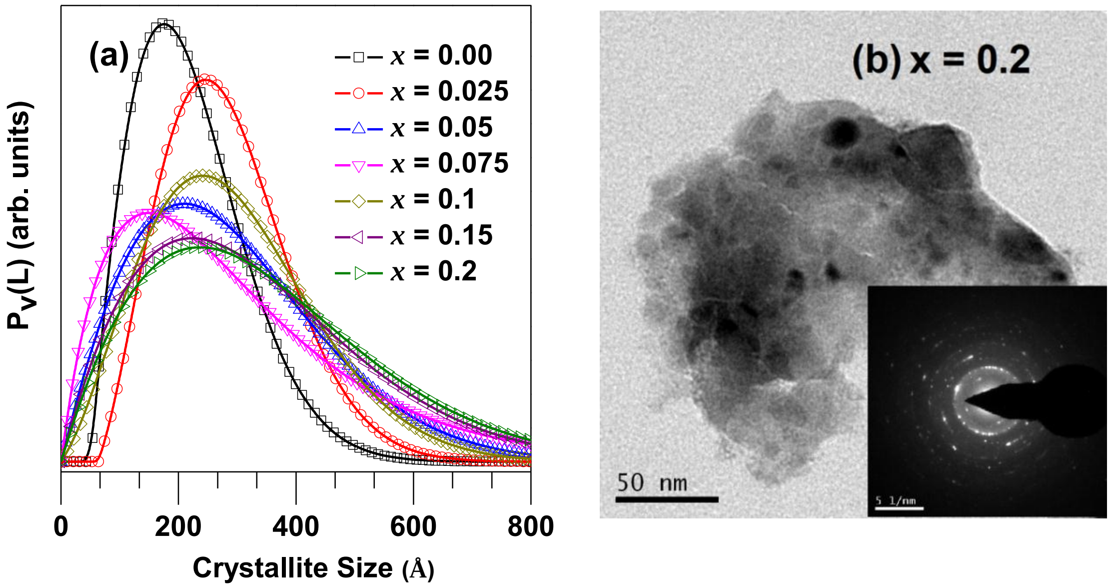

Figure 5.3 (a) The compositional variation of the average crystallite size of (1-x)BFO-xGM for $0.0 \leq x \leq 0.2$ estimated from BREADTH package, **(b)** TEM micrograph for $x = 0.2$ (Inset- SAED of $x = 0.2$).

The GM substitution effect on surface morphology and shape of the grains were observed by FESEM analyses. The FESEM micrographs of (1-*x*)BFO-*x*GM system, for $x = 0.0$, $x = 0.1$ and $x = 0.2$ are displayed in Fig. 5.4. Pure $BiFeO_3$ (*i.e.,* $x = 0.0$) shows non uniform grain size distribution with well separated grain boundaries. FESEM micrographs clearly indicate that the average grain size decreases with increasing composition. The SEM micrographs show the polycrystalline nature of microstructure with densely packed grains.

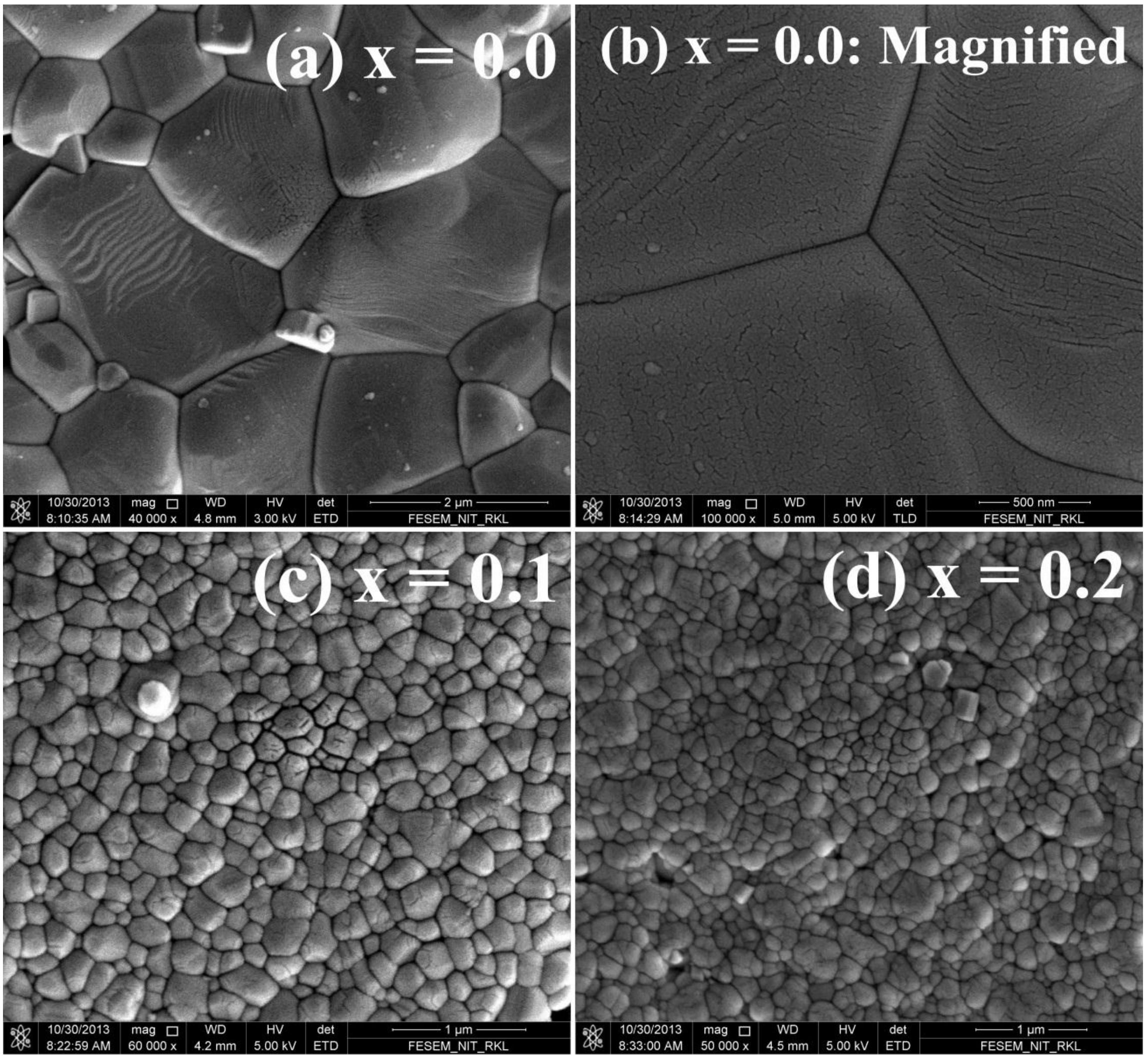

Figure 5.4 FESEM micrographs of (1-*x*)BFO-*x*GM system, for **(a)** $x = 0.0$, **(b)** $x = 0.0$: Magnified Scale, **(c)** $x = 0.1$, **(d)** $x = 0.2$.

5.3.2 Dielectric Properties

Figure 5.5(a) shows the dielectric permittivity as a function of temperature of the solid solution (1-x)BFO-xGM for $0.0 \leq x \leq 0.2$ at 1 MHz. Previously we have mentioned in Chapter-3 that for $x = 0.0$, two anomalies around 215 °C and 364 °C were noticed in temperature dependent dielectric study. The appearance of the anomaly at 215 °C can be explained by the Landau-Devonshire theory of phase transition which could due to the destruction of space modulated spin structure below the magnetic ordering of BFO or could be due to higher order magnetoelectric coupling coefficients [20-22]. The anomaly at 364 °C corresponds to antiferromagnetic phase transition temperature of BFO [13]. It is observed that with increase in composition anomaly at T_N gradually decreases monotonically up to $x = 0.15$ and slightly increases for $x = 0.2$. From structural studies, we also observed an increase in lattice strain and a decrease in crystallographic parameter "s-t" with composition which further supports the present decrease in magnetic ordering temperature T_N [13]. Both the anomalies are (*i.e.,* T_{ME} and T_N) merge at a higher composition ranges. Figure 5.5(b) shows the temperature dependent loss tangent (tan δ) of the solid solution (1-x)BFO-xGM for $0.0 \leq x \leq 0.2$ at 1 MHz. It is observed that tan δ increases monotonically without any anomalies. Here we have presented the dielectric data sufficiently at high frequency (*i.e.,* 1 MHz) to avoid the effect of interfacial polarization which often occur at lower frequency. According to recent investigations by Catlan, a combination of magneto resistance and the Maxwell-Wagner effect can also give rise to multiferroic artifact [23]. Figs 5.5(c) and (d) show the dielectric permittivity as function of temperature for different frequencies between 10 kHz to 1 MHz for $x = 0.1$ and $x = 0.2$. It is noticed that, for $x = 0.2$ the anomaly takes place around 250 °C which corresponds magnetic ordering temperature. This anomaly indicates the signature of ME coupling in the materials. However, the temperature corresponding to the peak in Fig 5.5(d) shows substantial frequency dispersion. The peak position shifts from 150 °C at 10 Hz to 250 °C at 1 MHz upon increasing frequency and is associated with decrease in the magnitude of the dielectric permittivity. This is a typical characteristic of relaxor ferroelectric materials. Here we observed that tan δ which is the ratio between conductivity and capacitance is more than one. This signifies that most of the measured impedance is not capacitive but resistive. Therefore, we except that the relaxor characteristic is extrinsic in nature. Similar types of observation have been reported elsewhere [24].

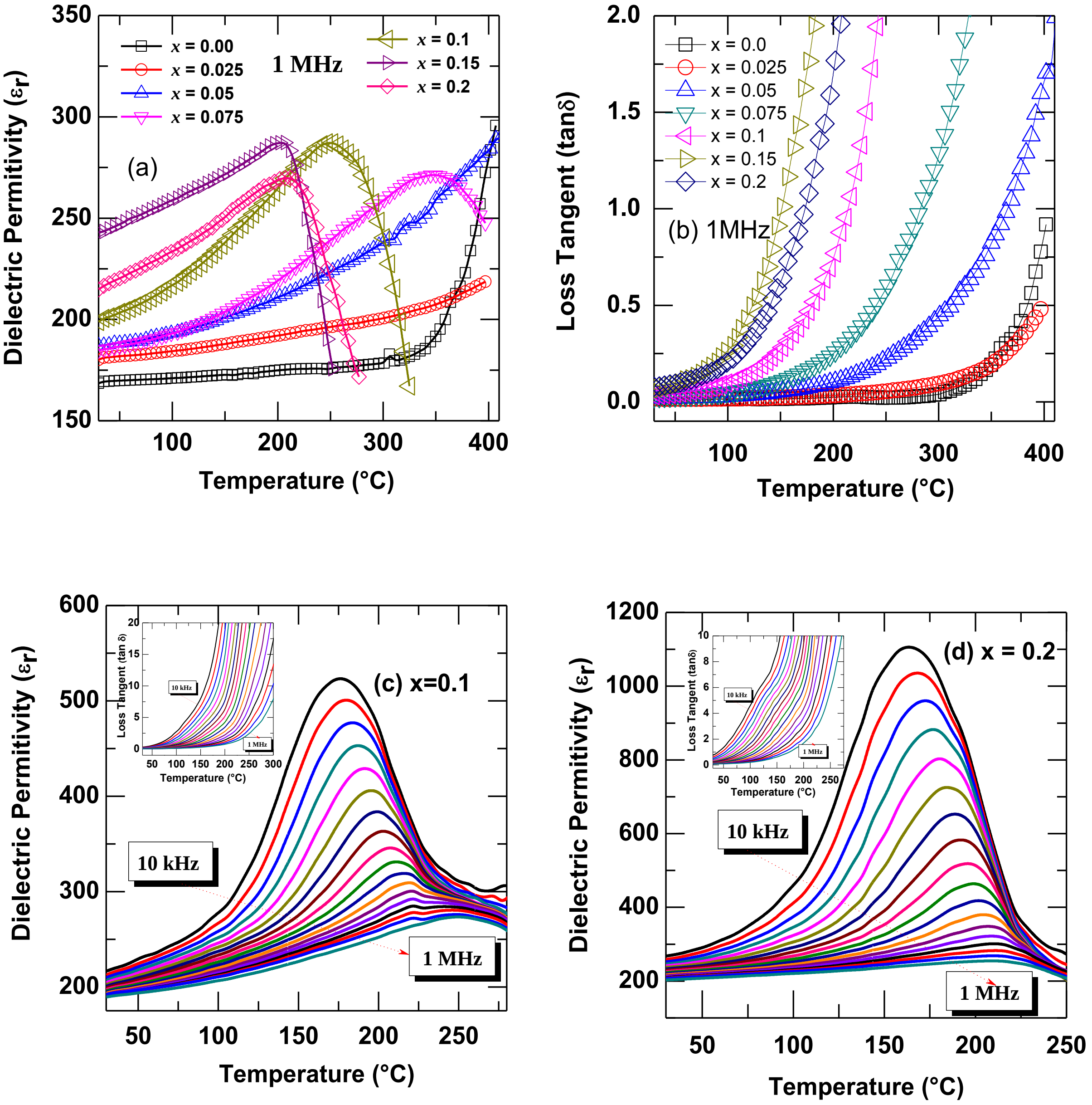

Figure 5.5 Temperature dependent dielectric parameters of (1-*x*)BFO-*x*GM for $0.0 \leq x \leq 0.2$: **(a)** ε_r vs. T at 1 MHz, **(b)** tan δ vs. T at 1 MHz. Temperature dependent dielectric permittivity at different frequencies between 10 kHz -1 MHz for **(c)** $x = 0.1$ and **(d)** $x = 0.2$ respectively. (Insets-temperature dependence of tan δ between 10 kHz -1 MHz for **(c)** $x = 0.1$ and **(d)** $x = 0.2$.)

In order to establish the intrinsic evidences of the dielectric anomaly at T_N we have carried out DSC measurements for x = 0.0, 0.05, 0.1 and 0.2 as shown in Fig 5.6. For all the compositions, DSC thermo-gram is characterized by an endothermic peak around AFM transition temperature (T_N). It is worth noting that, endothermic peak position (around T_N) in the DSC thermogram is nearly same as observed in temperature dependent dielectric studies. It is also observed form DSC plot that T_N decreases with increase in composition. Therefore, the observed of anomalies are genuine.

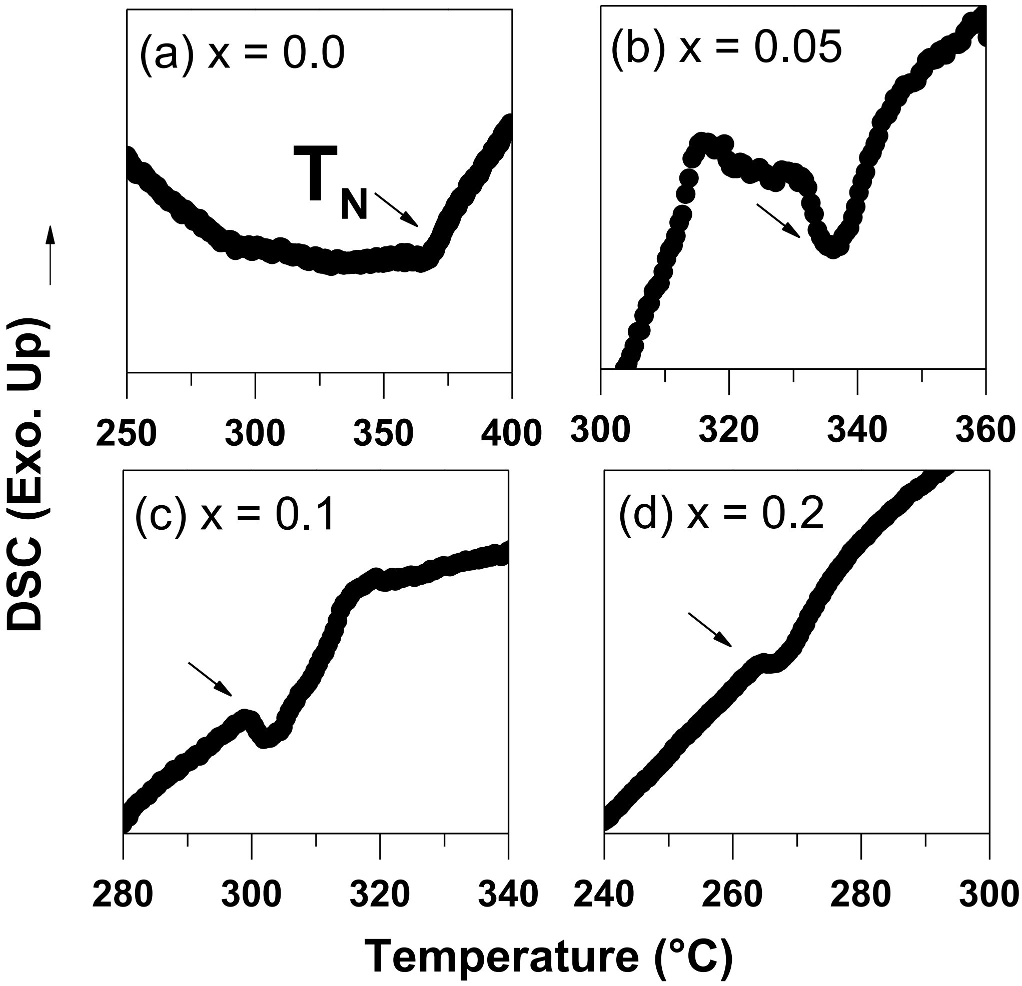

Figure 5.6 DSC thermo-grams of **(a)** x = 0.0, **(b)** x = 0.05, **(c)** x = 0.1, **(d)** x = 0.2.

5.3.3 Ferroelectric properties

Fig 5.7 shows ferroelectric hysteresis loops of (1-x)BFO-xGM for $0.0 \leq x \leq 0.2$ at RT. It was found that for $x = 0.0$, the magnitude of remnant polarization, coercive field and maximum polarization are 0.4μC/cm^2, 11.5 kV/cm and 1.3 μC/cm^2, respectively. In the present study, we could not observe saturated PE loop because of variable oxidation states of Fe (Fe^{2+} to Fe^{3+}) and low resistivity of the material [17, 25]. However, it is interesting to mention that an increase in magnitude of remnant polarization is observed on increasing composition.

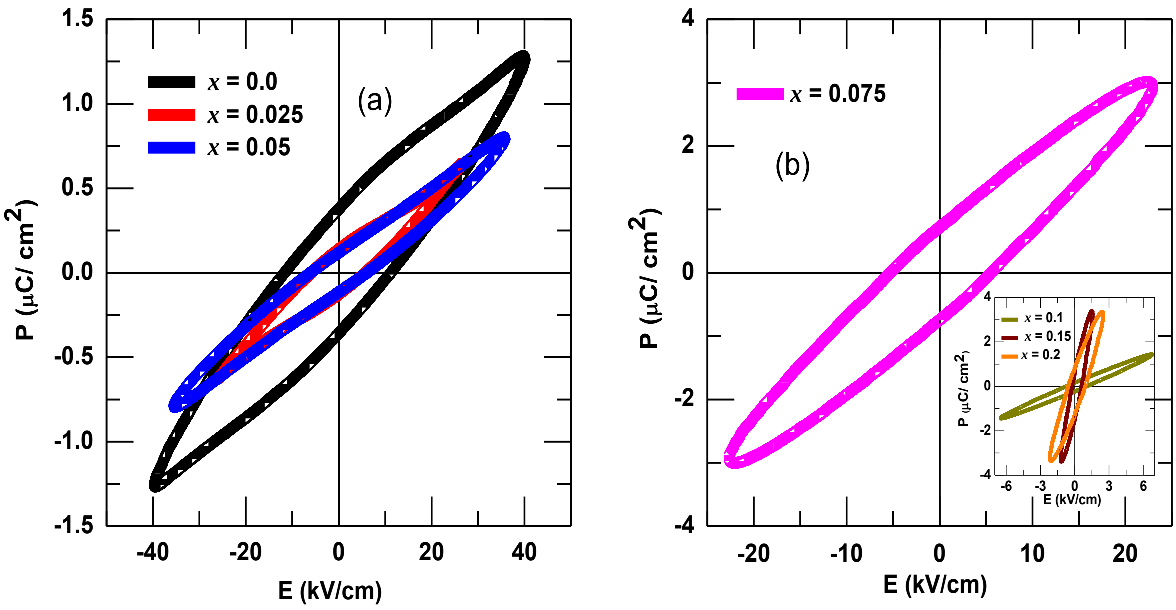

Figure 5.7 Room temperature ferroelectric hysteresis (P-E) loops of (1-x)BFO-xGM for **(a)** $0.0 \leq x \leq 0.05$, **(b)** $0.075 \leq x \leq 0.2$.

5.3.4 Complex Impedance Studies

Figure 5.8 represents the temperature dependence complex impedance spectra (*i.e.*, Nyquist plot: Imaginary Z vs. Real Z) of (1-x) BiFeO$_3$-xGdMnO$_3$ for $0.0 \leq x \leq 0.2$. We have fitted the Nyquist data using the equivalent circuit proposed in Chapter-4. It is observed that, at low temperature for all compositions Nyquist plot is linear. This signifies the insulating property of the material. With increase in temperature, the trend of forming semicircular arc is observed. The appearance of single semicircle is due to bulk properties of the material. At elevated temperatures, two overlapping semicircles are prominent with increasing compositions. The high frequency semicircular arc can be modeled by an equivalent circuit of parallel combination of a resistance (bulk resistance), capacitance (bulk capacitance) along with a constant phase element, whereas the low frequency semicircular can be modeled for

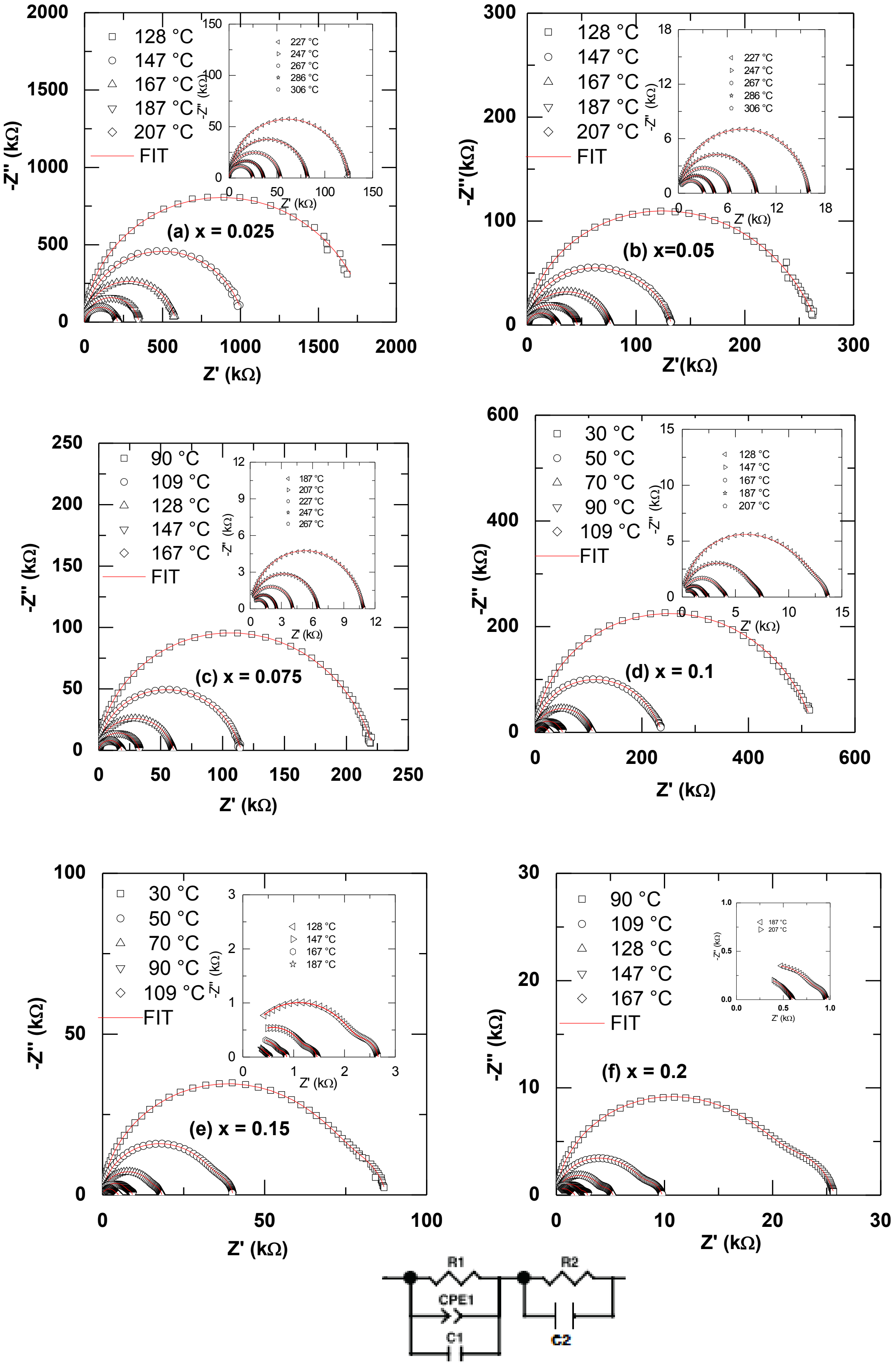

Figure 5.8 Complex impedance plot (open symbol), fitted data (solid line) of (1-*x*)BFO-*x*GM for 0.0 ≤ *x* ≤ 0.2 for different *x* and temperatures. The equivalent circuit is shown below.

parallel combination of a resistance (grain boundary resistance) and a capacitance (grain boundary capacitance). The experimental impedance data (open symbols) have been fitted (solid line) with the above proposed model by the commercially available software ZSIMP-WIN Version 3 and a close agreement between the experimental value and the fitted lines have been obtained as shown in Figure 5.8. Similar types of observations are also reported in the literature [26].

The dc conductivity due to the bulk and grain boundary contributions have been calculated from the temperature dependent resistances obtained after the Nyquist fit of the impedance data (c.f. Chapter-4). Fig 5.9(a) and (b) shows the variation of dc conductivity, σ_{dc} (due to bulk and grain boundary) as a function of $10^3/T$. It is observed that the dc conductivity decreases with increasing temperature. This indicates the negative-temperature coefficient of resistance (NTCR) characteristics which is usually observed in semiconductors [27]. The temperature dependence of conductivity obeys the Arrhenius relation $\sigma = \sigma_P \exp(-E_a/kT)$, where k is the Boltzmann constant, E_a is the activation energy and σ_P is the pre-exponential factor. We observed two different slopes in Arrhenius plot (σ_{dc} vs. $10^3/T$ (K^{-1})) suggesting two different conduction mechanisms (*i.e.*, activation energy values). The calculated activation energies for both grain and grain boundary are listed in Table 5.3.

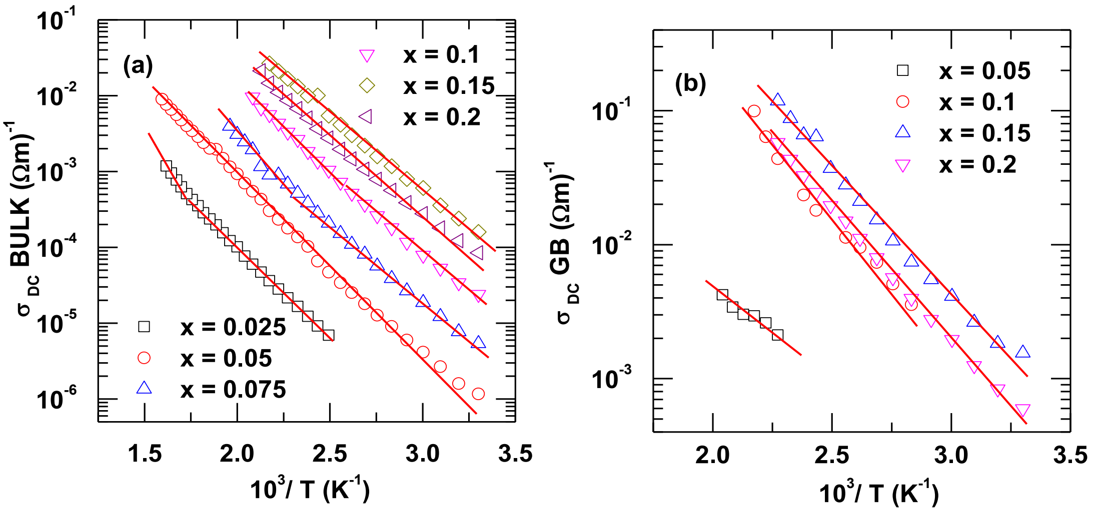

Figure 5.9 Variation in bulk and grain boundary conductivity with inverse of absolute temperature (*i.e.*, σ_{dc} *vs.* $10^3/T$) of (1-*x*)BFO-*x*GM for different *x*.

Table 5.3 Activation energy E_a (in eV) obtained from temperature dependent bulk resistance (R_B), grain boundary resistance (R_{GB}) for different compositions.

Composition (*x*)	Bulk		Grain Boundary
	Zone-I	Zone-II	
0.0	--	1.402	1.478
0.025	0.47	0.65	--
0.05	0.42	0.56	0.24
0.075	0.405	0.557	--
0.1	0.40	0.51	0.36
0.15	0.38	--	0.40
0.2	0.39	--	0.39

5.3.5 Magnetic Properties

Figs 5.10 (a) and (b) represent the RT magnetic hysteresis loops (M-H) of the solid solution of (1-x) $BiFeO_3$-$x$$GdMnO_3$ for $0.00 \leq x \leq 0.2$. As mentioned in Chapter-4, M-H loop of parent BFO shows linear character without spontaneous magnetization suggesting antiferromagnetic nature. This can be understood in the line of canted G-type antiferromagnetic spiral spin modulation in BFO [6]. On increasing composition up to $x = 0.1$, saturation magnetization and coercivity increases monotonically and attain the magnitude of 0.3 emu/gm and 600 mTesla respectively. Further increase in composition leads to enhancement in magnetization and decrease in coercivity. At $x = 0.15$ *i.e.,* after the structural phase boundary, the coercivity sharply decreases to 20 mTesla. Figure 5.10(a)-inset shows the variation of coercive field with composition x. This may be due to the paramagnetic character of $Pn2_1a$ phase at RT. The improved corecivity and magnetization could be attributed to following reasons: (a) nanoceramic synthesis and fabrication of solid solution leading to enhancement in strain and appearance of uncompensated spins due to spin cycloid modulation [6, 13, 17], (b) substitution of Gd^{3+} at Bi-site also further leads to collapse of space modulated spin structure, (c) substitution of magnetically active Mn^{3+} at Fe-site of BFO favors ferromagnetic interaction and (d) Fig 5.1 demonstrates the absence of impurity phase and suggests the intrinsic nature of magnetization of the system. To summarize, we establish that the enhancement in magnetization due to destruction of spin cycloid or structural instability.

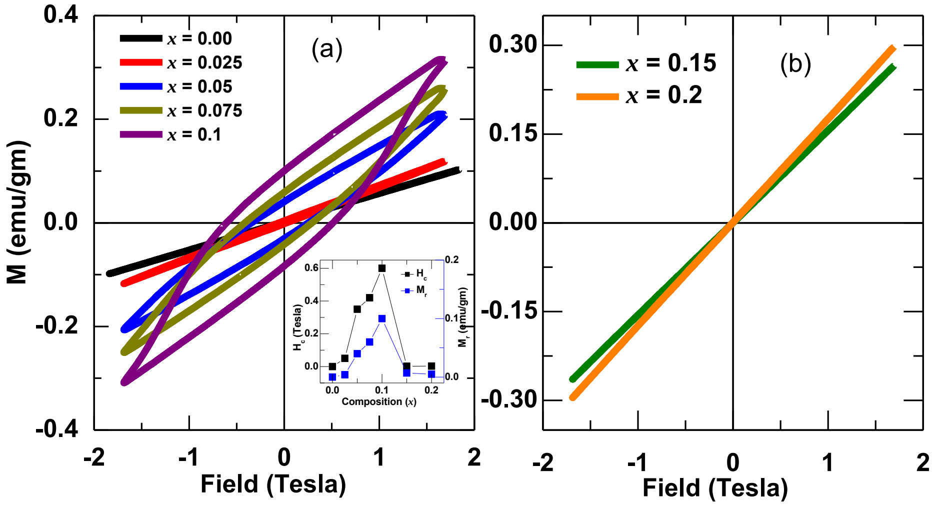

Figure 5.10 M-H hysteresis loops of (1-x)BFO-xGM for **(a)** $0.0 \leq x \leq 0.075$ (Inset shows compositional dependence of H_C and M_r), **(b)** $x = 0.15$ and $x = 0.2$ at RT.

5.3.6 Magnetoelectric Properties

In previous chapters, we have extensively discussed about the criterions for establishing the ME effect in magnetoelectrically ordered systems. These are as follows: (a) anomaly in temperature dependent dielectric permittivity at magnetic phase transition and (b) changes (increasing /decreasing monotonically) of the real part of dielectric permittivity as a function of magnetic field [28]. Fig 5.5 clearly supports the signature of first criterion. The second criterion is established as follows. Fig 5.11 shows the frequency dependencies of dielectric permittivity (ε_r), for $x = 0.05$, $x = 0.1$ and $x = 0.15$ at RT for different magnetic field ($0 \leq H \leq 2$ Tesla). It is also found that the dielectric permittivity decreases with an increase in the applied magnetic field throughout the frequency range of investigation. When magnetic field is applied to a magneto-electrically ordered system, strain is induced. This strain in turn induces a stress on the piezoelectric (for all ferroelectrics are piezoelectric), which generates the electric field and controls the polarization. Ultimately, change in dielectric permittivity occurs with application of magnetic field [29]. The magnitude of enhancement has been calculated by using the formula $MC\% = \frac{\varepsilon\,(H,T) - \varepsilon(0,T)}{\varepsilon(0,T)}$ and shown in Fig 5.11 (d) [30]. We observed an enhanced ME coefficient 8% at MPB $x = 0.15$ for 2 Tesla. The enhanced ME effect can be explained as the suppression of spin cycloid and MPB effect of the $BiFeO_3$-$GdMnO_3$ multiferroic system.

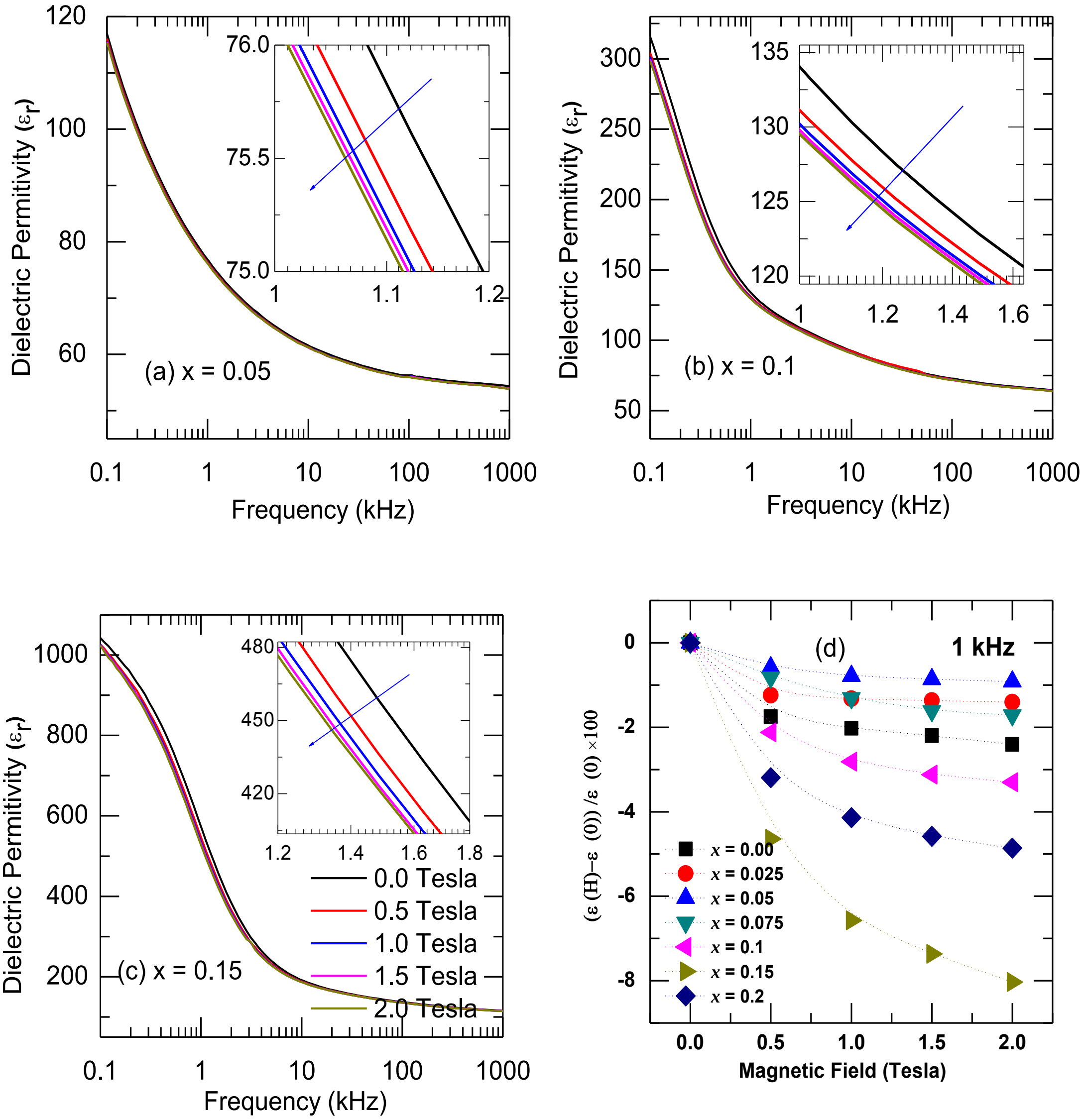

Figure 5.11 Frequency dependent ε_r for **(a)** x =0.05, **(b)** x = 0.1 and **(c)** x = 0.2 at different applied magnetic fields (0.0 ≤ H ≤ 2 Tesla: ΔH = 0.5 Tesla) (Inset shows the magnification in frequency dependence of ε_r and the arrow indicates increasing H). **(d)** Magnetic field dependent MC% of (1-x)BFO-xGM for 0.0 ≤ x ≤ 0.2 at 1 kHz.

5.3.7 Magneto-Impedance Studies

Fig 5.12 shows the RT Nyquist Plot of (1-x)BFO-xGM for x = 0.05, 0.1, 0.15 and 0.2 at different magnetic field (0 ≤ H ≤ 2 Tesla). For 0.025 ≤ x ≤ 0.075, we observed the appearance of single semicircular arcs corresponding to bulk property of the material [26-27]. But for x =0.15, x =0.1 and x = 0.2, the impedance spectra exhibited two overlapping semicircular arcs.

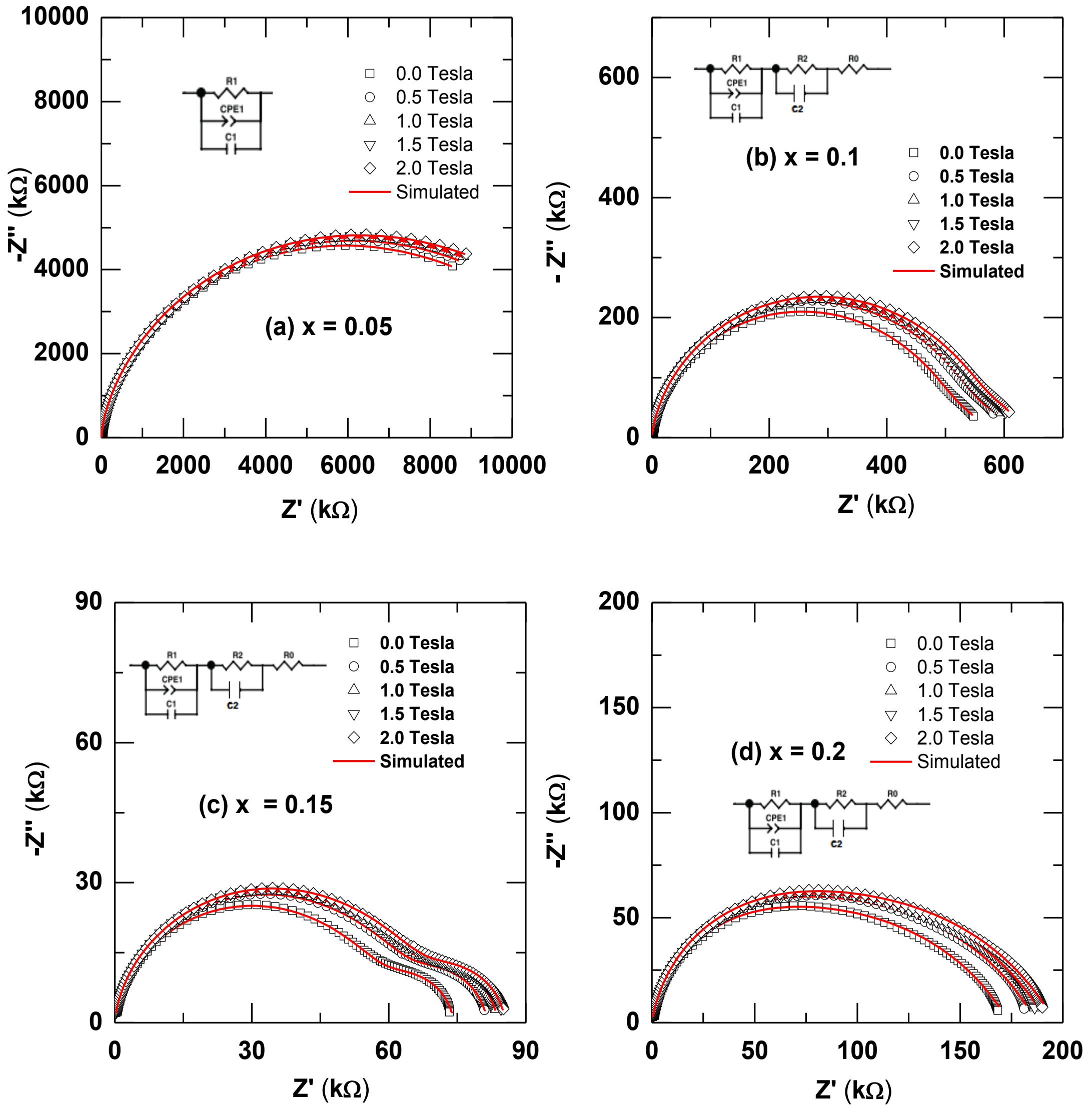

Figure 5.12(a)-(d) Magnetic field dependent complex impedance plot (open symbol), fitted data (solid line) of (1-x)BFO-xGM for $0.0 \leq x \leq 0.2$ at RT (Inset shows the equivalent circuit).

The high frequency semicircle relates to bulk contribution whereas low frequency is attributed to grain boundary property. We have fitted the magnetic field dependent Nyquist plot using the equivalent circuit as shown in inset of Fig 5.12. A close agreement between the experimental and the theoretical values has been obtained. The value of bulk capacitance and resistance found from the Niquist fittings are listed in Table 5.4 and 5.5. It is observed that bulk capacitance decreases on increasing magnetic field where as bulk resistance increases. For all composition we found similar nature of fall in dielectric permittivity as a function of magnetic field. Related types of reports have been witnessed in literatures [28].

Table 5.4 Bulk capacitance obtained from fitting of magnetic field dependent complex impedance plot at RT for different value of *x*.

Bulk Capacitance (10^{-11}) (F)							
Field (T)	$x = 0.0$	$x = 0.025$	$x = 0.05$	$x = 0.075$	$x = 0.1$	$x = 0.15$	$x = 0.2$
0	4.174	2.783	3.578	3.258	3.544	6.305	5.788
0.5	4.145	2.734	3.32	3.188	3.49	6.286	5.536
1	4.152	2.733	3.319	3.187	3.4	6.193	5.562
1.5	4.152	2.734	3.32	3.186	3.38	6.184	5.559
2	4.152	2.732	3.316	3.178	3.4	6.188	5.545

Table 5.5 Bulk resistance obtained from fitting of magnetic field dependent complex impedance plot at RT for different value of *x*.

Bulk Resistance (Ohm)							
Field (T)	$x = 0.0$ 10^6	$x = 0.025$ 10^7	$x = 0.05$ 10^7	$x = 0.075$ 10^6	$x = 0.1$ 10^5	$x = 0.15$ 10^4	$x = 0.2$ 10^5
0	8.6176	8.238	1.226	2.522	5.415	6.240	1.307
0.5	9.3114	8.812	1.358	2.671	5.761	6.841	1.394
1	13.469	8.897	1.379	2.749	5.834	7.021	1.428
1.5	14.609	8.978	1.387	2.792	5.892	7.106	1.446
2	15.589	9.007	1.395	2.819	5.965	7.159	1.459

5.4 Conclusions

To conclude, nanoceramic solid solution of (1-*x*)BFO-*x*GM, for $0.0 \leq x \leq 0.2$ were prepared by auto-combustion method. The fabrication of solid solution of BFO with GM found to induce a compositional driven structural phase transition from $R3c$ to $R3c+Pn2_1a$ at $x = 0.1$. For $x = 0.2$, the TEM characterization reveals the average crystallite size to be 30 nm. FESEM micrographs indicate a decrease in grain size on increasing composition. Dielectric study displayed two anomalies at 215 °C and 364 °C (T_N) for $x = 0.0$ corresponding to ME effect in the material. The temperature dependent dielectric studies suggest the magnetic ordering temperature T_N decreases on increasing compositions. DSC thermogram in corroboration with the dielectric and structural studies reveals the magnetic phase transition temperature. Enhanced magnetization properties were observed with increasing compositions and can be explained as suppression of space modulated spiral spin structure. Improved polarization hysteresis loops were also observed for higher compositions. The d. c.

conductivity (grain and grain boundary) decreased with increasing temperature and obeys Arrhenius behavior. Real part of dielectric permittivity decreases with increasing magnetic field. At RT, for 2 Tesla, 8% enhanced magneto-capacitance was observed for $x = 0.15$ composition. Magneto-impedance spectroscopy provided the signature of intrinsic magnetoelectric coupling in the material.

5.5 References

[1] K.F. Wang, J.M. Liu, Z.F. Ren, Adv. Phys**. 58,** 321 (2009).

[2] K. Noda, S. Nakamura, J. Nagayama and H. Kuwahara, J. Appl. Phys., **97**, 10C103 (2005)

[3] A. Pimenov, T. Rudolf, F. Mayr, A. Loidl, A. A. Mukhin, and A. M. Balbashov, Phys. Rev. B **74**, 100403(R) (2006)

[4] S. R. Das, R. N. P. Choudhary, P. Bhattacharya, R. S. Katiyar, P. Dutta, A. Manivannan, and M. S. Seehra, J. Appl. Phys. **101**, 034104 (2007).

[5] C.-H. Yang, T.Y. Koo, Y.H. Jeong, Solid State Communications **134**, 299 (2005).

[6] T. Park, G. C. Papaefthymiou, A. J. Viescas, A. R. Moodenbaugh, and S. S. Wong, Nano Lett., **7**, 766 (2007).

[7] S. M. Selbach, T. Tybell, M. Einarsrud, and T. Grande, Chem. Mater., **19**, 6478 (2007).

[8] S. N. Tripathy, B.G. Mishra, M. M. Shirolkar, S. Sen, S. R. Das, D. B. Janes, D. K. Pradhan, Mater. Chem. Phys. **141**, 423 (2013).

[9] S.R. Jain, K.C. Adiga, V.R. Pai Verneker, Combust. Flame **40**, 71 (1981).

[10] S. N. Tripathy, K. K. Mishra, S. Sen, B. G. Mishra, D. K. Pradhan, R.Palai, and D. K. Pradhan, J. Appl. Phys. **114**, 144104 (2013).

[11] J. Rodriguez-Carvajal, Physica B **192**, 55 (1993).

[12] H. D. Megaw and C. N. W. Darlington, Acta Cryst. **A31**, 161 (1975).

[13] S. M. Selbach, T. Tybell, M. Einarsrud, and T. Grande, Adv. Mater., **20**, 3692 (2008).

[14] G. Catalan and J. F. Scott, Adv. Mater. **21**, 2463 (2009).

[15] V.A. Khomchenko, V.V. Shvartsman , P. Borisov, W. Kleemann ,D.A. Kiselev , I.K. Bdikin , J.M. Vieira, A.L. Kholkin, Acta Materialia **57**, 5137 (2009).

[16] V. A. Khomchenko,I. O. Troyanchuk, M. I. Kovetskaya, and J. A. Paixao, J. Appl. Phys., **111**, 014110 (2012).

[17] G. Catalan, K. Sardar, N.S. Church, J. F. Scott, R. J. Harrison, and S. A. T. Redfern, Phys. Rev. B. **79**, 212415 (2009).

[18] A. G. Gavriliuk *et al.*, Phys. Rev. B **77**, 155112 (2008).

[19] D. Balzar, J. Appl. Crystallogr. **28**, 244(1995).

[20] G. L. Yuan and S. Or, J. Appl. Phys. **100,** 024109 (2006).

[21] L. Benguigui, Solid State Commun. **11**, 825 (1972).

[22] V. R. Palkar, J. John, and R. Pinto, Appl. Phys. Lett. **80**, 1628 (2002).

[23] G. Catalan, Appl. Phys. Lett., **88**, 102902 (2006).

[24] A. Singh, V. Pandey, R. K. Kotnala, and D. Pandey, Phys. Rev. Lett., **101**, 247602 (2008).

[25] R. Palai, R.S. Katiyar, H. Schmid, P. Tissot, S.J. Clark, J. Robertson, S.A.T. Redfern, G. Catalan and J.F. Scott, Phys. Rev. B **77,** 014110 (2008).

[26] D. C. Sinclair and A. R. West, J. Appl. Phys. **66**, 3850 (1989).

[27] D. K. Pradhan, R. N. P. Choudhary, C. Rinaldi and R. S. Katiyar J. Appl. Phys. **106** , 024102 (2009).

[28] R. Schmidt, J. Ventura, E. Langenberg, N. M. Nemes, C. Munuera, M. Varela, M. Hernandez, C. Leon, and J. Santamaria , Phys. Rev. B **86**, 035113 (2012).

[29] V.R. Palkar, D. C. Kundaliya, S. C. Malik and S. Bhattacharya, Phys. Rev. B **69**, 212102 (2004).

[30] P. Uniyal, K. L. Yadav, J. Phys.: Condens. Matter. **21,** 405901 (2009).

Chapter-6

Structural and Magnetoelectric Properties of Multiferroic $BiFeO_3$-$DyMnO_3$ Nanoceramics

Part of the content of this chapter has been published in the journal "**Journal of Applied Physics".** Satya N. Tripathy , D. K. Pradhan , K. K. Mishra , S Sen , R. Palai, M. Paluch , J. F. Scott , R. S. Katiyar , Dillip K. Pradhan, **J. Appl. Phys.117, 144103 (2015).**

Chapter-6 describes the structural and magnetoelectric properties of nanoceramic solid solution of (1-x)$BiFeO_3$-$x$$DyMnO_3$ (BFO-DM) for $0.0 \leq x \leq 0.2$ synthesized by auto-combustion method. The synthesized materials have been characterized and analyzed using X-ray diffraction, field emission scanning electron microscopy, temperature dependent spectroscopy, ferroelectric polarization (P-E loop), magnetic hysteresis (M-H loop), magneto-dielectric and magneto-impedance measurements with wide range of experimental conditions.

6.1 Introductory Remarks

Chemical substitutions have been successfully established as an appropriate methodology to improve the multiferroic properties of BFO [1-4]. This may be due to the possibility of driving the crystal symmetry of BFO near to a morphotropic phase boundary (MPB) and improving the piezoelectric, magnetic and magnetoelectric properties [1-4]. In the present chapter, we have presented a suitable approach of chemical modification to improve the magnetoelectric coupling of BFO by fabrication of solid solutions with $DyMnO_3$ (DM).

The rare earth manganite $DyMnO_3$ is a Type-II multiferroic material and stabilizes either in orthorhombic (*Pnma*) or hexagonal ($P6_3cm$) crystal structure at room temperature [3-4]. The antiferromagnetic transition temperature T_N of orthorhombic phase is reported to be around 40 K and ferroelectricity (T_C ~ 10 K) appears from the AFM ordering. $DyMnO_3$ in hexagonal phase has T_N around 70 K and their FE arise from a structural distortion having T_C much higher than 300 K with high polarization [3-4]. Therefore, it is expected that the synthesis of (1-x)$BiFeO_3$–x $DyMnO_3$ nanoceramic solid solution could bring down the magnetic ordering temperature of the solid solution towards RT [1-4]. The ionic radii of Bi^{3+} and Dy^{3+} are 1.17 Å and 1.07 Å for eight coordinated system, whereas the ionic radii of Fe^{3+} and Mn^{3+} are identical (0.645 Å) for high spin six coordination. The substitution of Dy^{3+} at Bi-site is also probable to switching off the lone pair activity of Bi leading to shift the FE transition towards RT [1-4].

In the present work, we have synthesized nanoceramic solid solution of (1-x) $BiFeO_3$–$x$$DyMnO_3$. The structural, microstructural, temperature dependent dielectric, ferroelectric, magnetic and magnetoelectric properties have been extensively investigated. Emphasis has been given to understand the importance of fabrication solid solution of BFO with DM on the possibility of the compositional driven structural phase transition and its relationship with the magnetoelectric (ME) properties.

5.2 Experimental Procedure

Nanoceramic solid solutions of (1-*x*)$BiFeO_3$-*x*$DyMnO_3$ (BFO-DY) for $0.0 \leq x \leq 0.2$ were synthesized using auto-combustion technique. High purity (99.9%) grade chemicals of $Fe(NO_3)_3.9H_2O$, $Bi(NO_3)_3.5H_2O$, Dy_2O_3, $(CH_3COO)_2Mn{\cdot}4H_2O$ were used as oxidizers, while urea was taken as fuel during synthesis. The details of the synthesis procedure have been discussed in Chapter-3 (Refs: 5-6). For pure BFO (*i.e.*, $x = 0.0$), the combustion residue was calcined at an optimized temperature of 550 °C for 3 h in air atmosphere. The compounds with compositional range, $0.025 \leq x \leq 0.1$ were calcined at 700 °C while those for $x = 0.15$ and 0.2 were calcined at 750 °C. The calcined powders were compacted into cylindrical pellets by hydraulic press with pressure 8×10^7 $kg.m^{-2}$ using polyvinyl alcohol (PVA) as binder. For composition $0.025 \leq x \leq 0.1$ and $0.15 \leq x \leq 0.2$, the pellets were sintered at 750 °C and 780 °C respectively. All the experimental conditions for characterization of the synthesized materials are same as discussed in Chapter-3 and 4.

6.3 Results and Discussion

6.3.1 Structural and Microstructural Properties

Figs 6.1(a) and (b) display XRD pattern of the solid solution of (1-*x*) BFO-*x* DM for $0.0 \leq x \leq 0.2$ at RT. Crystallographic analyses of the XRD pattern were carried out by Rietveld refinement technique using FULLPROF package [7]. Details of the refinement procedure and conditions have been discussed in Chapter-4. The experimental data points are represented as symbol (+) and theoretical data points are shown as solid line as shown in Fig 6.1(a). The difference between observed and theoretical pattern and Bragg positions are shown at the bottom of the plot. The rhombohedral crystal structure in *R3c* space group for $x = 0.0$ (*i.e.*, pure $BiFeO_3$) was used for Rietveld refinement and the best match (goodness of fit: $R_p = 9.8\%$, $R_{wp} = 15.9\%$, $\chi^2 = 1.59$) is obtained between calculated and observed diffraction spectra. There are three ions (Bi^{3+}/Dy^{3+}, Fe^{3+}/Mn^{3+}, and O^{2-}) in the asymmetric unit of the rhombohedral perovskite structure. The cations Bi^{3+}/Dy^{3+} and Fe^{3+}/Mn^{3+} ions occupy the 6(*a*) Wyckoff site at (0, 0, z) while O^{2-} anion at the 18(*b*) sites at (*x*, *y*, *z*) [6]. The refined lattice parameters and volume of primitive unit cell of BFO are, *a* = 5.5779 (09) Å, *c* = 13.8710 (23) Å and 62.293 $Å^3$, respectively which are

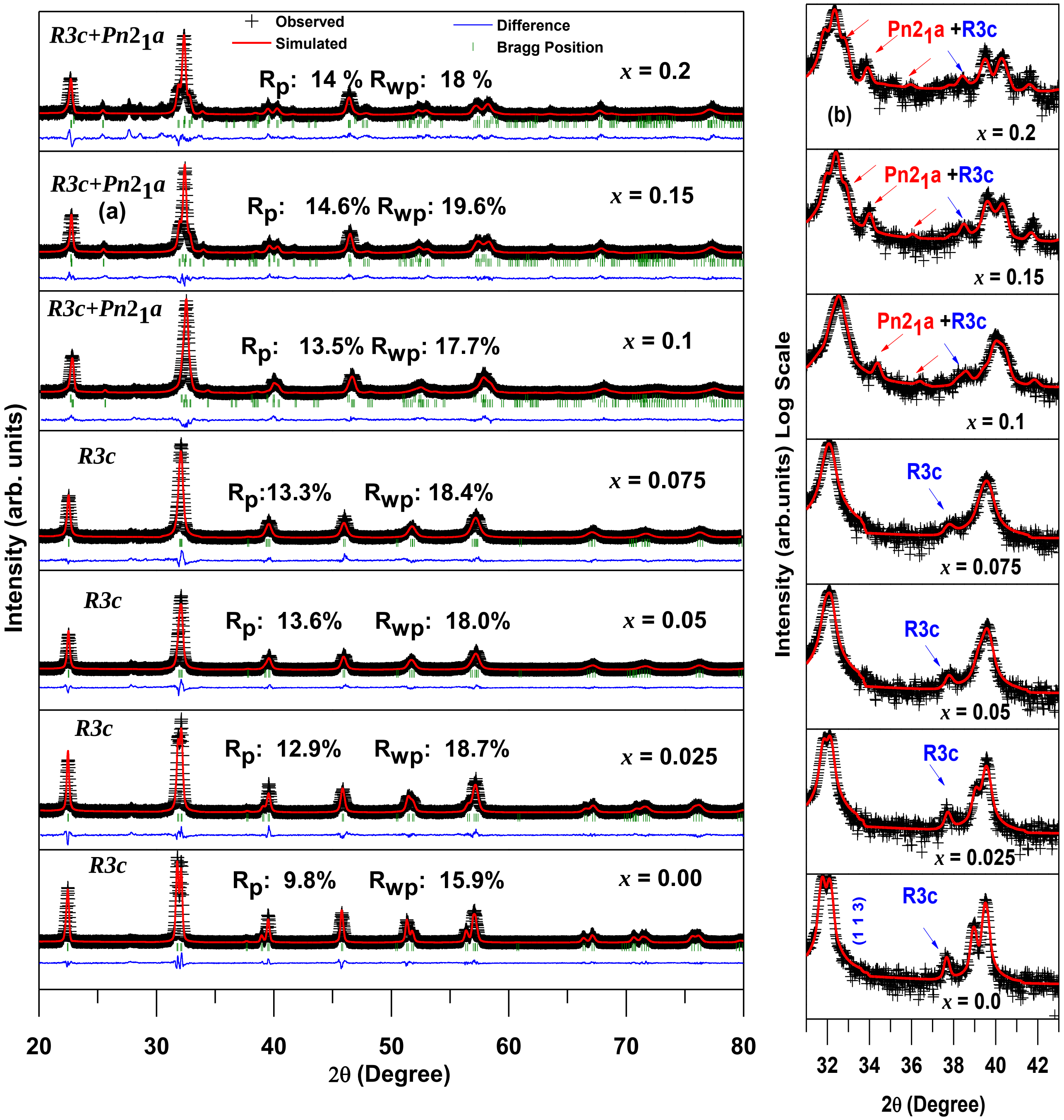

Figure 6.1(a) Rietveld refinement of X-ray diffraction patterns of the solid-solution of (1-x)BFO-xDM for $0.0 \leq x \leq 0.2$ at RT (linear scale), **(b)** the peak expanded in the 2θ regions $30\,° \leq 2\theta \leq 40°$ signifying cross over from *R3c* to *R3c*+*Pn2₁a* (log scale).

similar to reported values [8]. It is observed that with increase in DM content up to $x = 0.075$, XRD patterns are similar to the parent $BiFeO_3$ (*R3c* space group). This is evidenced by existence of characteristic super lattice reflection (113) around ≈ 38 degree of rhombohedral *R3c* phase as shown in Fig 6.1(b). Therefore, we have selected the *R3c* space group to refine the crystal structure up to $x = 0.075$. The intensity magnitude of the super lattice peak (113) reflection decreases with increase in composition. It can be mentioned here that the (113) reflection arises from anti-ferrodistortive tilting of the octahedra which gives rise to new oxygen planes and hence a low intensity peak is observed [9-10]. With increase in DM content, there is a splitting in the reflections, change in peak position, peak intensity and peak broadening in the diffraction pattern. It was observed that for $x = 0.2$, the XRD pattern is similar to $RMnO_3$/$RFeO_3$ (R: La^{3+}, Sm^{3+}, Gd^{3+}, Nd^{3+}, Dy^{3+}) which is described by *Pnma*/*Pbnm* space group. It is to be noted that *Pnma*/*Pbnm* structure is commonly observed in perovskites, RE ortho-ferrites, manganites and also as the high temperature crystal structure of $BiFeO_3$ [11-12]. The polar $Pn2_1a$ space group is a subgroup of nonpolar *Pnma* space group. A superposition of two crystallographic phases *i.e.*, rhombohedral and orthorhombic phases after $x = 0.075$ composition is supported by (i) appearance of reflection around ≈ 25 degree, (ii) splitting of reflection around ≈ 32 degree in to four peaks and (iii) presence of super reflection (1 1 3) as shown in Fig 6.1(b). Therefore Rietveld fittings are under taken using dual phase model ($R3c$+$Pn2_1a$) for composition range $0.1 \leq x \leq 0.2$ and observed satisfactory fit. Similar type of dual phase space group is reported on A-site modified BFO [13-14]. For $x = 0.1$ composition, it is found that 85% of rhombohedral *R3c* phase and remaining 15% that of orthorhombic $Pn2_1a$ phase. The appearance of orthorhombic symmetry or change of crystal structure starts at $x = 0.1$ and is the structural phase boundary of rhombohedral and orthorhombic phase. It was also found that $x = 0.15$, contains 45.35 % of *R3c* and 54.66 % of $Pn2_1a$ phase and $x = 0.2$, contains 25.80 % of *R3c* and 74.20 % of $Pn2_1a$ phase. The transition from rhombohedral to rhombohedral *plus* orthorhombic is very plausible. Therefore, for $x \geq 0.1$, coexistence of phases with increase in orthorhombic phase fraction is evident. The explanations for structural transformation are as follows: (a) Mn^{3+} weakly destabilizes *R3c* as compared to Fe^{3+}, and Dy^{3+} strongly destabilizes *R3c* phase, (b) substitution of Dy^{3+} at Bi-site switch off the stereochemically active lone pair of Bi^{3+} (c) chemical pressure of Dy^{3+} is much smaller than Bi^{3+}. The lattice parameters, Wyckoff notations and atomic positions for the coexisting *R3c* and $Pn2_1a$ space groups are represented in Table 6.1 and Table 6.2.

Table 6.1 Lattice parameters estimated from Rietveld refinement of (1-*x*)BFO-*x*DM for $0.0 \leq x \leq 0.2$ along with good-ness of fitting. The standard deviations are in parenthesis.

Composition (*x*)	Space group	Lattice Parameters (Å) a	b	c	χ^2
0.0	*R3c*	5.5779 (08)	5.5779 (08)	13.8711 (21)	1.59
0.025	*R3c*	5.5717 (11)	5.5717(11)	13.8303 (28)	1.17
0.05	*R3c*	5.5697(15)	5.5697 (15)	13.7698 (37)	1.55
0.075	*R3c*	5.5723(03)	5.5723 (03)	13.7319 (17)	1.40
0.1	*R3c* + $Pn2_1a$	5.5199 (08) 5.5356 (09)	5.5199(08) 7.7883 (11)	13.6620 (25) 5.44816 (07)	1.12
0.15	*R3c* + $Pn2_1a$	5.5101 (13) 5.6008 (09)	5.5101(13) 7.8113 (14)	13.6763 (46) 5.45105 (08)	1.11
0.2	*R3c* + $Pn2_1a$	5.4291 (12) 5.6165 (05)	5.4291(12) 7.8242 (09)	13.6647 (32) 5.45943 (06)	1.87

Table 6.2 Wyckoff notation and atomic positions of (1-*x*)BFO-*x*DM for $0.0 \leq x \leq 0.2$ used in Rietveld refinement procedure.

Composition (*x*)	Space group	Atom	Site	*x*	*y*	*z*
$0 \leq x \leq 0.075$	*R3c*	Bi/ Dy	6*a*	0.0000	0.0000	0.0000
		Fe/ Mn	6*a*	0.0000	0.0000	0.2212
		O	18*b*	0.4430	0.0120	0.9543
$0.1 \leq x \leq 0.2$	*R3c* +$Pn2_1a$	Bi/ Dy	6*a*	0.0000	0.0000	0.0000
		Fe/ Mn	6*a*	0.0000	0.0000	0.2212
		O	18*b*	0.4430	0.0120	0.9543
		Bi/ Dy	4*a*	0.0412	0.2758	0.9950
		Fe/ Mn	4*a*	0.4860	0.0182	0.0320
		O	4*a*	0.4908	0.3168	0.1416
		O	4*a*	0.2234	-0.0034	0.7778
		O	4*a*	0.7143	0.9491	0.2967

respectively. Beside this, no trace of impurity phases (*e.g.* $Bi_2Fe_4O_9$, $Bi_{25}FeO_{39}$ *etc.*) were detected up to $x = 0.15$. However for $x = 0.2$, presence of a minimal impurity phase could not be ruled out.

In order to probe the compositional driven structural phase transition as a function of composition, the normalized lattice parameters (*i.e.*, $a_H^N = a_{Hex}/\sqrt{2}$, $c_H^N = c_{Hex}/\sqrt{12}$) and ($a_O^N \approx b_O^N \approx (2)^{-1/2} a_{orth}$, $c_O^N = c_{orth}/2$) of *R3c* and *Pn2₁a* respectively are shown in Fig 6.2 (a). Similar type of normalization technique has also been adopted by Selbach *et al.* [9-10]. This normalization technique brings the unit cell parameters of both rhombohedral and orthorhombic space groups to similar magnitude for better exploration. With increase in composition, normalized lattice parameter of *R3c* phase decreases and approaches to similar magnitude for $x = 0.1$. After the structural phase boundary $x = 0.1$, normalized lattice parameters of *R3c* phase decreases sharply, whereas *Pn2₁a* phases increases with increase in composition representing a stronger phase. We observe that the compositional driven structural phase transition is accompanied by sharp change in unit cell parameters (*i.e.*, volume contraction: abruptly from one constant value to another) at $x = 0.1$. It can be pointed here that below and above the threshold composition $x = 0.1$, the primitive volume shows approximately linear character [13-14]. This signifies the uniform distribution of dopants (Dy^{3+} and Mn^{3+}) throughout the lattice.

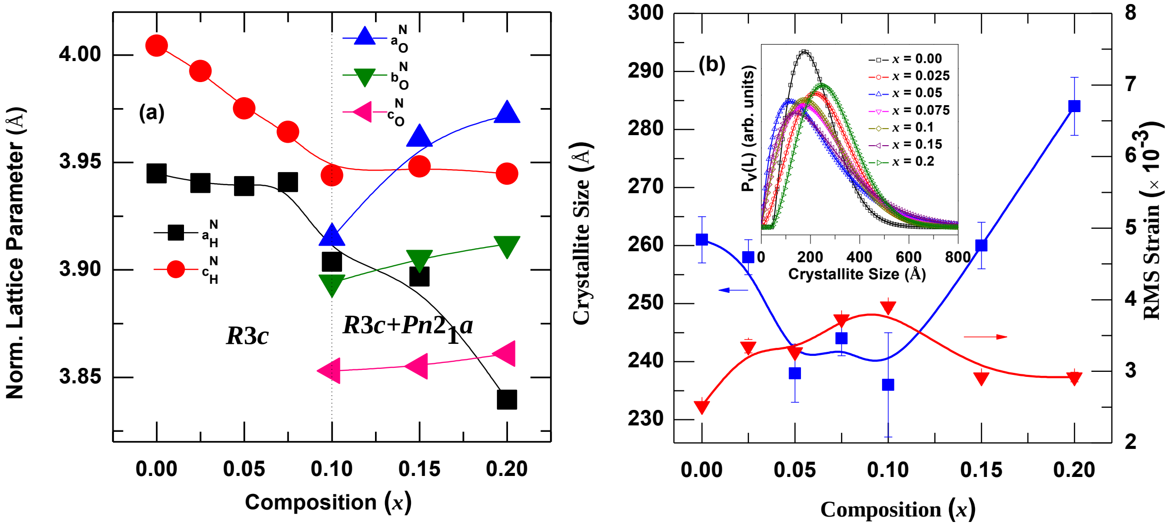

Figure 6.2 (a) Compositional dependence of normalized lattice parameters of *R3c* phase (*i.e.*, $a_H^N = a_{Hex}/\sqrt{2}$, $c_H^N = c_{Hex}/\sqrt{12}$) and *Pn*2₁*a* phase (*i.e.*, $a_O^N \approx b_O^N \approx (2)^{-1/2} a_{orth}$, $c_O^N = c_{orth}/2$). **(b)** Crystallite size and r. m. s strain estimated from Double-Voigt method as a function of x (Inset- Variation of $P_v(L)$ with composition).

The average crystallite sizes and lattice strain of (1-x) BFO-xDM system, for $0.00 \leq x \leq 0.2$ as a function of composition is shown in Fig 6.2 (b). In this context, we have adopted Fourier X-ray line profile analysis (XLPA) based on Double-Voigt method using program BREADTH [15]. Details of XLPA procedure are available in Chapter-2. For $x = 0.00$ volume-weighted domain size $<D_V>$ ranges from 100 Å to 500 Å with maxima around 260 Å and distribution function, $P_V(L)$ become narrower with increasing composition. This represents the uniform nature of distribution of crystallite sizes. The average crystallite size varies in the range 200 Å to 300 Å for BFO-DM system.

The DM modification effect on surface morphology and shape of the grains were observed by FESEM analyses. The FESEM micrographs of (1-x) $BiFeO_3$-$x$$DyMnO_3$ system for $x = 0.00$, 0.5, 0.1, 0.2 are displayed in Fig 6.3. Pure $BiFeO_3$ ($x = 0.0$) shows non uniform grain size distribution with average size around 2 μm. It can be noticed that with increase in x, average grain size decreases. The grains and grain boundaries are well distinct in all compositions.

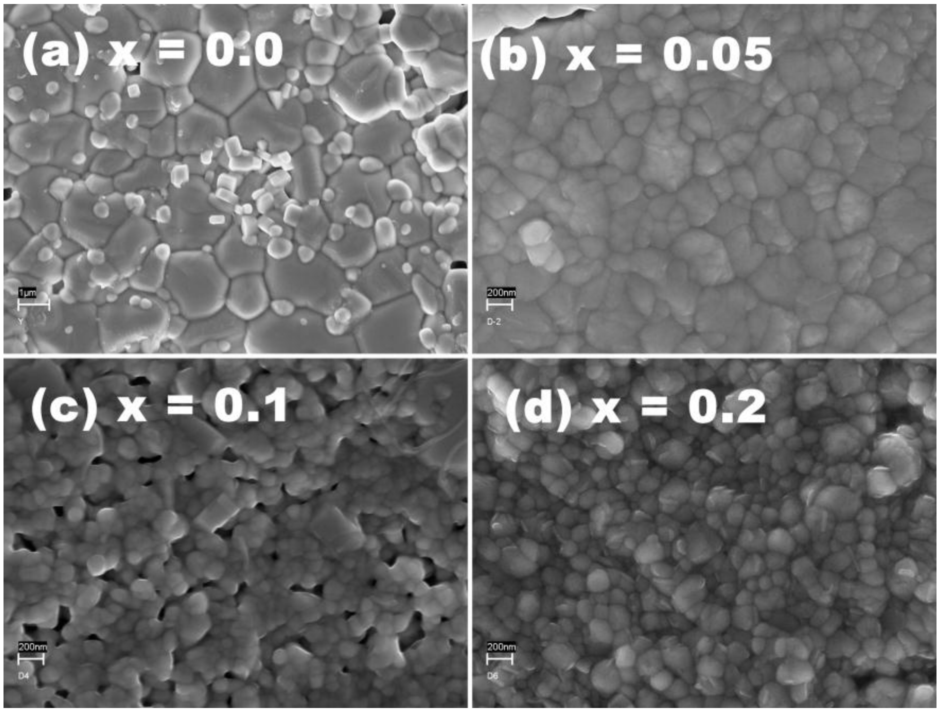

Figure 6.3 FESEM micrographs of (1-x)BFO-xDM system, for **(a)** $x = 0.0$, **(b)** $x = 0.05$ **(c)** $x = 0.1$, **(d)** $x = 0.2$.

6.3.2 Dielectric Properties

Figs 6.4(a) and (b) depict the temperature dependent behavior of dielectric permittivity (ε_r) and loss tangent (tan δ) at 100 kHz of (1-x) BFO- x DM for $0.0 \leq x \leq 0.2$. As discussed in Chapter-3, temperature dependent dielectric permittivity show two anomalies around 215 °C (T_{ME}) and 364 °C (T_N) for $x = 0.0$. The anomaly around 215 °C is not observed for the samples with $x = 0.025$, 0.05, and 0.075, while the sample with $x = 0.075$ shows an anomaly around 315 °C. The diffuse peak seen at 215 °C in BFO has been shifted and sharpen for the samples with $x = 0.1$, 0.15, and 0.2. The appearance of the anomaly around 215 °C (T_{ME}) can be explained by the Landau-Devonshire theory of phase transition and could be attributed to the destruction of space modulated spin structure below the magnetic ordering of BFO [16-18]. The anomaly observed at around 315 °C for composition $x = 0.075$ could correspond to the antiferromagnetic phase transition of BFO [9-10]. The anomaly due to antiferromagnetic phase transition is found to be decreased with increase in composition. This shifting of the anomaly in ε_r *vs.* T could be due to the change in antiferromagnetic ordering because of the lattice strain and magnetoelectric coupling. Furthermore, loss tangent increases with increase in temperature and composition. This may be due to the increase in dc conductivity as shown in Fig 6.4(b). It has been reported that the dielectric anomalies in multiferroic system may appear from a combination of magneto-resistance and the Maxwell-Wagner effect [19]. Since appearance of bulk permittivity takes place sufficiently at higher frequencies, it is necessary to represent the high frequencies dielectric response data. Figs 6.4(c) and (d) show the temperature dependent dielectric permittivity for $x = 0.075$, 0.1 and 0.2 at higher frequency (50 kHz to 1 MHz). It is observed that dielectric permittivity decrease with increase in frequency. This is a typical signature of polar dielectric materials. Since the dielectric anomalies are well distinct even at higher frequencies, the observed anomalies are credited only to magnetoelectric coupling in the material. In order to understand the ME effect, the magneto-dielectric measurements were carried out under various condition at RT and will be discussed later.

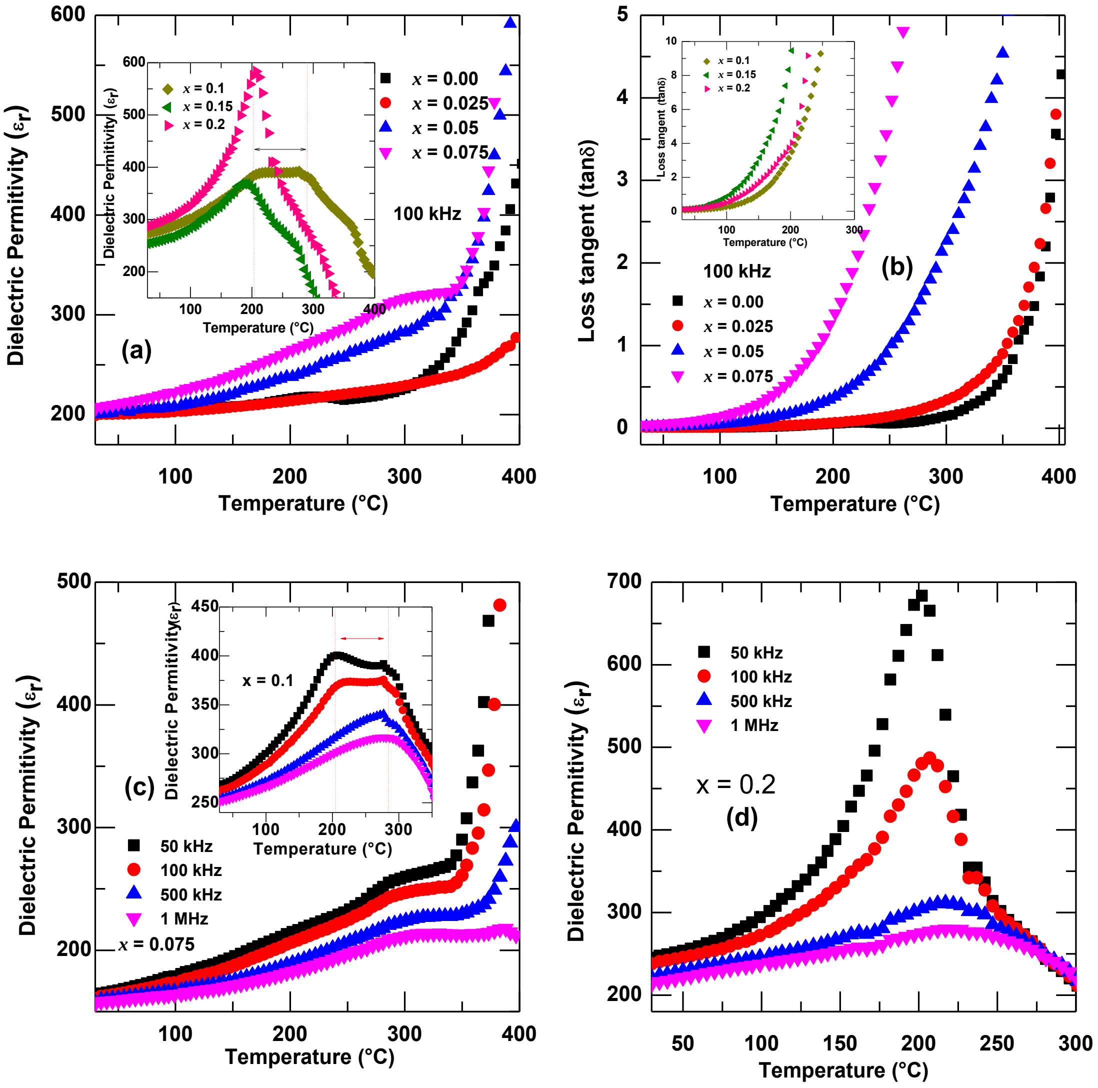

Figure 6.4 Temperature dependent dielectric parameters of (1-*x*) $BiFeO_3$ - *x*$DyMnO_3$ system for $0.0 \leq x \leq 0.2$: **(a)** ε_r vs. T at 100 kHz, **(b)** tan δ vs. T at 100 kHz. Temperature dependent dielectric permittivity at selected frequencies between 50 kHz -1 MHz for **(c)** x = 0.075 (Inset-temperature dependence of ε_r for x = 0.1) and **(d)** x = 0.2.

6.3.3 Ferroelectric Properties

Fig 6.5 shows the ferroelectric hysteresis loops of (1-x)BFO-xDM for $0.0 \leq x \leq 0.2$ solid solution at RT. It was found that for $x = 0.0$, the magnitude of remnant polarization, coercive field and maximum polarization are 0.4μC/cm^2, 11.5 kV/cm and 1.3 μC/cm^2, respectively. One can notice that a well saturated loop has not been achieved, which could be due to the low resistivity [2]. The variable oxidation states of Fe (Fe^{2+} to Fe^{3+}) in the material is still unavoidable and as a result, the oxygen vacancies are required for charge compensation, which could lead to the high conductivity [2]. Hence, the saturation in polarization-electric field (P-E) loop could not be observed even if maximum applied electric field due to the high leakage current. However, it can be mentioned here that an increase in magnitude of remnant polarization is observed on increasing x.

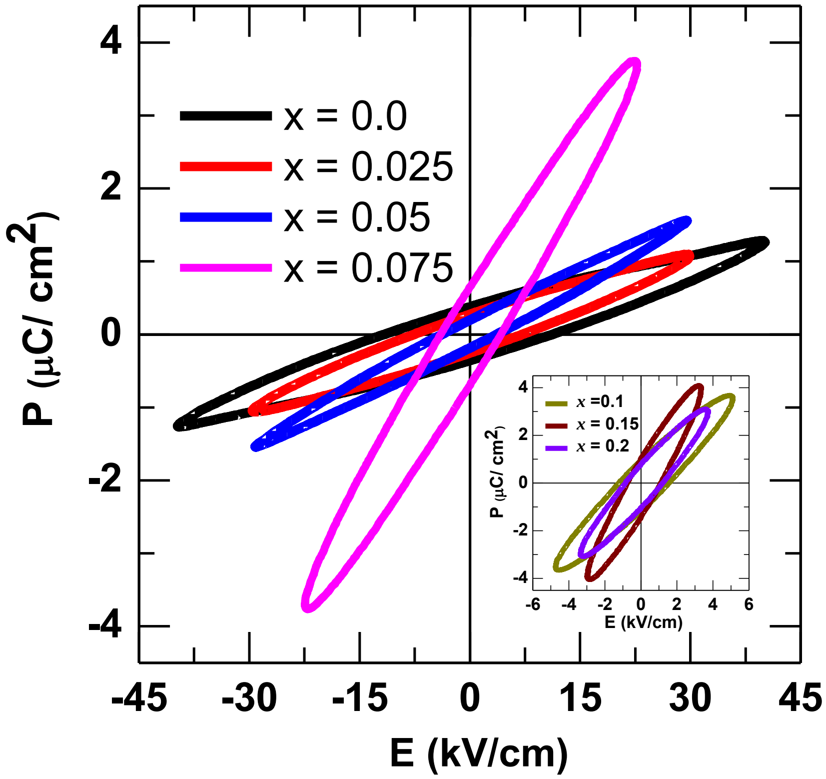

Figure 6.5 Room temperature ferroelectric hysteresis (P-E) loops of (1-x)BiFeO$_3$-xDyMnO$_3$ system for $0.0 \leq x \leq 0.2$.

5.3.4 Complex Impedance Studies

Figs 6.6 (a)-(f) represent the temperature dependence complex impedance spectra (*i.e.*, Nyquist plot: Imaginary Z vs. Real Z) of (1-x) $BiFeO_3$-$x$$GdMnO_3$ for $0.0 \leq x \leq 0.2$. We have fitted the Nyquist data using the equivalent circuit proposed in Chapter-4. It is observed that, at low temperature for all compositions Nyquist plot is linear. This signifies insulating property of the material. At elevated temperatures, two overlapping semicircles are prominent with increasing composition except few [20-26]. The high frequency semicircular arc can be modeled to an equivalent circuit of parallel combination of a resistance (bulk resistance), capacitance (bulk capacitance) along with a constant phase element, whereas the low frequency semicircular arc can be modeled for parallel combination of a resistance (grain boundary resistance) and a capacitance (grain boundary capacitance). The impedance data (symbols) have been fitted (solid line) with the above proposed equivalent circuit by the commercially available software ZSIMP-WIN Version 3 and a close agreement between the experimental value and the fitted lines have been obtained. Similar types of observations have been witnessed in the literature [20-26].

The d. c. conductivity due to the bulk and grain boundary contributions have been calculated from the resistances obtained after the Nyquist fit of the impedance data. Figure 6.7 shows the variation of dc conductivity (σ_{dc}) (due to bulk and grain boundary) as a function of $10^3/T$. It has been observed that the d. c. conductivity decreases with increasing temperature. This shows the negative-temperature coefficient of resistance (NTCR) features which is typically observed in semiconductors [26]. The temperature dependence of conductivity obeys the Arrhenius empirical relation $\sigma = \sigma_P \exp(-E_a/kT)$, where k is the Boltzmann constant, E_a is the activation energy and σ_P is the pre-exponential factor. We observed two different slopes in Arrhenius plot (σ_{dc} vs. $10^3/T$ (K^{-1}) plot) suggesting two different conduction mechanisms [26]. The calculated activation energies for both grain and grain boundary are listed in Table 6.3.

6.3.5 Magnetic Properties

Figure 6.8 shows the magnetic hysteresis loop of solid solution (1-x) BFO-xDM for $0.0 \leq x \leq 0.2$ at RT. The M-H dependence for $x = 0.0$ shows a linear response without possessing any spontaneous magnetization thus confirming the antiferromagnetic nature of the sample [1-3]. This can be explained due to the presence of canted G-type antiferromagnetic with spiral

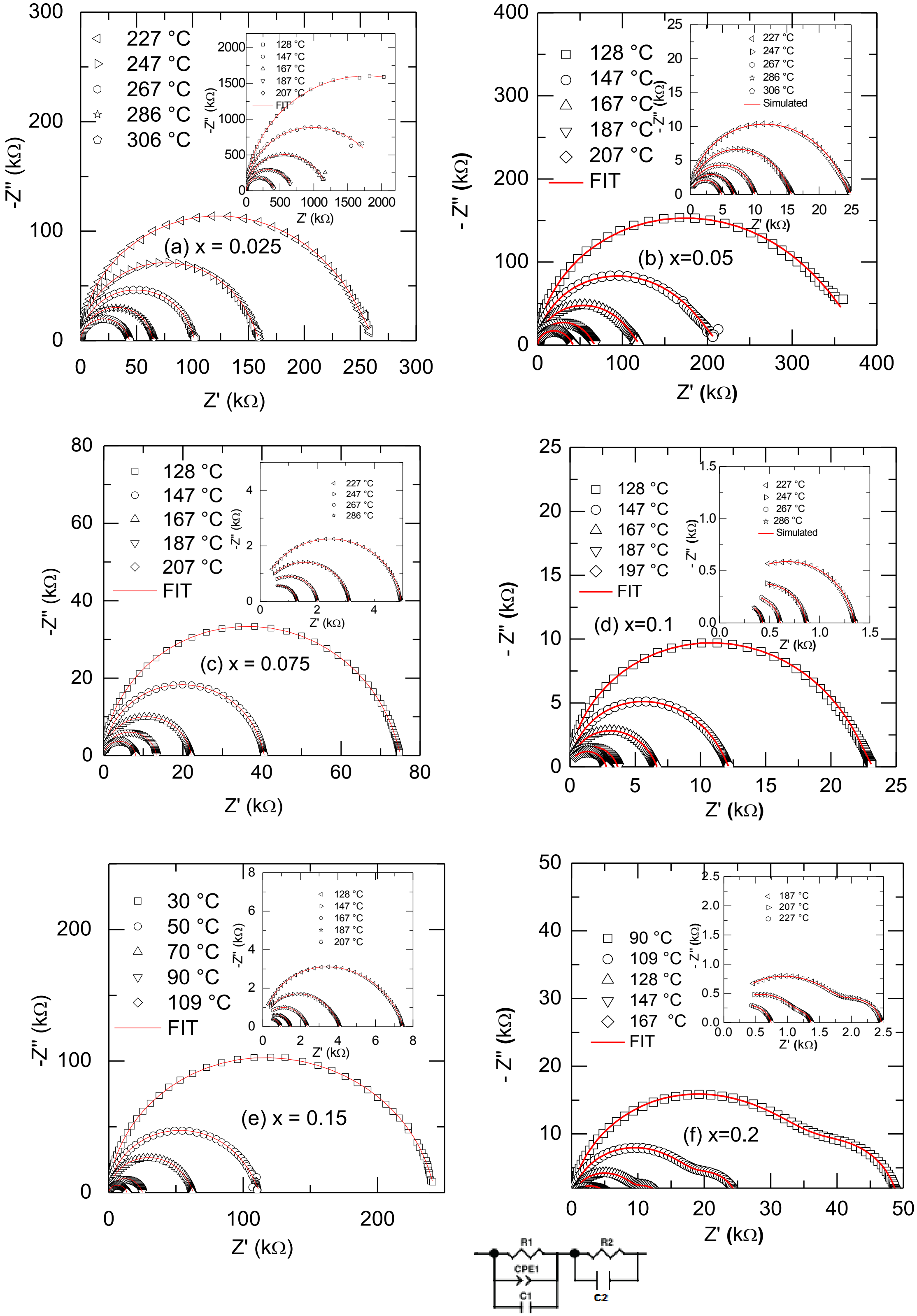

Figure 6.6 Complex impedance plot (open symbol), fitted data (solid line of (1-*x*)BFO-*x*DM for 0.0 ≤ *x* ≤ 0.2 for different *x* and temperatures. The equivalent circuit shown below.

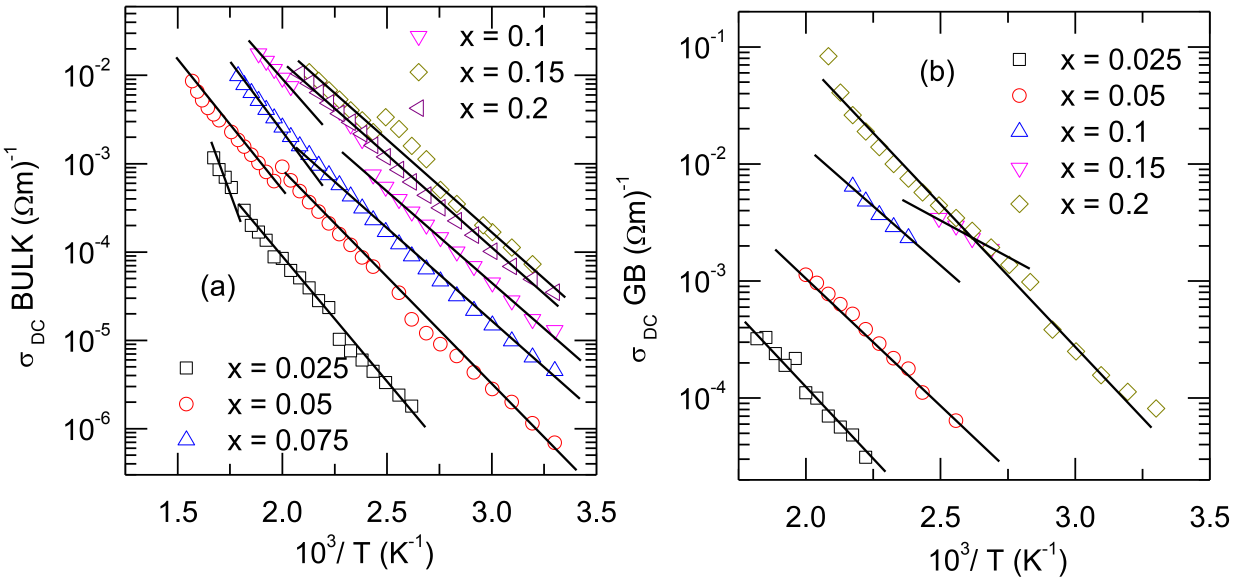

Figure 6.7 Variation in bulk and grain boundary conductivity with inverse of absolute temperature (*i.e.*, σ_{dc} vs. 10^3/T) of (1-*x*)BFO-*x*DM for different *x*.

Table 6.3 Activation energy E_a (in eV) obtained from temperature dependent bulk resistance (R_B), grain boundary resistance (R_{GB}) for different values of *x*.

Composition (*x*)	Bulk		Grain Boundary
	Zone-I	Zone-II	
0.0	--	1.402	1.478
0.025	0.86	0.56	0.54
0.05	0.64	0.47	0.43
0.075	0.58	0.42	--
0.1	0.49	0.40	0.48
0.15	--	0.41	0.25
0.2	--	0.40	0.27

modulated spin structure. As can be seen, the magnetization increases sharply with increasing *x* and reaches a maximum for *x* = 0.075 and further increasing shows reduction in the magnetization (c.f. inset Fig 6.8(a)). The coercivity and remnant magnetization for *x* = 0.075 are found to be H_c = 200 mT and M_r = 0.05 $emu.gm^{-1}$ respectively. The magnetic hysteresis loops of the DM modified BFO samples measured at RT indicate a typical weak ferromagnetic character. Néel's theory suggests that the large magnetic moment with reasonable hysteresis and the emergence of ferromagnetic like behavior in small antiferromagnetic particles were attributed to the incomplete spin compensation between the two sub-lattices [27]. The observation of enhancement in magnetization can be understood as follows: (a) with decrease in particle size, the surface-to-volume ratio rises significantly and particle's average magnetization increases due to uncompensated spins at the surface and/or (b) substitution of Dy^{3+} at *A*-site could also lead to collapse of space modulated spin structure and improve the magnetization. Since the magnetization is also affected by the nearest neighbors, with increasing DM concentration in BFO the nearest neighbors of Dy^{3+} and Fe^{3+} have been changed [6]. This could be a possible reason of reduction of magnetization in BFO with higher *x*. Furthermore, Dy^{3+} ions are highly magnetically active which subsidize to significant magnetization and coercivity in the DM modified samples, nevertheless spiral modulated spin structure still remains unchanged. According to the *Goodenough–Kanamori* rule, a strong antiferromagnetic interaction is probable between the Fe^{3+} ions and ferromagnetic interaction appear between the vacant Mn^{3+}orbital and filled Fe^{3+} orbital in perovskite or the breakdown of the balance between the antiparallel sub-lattice magnetization of Fe^{+3} due to metal ions substitution with a different valence [28]. It is worth noting that for compositions below *x* = 0.1 (*i.e.,* in the *R3c* phase of the DM modified BFO system); we have observed improved net magnetization. Fig 6.8(b) shows that after the structural phase boundary *i.e.,* for composition range ($0.1 \leq x \leq 0.2$) magnetization increases with the field with very slim hysteresis. This may be due the high paramagnetic feature of $Pn2_1a$ phase, which is evident from the fact that no saturation was observed. It has been reported that in compositional driven structural phase transition in $BiFeO_3$ from rhombohedral to orthorhombic, the parent rhombohedral phase is responsible for spontaneous ferroelectricity whereas orthorhombic phase is responsible for appearance of weak ferromagnetism. Moreover, the X-ray characterization clearly demonstrates nearly stoichiometric synthesis. So the possibility of extrinsic contribution from impurity phase $Bi_2Fe_4O_9$ is negligible as the magnetic ordering temperature of impurity phase $Bi_2Fe_4O_9$ is very much below RT. Therefore, we believe that the observation of the magnetization enhancement could be due to the suppression of cycloid spin structure and structural instability due to the solid solution of BFO with DM.

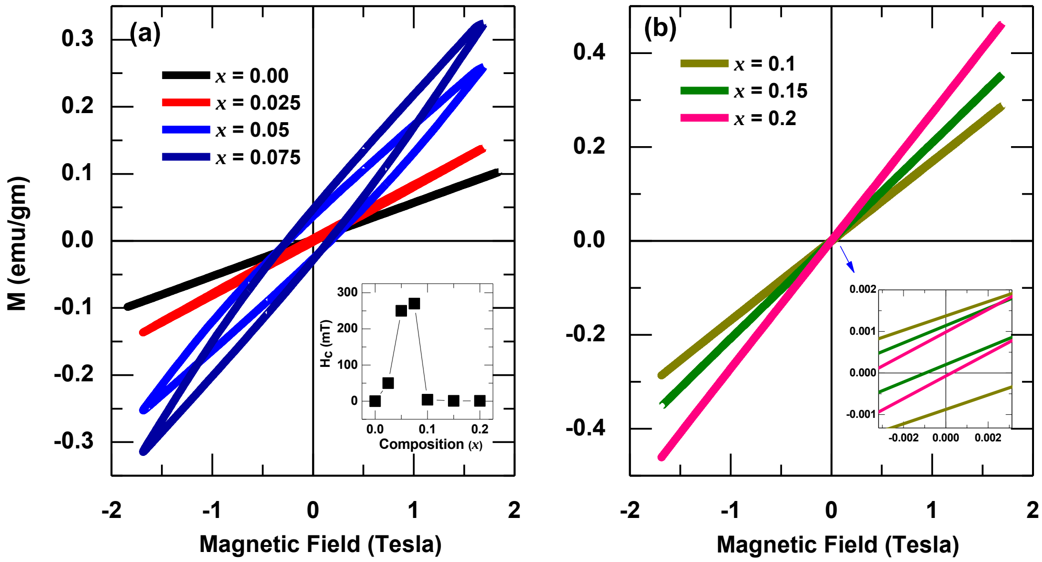

Figure 6.8 (a) M-H hysteresis loops for (1-*x*) $BiFeO_3$-*x*$DyMnO_3$ system for $0.0 \leq x \leq 0.075$ at room temperature (Inset shows compositional dependence (*x*) of coercive field, H_c). **(b)** M-H hysteresis curve of (1-*x*) $BiFeO_3$-*x*$DyMnO_3$ system for $0.1 \leq x \leq 0.2$ at room temperature (Inset shows magnification of MH loop at lower fields).

6.3.6 Magnetoelectric Properties

In order to understand the nature of the intrinsic magnetoelectric coupling in the samples, we carried out magneto-dielectric measurements as a function of frequency and magnetic field. Schmidt *et al.* [29-30]. have reported that the signature of true magnetoelectric coupling in multiferroic materials can be demonstrated by the following criterions. These are (a) anomaly across the magnetic transition in temperature dependent dielectric permittivity and (b) a change in real part of dielectric permittivity on application of magnetic field. The first criterion is supported by the temperature dependent dielectric studies. The proof of second criterion is explained as follows. Figs 6.9(a) to (d) show the frequency dependent behavior of dielectric properties at several magnetic field ($0 \leq H \leq 2$ T*:* $\Delta H = 0.5$ T) for *x* =0.05, *x* = 0.1, *x* = 0.15 and *x* = 0.2 within the frequency range 100 Hz to 1 MHz. It was observed that dielectric permittivity (ε_r) and loss tangent (tan δ) decrease with increase in magnetic field throughout the frequency range. Similar types of behavior have also been observed for all other compositions (not shown). On application of magnetic field to a magneto-electrically ordered system, strain is developed inside the material. For all ferroelectric and piezoelectric materials, this strain develops a stress which generates the electric field [29-30]. Consequently, a change in dielectric permittivity follows on application of magnetic field. This is an indicative of magnetoelectric coupling in the present system.

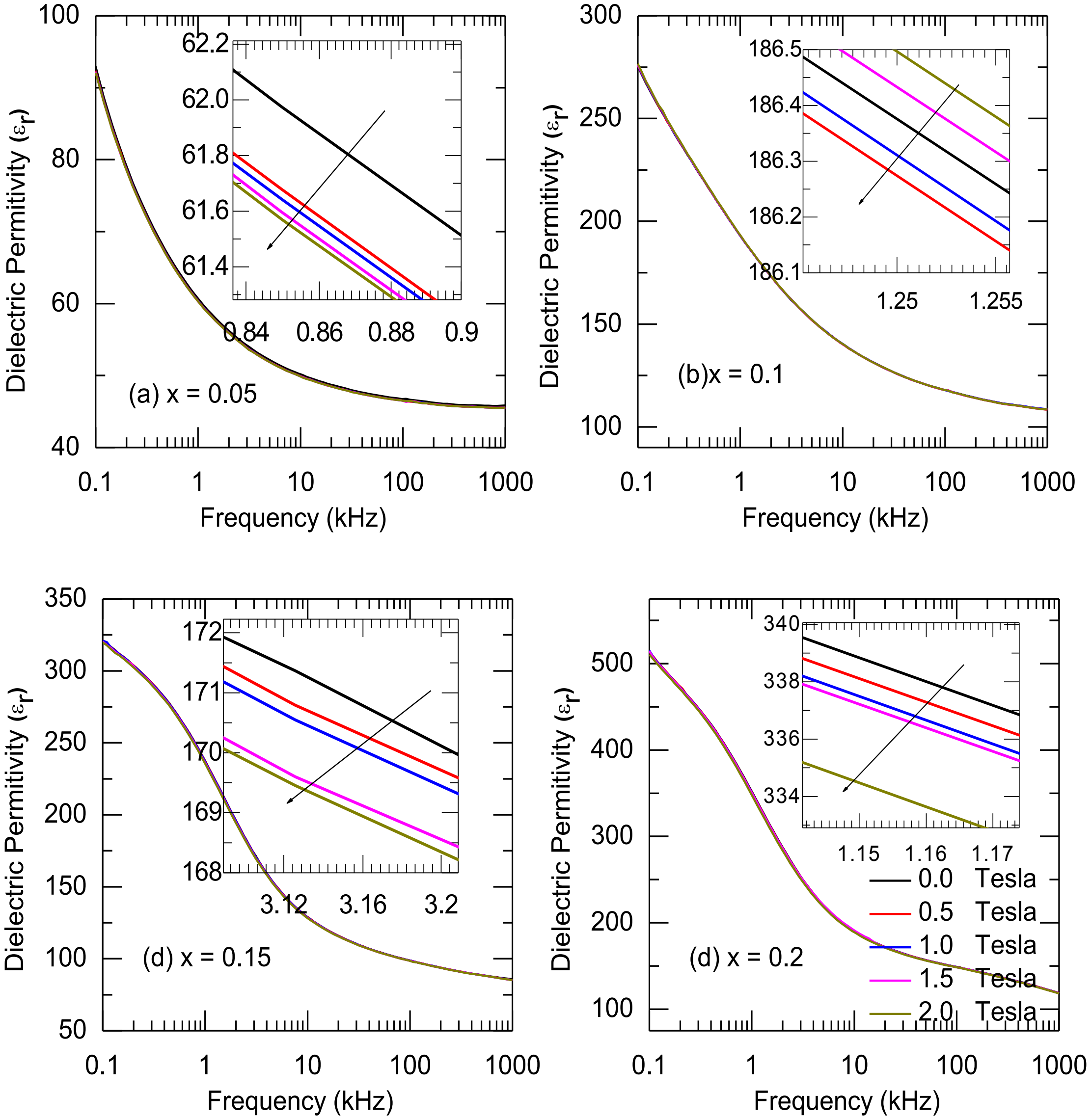

Figure 6.9 Frequency dependent behavior of ε_r for **(a)** x =0.05, **(b)** x = 0.1 **(c)** x = 0.15 and **(d)** x =0.2 at different applied magnetic fields ($0 \leq H \leq 2$ Tesla: $\Delta H = 0.5$ Tesla).The arrow indicates increasing magnetic field.

6.3.7 Magneto-impedance Properties

In order to reveal the intrinsic magnetoelectric coupling more rigorously we have plotted the imaginary part (Z'') of the impedance *vs.* real part ($Z^{'}$) (Nyquist plot) at RT for $x = 0.05$, $x = 0.1$, $x = 0.15$ and $x = 0.2$ at different applied magnetic fields ($0 \leq H \leq 2$ T: $\Delta H = 0.5$ T) as shown in Fig 6.10.

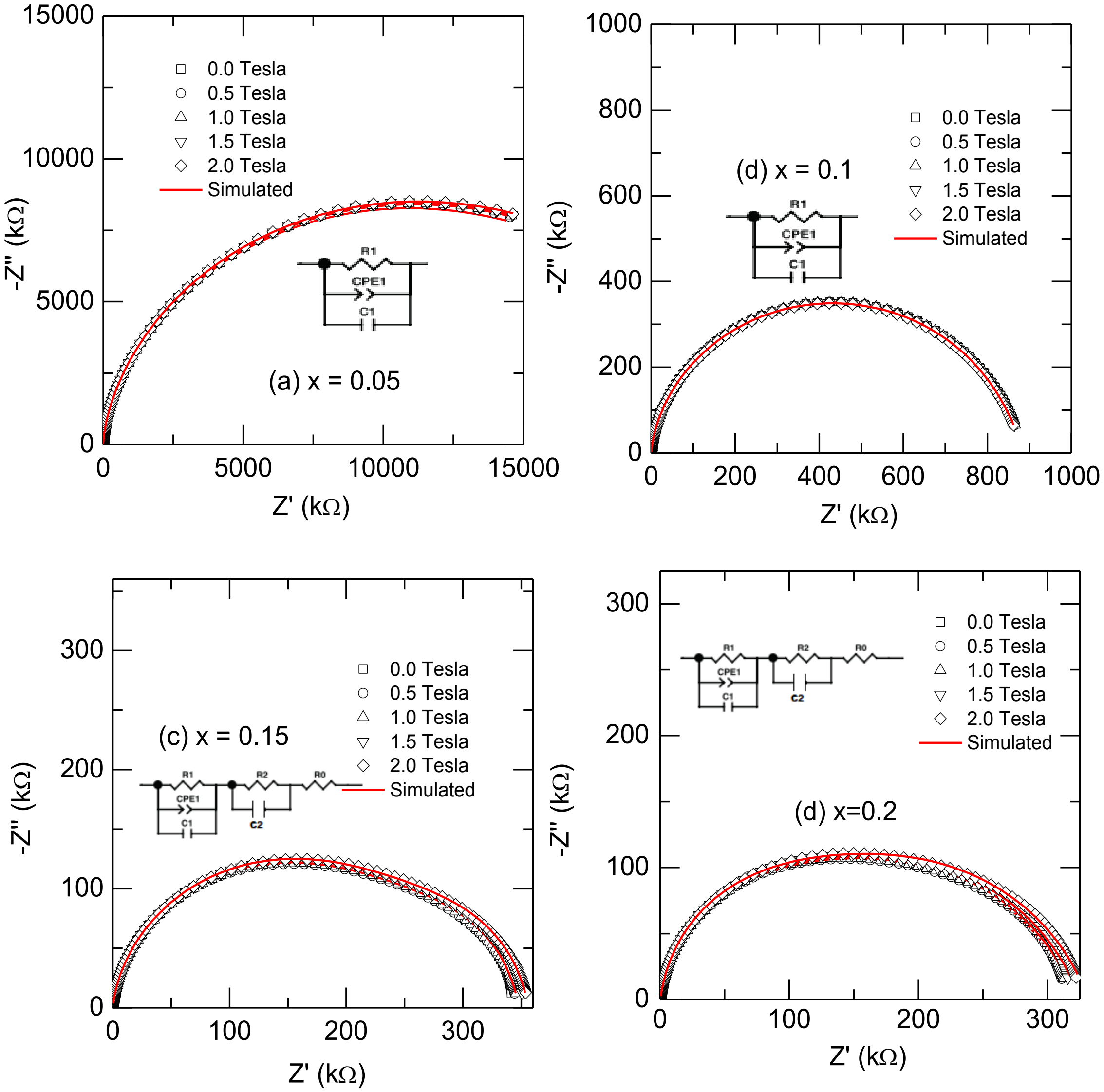

Figure 6.10 Magnetic field dependent complex impedance plot (open symbol), fitted data (solid line) of (1-x)BFO-xDM for **(a)** $x = 0.5$, **(b)** $x = 0.1$, **(c)** $x = 0.15$ and **(d)** $x = 0.2$ at RT. Inset shows the equivalent circuit to fit the Nyquist data.

The complex impedance spectrum and the equivalent circuit model are illustrated in Fig 6.10 [20-26]. Excellent fits were achieved in Nyquist plot for all values of applied magnetic field. It was observed that with increase in magnetic field the diameter of semicircle increases representing increase in bulk resistance. Moreover, it is intriguing to mention that the bulk permittivity (calculated from impedance data) decreases with increase in magnetic field as shown in Table-6.4 and Table-6.5. It is observed that bulk capacitance decreases with increasing magnetic field while bulk resistance increases [29-30]. The magneto-capacitance increased up to -18% at 2 Tesla for *x*=0.2. Since our sample is very resistive at RT and the measurement frequency range is not sufficiently high, therefore we did not see the cross-over from capacitive to inductive behavior in frequency dependent dielectric study. The imaginary part of the impedance usually goes from negative (capacitive) to positive (inductive) values at sufficiently high frequency. Therefore, we have not selected the inductive parameter in the represented circuit model. The observations of enhanced magnetoelectric coupling in the present study can be explained as follows: (a) synthesis of nano cermics leads to suppression or change of spin cycloid in BFO and (b) structural instability and destruction of spin cycloid resulted from DM substitution. Similar types of reports have been witnessed in literatures [20-26].

Table 6.4 Bulk capacitance obtained from fitting of magnetic field dependent complex impedance plot at RT for different value of *x*.

Bulk Capacitance (10^{-11}) in F							
Field (T)	$x = 0.0$	$x = 0.025$	$x = 0.05$	$x = 0.075$	$x = 0.1$	$x = 0.15$	$x = 0.2$
0	4.174	2.393	2.254	2.426	5.21	3.727	5.249
0.5	4.145	2.385	2.243	2.419	5.19	3.71	4.37
1	4.152	2.385	2.243	2.403	5.257	3.707	4.38
1.5	4.152	2.383	2.242	2.402	5.199	3.705	4.516
2	4.152	2.383	2.242	2.402	5.193	3.701	4.292

Table 6.5 Bulk resistance obtained from fitting of magnetic field dependent complex impedance plot at RT for different value of x.

Bulk Resistance in Ohm							
Field (T)	$x = 0.0$ 10^7	$x = 0.025$ 10^8	$x = 0.05$ 10^7	$x = 0.075$ 10^6	$x = 0.1$ 10^5	$x = 0.15$ 10^5	$x = 0.2$ 10^5
0.0	8.6176	1.844	2.553	4.456	7.659	2.739	2.404
0.5	9.3114	1.857	2.592	4.48	7.721	2.741	2.388
1.0	13.469	1.885	2.605	4.505	7.783	2.755	2.403
1.5	14.609	1.879	2.613	4.513	7.708	2.802	2.452
2.0	15.589	1.881	2.621	4.518	7.713	2.819	2.472

6.4 Conclusions

To conclude, nano ceramic solid solutions of (1-x) BFO-xDM, for $0.0 \leq x \leq 0.2$ were prepared by auto-combustion method. The fabrication of solid solution of BFO with DM found to prompt a compositional driven structural phase transition from $R3c$ to $R3c+Pn2_1a$ at $x = 0.1$. FESEM micrographs indicate a decrease in grain size on increasing composition. Dielectric study displayed two anomalies at 215 °C and 364 °C (T_N) for $x = 0.00$. The magnetic ordering temperature T_N decreases monotonically on increasing compositions. Enhanced magnetization properties were observed with increasing compositions and can be explained as suppression of space modulated spiral spin structure. Enhanced polarization hysteresis properties were also observed with compositions. It has been observed that the d. c. conductivity (grain and grain boundary) decreases with increasing temperature. This indicates the negative-temperature coefficient of resistance (NTCR). Real part of dielectric permittivity decreases with increasing magnetic field. Enhanced magneto-capacitance value around 18% was observed for $x = 0.2$ at RT for 2 Tesla. Magneto-impedance spectroscopy provided the signature of intrinsic magnetoelectric coupling in the material.

6.5 References

[1] C. Yang, D. Kan, I. Takeuchi, V. Nagarajan and J. Seidel, Phys. Chem. Chem. Phys., **14**, 15953 (2012).

[2] G. Catalan and J.F. Scott, Adv. Mater. **21**, 2463 (2009).

[3] K.F. Wang, J.M. Liu and Z.F. Ren, Adv. Phys. **58**, 321 (2009).

[4] J.-H. Lee, P. Murugavel, D. Lee, T. W. Noh, Y. Jo, M.-H. Jung, K. H. Jang, and J.-G. Park, Appl. Phys. Lett. **90**, 012903 (2007)

[5] S. N. Tripathy, B. G. Mishra, M. M. Shirolkar, S. Sen, S. R. Das, D. B. Janes, and D. K. Pradhan, Mater. Chem. Phys. **141**, 423 (2013).

[6] S. N. Tripathy, K. K. Mishra, S. Sen, B. G. Mishra, D. K. Pradhan, R.Palai, and D. K. Pradhan, J. Appl. Phys. **114**, 144104 (2013).

[7] J. Rodriguez-Carvajal, Physica B **192**, 55 (1993).

[8] R. Palai, R.S. Katiyar, H. Schmid, P. Tissot, S.J. Clark, J. Robertson, S.A.T. Redfern, G. Catalan and J.F. Scott, Phys. Rev. B **77,** 014110 (2008).

[9] S.M. Selbach, T. Tybell, M.A. Einarsrud, T. Grande, Chem. Mater. **19**, 6478 (2007).

[10] S. M. Selbach, T. Tybell, M. Einarsrud, and T. Grande, Adv. Mater. **20**, 3692 (2008).

[11] R. Haumont, Igor A. Kornev, S. Lisenkov, L. Bellaiche, J. Kreisel, and B. Dkhil, Phys. Rev. B **78**, 134108 (2008).

[12] R. Haumont, P. Bouvier, A. Pashkin, K. Rabia, S. Frank, B. Dkhil, W. A. Crichton, C. A. Kuntscher, and J. Kreisel., Phys. Rev. B 79, 184110 (2009).

[13] V. A. Khomchenko *et al*., J. Appl. Phys., **103**, 024105 (2008).

[14] V. A. Khomchenko *et al.,* J. Appl. Phys., **108**, 074109(2010)

[15] D. Balzar, J. Appl. Crystallogr. **28**, 244(1995).

[16] G. L. Yuan and S. Or, J. Appl. Phys. **100,** 024109 (2006).

[17] L. Benguigui, Solid State Commun. **11**, 825 (1972).

[18] V. R. Palkar, J. John, and R. Pinto, Appl. Phys. Lett. **80**, 1628 (2002).

[19] G. Catalan, Appl. Phys. Lett. **88**, 102902 (2006).

[20] A. R. James, S. Priya, K. Uchino, and K. Srinivas, J. Appl. Phys. **90**, 3504 (2001).

[21] S. Lanfredi, J. F. Carvalho, and A. C. Hernandes, J. Appl. Phys. **88**, 283 (2000).

[22] M. A. L. Nobre and S. Lanfredi, J. Appl. Phys. **93**, 5557 (2003).

[23] D. C. Sinclair and A. R. West, J. Appl. Phys. **66**, 3850 (1989).

[24] J. R. Macdonald, Solid State Ionics **13**, 147 (1984).

[25] J. R. Macdonald, Impedance Spectroscopy, Emphasizing Solid Materials and Systems, Wiley Interscience, New York, (1987).

[26] D. K. Pradhan, R. N. P. Choudhary, C. Rinaldi and R. S. Katiyar J. Appl. Phys. **106** , 024102 (2009).

[27] F. Z. Qian, J. S. Jiang, S. Z. Guo, D. M. Jiang, and W. G. Zhang , J. Appl. Phys. **106**, 084312 (2009).

[28] C.-H. Yang, T.Y. Koo, Y.H. Jeong, Solid State Communications **134**, 299 (2005).

[29] R. Schmidt *et al.*, Phys. Rev. B **86**, 035113 (2012).

[30] V.R. Palkar, D. C. Kundaliya, S. C. Malik and S. Bhattacharya, Phys. Rev. B **69**, 212102 (2004).

Chapter-7

Effect of Ba and Zr Co-substitution on Structural and Magnetoelectric Properties of $BiFeO_3$

Chapter-7 deals with correlation between crystal structure and magnetoelectric properties of $Bi_{1-x}Ba_xFe_{1-x}Zr_xO_3$ for $0.0 \leq x \leq 0.1$ nanoceramics synthesized by auto-combustion method. The synthesized materials have been characterized and analyzed using X-ray diffraction, field emission scanning electron microscopy, dielectric spectroscopy, impedance spectroscopy, magnetic hysteresis (M-H loop), magneto-dielectric and magneto-impedance spectroscopic measurement with wide range of experimental conditions.

7.1 Introductory Remarks

In previous chapters, we have comprehensively studied the structural transition and multiferroic properties of solid solution of $BiFeO_3$-$RMnO_3$ (R: Y^{3+}, Gd^{3+}, Dy^{3+}). In the contemporary chapter, we study the effect of Ba^{2+} (di-magnetic) and Zr^{4+} (non-magnetic) co-substitution on the structural and magnetoelectric properties of multiferroic BFO.

Recently, numerous experimental investigations have demonstrated the effect of co-substitution on the enhanced multiferroic properties of BFO. Chemical substitution induces chemical pressure in the unit cell of BFO. The effects of chemical pressure may also be exploited to bring the ferroic transitions (T_C or T_N) closer together, thereby enhancing magnetoelectric (ME) coupling [1-2]. Khomchenko *et al.* reported the crystal structure and enhanced multiferroic properties of diamagnetic (*i.e.*, Ca^{2+}, Sr^{2+}, Pb^{2+} and Ba^{2+}) substituted BFO [3]. They explained the enhanced multiferroic properties due to "unwind" the spiral spin structure of BFO which release the latent magnetic moment and enable linear magnetoelectric coupling. Wei *et al.* observed the phenomenon of cross over from antiferromagnetic to ferromagnetic nature in BFO due to nonmagnetic Zr^{4+} substitution [4]. Catlan *et al.* have reported the effect of Ca^{2+} substitution on the improved magnetoelectric coupling of $BiFeO_3$ [5]. Kawae *et al.* observed the improved ferroelectric and leakage behaviour in Mn and Ti modified $BiFeO_3$ thin films [6]. It has been found that substitution of Zr^{4+} at Fe-site of BFO, introduces Bi-vacancy, decreases the Fe-O-Fe bond angle and enhances the super-exchange interaction and magnetic ordering due to the tilting of oxygen octahedral [4]. However, the effect of co-substitution with non-magnetic ions at B-sites of BFO is not well understood. In the present work, we have co-substituted BFO with Ba^{2+} (diamagnetic) and Zr^{4+} (non-magnetic) at the Bi^{3+} and Fe^{3+} sites respectively, to compensate the cation deficiency and avoid Bi-vacancy due to Zr^{4+} substitution.

In the present Chapter, we investigate the effect of Ba-Zr co-substitution on the structural, microstructural, dielectric, impedance spectroscopic, magnetic, magneto-dielectric and magneto-impedance properties of BFO nanoceramics. Emphasis has been given to understand the structure property relationship and its correlation with the magneto-electric coupling.

7.2 Experimental Procedure

Nanoceramics $Bi_{1-x}Ba_xFe_{1-x}Zr_xO_3$ (BFO-BZ) for $0.0 \leq x \leq 0.1$ were prepared by auto-combustion method using analytical grade chemicals of $Fe(NO_3)_3.9H_2O$, $Bi(NO_3)_3.5H_2O$, $Ba(NO_3)_2$, $ZrO(NO_3)_2.H_2O$ as starting materials (oxidizers) and urea as fuel. Details of auto-combustion synthesis procedure and all the experimental conditions for characterization of the synthesized materials are discussed in Chapter-2, 3 and 4 [See Ref: 7-8].

7.3 Results and Discussion

7.3.1 Structural and Microstructural Properties

Fig 7.1 (a) depicts the X-ray diffraction spectra of $Bi_{1-x}Ba_xFe_{1-x}Zr_xO_3$ for $0.0 \leq x \leq 0.1$ at RT. Rietveld refinements were carried out using the FULLPROF package [9]. Details of the refinement procedure and conditions have been discussed in Chapter-5. The experimental data points are represented as symbol (+) and simulated data are shown as solid line as shown in Fig 7.1 (a).The difference between observed and simulated pattern is presented at the bottom of the plot. There are three ions (Bi^{3+}/Ba^{2+}, Fe^{3+}/Zr^{4+}, and O^{2-}) in the asymmetric unit of the rhombohedral perovskite structure. We have adopted the representations of atomic positions for hexagonal unit cell of *R3c* space group as per Megaw and Darlington as discussed in Chapter-5 [10]. Coordinates of all the atoms in the asymmetric unit cell of the *R3c* space group can also be written as a function of the atomic displacement parameters *s, t, d,* and *e* : Bi^{3+}/ Ba^{2+} $(0, 0, \frac{1}{4}+s)$, Fe^{3+}/Zr^{4+} (0, 0, t), O^{2-} $(\frac{1}{6}-2e-2d, \frac{1}{3}-4d, \frac{1}{12})$ [10]. For, $x = 0.0$ a best match is obtained between calculated and observed X-ray diffraction spectra (goodness of fit: R_p= 9.8%, R_{wp}= 15.9%, $\chi^2 = 1.59$) with refined lattice parameters are, a = 5.5779 (09) Å, c = 13.8710 (23) Å, which are similar to reported values [1-2]. The XRD spectra of all Ba-Zr modified BFO are analogous to the parent $BiFeO_3$ (*R3c* space group). This is evidenced by existence of characteristic super lattice reflection (113) around ≈ 38 degree of rhombohedral *R3c* phase [11]. Therefore, we have selected the *R3c* space group to refine the crystal structure for all compositions. The intensity of the superlattice peak (113) reflection decreases with increasing *x* as shown in the appropriate magnification (log scale) in Fig 7.1 (b). Since (113) reflection appears from anti-ferrodistortive tilting of the octahedral, this gives rise to new oxygen planes leading to low intensity [11]. The lattice parameters, Wyckoff notations and atomic positions for the *R3c* space groups are listed in Table 7.1 and Table 7.2 respectively. Figure 7.2(a) shows the variation of the normalized lattice parameters (*i.e.*, $a_H^N = a_{Hex}/\sqrt{2}$, $c_H^N = c_{Hex}/\sqrt{12}$) and c_H^N/a_H^N with composition. It shows that on increasing Ba-Zr content normalized lattice parameters and pseudo-tetraonality (c_H^N/a_H^N) decreases.

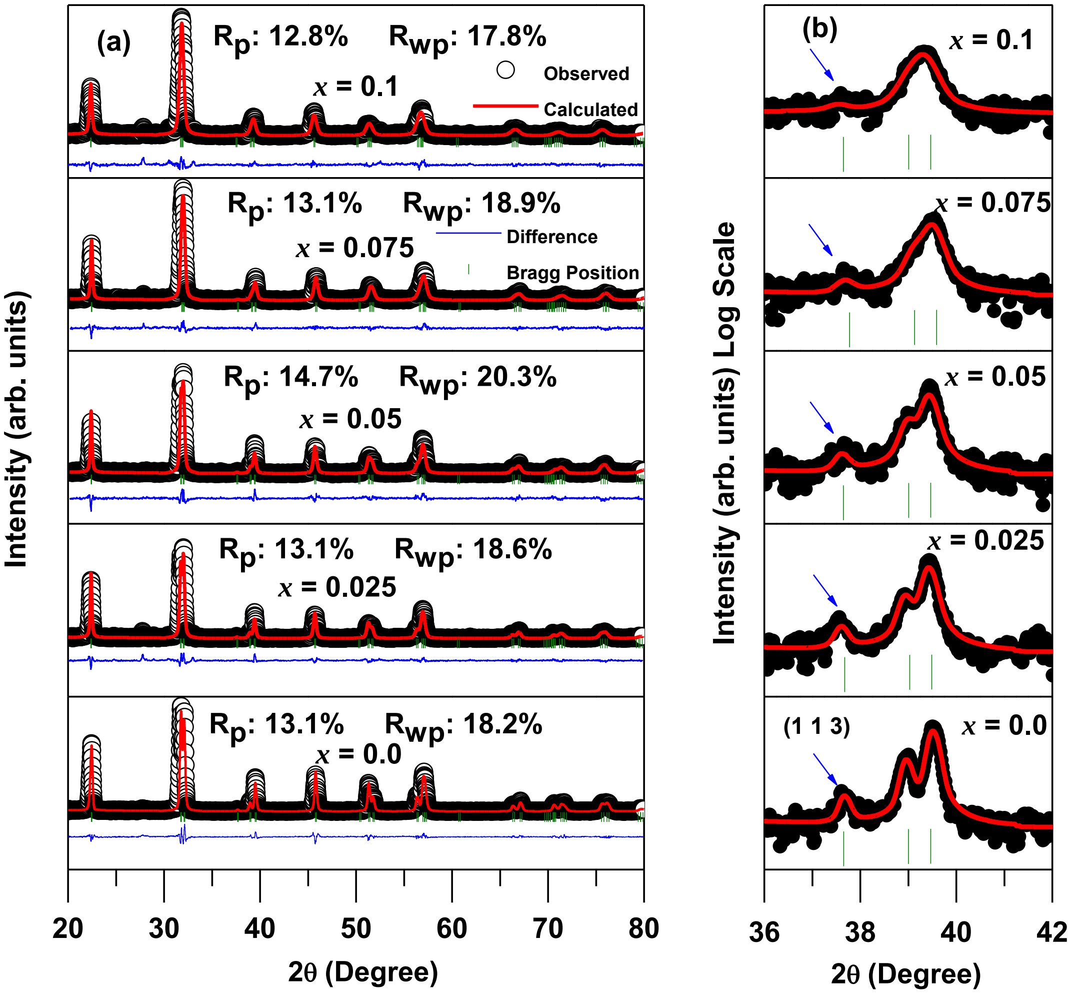

Figure 7.1 (a) Rietveld refinement result of XRD pattern of $Bi_{1-x}Ba_xFe_{1-x}Zr_xO_3$ for $0.0 \leq x \leq 0.1$ at RT, **(b)** XRD pattern expanded in $36° \leq 2\theta \leq 42°$ indicating (113) super reflection of *R3c* phase (log scale).

This signifies the increase in lattice strain with increasing composition. The variations of atomic displacement parameters (*i.e.*, *s*, *t*, *d*, *e*, and ω) with composition have been represented in Table 7.3. It is to be noted that *s*, *t*, and *ω* parameter decreases on increasing composition. Selbach *et al.* have reported that "*s*-*t*" is a measure of crystallographic polarization and there exists a linear relationship between *s*-*t* and T_N [12]. We found that on increasing composition the magnitude of "*s*-*t*" decreases, suggesting a decrease in T_N with increase in composition. Further, in order to demonstrate the effect of peak broadening due to small crystallite size qualitatively and quantitatively we have adopted the Double-voigt method using BREATH package [13]. This method is similar to Warren-Averbach method. Fig 7.2(b) shows the volume-weighted domain size distribution function, $P_v(L)$ as a function of crystallite size (L) for $0.0 \leq x \leq 0.1$. It is observed that the true crystallite size of $Bi_{1-x}Ba_xFe_{1-x}Zr_xO_3$ for $0.0 \leq x \leq 0.1$ varies between 100 Å to 600Å.

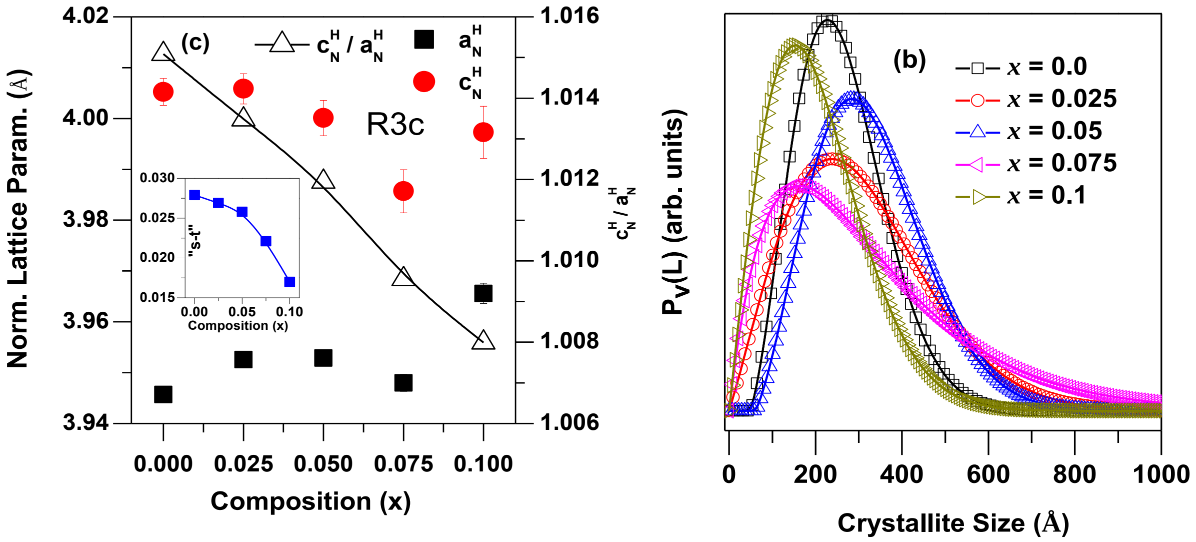

Figure 7.2 (a) Compositional dependence of normalized lattice parameters (*i.e.*, $a_H^N = a_{Hex}/\sqrt{2}$, $c_H^N = c_{Hex}/\sqrt{12}$) and ($c_H^N / a_H^N$) (Inset- variation of "s-t" with *x*) and, **(b)** Volume-weighted domain size distribution function, $P_v(L)$ as a function of crystallite size (L).

Table 7.1 Lattice parameters of $Bi_{1-x}Ba_xFe_{1-x}Zr_xO_3$ for $0.0 \leq x \leq 0.1$ estimated from Rietveld refinement with good-ness of fitting parameters. The standard deviations are in parenthesis.

Composition (x)	Space group	Lattice Parameters (Å)			χ^2
		a	*b*	*c*	
0.0	*R3c*	5.57924 (10)	5.57924 (10)	13.87416 (26)	1.59
0.025	*R3c*	5.58895 (11)	5.58895 (11)	13.87628 (29)	1.61
0.05	*R3c*	5.58938 (16)	5.58938 (16)	13.85636 (34)	1.38
0.075	*R3c*	5.58247 (13)	5.58247 (13)	13.80651 (42)	1.44
0.1	*R3c*	5.60734 (20)	5.60734 (20)	13.84659 (51)	1.40

Table 7.2 Atomic positions for hexagonal unit cell of *R3c* space group as per Megaw and Darlington used in Rietveld refinement.

Composition (x)	Space group	Atom	Site	x	y	z
$0.0 \leq x \leq 0.1$	*R3c*	Bi^{3+}/Ba^{2+}	6*a*	0.0	0.0	0.293
		Fe^{3+}/Zr^{4+}	6*a*	0.0	0.0	0.019
		O^{2-}	18*b*	0.231	0.337	1/12 (Fixed)

Table 7.3 Atomic displacement parameters *s, t, d, e* and ω obtained from Rietveld refinement for different value of *x*.

Composition (x)	s	t	d	e	ω
0.0	0.0472	0.0193	-0.0010	-0.0316	12.34
0.025	0.0458	0.0189	-0.0029	-0.03528	13.72
0.05	0.0385	0.0127	0.0006	-0.03333	12.99
0.075	0.0371	0.0150	0.0004	-0.02905	11.37
0.1	0.0402	0.0232	-0.0013	-0.02537	10

Figure 7.3 shows the field emission scanning electron micrographs for $x = 0.0$, $x = 0.05$ and $x = 0.1$. As can be seen, the grains are densely populated with well-defined grain boundary without any voids and defects. $BiFeO_3$ (x =0.0) shows highly non-uniform grain size distribution ranging from ~3 μm to ~300 nm, whereas average grain size of 20-50 nm has been observed with Ba-Zr co-substituted samples. There is a decrease in avg. grain size with increase in Ba-Zr substitution.

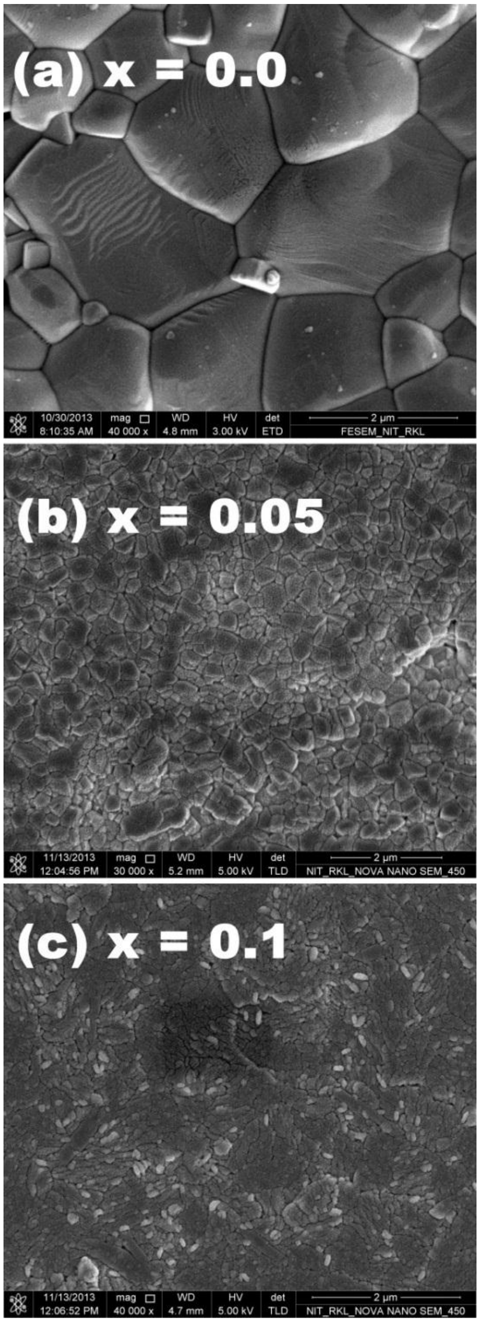

Figure 7.3 FESEM micrographs of $Bi_{1-x}Ba_xFe_{1-x}Zr_xO_3$ for **(a)** $x = 0.0$ **(b)** $x = 0.05$ **(c)** $x = 0.1$.

7.3.2 Dielectric Properties

Fig. 7.4(a) compares the temperature dependent dielectric permittivity (ε_r) of $Bi_{1-x}Ba_xFe_{1-x}Zr_xO_3$ for $0.0 \leq x \leq 0.1$ at 100 kHz. It is observed that for $x = 0.0$, the temperature dependent dielectric permittivity displayed two anomalies around 215 °C and 365 °C (small hump) as shown in Fig 7.4 (c). The observed anomaly around 365 °C is attributed to antiferromagnetic phase transition (T_N) whereas the anomaly around 215 °C (T_{ME}) due to higher order magnetoelectric coupling and can be explained due to destruction/ suppression of space modulated spin structure below magnetic ordering temperature [11-12]. This is further supported by Landau-Devonshire theory of phase transition [14-15]. On increasing composition both the anomalies gradually becomes more prominent associated with the increase in dielectric permittivity. The anomaly corresponding to the T_N decreases drastically on increasing composition. Since the magnetic ordering is also affected by the nearest neighbors and coordination number, with increasing Ba-Zr concentration in BFO the nearest neighbors of Fe^{3+} have been changed. This could be the possible reason of the reduction of magnetic ordering temperature in BFO with higher BZ concentration. But for $x = 0.1$, along with the above two anomalies, we observe another new anomaly around 56 °C. The appearance of the new peaks could be due to the magnetic frustration of paramagnetic and weakly ferromagnetic orderings as the ionization potential of Zr^{4+} (34 eV) is quite high compared to the Ba^{2+} (10 eV), which could lead to the valence fluctuation of cations. Temperature dependence loss tangent also showed anomaly around the magnetic phase transition further supporting the signature of magnetoelecric coupling in the present system as depicted in Figure7.4 (b). It is further to be noted that we have presented the dielectric data sufficiently at higher frequencies to avoid the interfacial effects as shown in Figs 7.4 (c) and (d) [16]. So, we can conclude that the dielectric anomalies originated from bulk properties are genuine. It is also evident from structural studies that (a) increase in lattice strain and, (b) cooperative crystallographic displacement parameter "s-t" decreases with composition. Both the parameters suggest a decrease in magnetic ordering temperature which corroborates with the temperature dependent dielectric study [10-12].

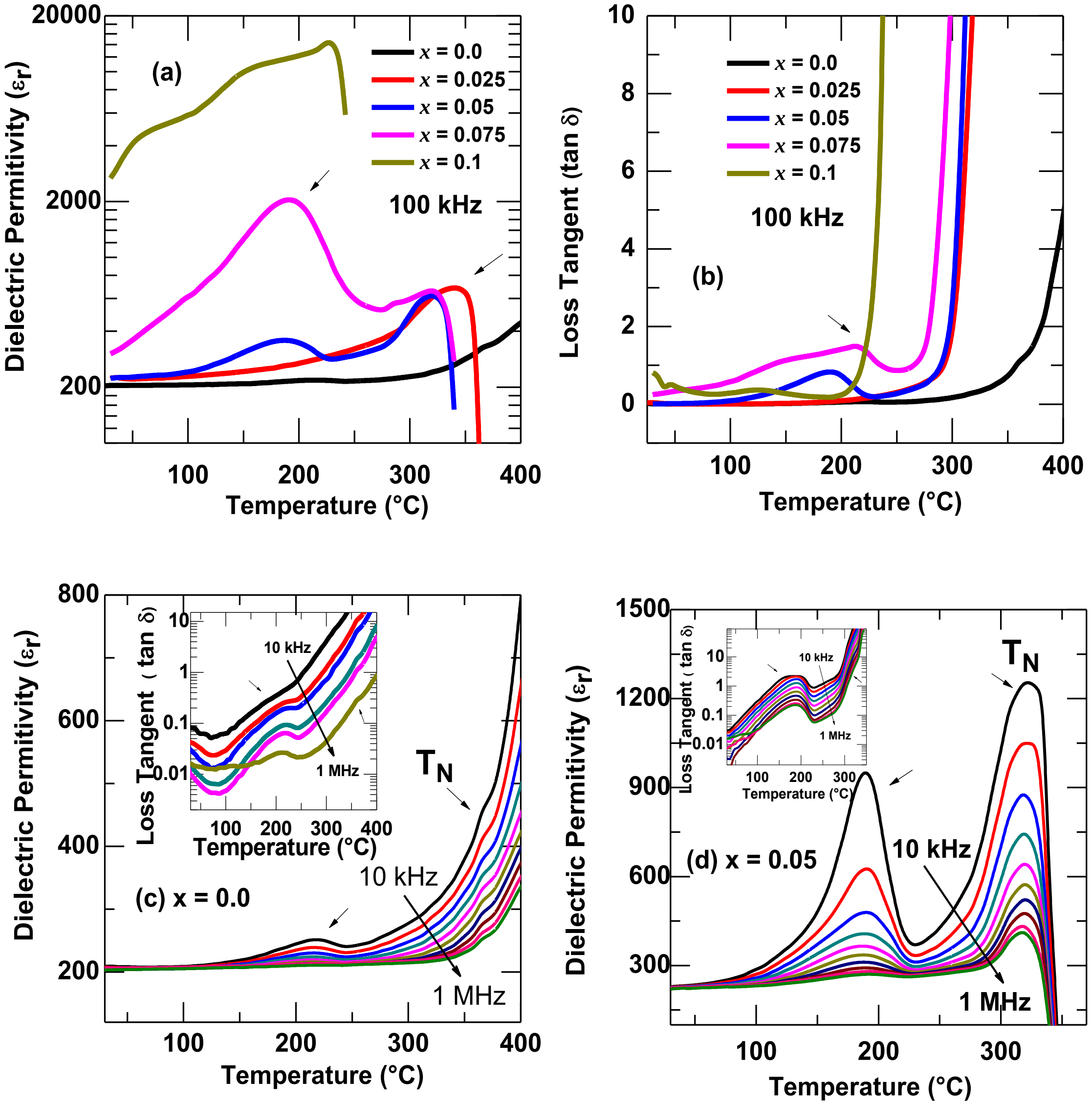

Figure 7.4 Temperature dependent dielectric parameters of $Bi_{1-x}Ba_xFe_{1-x}Zr_xO_3$ for $0.0 \leq x \leq 0.1$ **(a)** ε_r vs. T at 100 kHz, **(b)** tan δ vs. T at 100 kHz. Temperature dependent dielectric permittivity at selected frequencies between 10 kHz -1 MHz for **(c)** $x = 0.0$ (Inset-temperature dependence of tan δ for $x = 0.0$) and **(d)** $x = 0.05$ (Inset-temperature dependence of tan δ for $x = 0.05$).

7.3.3 Complex Impedance Studies

Figure 7.5 represents the temperature dependence complex impedance spectra (*i.e.*, Nyquist plot: Imaginary Z vs. Real Z) of $Bi_{1-x}Ba_xFe_{1-x}Zr_xO_3$ for $0.0 \leq x \leq 0.1$. We have fitted the Nyquist data using the equivalent circuit shown in Fig 7.5. It is evident from figure that, at low temperature for all compositions Nyquist plot display linear behavior and demonstrates insulating property of the material. At higher temperatures, two over lapping semicircles are observed for all compositions suggesting the existence of bulk and grain boundary effect. The impedance data (symbols) have been fitted (solid line) by the proposed model (See Fig 7.5) by the commercially available software ZSIMP-WIN Version 3 and a close agreement between the experimental value and the fitted lines have been observed. Similar types of observations are reported in the literature [17-24].

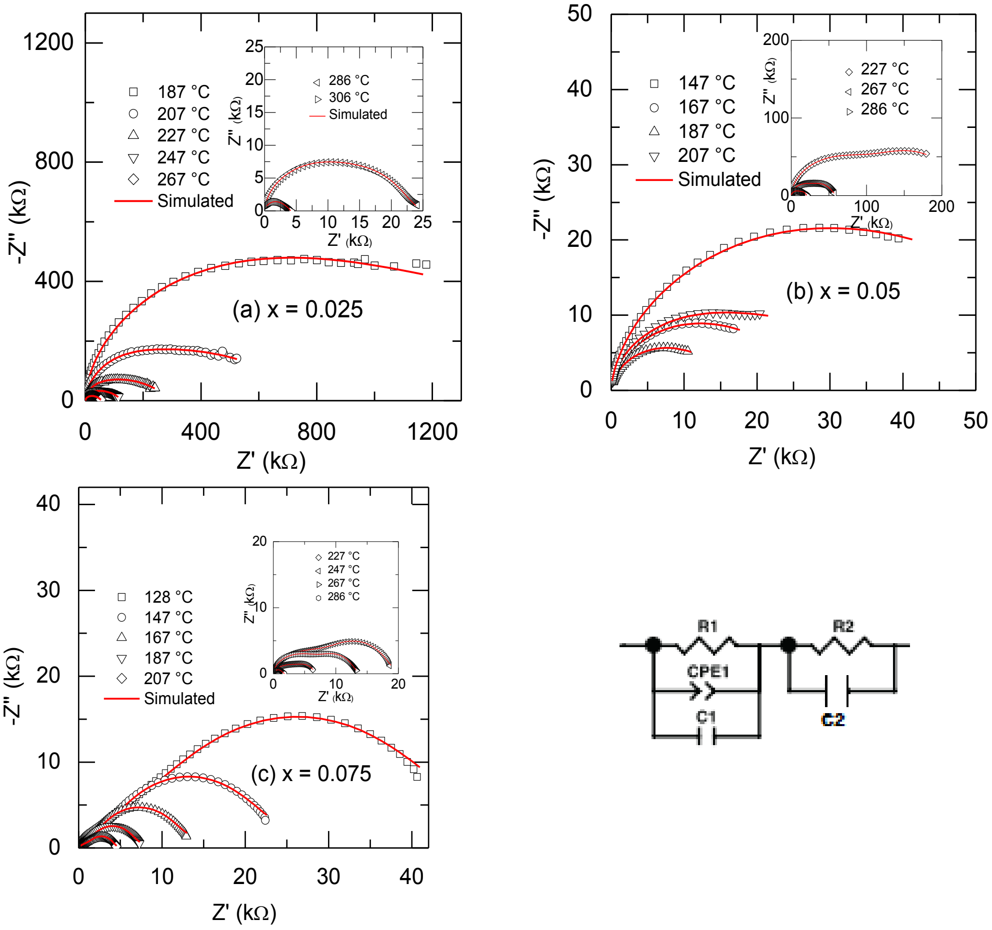

Figure 7.5 Complex impedance plot (open symbol), fitted data (solid line) of $Bi_{1-x}Ba_xFe_{1-x}Zr_xO_3$ for $0.0 \leq x \leq 0.1$ for different x and temperatures. The equivalent circuit is shown aside.

After the Nyquist fit of complex impedance spectra, the d. c. conductivity due to the bulk and grain boundary contributions have been calculated. Fig 7.6 shows the variation of dc conductivity (σ_{dc}) (due to bulk and grain boundary) as a function of $10^3/T$. It has been observed that the d. c. conductivity decreases with increasing temperature indicating negative-temperature coefficient of resistance (NTCR) [25].The temperature dependence of conductivity follows the Arrhenius empirical relation $\sigma = \sigma_P \exp(-E_a/kT)$, where k is the Boltzmann constant, E_a is the activation energy and σ_P is the pre-exponential factor. We observed two different slopes in Arrhenius plot (σ_{dc} vs. $10^3/T$ (K^{-1}) plot) suggesting two types of conduction mechanisms (*i.e.*, activation energy values). The calculated activation energies for both grain and grain boundary are listed in Table 7.4.

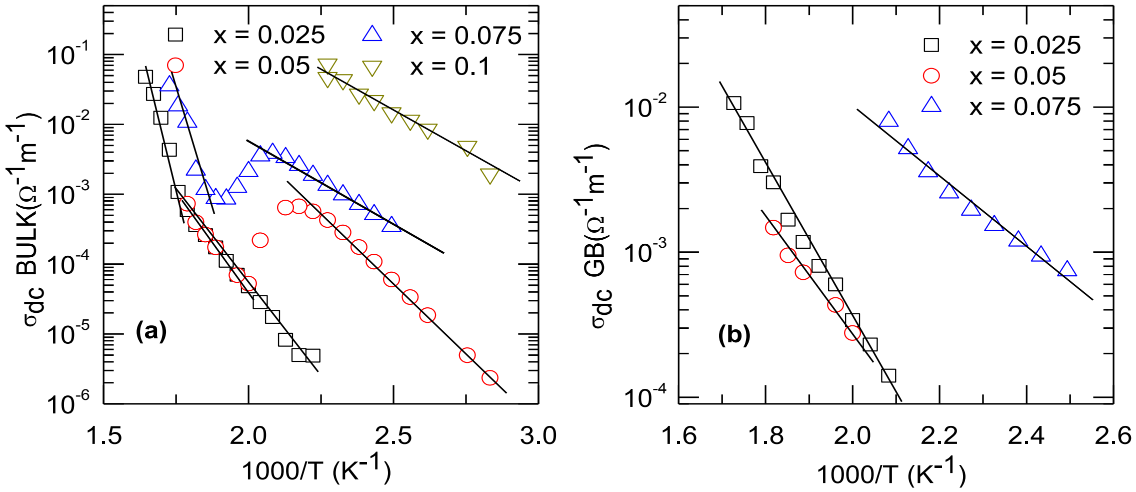

Figure 7.6 Variation in bulk and grain boundary conductivity with inverse of absolute temperature (*i.e.*, σ_{dc} vs. $10^3/T$) of $Bi_{1-x}Ba_xFe_{1-x}Zr_xO_3$ for different *x*.

Table 7.4 Activation energy E_a (in eV) obtained from temperature dependent bulk resistance (R_B), grain boundary resistance (R_{GB}) for different compositions.

Composition (x)	Bulk		Grain Boundary
	Zone-I	Zone-II	
0.0	--	1.402	1.478
0.025	1.03	2.97	1.044
0.05	0.94	2.12	0.88
0.075	0.49	1.10	0.48
0.1	0.51	--	--

7.3.4 Magnetic Properties

Figs 7.7(a) and (b) show the MH loop of $Bi_{1-x}Ba_xFe_{1-x}Zr_xO_3$ for $0.0 \leq x \leq 0.1$. As can be seen, BFO shows linear M-H loop without having any spontaneous magnetization suggesting antiferromagnetic nature. This can be described in terms of the presence of canted G-type anti-ferromagnetic spiral spin modulation in BFO [1-2]. With increasing composition up to $x = 0.05$ magnetization have similar magnitude as that of parent but improved magnetic properties were observed for $x = 0.075$ and 0.1. For $x = 0.1$ well saturated magnetic hysteresis loop is observed with H_c = 100 mTesla and M_r = 0.04 emu/g. The enhanced magnetization may be due to suppression of spin cycloid induced because of co-substitution and/or smaller crystallite compared to the size of spin cycloid. When Fe^{3+} ions is replaced by Zr^{4+} ions in the AFM ordering of Fe^{3+} sub-lattice, the balance between two adjacent anti parallel spin of Fe^{3+} gets perturbed. Eventually a ferromagnetic interaction via oxygen, instead of anti-ferromagnetic coupling is preferred due to the straightening out of the Fe-O-Zr bond angle [4, 26]. Hence, Zr^{4+} substitution offers a unidirectional alignment of spins in the system leading to ferromagnetic behaviour.

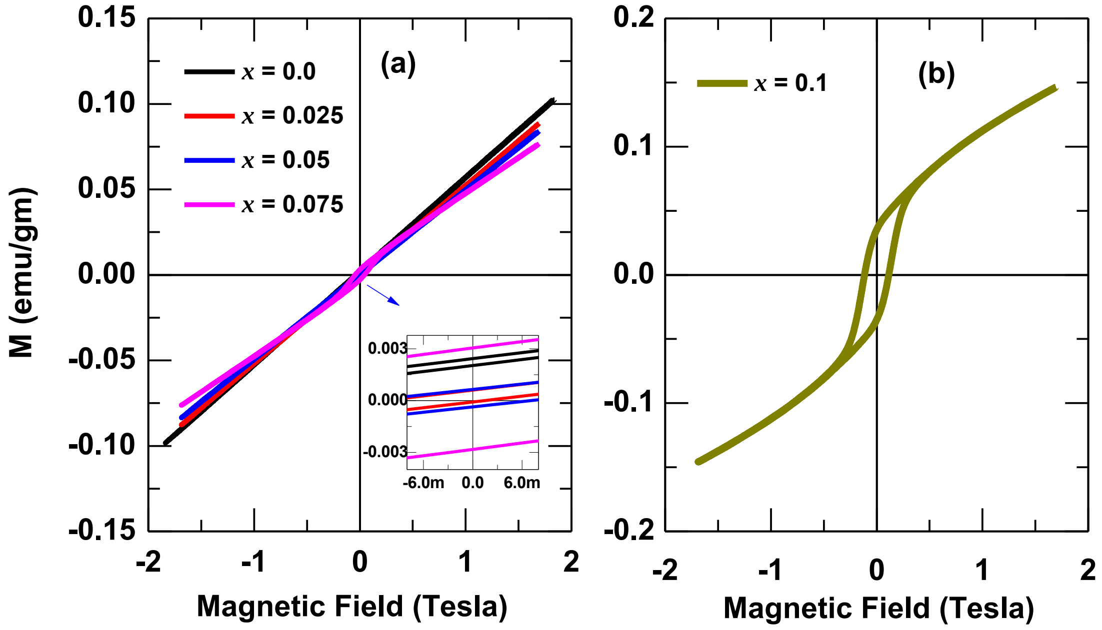

Figure 7.7 (a) M-H hysteresis loops of $Bi_{1-x}Ba_xFe_{1-x}Zr_xO_3$ **(a)** for $0.00 \leq x \leq 0.075$ (Inset- magnification of MH loop at lower fields) **(b)** for $x = 0.1$ at RT.

From structural study, it is evident that lattice strain rises with increasing composition as the ionic radii of Ba^{2+} (1.49 Å) and Zr^{4+} (0.86 Å) are larger compared to the ionic radii of Bi^{3+} (1.17 Å) and Fe^{3+} (0.78 Å). This could facilitate the decrease in distance between Fe^{3+} ions and oxygen and leading to stronger super exchange interaction resulting enhanced magnetic interaction and magnetization. Moreover, as already mentioned synthesis of nanoparticles size less than the size of the spin cycloid could further enhance the magnetic properties due to suppression of cycloid spin structure, which corroborates with our X-ray line profile analysis.

7.3.5 Magnetoelectric Coupling

In order to reveal the coupling between electric and magnetic ordering in the $Bi_{1-x}Ba_xFe_{1-x}Zr_xO_3$ system, we have carried out magneto-dielectric measurements at different magnetic fields and frequencies. It has been reported that the signature magneto-electric coupling in multiferroics can be established by the following criteria: (a) the observation of an anomaly at magnetic transition temperature in temperature dependent dielectric permittivity (b) changes in the capacitance with the application of a magnetic field [27]. The first criterion is satisfied which is explained in the dielectric study. To establish the second condition, the frequency dependant dielectric permittivity measurements of $x = 0.025$, $x = 0.05$, $x = 0.075$ at RT carried out at different magnetic fields ($0.0 \leq H \leq 2$ T*:* $\Delta H = 0.5$ T) as shown in Figs 7.8(a) to (d). As can be seen, the dielectric permittivity (ε_r) decreases with increase in magnetic field indicating a negative magneto-dielectric effect. The product of spin-pair correlation of neighbouring spins and the coupling constant decide the negative or positive sign of the magneto-dielectric effect. Similar types of behaviour have also been observed. The multiferroic materials under the magnetic field will produce magnetostrictive strain and if there is coupling with the ferroelectric (piezoelectric) order it can induce electric field [28]. This induced field can affect in the dielectric permittivity, as observed in the present study. This is an evidence of true magnetoelectric coupling in the system at RT.

7.3.6 Magneto-Impedance Studies

Figure 7.9 shows the RT complex impedance spectra (-Z" vs. Z') of $Bi_{1-x}Ba_xFe_{1-x}Zr_xO_3$ for $0.0 \leq x \leq 0.075$ for different static magnetic field ($0 \leq H \leq 2$ Tesla). For $x = 0.025$, we observed appearance of single semi-circular arcs which is of non-Debye type [17-24]. But, for $x = 0.05$

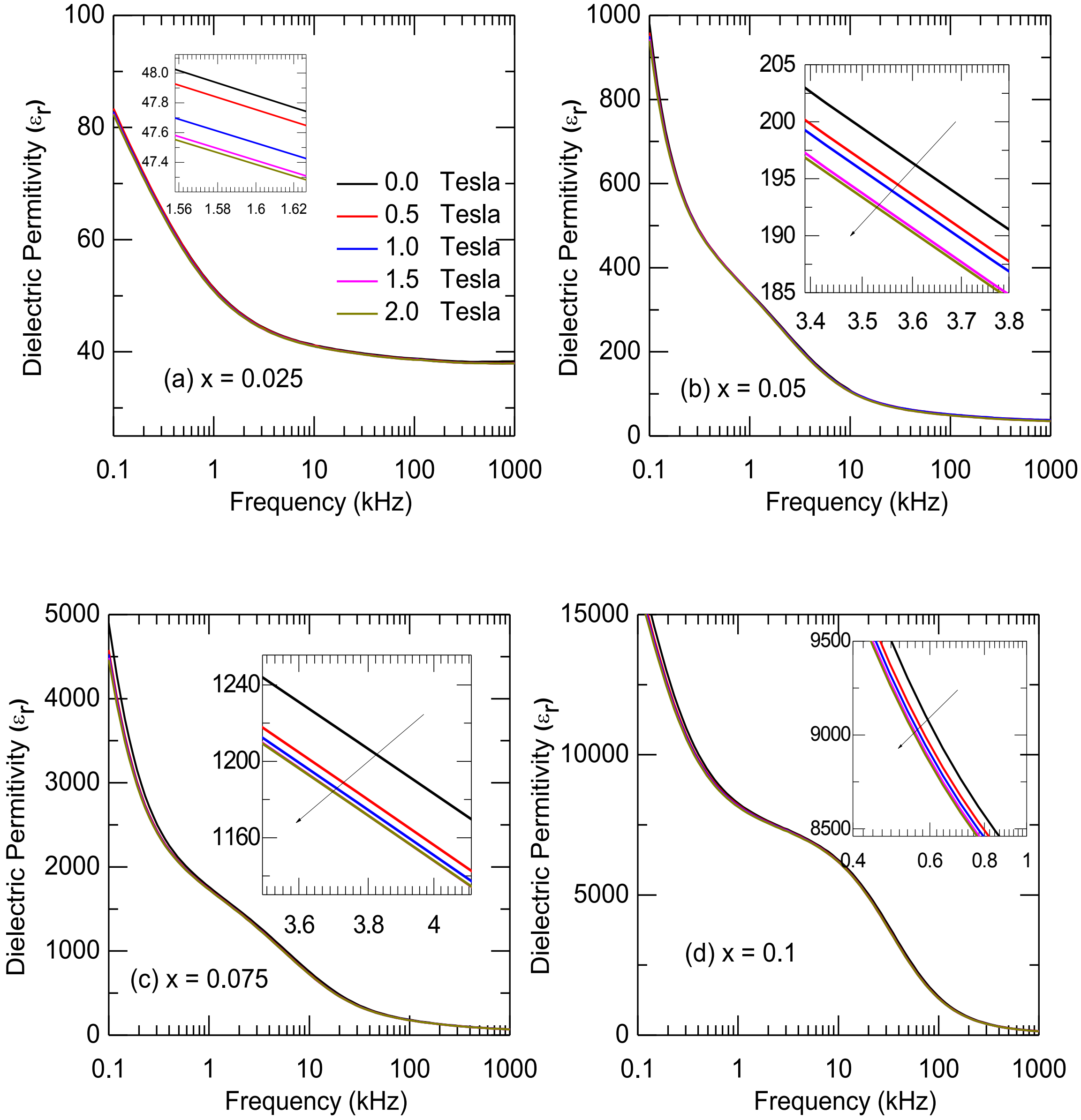

Figure 7.8 Frequency dependent behaviour of ε_r of $Bi_{1-x}Ba_xFe_{1-x}Zr_xO_3$ for **(a)** x =0.025, **(b)** x = 0.05, **(c)** x = 0.075 and **(d)** x =0.1 at different applied magnetic fields (0 ≤ H ≤ 2 Tesla: ΔH = 0.5 Tesla) at RT.

and *x*= 0.075, the impedance spectra exhibited two overlapping semi-circular arcs. The high frequency semicircle relates to bulk contribution whereas low frequency is attributed to grain boundary property. We have fitted the magnetic field dependent Nyquist plot using the equivalent circuit as shown in inset of Fig 7.9. A close agreement between the experimental value and the theoretical values has been obtained. The bulk capacitance and resistance found from the Nyquist fittings are listed in Table 7.5 and 7.6 respectively. It is observed that bulk capacitance decrease on increasing magnetic field where as bulk resistance increases. Similar types of reports have been witnessed in literatures [27-30].

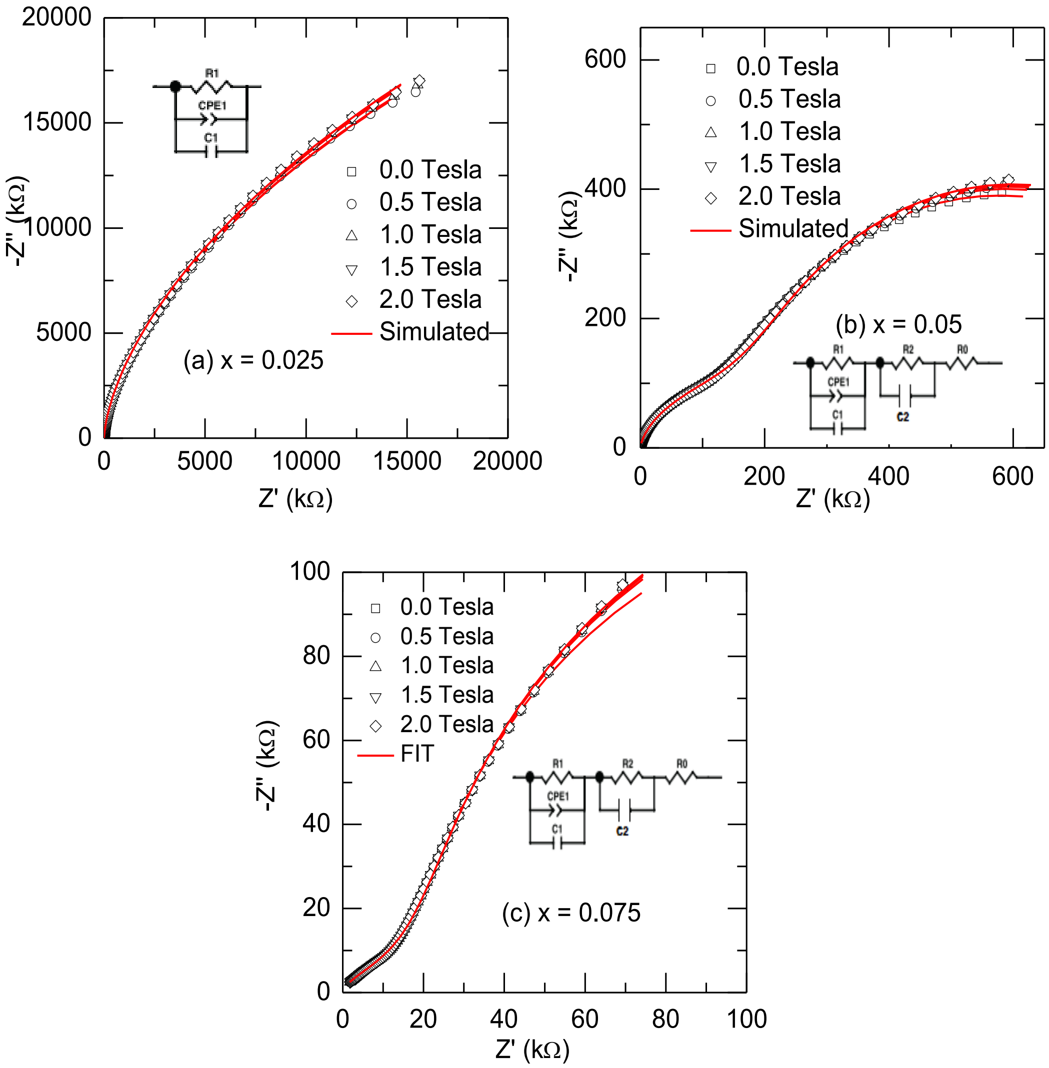

Figure 7.9 Magnetic field dependent complex impedance plot (open symbol), fitted data (solid line), of $Bi_{1-x}Ba_xFe_{1-x}Zr_xO_3$ for **(a)** *x* = 0.025, **(b)** *x* = 0.05 and **(c)** *x* = 0.075 at RT. Inset shows the equivalent circuit.

Table 7.5 Bulk capacitance obtained from fitting of magnetic field dependent complex impedance plot at RT for different value of *x*.

Bulk Capacitance (10^{-11}) in F			
Field (T)	*x* = 0.025	*x* = 0.05	*x* = 0.075
0.0	2.327	2.064	2.153
0.5	2.315	2.097	2.101
1	2.314	2.096	2.09
1.5	2.313	1.943	2.091
2.0	2.313	1.942	2.087

Table 7.6 Bulk resistance obtained from fitting of magnetic field dependent complex impedance plot at RT for different value of *x*.

Bulk Resistance in Ohm			
Field (T)	*x* = 0.025 10^8	*x* = 0.05 10^5	*x* = 0.075 10^4
0	1.594	3.01	4.614
0.5	1.608	3.04	4.626
1	1.744	3.038	4.636
1.5	1.774	3.092	4.653
2	1.775	3.0945	4.678

7.4 Conclusions

In conclusion, nanoceramics $Bi_{1-x}Ba_xFe_{1-x}Zr_xO_3$ for $0.0 \leq x \leq 0.1$ were successfully synthesized using auto-combustion method. Rietveld refinement results showed that all the samples have rhombohedral crystal structure with *R3c* space group. FESEM showed the decrease in grain size with increasing composition. Temperature variation of dielectric permittivity showed an anomaly around magnetic transition temperature indicating the existence of the magnetoelectric coupling. The d. c. conductivity (grain and grain boundary) decreased with increasing temperature suggesting the negative-temperature coefficient of resistance (NTCR) behaviour.

Magnetic hysteresis loop measurements at RT showed enhancement in magnetization with weak ferromagnetic behaviour for higher concentration. Frequency dependent magnetodielectric measurements showed the existence of magnetoelectric coupling at RT. Magneto-impedance spectroscopy provided the signature of intrinsic magnetoelectric coupling in the material. An enhancement in magnetoelectric properties was found in BFO with co-substitution of Ba^{2+} and Zr^{4+} non-magnetic ions, which could be useful for device applications.

7.5 References

[1] K.F. Wang, J.M. Liu, Z.F. Ren, Adv. Phys. **58**, 321 (2009).

[2] G. Catalan and J. F. Scott, Adv. Mater. **21**, 2463 (2009).

[3] V. A. Khomchenko et al., J. Appl. Phys. **103,** 024105(2008).

[4] J Wei, R Haumont, R Jarrier, P Berhtet, B. Dkhil, Appl. Phys. Lett. **96** 102509 (2010).

[5] G. Catalan, K. Sardar, N. S. Church, J. F. Scott, R. J. Harrison, and S. A. T. Redfern Phys. Rev. B **79**, 212415 (2009).

[6] T. Kawae, Y. Terauchi, H. Tsuda, M. Kumeda, and A. Morimoto, Appl. Phys. Lett. **94**, 112904 (2009).

[7] S. N. Tripathy, B. G. Mishra, M. M. Shirolkar, S. Sen, S. R. Das, D. B.Janes, and D. K. Pradhan, Mater. Chem. Phys. **141**, 423(2013).

[8] S. N. Tripathy, K. K. Mishra, S. Sen, B. G. Mishra, D. K. Pradhan, R.Palai, and D. K. Pradhan, J. Appl. Phys. **114**, 144104(2013).

[9] H. Rietveld, J. Appl. Crystallogr., **2**, 65 (1969).

[10] H. D. Megaw, C. N. W. Darlington, Acta Crystallogr. Sect. **A 31**, 161(1975).

[11] S. M. Selbach, T. Tybell, M. Einarsrud, and T. Grande, Adv. Mater. **20**, 3692 (2008).

[12] S.M. Selbach, T. Tybell, M.A. Einarsrud, T. Grande, Chem. Mater. **19**, 6478 (2007).

[13] D. Balzar, J. Appl. Crystallogr. **28**, 244 (1995).

[14] G. L. Yuan and S. Or, J. Appl. Phys. **100**, 024109 (2006).

[15] L. Benguigui, Solid State Commun. **11,** 825 (1972).

[16] G. Catalan, Appl. Phys. Lett. **88**, 102902(2006).

[17] A. R. West, D. C. Sinclair, and N. Hirose, J. Electroceram. **1**, 65 (1997).

[18] R. Schmidt, W. Eerenstein, T. Winiecki, F. D. Morrrison, and P. A. Modgley, Phys. Rev. B **75**, 245111 (2007).

[19] A. R. James, S. Priya, K. Uchino, and K. Srinivas, J. Appl. Phys. **90**, 3504 (2001).

[20] S. Lanfredi, J. F. Carvalho, and A. C. Hernandes, J. Appl. Phys. **88**, 283 (2000).

[21] M. A. L. Nobre and S. Lanfredi, J. Appl. Phys. **93**, 5557 (2003).

[22] D. C. Sinclair and A. R. West, J. Appl. Phys. **66**, 3850 (1989).

[23] J. R. Macdonald, Solid State Ionics **13**, 147 (1984).

[24] J. R. Macdonald, Impedance Spectroscopy, Emphasizing Solid Materials and Systems, Wiley Interscience, New York, (1987).

[25] D. K. Pradhan, R. N. P. Choudhary, C. Rinaldi and R. S. Katiyar J. Appl. Phys. **106** , 024102 (2009).

[26] Z. Xu *et al.*, J. Appl. Phys. **114**, 154103 (2013).

[27] R. Schmidt *et al.*, Phys. Rev. B **86**, 035113 (2012).

[28] V.R. Palkar, D. C. Kundaliya, S. C. Malik and S. Bhattacharya, Phys. Rev. B **69**, 212102 (2004).

[29] T. Katsufuji and H. Takagi, Phys. Rev. B **64**, 054415 (2001).

[30] T. Katsufuji and H. Takagi, Phys. Rev. B **69**, 064422 (2004).

Chapter-8

Conclusions and Future Scopes

This chapter mainly describes the summary, conclusion and future scopes of the results discussed in the present investigation.

8.1 Summary and Conclusions

The ultimate application of multiferroic materials for functional device desires performance at room temperature. So far, most of the reported multiferroics show weak magnetoelectric properties at RT which is the main barrier for multifunctional device applications. In order to overcome the challenges, the present thesis is devoted to the study of phase transition and magnetoelectric coupling of $BiFeO_3$ based materials. In the present work, we have synthesized nanoceramic solid solutions of $(1\text{-}x)BiFeO_3–xRMnO_3$ (R: Y^{3+}, Gd^{3+}, Dy^{3+}) (BFO-RM) for $0.0 \leq x \leq 0.2$ and $Bi_{1\text{-}x}Ba_xFe_{1\text{-}x}Zr_xO_3$ (BFO-BZ) for $0.0 \leq x \leq 0.1$ system synthesized by auto-combustion technique. These proposed samples were prepared with an aim to improve the magnetoelectric properties. The structural, microstructural, temperature dependent dielectric, ferroelectric, magnetic and magnetoelectric properties have been investigated systematically.

Based on the optimization conditions, characterization and experimental results with analyses of the data, the following summary and conclusions have been drawn.

(1) High purity polycrystalline nanoceramic BFO powders were synthesized by auto-combustion method using urea as a fuel and metal nitrates as oxidizers. The fuel to oxidizer ratio (F/O) = 0.75 is found to be the optimized condition for synthesis of single phase nanoceramic BFO [1]. Hence, all the proposed materials were prepared for F/O = 0.75 at optimized calcinations temperature to get phase pure materials. The synthesis of single phase material was confirmed using X-ray powder diffraction analysis.

(2) Crystallographic analysis of XRD data were carried out using Rietveld refinement technique for all the samples [2]. This analysis indicates that $BiFeO_3$ samples exhibit rhombohedral crystal structure with *R3c* space group. Fabrication of solid solution of BFO with $YMnO_3$ induced a compositional driven structural phase transition from *R3c* (rhombohedral) to a coexistence of rhombohedral and orthorhombic (*R3c+Pbnm*) phase beyond $x = 0.1$ [3]. But for solid solution of $BiFeO_3–RMnO_3$ (R: Gd^{3+}, Dy^{3+}), a structural transformation from rhombohedral (*R3c*) to rhombohedral plus orthorhombic

($R3c+Pn2_1a$) was observed at $x = 0.1$. All Ba-Zr co-substituted BFO samples exhibited rhombohedral crystal structure. The compositional driven structural phase transitions were well supported by the anomaly in lattice parameters and pseudo-tetragonality (c/a) ratio from x-ray diffraction analysis. With increase in RM concentration in the solid-solution, the transition from rhombohedral to rhombohedral plus orthorhombic phase is expected due to following reason: (i) the Mn^{3+} cation weakly destabilize *R3c* as compared to that of R^{3+}, whereas R^{3+} strongly destabilizes perovskite *R3c* phase due to chemical pressure of R^{3+} is much smaller than Bi^{3+} [2]. So, the fabrication of solid solution of BFO with RM drives the crystal symmetry of BFO near to the morphotropic phase boundary (MBP). Hence enhanced magnetoelectric properties were observed.

(3) Variance range and Fourier analysis of broadened X-ray line profile analysis have provided the estimation of crystallite size and strain of the samples [1, 4]. The average crystallite size of the studied materials varies in the range 200-400 Å. From the transmission electron micrographs, we have also estimated the average crystallite size of the synthesized samples and are found to be around 300 Å. The observed crystallite sizes from TEM characterization are in good agreement with that obtained from XLPA studies and are well within the calculated error bar [1-2]. The observed reflections from SAED pattern are in agreement with Rietveld refinement results.

(4) Field emission scanning electron micrographs showed that the average grain size decreases with increasing compositions for all RM and Ba-Zr modified samples. The surface morphology indicates that grains are more or less densely packed with well separated grain boundary.

(5) The temperature dependent dielectric permittivity displayed two anomalies around 215 °C and 364 °C for pure BFO. The observed anomaly around 364 °C is attributed to AFM phase transition (T_N) whereas the anomaly around 215 °C (T_{ME}) is due to the higher order magnetoelectric coupling. This higher order magnetoelectric coupling can be explained due to destruction/suppression of space modulated spin structure below magnetic ordering temperature [5-7]. The anomaly around magnetic transition temperature (T_N)

was observed from temperature dependent dielectric plot (*i.e.*, magneto-electric coupling) has been understood on the line of Gibbs's Free energy. According to Landau-Devonshire theory, the polarization and magnetization for a multiferroic system are defined as differentiation of free energy (F) [8-9],

$$M_i(\vec{E},\vec{H}) = \frac{-\partial F}{\partial H_i} = M_i^S + \mu_0\mu_{ij}H_j + \alpha_{ij}E_i + \beta_{ijk}E_iH_j + \frac{1}{2}\gamma_{ijk}E_jE_k - \ldots$$

$$P_i(\vec{E},\vec{H}) = \frac{-\partial F}{\partial E_i} = P_i^S + \varepsilon_0\varepsilon_{ij}E_j + \alpha_{ij}H_j + \frac{1}{2}\beta_{ijk}H_jH_k + \gamma_{ijk}H_iH_j - \ldots$$

Where E, H, P^s, M^s are the electric field, magnetic field, polarization, and magnetization, respectively. Here 'α' corresponds to linear magnetoelectric effect. The parameters β and γ refer to higher order magnetoelectric coefficients. The appearance of dielectric anomaly near the antiferromagnetic transitions is due to the magneto-electric coupling through the magnetoelectric coefficients (*i.e.*, α, β_{ijk} and γ_{ijk}). When the spin cycloid destroyed below T_N, antiferromagnetic order influences the ferroelectric ordering through the magneto-electric coefficients and leads to dielectric anomalies. It has also been reported that an abrupt change in lattice parameter occurs around antiferromagnetic to paramagnetic transition [10]. This implies that a structural change occurred near Neel temperature T_N and a coexistence of antiferromagnetic and paramagnetic phases leads to a structural phase boundary. Since both of the phases have different physical properties, an anomaly is expected in dielectric permittivity which is supported by Landau-Devonshire theory [6, 10]. On increasing RM and Ba-Zr compositions, T_N decreased towards room temperature, indicating the evidence of improved magnetoelectric coupling in the synthesized materials. The decrease in T_N with increase in composition could be due to reduction in unit cell volume as observed from XRD analysis [2]. Calorimetric studies displayed endothermic peak around T_N for $BiFeO_3$–$GdMnO_3$ system, further supporting the temperature dependent dielectric studies.

(6) The substitution of RM leads to an improvement in ferroelectric properties. We could not observe saturated PE loop because of variable oxidation states of Fe (Fe^{2+} to Fe^{3+}) and

low resistivity of the material [11].

(7) The complex impedance spectroscopic analysis enables us to separate the contribution of both grain and grain boundary effect from the overall electrical properties of the materials [12-18]. From the temperature dependent Nyquist plot, both the grain and grain boundary contributions have been observed at higher temperature whereas only grain contribution is observed at lower temperatures. An equivalent circuit consisting of grain and grain boundary contribution has been proposed to fit the experimental data. The assignment of equivalent circuit models were in good agreement with the experimental data. Both the grain and grain boundary resistances (obtained after fitting procedure) found to be decreased with increase in temperature for all the compositions suggesting negative temperature coefficient of resistance (NTCR) behavior like semiconductor materials [12-18]. The temperature variation of the bulk and grain boundary electrical conductivity obeyed the Arrhenius behavior suggesting the thermally activated conduction mechanism [12-18]. Two different values of activation energy calculated from the slope of Arrhenius plot of bulk conductivity suggested two different types of conduction process.

(8) Enhanced magnetic properties of the compounds were observed with increasing RM compositions. Appearance of switching effect takes place with YM modification for $x \geq 0.1$ [2]. The improvement in observed magnetization is due to suppression of spin cycloid or structural instability due to the fabrication of solid solution BFO with RM. But for $Bi_{1-x}Ba_xFe_{1-x}Zr_xO_3$, a cross-over from antiferromagnetism to weak ferromagnetism was observed at $x = 0.1$ with enhanced magnetization compared to parent $BiFeO_3$. When Fe^{3+} ions are replaced by Zr^{4+} ions in the AFM ordering of Fe^{3+}sub-lattice, the balance between two adjacent anti-parallel spin of Fe^{3+} got perturbed. Eventually a ferromagnetic interaction via oxygen, instead of antiferromagnetic coupling is preferred due to the straightening out of the Fe-O-Zr bond angle [19-20]. Hence, Zr^{4+} substitution offers a unidirectional alignment of spins in the system leading to weak ferromagnetic behavior.

(9) Room temperature magneto-dielectric and magneto-impedance studies indicated the evidence of intrinsic magnetoelectric behavior in the samples [21-23]. The magneto-

capacitance for all samples decreased with increasing magnetic field and frequency. The product of spin-pair correlation of neighboring spins and the coupling constant decide the negative or positive sign of the magneto-dielectric effect [21-23]. For Pure BFO, magneto-capacitance (MC %) enhanced up to 3.6% at 2 Tesla. Fabrication of BFO with RM lead to a significant enhancement in ME coefficient. The MC % magnitudes increased to 5.5% for $x = 0.2$, 8 % for $x = 0.15$ and 18 % for $x = 0.2$ of YM, GM and DM modified samples at 2 Tesla respectively. The observed trend in magneto-dielectric response could be interpreted as follows: (a) synthesis of nanoceramics leads to destruction/ suppression of spin cycloid. This implies that introduction of strain in the samples for all RM and Ba-Zr modified BFO samples leading to enhanced magneto-dielectric response and (b) structural investigation demonstrated an increase in lattice strain and appearance of MPB beyond $x = 0.1$ which further improves ME coupling. The bulk capacitance and resistance were calculated after fitting the magnetic field dependent Nyquist plot. It was observed that the bulk capacitance decreased on increasing magnetic field where as on the other hand the bulk resistance increased [21-23]. The observation of intrinsic magnetoelectric behavior has been verified based on the following conclusions: (i) appearance of anomaly in temperature dependent dielectric permittivity around T_N and (ii) change in the real part of permittivity on the application of magnetic field [21-23].

Hence, fabrication of nanoceramic solid solutions of $BiFeO_3$–$RMnO_3$ (R: Y^{3+}, Gd^{3+}, Dy^{3+}) and $Bi_{1-x}Ba_xFe_{1-x}Zr_xO_3$ play an important role on enhancement of the magnetoelectric multiferroic properties and its possible multifunctional device applications. This type of interesting observation on magnetoelectric properties of multiferroic nanoceramics in the present investigation is rather fascinating and stimulates further experimental exploration and theoretical explanations.

8.2 Future Scopes

In the present dissertation, it has been clearly established that both the fabrication of nanoceramic solid solution and co-substitution improve the multiferroic behavior of BFO. A lot of further studies on different aspects can also be possible for fundamental interest and also for novel multifunctional device applications.

The followings are the future scope of the present work.

(1) Novel synthesis methods such as soft chemical route for nanoceramics and thin film deposition techniques to get epitaxial thin film can also be adopted to prepare the desired materials.

(2) The *in-situ* temperature dependent X-ray diffraction and Raman spectroscopic techniques can be used to further support and study the anomalies observed from dielectric study and magnetoelectric effect.

(3) Temperature dependent Neuron scattering can be employed to study the magnetic structure of the samples.

(4) *In-situ* TEM/HRTM, Piezoforce microscopy studies can be carried out to get the information about the domain wall motion.

(5) Temperature dependent magnetic studies can be carried out to investigate the magnetic transitions and ordering in the materials.

(6) X-ray photoelectron spectroscopy and Mössbauer spectroscopy can be used to identify the oxidation state variation of the ions at different conditions for better understanding of magnetic properties.

8.3 References

1. S. N. Tripathy, B.G. Mishra, M. M. Shirolkar, S. Sen, S. R. Das, D. B. Janes, D. K. Pradhan, Mater. Chem. Phys. **141**, 423 (2013).
2. J. Rodriguez-Carvajal, Physica B **192**, 55 (1993).
3. S. N. Tripathy, K. K. Mishra, S. Sen, B. G. Mishra, D. K. Pradhan, R.Palai, and D. K. Pradhan, J. Appl. Phys. **114**, 144104 (2013).
4. D. Balzar, J. Appl. Crystallogr. **28**, 244(1995).
5. G. L. Yuan and S. Or, J. Appl. Phys. **100,** 024109 (2006).
6. L. Benguigui, Solid State Commun. **11**, 825 (1972).
7. S.M. Selbach, T. Tybell, M.A. Einarsrud, T. Grande, Chem. Mater. **19**, 6478 (2007).
8. M. Fiebig, J. Phys. D: Appl. Phys. **38**, R123 (2005).
9. K.F. Wang, J.M. Liu, Z.F. Ren, Adv. Phys. **58**, 321 (2009).
10. V. R. Palkar, J. John, and R. Pinto, Appl. Phys. Lett. **80**, 1628 (2002).
11. G. Catalan, J.F. Scott, Adv. Mater. **21**, 2463 (2009).
12. A. R. James, S. Priya, K. Uchino, and K. Srinivas, J. Appl. Phys. **90**, 3504 (2001).
13. S. Lanfredi, J. F. Carvalho, and A. C. Hernandes, J. Appl. Phys. **88**, 283 (2000).
14. M. A. L. Nobre and S. Lanfredi, J. Appl. Phys. **93**, 5557 (2003).
15. D. C. Sinclair and A. R. West, J. Appl. Phys. **66**, 3850 (1989).
16. J. R. Macdonald, Solid State Ionics, **13**, 147 (1984).
17. J. R. Macdonald, Impedance Spectroscopy, Emphasizing Solid Materials and Systems, Wiley Interscience, New York, (1987).
18. D. K. Pradhan, R. N. P. Choudhary, C. Rinaldi and R. S. Katiyar J. Appl. Phys. **106** , 024102 (2009).
19. J Wei, R Haumont, R Jarrier, P Berhtet, B. Dkhil, Appl. Phys. Lett. **96** 102509 (2010).
20. Z. Xu et al., J. Appl. Phys. **114**, 154103 (2013).
21. R. Schmidt et al., Phys. Rev. B **86**, 035113 (2012).
22. V.R. Palkar, D. C. Kundaliya, S. C. Malik and S. Bhattacharya, Phys. Rev. B **69**, 212102 (2004).
23. T. Katsufuji and H. Takagi, Phys. Rev. B **64**, 054415 (2001).

I. List of Publications (Peer reviewed Journals)

1. **Satya N. Tripathy**, B. G. Mishra, M. M. Shirolkar, S. Sen, S. R. Das, D. B. Janes and Dillip K. Pradhan, Structural, Microstructural and Magnetoelectric Properties of Single-phase $BiFeO_3$ Nanoceramics Prepared by Auto-combustion Method.
   Mater. Chem. Phys. 141, 423 (2013).

2. **Satya N. Tripathy**, K. K. Mishra, S. Sen, B. G. Mishra, Dhiren K. Pradhan, R. Palai, and Dillip K. Pradhan, Phase Transition and Magnetoelectric Coupling of $BiFeO_3$–$YMnO_3$ Multiferroic Nanoceramics.
   J. Appl. Phys. 112, 114, 144104 (2013).

3. **Satya N. Tripathy ,** Dhiren K. Pradhan , Karuna K. Mishra , S. Sen , Ratnakar Palai , Marian Paluch , James F Scott , Ram S. Katiyar , Dillip K. Pradhan, Phase Transition and Enhanced Magneto-Dielectric Response in $BiFeO_3$-$DyMnO_3$ Multiferroics
   J. Appl. Phys., Accepted (2015).

4. **Satya N. Tripathy,** Dhiren K. Pradhan, Shrabnee Sen, Braja G. Mishra, Ratnakar Palai, James F. Scott, Ram S. Katiyar, and Dillip K. Pradhan, Role of Ba and Zr Co-substitution on Dielectric and Magnetoelectric Properties of $BiFeO_{3.}$
   Submitted

5. ***Satya N. Tripathy**, K. K. Mishra, S. Sen and Dillip K Pradhan, Dielectric and Raman Spectroscopic Studies of $Na_{0.5}Bi_{0.5}TiO_3$–$BaSnO_3$ Ferroelectric System.
   J. Am. Ceram. Soc., Accepted (2014)

6. *Karuna K. Mishra, A.K. Arora, **Satya N. Tripathy**, Dillip K. Pradhan, Dielectric and polarized Raman spectroscopic studies on $0.85Pb(Zn_{1/3}Nb_{2/3})O_3$- $0.15PbTiO_3$ single crystal.
   J. Appl. Phys. 112, 073521 (2012).

7. *Dhiren K. Pradhan, Venkata S. Puli, **Satya N. Tripathy**, Dillip K. Pradhan, J. F. Scott, and Ram S. Katiyar , Room Temperature Multiferroic Properties of $Pb(Fe_{0.5}Nb_{0.5})O_3$ –$Co_{0.65}Zn_{0.35}Fe_2O_4$ Composites.
   J. Appl. Phys. 114, 234106 (2013)

8. *Dillip K. Pradhan and **Satya N. Tripathy**. Effect of Plasticizer Concentration on Microstructural and Dielectric Properties of Polymer Composite Electrolyte.
   Advances in Chemical Sciences, 2, 114, (2013).

* Not Related to Thesis Work.

II. Conference Proceedings

1. Synthesis and Characterization of Single Phase $BiFeO_3$ Nanoceramics, **Satya N. Tripathy**, B.G.Mishra, R.N.P Choudhary and Dillip K. Pradhan, National Seminar on Physics and Technology of Novel Materials (PTNM-2010), 25-27th, February 2010, Sambalpur University, Orissa, India.

2. Structural and Microstructural Properties of $BiFeO_3$ Nanocramics. **Satya N. Tripathy**, B.G.Mishra, R.N.P Choudhary and Dillip K. Pradhan, XVI National Seminar on Ferroelectrics and Dielectrics (NSFD- XVI). 2nd to 4th December, 2010, Department of pure and Applied Physics, Guru Ghasidas University, Bilaspur (C.G).

3. X-ray Line Broadening Analysis and Ferroelectric Properties of Single Phase $BiFeO_3$ Nanoceramics, **Satya N. Tripathy**, Shrabanee Sen and Dillip K. Pradhan, 2nd National Seminar on Physics and Technology of Novel Materials (PTNM II- 2012), 10-11th, March, 2012, Sambalpur University, Orissa, India.

4. Structural, Electrical and Magnetic Properties of $BiFeO_3$-$YMnO_3$ Nano-sized Solid Solution **Satya N. Tripathy,** B.G.Mishra and Dillip K Pradhan, XVII National Seminar on Ferroelectrics and Dielectrics (NSFD- XVII). 17th to 19th December, 2012, Department of Physics, Siksha 'O' Anusandhan University ITER,Bhubaneswar, Odisha-751030. **(Best Poster Award).**

5. Dielectric and Raman Spectroscopic studies on $(1-x)Na_{0.5}Bi_{0.5}TiO_3$-$xBaSnO_3$ Lead free ferroelectrics. Dillip K Pradhan, **Satya N. Tripathy**, Karuna Kara Mishra XVII National Seminar on Ferroelectrics and Dielectrics (NSFD- XVII). 17th to 19th December, 2012, Department of Physics, Siksha 'O' Anusandhan University ITER, Bhubaneswar, Odisha-751030.

6. Evidence of Intrinsic Magnetoelectric Coupling in $BiFeO_3$-$GdMnO_3$ Nano-sized Solid solution, Dillip K. Pradhan, **Satya N. Tripathy**, Dhiren K. Pradhan, and R. Palai International Conference on Multifunctional Materials, 5th -7th February, 2014, Materials Science Centre, IIT, Kharagpur-721302 (WB).

7. Studies of Structural and Magnetoelectric Properties of $Bi_{1-x}Ba_xFe_{1-x}Zr_xO_3$ Nanoceramics. **Satya N. Tripathy**, Dhiren K. Pradhan, S. Sen, R. Palai, and Dillip K. Pradhan International Conference on Multifunctional Materials, 5th -7th February, 2014, Materials Science Centre, IIT, Kharagpur-721302 (WB).

Satya Narayan Tripathy
Curriculum Vitae

Satya N. Tripathy
Ferroics Laboratory,
Department of Physics and Astronomy,
National Institute of Technology, Rourkela
Rourkela-769008, Odisha, INDIA.
Email: satyanarayantripathy@gmail.com
Mobile: +91-9124042466

Educational Qualification

Ph. D. Condensed Matter Physics: (2009-2014) National Institute of Technology, Rourkela, India. **(9.81 cgpa/10) (Advisor:** Prof. Dillip K. Pradhan**)**

M. Sc. Physics: (2007-2009) National Institute of Technology, Rourkela: **(8.01 cgpa /10)**

B. Sc. Physics: (2004-2007) B. J. B Autonomous College, Bhubaneswar: **87.37% (Topper)**

+2: (2002-2004) B.J.B Junior College, Bhubaneswar: **80.66%**

10th Govt. High School Unit-1, Bhubaneswar. **84.8%**

Area of Interset

Multiferroics, Ferroelectrics, X-ray Crystallography, Glass Transition.

Award/ Significant achievements

(1) Physics (Hons.) Topper 2007 in B.J.B, Autonomous College, Bhubaneswar, Odisha.

(2) Best Poster Award at XVII National Seminar on Ferroelectrics and Dielectrics (NSFD XIV), 17-19, Dec. 2012, Siksha 'O' Anusandhan University, ITER, Bhubaneswar.

(3) Qualified GATE 2009 and National Top 1% in IAPT Exam 2007.

Personal Details

Father's Name	Purna Chandra Tripathy
Mother's Name	Pramodini Tripathy
Date of Birth	02-06-1986
Sex	Male
Nationality	Indian
Category	General
Language Known	English, Hindi, Oriya
Residential Address	Q. No-17/6, Type-II Unit-I, Bhubaneswar-751009 Odisha, INDIA